New Catalysts for Advanced Biofuels Synthesis and Cooperative Catalysis

Taha Alghamdi

A dissertation submitted to Cardiff University in accordance with the requirements for the award of the Degree of Doctor of Philosophy in the School of Chemistry.

January 2025

Abstract:

This thesis investigates the catalytic upgrading of lower alcohols, such as ethanol and methanol, into higher-value alcohols through the Guerbet reaction, focusing on the production of isobutanol. The Guerbet reaction offers significant potential for sustainable biofuel synthesis, and this work addresses key aspects of catalyst design, ligand effects, and reaction condition optimisation.

Key advances are presented in using monodentate phosphine ligands with ruthenium catalysts, achieving high yields and selectivity for isobutanol production. The electronic and steric properties of ligands were systematically analysed, demonstrating the importance of balancing these effects to stabilise reactive intermediates and minimise undesirable side reactions. A detailed study of cone angles and electronic parameters provides valuable guidance for optimising ligand design and catalytic performance.

The work also highlights the promising role of 1,1'-bis(diphenylphosphino)ferrocene (dppf) ligands in enhancing catalytic activity. Combining ruthenium catalysts with dppf significantly improved the upgrading of ethanol and methanol, resulting in higher yields and improved selectivity. These findings underline the potential of bidentate ligands to advance biofuel catalysis and bridge the gap between academic research and industrial applications.

Additionally, the thesis explores the synthesis and characterisation of Frustrated Lewis Pair (FLP) systems as a novel contribution to catalytic research. Palladium-based FLPs were successfully synthesised, offering new insights into their structural and electronic properties. While this study did not evaluate their catalytic performance, these systems lay the groundwork for future research into hydrogen activation and alcohol upgrading applications.

This thesis contributes to the broader understanding of homogeneous catalysis and its role in sustainable energy solutions by addressing challenges in catalytic efficiency, selectivity, and stability. The findings provide a foundation for advancing isobutanol production and support the development of greener biofuel technologies.

Acknowledgement

Embarking on my PhD journey was not just an academic pursuit, but a transformative period filled with challenges and triumphs. As I stand at the final stages of this incredible journey, I am grateful for the unwavering support and encouragement that shaped my path.

Firstly, I express my profound appreciation to Professor Duncan Wass, my supervisor and mentor. His steadfast support during the personal challenges, demonstrated true mentorship. Professor Wass's guidance and understanding were instrumental in navigating through the storm. I am profoundly grateful for his presence in my academic life.

To my parents and family, your love and support were my anchor when my life felt adrift. Your encouragement helped me regain my footing, and your unwavering belief in my capabilities fuelled my determination to succeed.

My heartfelt thanks go to my beloved wife, Bayan, whose presence brought joy and stability to my life. Her love and positivity were transformative, making every challenge more manageable and every success more meaningful.

I extend my gratitude to Dr Richard Wingad and Dr Prashant Kumar, whose guidance and collaboration in the lab enriched my research experience. Their expertise and camaraderie were invaluable during my academic pursuits.

A special note of gratitude to the government of Saudi Arabia for their sponsorship and financial support throughout my PhD. Their investment in my education has been a cornerstone in realising this academic achievement.

I would also like to acknowledge every member of our research group. Your camaraderie and support, both in academic and personal matters, created a nurturing environment that fostered success. To all who were part of my PhD journey, big or small, your contributions have not gone unnoticed. Thank you for being there when I needed support, encouragement, and understanding.

Table of Contents:

List of Tables:

List of Figures:

List of Schemes:

List of Abbreviations:

ABE	Acetone-Butanol-Ethanol
ABV	Alcohol by Volume
AC	Aldol Condensation
Ar	Aryl
BAF	Tetrakis[3,5-bis(trifluoromethyl)phenyl]borate
COD	1,5-Cyclooctadiene
Cp	Cyclopentadienyl
Cp*	Pentamethylcyclopentadienyl
Cy	Cyclohexyl
d	Doublet
DCM	Dichloromethane
DH	Dehydrogenation
diip	di-*iso*-propyl
d^{i}ppf	1,1’-Bis(di-*iso*-propylphosphino)ferrocene
DMSO	Dimethyl Sulfoxide
dppb	1,4-Bis(diphenylphosphino)butane
dppf	1,1’-Bis(diphenylphosphino)ferrocene
dppm	1,1-Bis(diphenylphosphino)methane
d^{t}bpf	1,1’-Bis(di-*tert*-butylphosphino)ferrocene
ESI-MS	Electrospray Ionisation Mass Spectrometry
EtOH	Ethanol
Et_2O	Diethyl ether
GC	Gas Chromatography
h	hour
HAP	Hydroxyapatite
^{i}Pr	*iso*-propyl
LA	Lewis Acid
LB	Lewis Base
m	Multiplet
Me	Methyl
MEK	Methyl Ethyl Ketone (Butanone)
MeOH	Methanol
Mes	Mesityl
NMR	Nuclear Magnetic Resonance
OMe	Methoxy
o-tol	*ortho*-tolyl
PPh_3	Triphenylphosphine
ppm	Parts per Million
PTFE	Polytetrafluoroethylene
q	Quartet
RDS	Rate-Determination Steps
s	Singlet
sept	Septet
^{t}Bu	*tert*-butyl

Chapter 1: Introduction

1.1. Fossil Fuels

Global energy demand has steadily risen, with fossil fuels dominating the energy mix. According to recent reports, fossil fuels accounted for over 80% of the global primary energy consumption in 2021, highlighting the persistent reliance on these sources despite the increasing focus on renewable energy alternatives.[1] The continued reliance on fossil fuels significantly contributes to environmental issues, particularly greenhouse gas emissions, which drive climate change.[2] The urgent transition to cleaner energy alternatives is critical to addressing these global challenges.[3] The process of fractionation and refining crude oil yields a range of liquid transportation fuels, producing different grades. Among these fuels, petrol is prominent in the global transportation fuel market.[4] Fossil fuels are utilised for the purpose of electricity generation as well as in many manufacturing operations. Intermediate and speciality chemicals are produced by extracting hydrocarbons from crude oil.

Fossil fuels derive their name from their origin, as they have been formed from the transformation of ancient organic matter over millions of years.[5] Hence, these fuel sources are finite, characterised by limited reserves, and are currently undergoing rapid depletion worldwide.[6]

The concentration of fossil fuel deposits is limited to a few places, resulting in a reliance of numerous nations on a select few. This phenomenon exposes states that rely on external sources for their fuel supply to several vulnerabilities, such as the unpredictability of fuel availability due to natural disasters, political instability, or armed conflicts. Additionally, these nations are susceptible to swings in fuel costs.

Upon combustion, fossil fuels emit carbon dioxide (CO_2) in amounts directly proportional to the number of carbon atoms in the fuel. Assuming an average petrol vehicle achieves approximately 22.2 miles per gallon and covers around 11,500 miles annually, each gallon of petrol burned results in the emission of about 8,887 grams of CO_2.[7] The use of fossil fuels has increased atmospheric carbon dioxide (CO_2)

levels by around 70 parts per million (ppm) compared to the pre-industrial era.[8] The present concentration of atmospheric CO_2 reflects a notable rise of 20% over the past Century.[9] Figure 1-1 depicts CO_2 emissions over the past two centuries, highlighting a marked increase starting from the early 20th century.

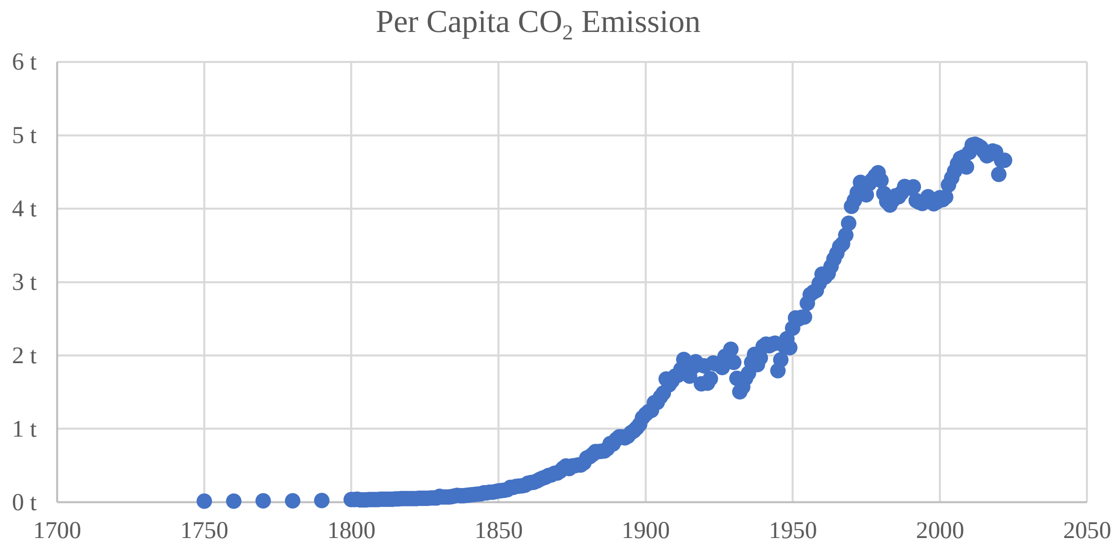

Figure 1-1: Adapted per capita CO_2 emissions from fossil fuels and industry. Data source: Global Carbon Budget (2023); Population based on various sources (2023), OurWorldInData.org/co2-and-greenhouse-gas-emissions | CC BY

The increasing concentration of atmospheric CO_2 drives global warming due to its role as a greenhouse gas. CO_2 absorbs infrared radiation from the Earth's surface, trapping heat in the atmosphere and increasing surface temperatures. This process, known as the greenhouse effect, leads to significant changes in climatic patterns, including desertification, rising sea levels, and the increased intensity and frequency of extreme weather events such as storms.[10]

The combustion of fossil fuels is known to have adverse impacts on human health. In addition to carbon dioxide (CO_2), various other chemicals are emitted, which harm the ecosystem. The combustion of fossil fuels results in heightened levels of air pollution, particularly inside urban areas. Emitting sulphur dioxide (SO_2) and nitrogen oxides (NO_x) leads to acid rain. Numerous contaminants that threaten human health, including carbon monoxide, hydrocarbons, and particulate matter, are also emitted.[8]

Fossil fuels are a finite resource, subject to price and supply fluctuations. Their combustion is a primary driver of climate change due to releasing significant amounts of carbon dioxide (CO_2) and other greenhouse gases. Additionally, fossil fuel extraction and use have adverse environmental effects, such as habitat destruction and air and water pollution.[10] These issues can be summed up as challenges with fossil fuels. Finding energy sources other than fossil fuels is urgently needed due to the expanding global population, accelerated technological advancement, and escalating economic and social growth. Using and developing dependable, sustainable, and, ideally, environmentally neutral energy sources require long-term planning. As a result, interest in supposedly "renewable energy" is booming. Solar, tidal, wind, geothermal, nuclear, and biomass energy are sustainable fuels that can replace fossil fuels. By being sustainable, enhancing socioeconomic conditions, and having minimal environmental impact, renewable energy sources outperform the drawbacks of fossil fuels.

1.2. Biofuels

Some 90% of the total energy produced in 1830 came from renewable sources, such as wood.[9, 11] By 1900, biomass and coal accounted for approximately an equal proportion of energy sources, while petrol contributed a tiny fraction to the overall energy output. However, by 1975, coal and petrol emerged as the predominant energy sources. Renewable fuels are seeing a comeback as an alternative energy source due to the issues connected with fossil fuels, as outlined in Section 1.1. The representation (Figure 1-2) illustrates the predominant worldwide energy consumption attributed to various energy sources from 1970 to projected figures for the year 2040.[12]

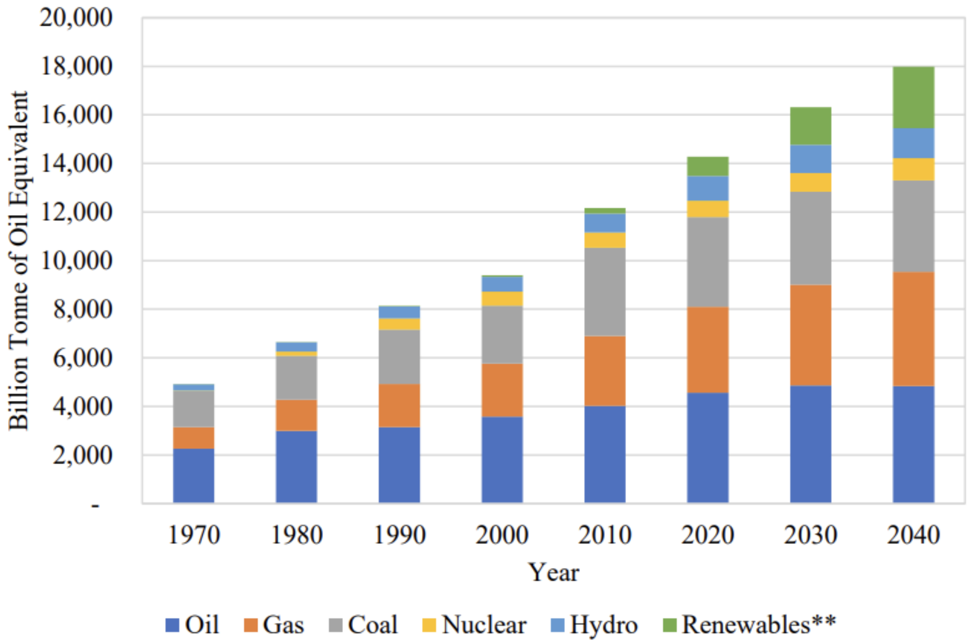

Figure 1-2: Sources of primary energy demand from 1970 to 2040. Figure adapted from BP Energy Outlook 2018.[12] This was the last edition in which the data was presented in this specific format.

Renewable energy encompasses several sources, such as wind, solar, geothermal, and biofuels. During the initial years of the 21st Century, renewable energy sources constituted an estimated range of 1.5% to 3.5% of the primary energy supply.[12-13] This category of energy sources is expected to increase the fastest, contributing 14% of the world's primary energy consumption by 2040.

Because it is plentiful and sustainable, biomass is the perfect renewable fuel source. For thousands of years, humans have used biomass (mainly wood) as a source of energy. Animal-based biomass, such as animal fat, is also employed as a fuel source, although it is frequently thought of as being derived from plants. The work in this thesis is relevant to developing biofuels made from biomass produced by plants. The term "biofuel" encompasses all forms of solid, liquid, and gaseous fuels generated from biomass.[6] Biofuels are classified as those obtained from biomass, either whole or partially. This characteristic of deriving from biomass offers the benefit of being an environmentally friendly and sustainable carbon source.[13-14] Biomass is considered a renewable resource due to its ability to be replenished. For instance, when a plant crop is harvested for the production of biofuel, it has the potential to be regrown. In principle, it is widely acknowledged that this particular substance is CO_2 neutral, as the quantity of CO_2 emitted during combustion is proportional to the amount absorbed during the growth of the biomass material.[6, 8] While this assertion generally remains valid, it is crucial to exercise caution in handling biomass to ensure the preservation of CO_2 neutrality. This caution is essential when contemplating the various processes involved in biomass production, such as the fertilisation of food crops or the clearance of land.[15] The primary source of liquid transportation fuels is derived from fossil fuels, highlighting the need to investigate alternative sources to support the shift towards a sustainable green energy economy. Three main categories of biomass feedstocks are commonly used to produce renewable liquid fuels. These include starchy feedstocks, which are primarily used in the production of bioethanol; triglyceride feedstocks, which are employed in the production of biodiesel; and lignocellulosic feedstocks, which are utilised in the production of second-generation bioethanol as well as intermediate chemicals with practical applications.[16] In the context of renewable energy sources, biodiesel, bioethanol, and biobutanol are the only liquid forms available. This thesis focuses on liquid biofuels that exhibit the capacity to function as a viable alternative to petrol.

When inquiring about a potential substitute for petrol, alternative fuels must meet some pre-established requirements. The fuel must exhibit environmental friendliness and cost-effectiveness, encompassing production and consumer considerations. Furthermore, it is imperative to maintain investment expenditures at a fair level to fuel development, manufacture, and utilisation. For the fuel to be considered feasible, it must exhibit energy content that is on par with conventional fossil fuels while also being economically competitive. Furthermore, it would be beneficial if the fuel exhibits compatibility with the current distribution infrastructure, specifically petrol stations, and can be efficiently employed in internal combustion engines. By ensuring strict adherence to this compatibility condition, renewable fuels can effectively serve as seamless alternatives to petrol, supporting a smooth transition towards sustainable fuel usage. For biofuels to become a viable alternative to fossil fuels, biomass must be derived from crops that exhibit specific attributes. These attributes include minimal maintenance needs, the capacity to flourish in less fertile and, therefore, less valuable land, high productivity, rapid growth, and cost-effectiveness in the production process.[6, 13]

1.3. Alcohols as Sustainable Alternatives to Petrol

1.3.1. Bioethanol:

Bioethanol is widely recognised as the primary liquid biofuel on a global level.[14, 16] The recognition of bioethanol's potential as a liquid transportation fuel dates back to the early 1900s when Henry Ford constructed the first combustion engine designed expressly for ethanol operation.[8-9, 16] However, ethanol was eventually replaced due to the widespread availability of cost-effective petrol fuels.[17] In the present period, there is a growing need to prioritise fuel security, manage the fluctuations in fossil fuel prices, and address environmental concerns. As a result, there has been a resurgence of interest in utilising ethanol as a feasible alternative to petrol.

Ethanol production can be accomplished by the ethylene hydration process facilitated by an acid catalyst, typically phosphoric acid.[17] This procedure's successful implementation requires applying severe reaction parameters, including temperature ranges of 250 to 300 °C and pressure ranges of 60 to 70 atm. Furthermore, the ethylene feedstock utilised in this process is obtained from either petrol or natural gas sources. This method is utilised worldwide to produce approximately four billion litres of ethanol.[11] In an alternative methodology, the sugars found in biomass undergo a series of fermentation processes, producing ethanol, commonly referred to as bioethanol. The primary approach utilised in commercial environments for ethanol generation involves the exploitation of the yeast strain *Saccharomyces Cerevisiae*.[18] Nevertheless, various microorganisms can also be utilised for this specific objective (see Section 1.3.1.1 for more information). Different sources of sugar undergo fermentation, with the choice of source being determined by their availability and suitability for the particular bioethanol production setting. The combustion of bioethanol leads to the release of carbon dioxide (CO_2). However, it is noteworthy that atmospheric CO_2 can undergo a further transformation into sugars through photosynthesis. Fossil fuels are utilised in the bioethanol manufacturing process, yet, a positive energy balance is found, resulting in the generation of 9.3 units of renewable energy for every unit of fossil fuel consumed. This good outcome is particularly evident when sugarcane is exploited as a biomass source. Moreover, there is anticipated to be a potential rise to 11.6 units of renewable energy soon due to technological advancements.[17] The yearly bioethanol production of the United States and Brazil exceeds 94 billion litres, constituting approximately 85% of the global output.[17, 19] Corn is the predominant source of fermentation biomass in the United States, while sugarcane is the preferred crop in Brazil owing to its environmental suitability. To reduce its reliance on a limited number of oil-producing nations after the oil crisis of the 1970s, the Brazilian government supported the use of bioethanol, initially as a supplementary component for petrol and subsequently as an environmentally friendly fuel for cars.[17] The utilisation of bioethanol in Brazil had fluctuations in popularity due to fluctuations in oil prices. However, as the 21st Century commenced, bioethanol emerged as the dominant fuel in the market.[17] Brazil exhibits a notable presence of fuel-flexible automobiles within its market, with an adequate percentage of vehicles made in 2015, precisely 85%, equipped with this feature. Moreover, a significant percentage, amounting to 40% of the fuel consumed by cars in Brazil is derived from bioethanol sources.[20] These vehicles possess the capacity to operate on either pure ethanol or ethanol-petrol blends, with automatic adjustments made to the engine to facilitate the efficient utilisation of either fuel option. Despite its relatively lower level of industrialisation, Europe is a significant bioethanol producer. The primary biomass sources for European bioethanol production include sugar beetroot, wheat, and residual waste from winemaking.

Table 1-1: A comparison of fuel properties of petrol, ethanol, and 1-butanol.

Properties	**Petrol**	**Ethanol**	**1-Butanol**
Density, g/mL at 20 °C	0.69-0.80	0.79	0.810
Atmospheric boiling point, °C	27-225	78	118
Latent heat of vaporisation, MJ/L at 20 °C	0.251	0.662	0.474
Flash point, °C	-43 to -39	12.8	35
Autoignition point, °C	257	423	385
Energy density, MJ/L	32	19.6	29.2
Air-to-fuel ratio	14.6	8.9	11.2
Water solubility, %	negligible	100	7
Octane number	88-99	108-129	96
Vapour pressure, kPa at 38 °C	42-103	16	2.3

Values combined from several literature sources.[8, 11, 20-21]

Two significant benefits of bioethanol are its sustainability and availability. The existing infrastructure is sufficient for the large-scale production of bioethanol. Unfortunately, ethanol exhibits a lower energy density than petrol, as seen in Section 1.3.1.3. However, bioethanol presents certain advantages. Table 1-1 presents a comparative analysis of the fuel properties of bioethanol and petrol. Bioethanol is utilised as a fuel additive to boost the octane rating of petrol due to its superior octane number compared to petrol.[21h, 22] Ethanol exhibits potential for application in thermally efficient engines with high compression ratios since it demonstrates a capacity to withstand higher compression levels without experiencing the phenomenon of engine knocking. This phenomenon leads to enhanced power generation and improved fuel efficiency compared to traditional compression engines.[8-9, 20, 22] Nevertheless, these engines still exhibit lower efficiency compared to their petrol equivalents. As a result, ethanol is commonly blended with petrol at a proportion of 10% (E10), making it compatible with unmodified engines. Alcohols have a high degree of combustion efficiency and a lower air-to-fuel ratio than petrol, reducing carbon monoxide emissions (CO). Alcohols can be classified as fuels that undergo partial oxygenation.[11, 21h] When subjected to combustion, alcohol-based fuels exhibit lower nitrogen oxides (NO_x) and hydrocarbon emissions than petrol.[8, 22] Ethanol presents enhanced safety characteristics in terms of transportation and storage owing to its comparatively higher autoignition and flash point temperatures than petrol.[21h] Since bioethanol is derived from crops, it can be produced close to where it is required, eliminating the need for transportation and allowing local communities to become independent of external fuel sources.[13] The crops used to make bioethanol should be adapted to the environment in which they will be consumed. For instance, bamboo has been considered a suitable crop in China,[23] while poplar trees and potatoes have also been studied as potential sources of bioethanol in Spain and Tunisia, respectively.[24]

1.3.1.1. The Fermentation Process:

Plants use the process of photosynthesis to transform atmospheric carbon dioxide (CO_2) and water into carbohydrates and oxygen.[6, 11] *Photosynthesis*, a unique natural process, is a testament to the wonders of life on Earth. Organisms containing chlorophyll, such as green plants, algae, and certain bacteria, harness light and convert it into chemical energy. The sun, the primary energy source, powers this process in the Earth's biosphere, where life thrives. This makes photosynthesis a vital mechanism for sustaining life on the planet.[6] A generalised, unbalanced chemical equation for photosynthesis is as follows:

$$CO_2 \quad + \quad 2\,H_2A \quad + \quad \text{Light Energy} \quad \longrightarrow \quad (CH_2O) \quad + \quad H_2O \quad + \quad A_2$$

Scheme 1-1: General equation for photosynthesis

The formula H_2A denotes a substance capable of undergoing oxidation, meaning it can lose electrons. On the other hand, CH_2 is a generic formula used to describe the carbohydrates the developing organism assimilates. Algae and green plants comprise the bulk of photosynthetic organisms, use water (H_2O) as H_2A and produce oxygen (O_2) as A_2, the most crucial and comprehensively studied process. However, many photosynthetic bacteria use hydrogen sulphide (H_2S) as H_2A instead.[6]

Photosynthesis unfolds in two distinct stages: a series of light-dependent reactions, impervious to temperature, and a series of temperature-dependent reactions, unaffected by light. The rate of the first series, known as the light reaction, can be amplified by increasing light intensity (within specific limits), but temperature has no such effect. Conversely, the rate of the second series, known as the dark response, can be accelerated by raising the temperature (within specific boundaries) but not by increasing the intensity of light. This intricate interplay between light and temperature underscores the profound nature of photosynthesis, leaving us in awe of its complexity.[6]

The diagram presented in Scheme 1-2 illustrates the equation representing the photosynthetic process leading to the synthesis of glucose in presence of light energy. In addition to its role as an energy source, glucose is the precursor for several essential biosynthetic compounds. The configuration of the anomeric carbon is responsible for the manifestation of glucose in either the α- or β-form.

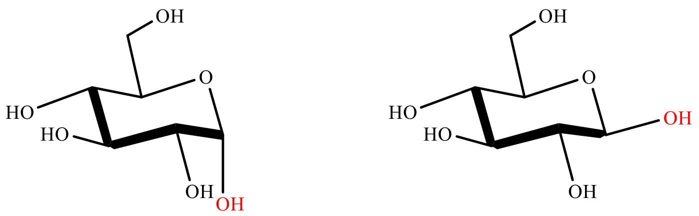

α-Glucose β-Glucose

Scheme 1-2: General equation describing the structure of glucose and its production during photosynthesis.

Glycosidic linkages facilitate binding sugar molecules, such as glucose, to one another. The 1,4'-glycosidic linkage, which connects the C_1 anomeric carbon of one glucose monomer with the C_4 alcohol of another glucose monomer, holds importance in the fermentation process. The connection between glucose polysaccharides, cellulose and starch can be observed in Figure 1-3. The complicated structure of starch comprises many polysaccharides, namely amylose and amylopectin.[11, 16, 25]

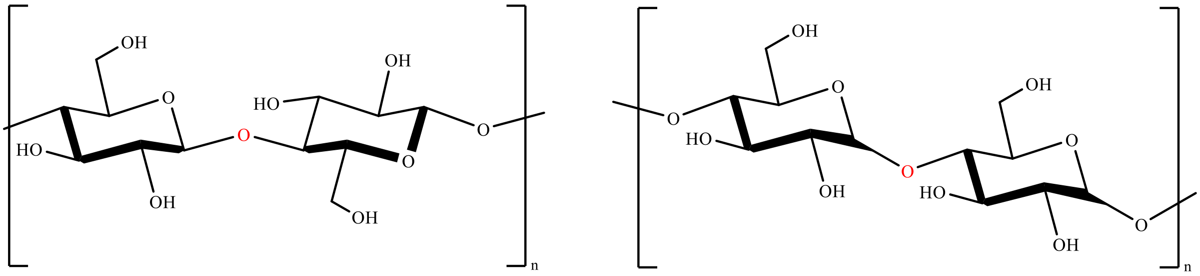

Cellulose Amylose

Figure 1-3: The structure of cellulose and amylose

Cellulose and starch are composed of glucose monomers but differ in the glycosidic linkage type present. Cellulose has β-glycosidic links, whilst α-glycosidic connections characterise starch. This distinction in the stereochemistry of the glycosidic linkage sets these two polysaccharides apart.[6] The production of bioethanol carries substantial ramifications. The stereochemistry of cellulose presents challenges in accessing glucose monomers due to the resistance of β-linkages to hydrolysis, in contrast to the relative ease with which starch may be hydrolysed. Humans cannot digest items containing cellulose due to the exact underlying cause. Hence, the primary focus of first-generation bioethanol production is using quickly processed starch and monosaccharide feedstocks obtained from edible crops, employing well-established technology.[9, 26] Fermentable sugars can be obtained from crops like sugarcane, corn, potatoes, sugar beets, and wheat, with the latter serving as Europe's primary bioethanol supply.[8, 27] Sources of simple monosaccharides, such as sugarcane molasses, can initiate fermentation with minimal necessary processing. Nevertheless, to utilise disaccharides or starch as energy sources, it is necessary to provide the yeast with accessible monosaccharide sugars.[17, 26a] Figure 1-4 briefly summarises the sequential stages involved in the fermentation process for ethanol production.[16, 28] The rigidity of the material's cellular walls is disrupted by grinding or milling methodologies, facilitating the extraction of sugars. The disaccharide or polysaccharide is subsequently subjected to hydrolysis using either diluted acid treatment or enzyme-catalysed hydrolysis. This process breaks down the sugars into monosaccharides, such as glucose and fructose, which can then undergo fermentation.[11] However, it is essential to undergo pre-treatment to extract fermentable sugars from other biomass sources, such as lignocellulosic biomass (refer to Section 1.3.1.2).

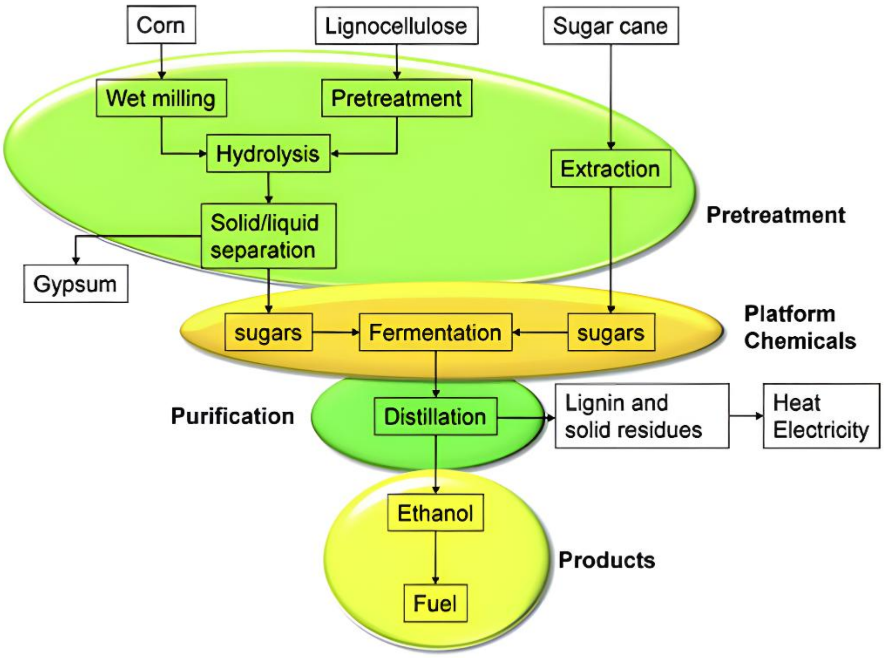

Figure 1-4: The stages of bioethanol production.[29]

Microorganisms ferment the free glucose monomers to create ethanol and carbon dioxide (Scheme 1-3).[11, 30] Various yeast strains, including bacteria and members of the *Saccharomyces* family, can carry out fermentation.[17, 28a] Glycolysis, the initial stage of fermentation, is the process by which glucose is split into two pyruvate molecules. The following step involves the conversion of pyruvate to acetaldehyde, which releases carbon dioxide. Acetaldehyde is then converted to ethanol. The fermentation broth (the effluent from the fermenter), generally produced in a batch operation over two days, will have an ethanol concentration between 8 and 15 wt.%.[11, 31] Following distillation to remove impurities, the remaining fermentation broth yields pure bioethanol.[11] The first distillation raises the ethanol content to 55 wt.%. The ethanol concentration is subsequently raised to 95 wt.% through a second distillation, with the concentration being constrained by the azeotropic ethanol: water mixture. The next step is to obtain anhydrous, or absolute, ethanol using either azeotropic distillation with benzene, cyclohexane, or drying agents such as molecular sieves.

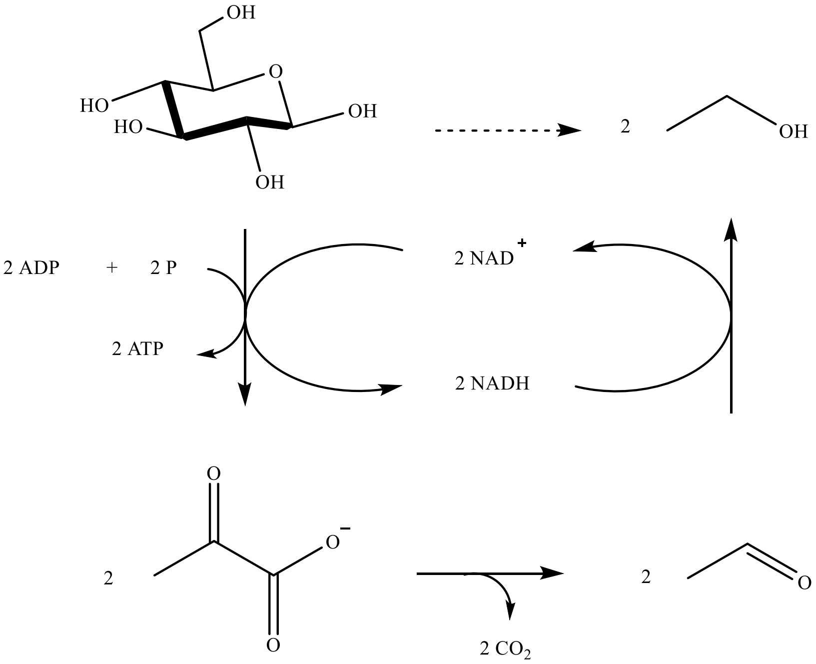

Scheme 1-3: Fermentation of glucose into ethanol and CO_2 with a streamlined procedure.[32]

1.3.1.2. Second and Third Generation Bioethanol

While the crops mentioned in Section 1.3.1.1 are considered suitable feedstocks for bioethanol production, the "food vs. fuel" debate negatively impacts the reputation of first-generation bioethanol.[21e, 33] In light of the global food shortage, a prevalent argument suggests that using food crops for bioethanol production should be reconsidered. The question arises about whether it is justifiable to allocate arable land for fuel production instead of food production. The production of bioethanol from food crops may lead to an increase in food expenses. As a result, notable progress has been made in producing "second generation" bioethanol, derived from lignocellulosic material present in plant cell walls, instead of being sourced from food-based materials.[16, 26, 33a] This substance is widely available and can be found in various forms of botanical matter, resolving the ongoing discourse surrounding the conflict between food and fuel, as it is indigestible by the human body. Grass and trees are viable sources of lignocellulose due to their ability to thrive in poor soil conditions. Additionally, waste materials such as sugarcane bagasse, rice straw, sago hampas, food waste, and paper manufacturing waste can also serve as excellent sources of lignocellulose.[13, 34] Waste lignocellulosic material, generated globally exceeding 2 x 10^{11} tonnes per year, is the primary source of carbohydrates.[21e, 35] Nevertheless, the processing of lignocellulosic material presents more significant challenges than starch.[21e, 36] The cost of bioethanol derived from lignocellulosic feedstocks is approximately twice as high as that of first-generation bioethanol, primarily attributed to the complexities involved in its production process.[16]

The lignocellulosic biomass primarily comprises three primary constituents: cellulose, hemicellulose, and lignin. Cellulose constitutes the most significant proportion (40-50%) of the lignocellulosic structure, followed by hemicellulose (25-35%) and lignin (15%).[6, 9, 11, 16, 25, 34] Lignin is a polymer characterised by its ability to provide structural rigidity and hydrophobic properties, which consists of phenylpropane molecules that have been methoxylated.[6] The hemicellulose polymer comprises of five sugar monomers: D-xylose (the most abundant monomer), L-arabinose, D-galactose, D-glucose, and D-mannose.[6] Cellulose, a polysaccharide consisting of glucose molecules connected by 1,4'-β-glycosidic bonds, provides strength and rigidity through its ability to prevent hydrolysis. The fermentation of bioethanol relies on the cellulose component present in lignocellulose. However, the extraction and hydrolysis processes present challenges since the sugars are enclosed within the cell walls of hemicellulose and lignin. In order to eliminate the protective matrix and extract the cellulose, the lignocellulosic material requires expensive pre-treatment in challenging conditions.[13-14, 37] Various physical and chemical pre-treatment approaches can be employed prior to enzyme hydrolysis, such as alkaline hydrogen peroxide treatment, acid and ammonia treatment, steam explosion, or solvent treatment.[17, 38]

The application of genetic engineering is now under investigation to improve the cost-effectiveness of second-generation bioethanol production through enhanced cellulose extraction from the cell wall.[33a, 39] The genetic composition of crops can be modified to improve the availability of cellulose.[13] For example, this might potentially compromise the structural integrity of the protective matrix's lignin, pectin, and hemicellulose components, thereby facilitating the accessibility of cellulolytic enzymes and promoting the hydrolysis of cellulose.[39a] An alternate option involves the utilisation of paracrystalline cellulose, which has a greater surface area available for interaction with cellulolytic enzymes, hence facilitating its degradation compared to crystalline cellulose.[39a] Rather than directly modifying the cell wall's composition, an alternative approach focuses on modifying the organisms that can disrupt cell walls. This approach has allocated equal importance to utilising both yeast and bacteria.[39a] The utilisation of algae for the production of third-generation bioethanol is an emerging technological advancement.[6, 16, 28a, 34, 40] Algae has unique benefits compared to plant crops, as it does not require arable land, fertilisers, or pesticides, has minimal environmental impact, and consumes less water. In contrast to other crops, algae can be grown throughout the year. Compared to alternative biomass sources, algae exhibit a higher capacity for biomass production per hectare.[40] Nevertheless, third-generation bioethanol development is in its infancy, and its influence on the energy market is not expected to be significant for several years.

1.3.1.3. Disadvantages of Bioethanol:

Despite the environmentally friendly attributes associated with bioethanol, its widespread usage is hindered by several disadvantages, as indicated in Table 1-1.[41] The miscibility of ethanol with water poses significant challenges regarding storage and transportation, and this is due to the ability of ethanol and water to separate and dilute within tanks, hence complicating the transportation of ethanol through pre-existing infrastructure. Ethanol shows corrosive properties towards engines, fuel systems, and infrastructure, with the level of corrosion intensifying as the ethanol concentration in petrol-ethanol mixes rises.[8] The relatively lower vapour pressure than petrol poses challenges for initiating cold starts.[21b, 22] The volumetric energy density of ethanol is around 66% of that of petrol[21h], indicating that a smaller amount of energy is generated during the combustion of bioethanol compared to petrol when considering similar fuel volumes. As an illustration, it can be observed that the fuel consumption in E100 engines exhibits an approximate increase of 50% in comparison to petrol engines, mainly due to the reduced energy density associated with E100 fuel.[11, 20, 21e, 22]

While bioethanol is frequently used in petrol blends, conventional petrol-powered cars require modifications to utilise pure bioethanol as a fuel due to the different combustion characteristics of ethanol compared to petrol.[8] Similarly, it is required to modify fuel infrastructure, including petrol stations. In conclusion, the disadvantages associated with bioethanol surpass the advantages of this particular biofuel, hence restricting its extensive application to a select number of countries. The potential to transform this easily accessible and environmentally friendly alcohol into a more effective fuel that minimises the disadvantages associated with bioethanol would yield significant benefits.

1.3.2. Advanced Biofuels – Biobutanol

Advanced biofuels can be broadly characterised as being sourced from inedible biomass, specifically lignocellulose. According to this particular delineation, advanced biofuels encompass second or third-generation bioethanol. An alternative perspective states that advanced biofuels possess improved characteristics compared to bioethanol. These characteristics enable the utilisation of the fuel in existing engine technology without demanding any modifications to the engine. Alternatively, these properties may provide technical advantages, such as a notable energy density or octane number. Advanced biofuels cover several fuels, such as biobutanol and other higher alcohols, that exhibit qualities similar to petrol compared to bioethanol.[29]

Butanol exhibits enhanced fuel characteristics compared to bioethanol and shows comparable fuel qualities to petrol.[21a, e, f] The fuel characteristics of 1-butanol are compared to those of petrol and ethanol in Table 1-1. Butanol exhibits a significantly higher energy density, surpassing that of ethanol by 30% and reaching 90% of the energy density of petrol. Butanol has the potential to be included in petrol blends or utilised as an independent fuel in existing engine technology, thereby making use of the present infrastructure for distribution.[15b, 20, 21e] Butanol exhibits non-corrosive properties and displays little miscibility with water, facilitating its convenient storage and transportation. Due to its hygroscopic nature, ethanol is often blended with petrol at the point of use. However, in contrast, butanol-petrol blends have the advantage of being able to be prepared in advance.[29]

Table 1-2: A comparison of fuel properties of the four isomers of butanol.

Properties	**1-Butanol**	***tert*-Butanol**	**2-Butanol**	**Isobutanol**
Density, g/mL at 20 °C	0.810	0.791	0.806	0.802
Atmospheric boiling point, °C	118	83	100	108
Latent heat of vaporisation, MJ/L at 20 °C	0.474	0.415	0.444	0.454
Flash point, °C	35	11	24	28
Autoignition point, °C	385	478	406	430
Energy density, MJ/L	29.2	26.1	28.9	31.4
Air-to-fuel ratio	11.2	11.1	11.1	11.2
Water solubility, %	7	100	37	8.5
Octane number	96	104-110	101	113
Vapour pressure, kPa at 38 °C	2.3	12	6.2[a]	3.9

[a] Measured at 40 °C. Values combined from several literature sources.[20-21, 21c-g, 42]

1-Butanol is frequently seen as a potential substitute for petrol; however, it is essential to note that butanol exists in four distinct isomeric forms. Table 1-2 displays the fuel parameters of each isomer. tert-Butanol is considered unsuitable for fuel applications primarily due to its relatively high melting point of 25 °C, which causes it to solidify at or near room temperature, unlike other isomers that remain liquid under the same conditions. Consequently, it will not be further examined within the context of this discourse. Nevertheless, both isobutanol and 2-butanol possess characteristics that render them viable alternatives to petrol. The energy density of 2-butanol is comparable to that of 1-butanol; however, its octane number is higher, measuring 101.[21c, 43] 1-Butanol is frequently seen as a potential substitute for petrol; however, it is essential to note that butanol exists in four distinct isomeric forms. Table 1-2 displays the fuel parameters of each isomer. *tert*-Butanol is classified as unsuitable for fuel applications primarily due to its relatively high melting point of 25 °C, which is higher than other alcohols that remain liquid at room temperature. Consequently, it will not be further examined within the context of this discourse. Nevertheless, both isobutanol and 2-butanol possess characteristics that render them viable alternatives to petrol. 2-Butanol has the lowest boiling point among the three isomers acceptable for fuel applications while displaying the most considerable vapour pressure. This characteristic facilitates the process of initiating combustion under cold start conditions. Furthermore, it is essential to acknowledge that the flash point of 2-butanol is lower than 1-butanol, although its autoignition temperature is higher than that of 1-butanol. This characteristic reduces the likelihood of early fuel ignition, limiting the possibility of engine "knocking". Isobutanol exhibits a higher energy density than 1-butanol and 2-butanol, contributing to approximately 98% of the energy density observed in petrol. Due to its chain branching, isobutanol has the highest-octane number (113) among all isomers of butanol, rendering it equivalent to bioethanol in terms of this property.[15b, 21c, 44]

All butanol isomers are commonly utilised as solvents in various applications. 1-Butanol finds applications in various sectors, including paint, cosmetics, and plasticiser, and in producing chemical intermediates such as butyl esters and butyl ethers.[21c, 45] Isobutanol is employed as an additive in paint formulations, as well as being utilised in industrial cleansers and as an element in ink compositions.[21c] Most 2-butanol undergoes a conversion process to produce 2-butanone, also known as methyl-ethyl ketone (MEK), a highly valuable solvent in various industrial applications.[21c, 43] The perfume and flavourings business also employs the volatile esters of 2-butanol.[21c]

1.3.2.1. Butanol Synthesis from Petrochemical Feedstocks

The Oxo process is the dominant method employed for the synthesis of butanol. The Oxo process is a chemical reaction that produces alcohols from petrochemical feedstocks through the utilisation of a metal catalyst and application of high pressure.[20, 21c, d, 26a, 45a, 46] The formation of 1-butanol involves the hydroformylation of propylene using cobalt or rhodium catalysts under high pressure conditions, resulting in the production of butyraldehyde (Scheme 1-4).[47] Subsequently, the aforementioned intermediate undergoes hydrogenation using a nickel catalyst, resulting in the production of 1-butanol as the intended outcome. Isobutanol, which is a branched isomer, can be synthesised using the same method. The proportion of linear to branched alcohol can be manipulated by modifying the catalytic system. The Reppe synthesis and direct higher alcohol synthesis (HAS) are two viable pathways for the generation of butanol.[20, 21d, 45a, 48] The production of 2-butanol occurs at a significant scale by the process of butene hydration, utilising petrochemical feedstocks.[43]

The Oxo method incurs significant costs due to its substantial energy requirements, making it environmentally unfavourable from the sustainability viewpoint.[49] The initial components, propylene, and syngas are obtained from non-renewable energy sources, although sustainable methods are available for generating syngas.[26a] As a result, the price of butanol experiences fluctuations following changes in fossil fuel costs. Using carbon monoxide, a hazardous gas, under high pressure is also unfavourable. The utilisation of these techniques for the production of butanol as a fuel is not deemed cost-effective.[20] For the widespread utilisation of butanol as a substitute for petrol, ensuring its production from cost-effective raw materials and at a high-efficiency rate is crucial.

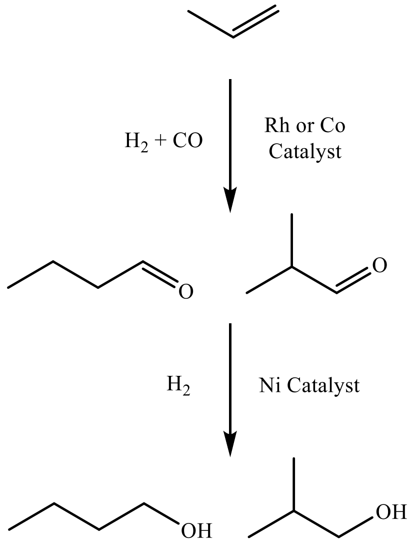

Scheme 1-4: The Oxo process to produce butanol.[21c]

1.3.2.2. Butanol Synthesis via Fermentation

Louis Pasteur initially observed butanol production through bacterial fermentation in the 1860s and was later employed for commercial purposes by Chaim Weizmann.[15b, 21a, d] The process of fermentation discussed here is commonly referred to as the acetone-butanol-ethanol (ABE) process. The term arises from the production of mixtures, including acetone, butanol, and ethanol, which are frequently synthesised by the fermentation activities of bacterial strains belonging to the *Clostridia* species.[20-21, 21c-e, 50] From a sustainability standpoint, the abovementioned method presents a promising pathway for manufacturing 1-butanol; however, it is worth noting that the yields obtained are meagre due to the toxicity of the fermentation by-products towards the bacteria.[51] As an illustration, *Clostridium spp.* has a limited tolerance towards 1-butanol concentration, typically not exceeding 2%.[21c, e] The selectivity towards 1-butanol is relatively moderate, and having other by-products demands significant expenses in downstream processing for the separation and recovery of 1-butanol from the reaction mixture.[20] Metabolic production of isobutanol can be facilitated through recombinant bacteria, resulting in enhanced yields although the normal range of isobutanol production achieved through this method is limited to 3-20 g/L.[41, 44a, 52]

Enhancing this process's economic and sustainable aspects is a subject of extensive academic study.[21c, d, 41, 44a, 53] As an illustration, many strains of *Clostridium spp.* have been genetically modified to facilitate the conversion of diverse feedstocks, such as glucose, cornflour, glycerol, and syngas, into butanol.[41] The issue of *food vs fuel* presents a significant challenge to biobutanol production, similar to the one faced in bioethanol fermentation. Nevertheless, it is noteworthy that lignocellulosic waste material has the potential to serve as a viable feedstock in the ABE process.[17, 54] An alternate strategy involves the transfer of the butanol pathway genes from *Clostridium spp.* into different bacterial species. This approach presents several advantages, including enhanced growth rates, increased tolerance to high butanol concentrations, and the potential to metabolise alternative feedstocks.[21a, 41] Efforts are underway to build systems that may effectively remove butanol during its production, while the current understanding suggests that this strategy could be more economically feasible.[21e]

In contrast to 1-butanol, the metabolic production of 2-butanol is not promising.[43] Significant advancements in genetic engineering have been made to improve the production of 2-butanol by bacterial engineering; however, these advancements have been limited in scope.[55] Nevertheless, similar to the synthesis of other isomers of butanol, the yields obtained are minimal, often less than 1.0 gm/l.

The ABE process is hindered by its low butanol yield and inadequate selectivity, restricting its application for biobutanol production. Consequently, this technology is considered economically unfeasible for large-scale commercial applications. There is a pressing need for the development of alternative methodologies that can effectively and efficiently sustainably generate biobutanol while achieving high production yields and favourable selectivity. One potential approach to biobutanol production is the conversion of bioethanol into this advanced type of biofuel. This technique employs a readily available bioethanol feedstock, which has already been extensively produced on a commercial scale and transforms it into butanol to harness the improved fuel characteristics offered by this alternative fuel.

1.4. Hydrogen Borrowing

Hydrogenation is a widely occurring chemical process with many applications, from producing high-quality compounds to creating regular margarine.[56] A significant category of hydrogenation processes is transfer-hydrogenations, in which hydrogen can be transferred from one molecule to another instead of using hydrogen gas.[57] Hydrogen autotransfer, also known as borrowing hydrogen, shares similarities with transfer hydrogenation but with a critical distinction. In hydrogen autotransfer, the hydrogen temporarily removed from the substrate is utilised in an intermediate reaction before being returned to the final product. In contrast, transfer hydrogenation involves directly transferring hydrogen from a donor to an acceptor without forming intermediates.[58] The schematic diagram illustrates the general route (Scheme 1-5).

Converting bioethanol to butanol demands forming a novel C-C bond and eliminating one equivalent of water, as illustrated in Scheme 1-5. According to the tenets of green chemistry, carrying out the process at the atomic level is essential while refraining from using hazardous reagents and harsh reaction conditions.

Scheme 1-5: A way to convert a bioethanol feedstock into butanol.

The utilisation of hydrogen borrowing, also known as hydrogen autotransfer, has proven to be a practical approach for forming a novel carbon-carbon (C-C) bond through the alkylation of a carbonyl compound with an alcohol (shown in Scheme 1-6), another hydrogen borrowing strategy can be employed to build a C-N bond by substituting the alcohol with an amine in the reaction with the carbonyl compound.[59] This approach prevents reagents such as alkyl halides, traditionally used with a strong base for forming novel C-C bonds with carbonyls and is seen as unfavourable due to using harmful chemicals and generating waste salts.[60]

Alcohols are compounds that exhibit relatively low reactivity and demand activation through different processes, typically involving treatment with acid or base. Alternatively, the alcohol functional group can be transformed into a more reactive leaving group, such as tosylate, triflate, sulfonate, or halide. This approach yields by-products, exhibits insufficient atom efficiency, and frequently employs harmful chemicals. The "one-pot" hydrogen borrowing strategy involves the initial conversion of the alcohol into a carbonyl molecule with higher reactivity using metal-assisted dehydrogenation. This technique allows for using the reactivity associated with the carbonyl functional group. In basic conditions, the resulting carbonyl intermediate can react with a ketone, forming an α,β-unsaturated carbonyl molecule by an aldol condensation reaction. The alkene undergoes hydrogenation using a catalyst, resulting in the formation of a ketone product. The reaction is named "hydrogen borrowing" due to the initial extraction of hydrogen from the alcohol substrate, followed by its subsequent return into the unsaturated aldol product. The lone resulting by-product is water, thus minimising waste generation and promoting a high atom economy. Efficient homogeneous hydrogen-borrowing catalysts have been discovered as ruthenium and iridium catalysts.[51, 59-60]

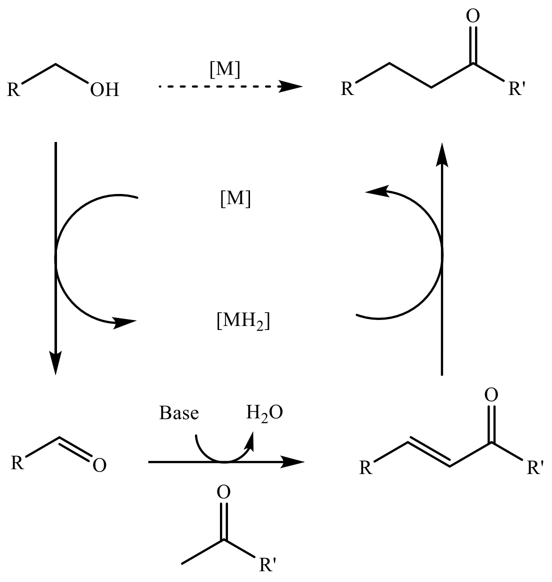

Scheme 1-6: A borrowed hydrogen strategy to form a new C-C bond.

Hydrogen borrowing reactions exhibit a close relationship with the transfer hydrogenation reaction. The process entails the extraction of hydrogen from an alcohol by the use of a catalyst composed of a late-transition metal. This extracted hydrogen is subsequently transferred to an unsaturated molecule, thereby eliminating the requirement for the utilisation of molecular hydrogen.[59b] The hydrogen borrowing method involves two key steps: first, the dehydrogenation of the alcohol to form an intermediate aldehyde or ketone, and second, the hydrogenation of an α,β-unsaturated carbonyl compound using the hydrogen released during the first step. This hydrogen is temporarily borrowed and returned in the final hydrogenation step. These steps are similar to those employed in the transfer hydrogenation strategy, where hydrogen is directly transferred from a donor molecule to an acceptor without intermediate formation. However, hydrogen participates in an additional intermediate reaction before being returned to the product in hydrogen borrowing.[61]

The above-mentioned hydrogen borrowing method can be altered to facilitate the conversion of two alcohols into carbonyl compounds, as compared to the traditional method of introducing a single carbonyl molecule as a reagent. Furthermore, the aldehyde product has the potential to undergo further hydrogenation, resulting in the formation of alcohols. This process enables the conversion of simple alcohols into alcohols with longer carbon chains. The hydrogen borrowing approach can effectively convert bioethanol to butanol, a process commonly referred to as the Guerbet reaction.[51, 62]

1.5. The Guerbet Reaction

1.5.1. Early Guerbet Chemistry

The Guerbet reaction is a chemical transformation that involves the conversion of a shorter-chain alcohol into a longer-chain alcohol by forming a new carbon-carbon (C-C) bond employs a hydrogen borrowing method to achieve the desired outcome.[51, 59b, d] The Guerbet reaction leads to generating a primary alcohol with a β-branch. The approach in question was initially developed by Marcel Guerbet over 100 years ago. Since then, Guerbet alcohols have been widely utilised in various industries, such as lubrication, detergent production, plasticisation, and surfactant formulation, which is primarily due to the unique branching structures of these alcohols, which exhibit regiospecific properties.[63] Guerbet employed temperatures over 200 °C in conjunction with a sodium alkoxide base to facilitate the synthesis of (C-C) bonds.[64] Moreover, hydrogen transfer catalysts have been applied, resulting in a decrease in the necessary reaction temperature. While the development of Guerbet chemistry mainly relied on heterogeneous catalysts, this work will examine many instances of homogeneous catalysts in the subsequent sections.

Viebel and Neilsen were the original researchers who revealed the underlying mechanism of the Guerbet reaction, as illustrated in Scheme 1-7.[65] The process initiates with the catalytic dehydrogenation of an alcohol, resulting in the formation of an aldehyde. The aldehyde, after that, undergoes embolisation under basic conditions, facilitating an aldol condensation reaction and forming water as the lone by-product of this reaction. Subsequently, the catalyst facilitates the reduction of the resulting α, β-unsaturated compound, leading to the formation of a higher alcohol. The reaction can be classified as a "borrowing hydrogen" type, as the hydrogen extracted from the alcohol substrate by the catalyst is afterwards reintroduced into the unsaturated intermediate product. The alcohol produced can be the substrate in a subsequent cycle, leading to increased alcohol production. Numerous varieties of alcohols have been documented to undergo Guerbet coupling, wherein alkoxide or hydroxide bases are commonly employed as the base. In the temperature range below 140 °C, it has been observed that the rate at which aldehydes are formed from alcohols is the step that limits the overall reaction rate.[63] The rate-limiting stage in the aldol condensation reaction occurs at a temperature ranging from 160 to 180 °C.

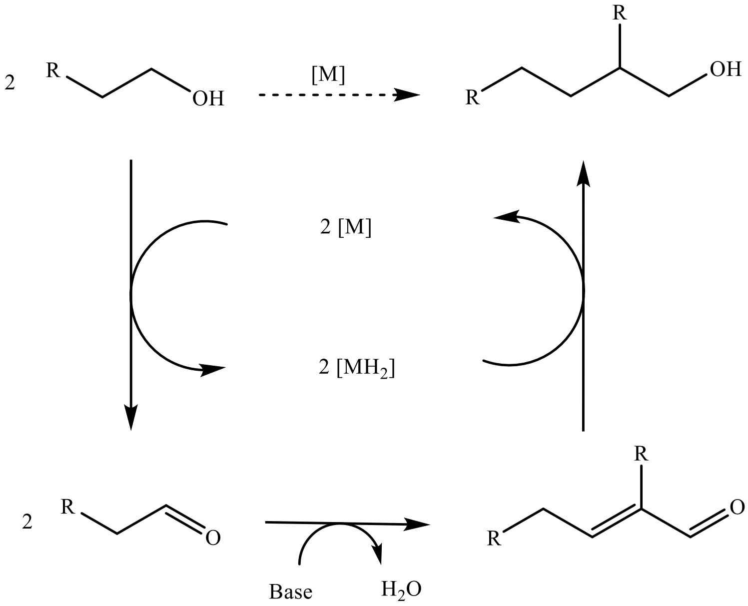

Scheme 1-7: Guerbet reaction mechanism.

1.5.2. Overview of Guerbet Systems

The Guerbet reaction mechanism involves several key steps: dehydrogenation of alcohol, aldol condensation of the resulting aldehyde, and hydrogenation of the unsaturated intermediate formed in the final stage of the process. Each step contributes to the overall reaction rate, with some identified as rate-determining under typical reaction conditions.[66] The initial step, in which alcohol is converted to aldehyde through dehydrogenation, is likely the slowest, especially at lower temperatures. This is because activating the alcohol substrate requires a significant conformational change, which is energetically demanding and a crucial factor in setting the reaction rate. Ethanol presents a greater challenge, as its activation energy is higher than that of longer-chain alcohols.

After dehydrogenation, the aldehyde undergoes aldol condensation to form a β-unsaturated carbonyl compound. This step generally proceeds more rapidly at elevated temperatures, though it can also influence reaction selectivity. The rate of enolate formation in this step is affected by the base's strength and the catalyst's coordination environment.[66]

In the final hydrogenation step, the unsaturated intermediate is converted back to an alcohol, using the hydrogen initially extracted in the first step as a "reserve." Understanding which steps rate-determining are provides valuable insights into improving catalyst performance.[62] By optimising the catalyst for dehydrogenation or enhancing the reactivity of intermediate species with more excellent selectivity, the Guerbet reaction can be more cost-effective and efficient, making it a viable route for biofuel production and contributing to sustainable development.

The Guerbet reaction has been extensively studied and documented, displaying various alcohols.[67] Heterogeneous catalysis is dominant in Guerbet chemistry, especially in its early stages.[62, 68] Metal oxide catalysts are frequently employed in catalysing the coupling of short-chain alcohols with longer-chain alcohols, encompassing alkali and transition metal oxides.[69] However, the frequently found high temperatures above 450 °C and the necessary high pressures hinder the utilisation of these diverse systems.[69b]

In 1972, Ugo and colleagues reported an early instance of a homogeneous catalytic Guerbet system.[70] The condensation of 1-butanol was carried out using homogeneous catalysts of ruthenium and rhodium combined with tertiary phosphines. The reaction conditions were mild, with temperatures below 140 °C and ambient pressure. In 1985, Burk *et al*. published a study describing a homogeneous Guerbet system for coupling 1-pentanol. The system employed $[Rh(COE)_2Cl]_2$ (COE: cyclooctene) as the catalyst, coupled with a dppm ligand (dppm: 1,1-bis(diphenylphosphino)methane) in a 1:1 molar ratio in addition to an alkoxide co-catalyst was utilized.[71] Nevertheless, the researchers saw that a diverse system emerged during the reaction, and this heterogeneous system, rather than the original homogeneous one, accounted for the system's heightened activity. According to the authors, the water by-product was found to harm the Guerbet system.

In the context of the 21st Century, Ishii *et al.* employed homogeneous iridium catalysts to facilitate the Guerbet condensation reaction of primary alcohols, resulting in the formation of β-alkylated alcohols with increased molecular complexity.[72] The model system employed for converting 1-butanol to 2-ethyl-1-hexanol involved the utilization of the catalyst $[Cp^*IrCl_2]$, which was determined to exhibit the highest activity level. The optimal conditions shown in Scheme 1-8 were established, leading to a significant increase in product yield (93%) and exceptional selectivity (99%). The utilization of 1,7-octadiene was considered for achieving optimal activity, primarily owing to its function as a hydrogen acceptor. The utilization of *p*-Xylene as a co-solvent was found to be unimportant, as satisfactory yields were obtained when 1-butanol was employed without any other solvents. The model system successfully converted several primary alcohols into β-alkylated alcohols efficiently.

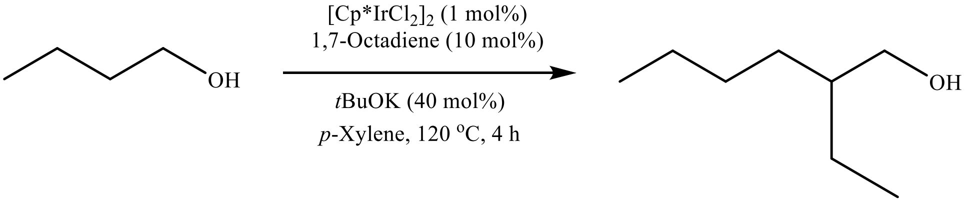

Scheme 1-8: Iridium catalysed conversion of 1-butanol to 2-ethyl-1-hexanol.[72]

1.6. Ethanol Upgrading to Butanol via the Guerbet Reaction

1.6.1. Ethanol Coupling to 1-Butanol

The investigation of ethanol conversion to butanol has predominantly focused on synthesizing 1-butanol.[73] The Guerbet reaction, illustrated in Scheme 1-9, converts ethanol to 1-butanol. The initial step involves the dehydrogenation of ethanol to produce acetaldehyde. Subsequently, under alkaline conditions, an aldol condensation reaction occurs, leading to the formation of crotonaldehyde. Notably, water is the sole by-product generated during this process. Following that, crotonaldehyde undergoes hydrogenation to yield 1-butanol.

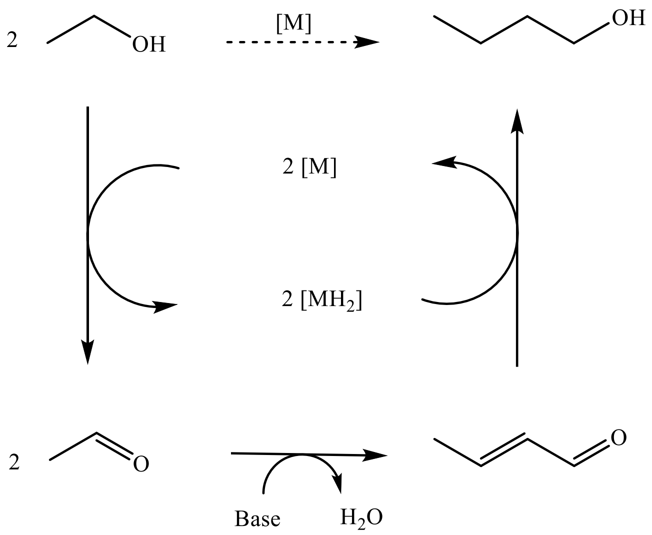

Scheme 1-9: The Guerbet reaction for the conversion of ethanol to 1-butanol.

In contrast to the Guerbet reaction involving longer-chain alcohols, using ethanol as a substrate presents challenges primarily due to the unfavourable thermodynamics of ethanol dehydrogenation. Ethanol requires higher energy input for dehydrogenation than longer-chain alcohols, making forming acetaldehyde less efficient. This inefficiency in the dehydrogenation phase is a key obstacle in ethanol-based Guerbet reactions, resulting in lower yields and more difficult reaction conditions.[64] Due to this reason, a considerable number of documented ethanol upgrading Guerbet processes employ high reaction temperatures (and frequently high pressures) utilising heterogeneous catalysts.[45b, 62, 73b, 74] Extensive research has been conducted on ethanol upgrading, focusing on basic metal oxides, hydroxyapatite (HAP) with the chemical formula $Ca_{10}(PO_4)_6(OH)_2$, and alumina-supported metal catalysts.[20, 21f, 27a, 47, 51, 75] In 1957, Dvornikoff and Farrar documented their use of a tri-component system consisting of potassium carbonate, magnesium oxide, and copper chromite to enhance the quality of ethanol.[76] A 20% ethanol conversion was obtained through heating at a temperature of 230 °C for 8 hours. However, it is essential to note that the conversion rate was hindered by the adverse effects caused by the production of water. The main product detected in this study was 1-butanol, although it should be noted that other higher alcohols were generated. Tsuchida *et al.* successfully synthesised heterogeneous catalysts based on hydroxyapatite (HAP) that efficiently convert ethanol into 1-butanol.[47] The Ca/P ratio influenced the selectivity of the reaction, with an optimal ratio of 1.64 yielding the highest selectivity for 1-butanol at a temperature of 400 °C. Specifically, this condition resulted in a selectivity of 62% for 1-butanol, while ethanol conversion reached 23%. The selectivity was further enhanced by reducing the reaction temperature to 300 °C, resulting in a selectivity of 76%. The calcium (Ca^{2+}) and phosphate ($PO_4{}^{3-}$) present in hydroxyapatite (HAP) can be replaced with alternative cations and anions in order to alter the characteristics of the catalyst. In light of this finding, Onda *et al.* observed a notable enhancement in the selectivity of 1-butanol by replacing Sr^{2+} with Ca^{2+} in HAP catalysts.[75l] The Sr-P HAP catalyst exhibited a selectivity of 81% towards producing 1-butanol, whereas the unmodified Ca-P HAP catalyst attained a selectivity of 75%. However, the conversion of ethanol was less than 8%. A subsequent study conducted by the same researchers showed that raising the Sr/P ratio to 1.70 in the Sr-P HAP catalyst resulted in an enhanced selectivity of 86% at an ethanol conversion rate of 11%.[75k]

The study conducted by Riittonen *et al.* examined various catalysts, including Ru-, Rh-, Pd-, Pt-, Ag-, Ni-, and Au-Al_2O_3, to assess their performance in ethanol conversion, and the Ni-Al_2O_3 catalyst, containing 20.7 wt% Ni, exhibited the highest ethanol conversion rate of 25% with a favourable selectivity of 80% towards 1-butanol, which was attained after subjecting the catalyst to reaction conditions of 72 hours at a temperature of 250 °C and an autogenous pressure.[21f] In their study, Miller *et al.* employed Ni-Al_2O_3 catalysts but incorporated La_2O_3 to mitigate the occurrence of ethyl acetate and ether-forming side reactions.[49] The selectivity towards 1-butanol was found to be unsatisfactory, reaching a maximum of 45%, and there was a notable increase in the creation of other alcohols.

In 2014, Xu and Mu *et al.* developed homogeneous iridium catalysts with phenanthroline-based ligands for converting 1-butanol to 2-ethylhexanol in aqueous conditions, achieving up to 59% yield at 88% selectivity.[77] The *in situ* generated iridium catalysts were then immobilised on activated carbon (5 wt% Ir), which enabled catalyst recycling without activity loss. Following the development of a heterogenised system, aqueous ethanol was upgraded to 1-butanol in the presence of potassium hydroxide base, producing 1-butanol in 25% yield at 56% selectivity.

Although numerous examples of the conversion of ethanol to 1-butanol in a heterogeneous catalytic system exist, on the whole, these systems are limited by low ethanol conversion and/or poor selectivity.[51] Harsh reaction conditions such as high temperatures and/or pressures are often used. Using homogeneous catalysts offers a better understanding of the catalyst at the molecular level and could lead to better selectivity control. However, reports of homogeneous catalyst systems are relatively rare compared to their heterogeneous counterparts.

1.6.2. Ethanol/Methanol Coupling to Isobutanol

Investigating isobutanol production through the Guerbet reaction has received less attention than creating 1-butanol, especially in homogeneous catalysis. While it is impossible to produce the branched structure of isobutanol by only coupling ethanol, combining ethanol and methanol can undergo cross-coupling reactions, forming isobutanol. Methanol can be acquired using sustainable sources, including the process of carbon dioxide hydrogenation or the use of biomass-derived syngas.[26a] Scheme 1-11 illustrates the fundamental Guerbet pathway for converting ethanol/methanol into isobutanol, encompassing two distinct Guerbet cycles. During the initial cycle, ethanol and methanol undergo dehydrogenation reactions to yield acetaldehyde and formaldehyde, respectively. The following steps involve cross-aldol condensation and hydrogenation, resulting in the production of 1-propanol. Subsequently, the second Guerbet cycle involves coupling 1-propanol with an additional equivalent of methanol, forming isobutanol. Two water molecules are generated as a consequence of these two cycles. The high selectivity for isobutanol over other Guerbet alcohols, such as the homocoupling of ethanol resulting in 1-butanol, poses a significant obstacle in this chemical reaction.

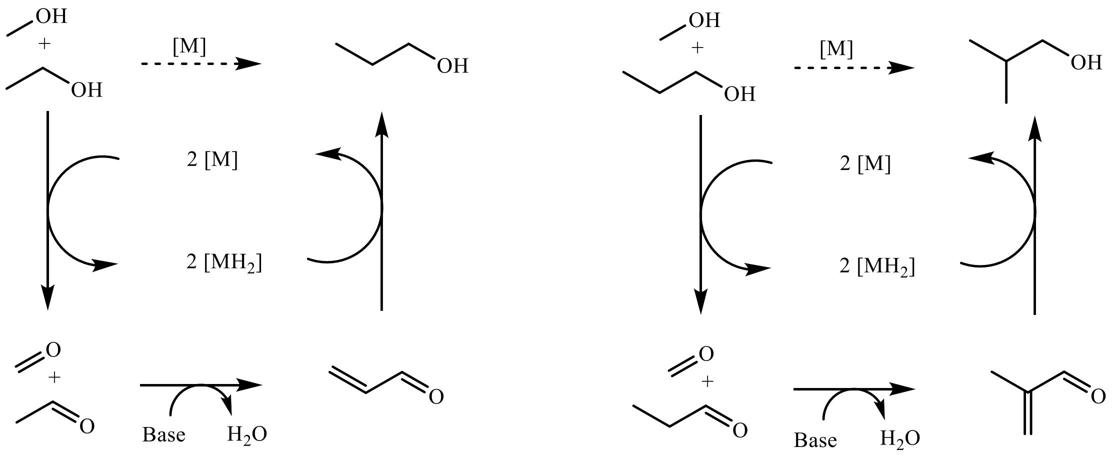

Scheme 1-10: Guerbet pathway for ethanol/methanol upgrading to isobutanol.

The Guerbet reaction requires carefully optimised design of homogeneous catalytic systems. Understanding the role and strength of each catalytic component in the reaction mechanism is essential to identifying the best catalyst combination for maximising efficiency and selectivity.[62] Four main components comprise these catalysts: the metal centre, primary and secondary ligands, and a base. Each plays an individual yet interconnected role in the transformation process.

The choice of metal centre in alcohol conversion reactions significantly impacts the reaction's efficiency. Ruthenium-based complexes, such as $[RuCl_2(p\text{-cymene})]_2$, $Ru_3(CO)_{12}$, and $[RuCl_2(DMSO)_4]$, are among the most effective in facilitating the dehydrogenation and hydrogen transfer steps of the Guerbet process.[68a] The catalytic cycle's performance relies on the metal centre's ability to transform substrates effectively. Ruthenium's electronic configuration allows it to activate the alcohol while stabilising various intermediates. Compared with metals like iridium and rhodium, ruthenium shows superior activity and selectivity, particularly under milder conditions.[68a] Thus, using ruthenium-based complexes can yield more favourable results in alcohol conversion reactions.

Primary ligands also play a vital role in this reaction. Monodentate phosphorus-based ligands (P-ligands), such as PPh_3, significantly influence the electronic and steric environment at the metal centre. The choice of ligand affects the dehydrogenation and hydrogenation steps, critical to the overall reaction.[62] Strong electron-donating ligands increase electron density at the metal centre, facilitating alcohol substrate activation. Conversely, electron-withdrawing ligands can enhance the metal's ability to stabilise reactive intermediates, although they may reduce overall activity.

Secondary ligands, such as hemilabile phosphines, contribute to the reaction by stabilising key intermediates and influencing catalytic performance.[62] These ligands' ability to reversibly coordinate with the metal is essential, particularly for the hydrogen transfer steps. This flexibility supports higher reaction rates and improved selectivity in the Guerbet process.

Selecting an appropriate base, such as sodium methoxide (NaOMe), is also vital in the Guerbet reaction due to its role in aldol condensation and alcohol deprotonation. A strong base is necessary for forming reactive intermediates involved in new C–C bond formation.[62] However, the base's impact on catalyst stability must be carefully considered, as it can affect catalyst durability. Interactions between the base and metal centre can either enhance or diminish the stability and effectiveness of the active species within the catalyst.

The efficiency of the Guerbet reaction ultimately depends on the synergistic interplay between these components. A well-designed catalytic system minimises side reactions and maximises selectivity for the desired product – 1-butanol (from ethanol) or isobutanol (from cross-coupling ethanol and methanol). Understanding the role of each catalytic element is fundamental to advancing more effective and sustainable biofuel production practices.

In terms of heterogeneous catalysis, numerous instances of isobutanol production via a heterogeneous catalysed Guerbet route have been documented.[78] The initial instance of ethanol/methanol coupling leading to the formation of isobutanol was documented by Ueda *et al.* in 1990. A range of solid-base metal oxides, including MgO, ZnO, CaO, and ZrO_2, as well as metal-containing MgO catalysts (3 wt% Mn-, Cr-, Zn-, Al-, Na-, or Cs-MgO), were evaluated for their catalytic activity. Among these catalysts, the MgO catalyst exhibited the highest ethanol conversion rate of 60% and a selectivity of 46% towards isobutanol. These results were obtained under conditions of 360 °C and atmospheric pressure.[79] The authors of a subsequent study expanded upon their previous work by incorporating the coupling of methanol and additional primary alcohols (ranging from C_2 to C_5) over MgO catalysts. This reaction exhibited favourable ethanol conversion rates of 50-60% under atmospheric pressure and at a temperature of 362 °C, and it was conducted in a continuous flow reactor setup.[80]

Carlini *et al.* (2002) documented the use of copper-based heterogeneous catalysts to convert methanol/propanol mixtures. This process, conducted at temperatures ranging from 180 to 220 °C, involved the addition of NaOMe and resulted in the production of isobutanol. Subsequently, the researchers expanded their investigation to incorporate heterogeneous catalysts supported by Ru, Rh, Ni, and Pd, as well as homogeneous Ni and Pd catalysts.[81] The reaction methodology was expanded to enable the direct coupling of ethanol/methanol mixtures with isobutanol. The copper chromite/MeONa system demonstrated superior performance to the Cu-Raney/MeONa system, exhibiting up to 61% ethanol conversions and an impressive isobutanol selectivity of up to 98%. The primary products consisted of isobutanol and 1-propanol as an intermediate.[82] The observation of the products resulting from the coupling of the C_3 and C_4 species, namely 2-methyl-1-pentanol and 2-methyl-1-butanol, was not made. The inactivation of NaOMe by hydrolysis, resulting in NaOH formation, clarifies the reason for employing stoichiometric amounts of NaOMe as a base.

In a previous study (Section 1.6.1), immobilised iridium catalysts with phenanthroline-based ligands demonstrated exceptional performance in the conversion of ethanol to 1-butanol; building upon this success, Xu and Mu *et al.* utilised this group of catalysts in conjunction with K_3PO_4 (at a 1:1 ratio with ethanol) for the upgrading of aqueous ethanol/methanol mixtures, and the resulting process yielded isobutanol with a selectivity of 91% and achieved a reasonable ethanol conversion rate of 52% in 32 h.[52a]

There is a lack of homogeneous instances in which ethanol/methanol is upgraded to isobutanol, with the initial instance being documented by Wass *et al.* in 2016 (see Section 1.7). The utilisation of a 2-phosphinophosphinine complex (illustrated in Scheme 1-12) in the process of ethanol/methanol upgrading was documented by Mansell and Wingad *et al*.[83] A satisfactory isobutanol yield of 38% was attained with a favourable selectivity of 88% following a reaction duration of 2 hours. The isobutanol yield further improved to 50% while maintaining a selectivity of 96% when the reaction duration was extended to 20 hours.

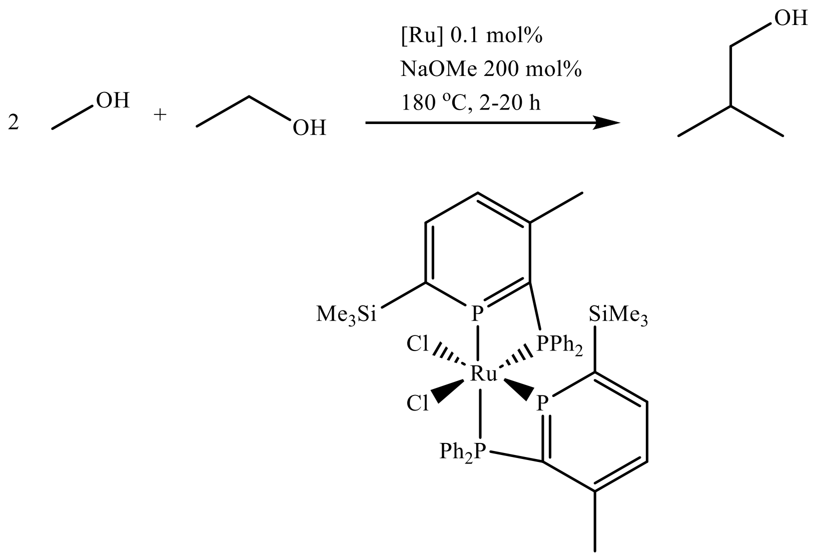

Scheme 1-11: An ethanol/methanol upgrading system employing a 2- phosphinophosphinine-ruthenium catalyst.[83]

1.6.3. Ethanol Coupling to 2-Butanol

Significant advancements have been achieved in applying the Guerbet reaction to enhance ethanol to produce 1-butanol and isobutanol. However, further investigation is required to identify viable pathways for synthesising the third isomer, 2-butanol. There exists a single example in the literature documenting the conversion of ethanol to 2-butanol, despite the accidental observation of 2-butanol synthesis as a secondary by-product in similar procedures.[84] The Cu-Mg-Al mixed oxide catalysts were employed to convert ethanol feedstocks into 1-butanol and 1,1-diethoxyethane.[85] It is interesting to note that the utilisation of $Cu_{20}MgAl_3O$ or CuO heterogeneous catalysts at a temperature of 200 °C resulted in the production of 2-butanol as a secondary product with a ratio of 1-butanol to 2-butanol obtained was 3.9 and 3.5 correspondingly. However, the ethanol conversion was relatively low, measuring less than 6%. The exclusive industrial production of 2-butanol from petrochemical feedstocks demands developing a Guerbet system that can convert bioethanol into 2-butanol, making it a highly desired objective.

1.7. Previous Work in the Wass Group

The Wass group published a study in 2013 that presented a method for enhancing the quality of ethanol using a catalyst called $[RuCl(\eta^6$ - *p*-cymene)(dppm)]Cl, along with a NaOEt base. The study demonstrated that this catalyst, combined with the base, produced 1-butanol with a high yield of 20% within 4 hours, and the selectivity for 1-butanol achieved in this study was remarkable, reaching 94%, which had not been achieved before.[86] (Scheme 1-13, dppm = 1,1-bis(diphenylphosphino)methane). Interestingly, using the additive 1,7-octadiene and the catalyst pre-activation phase, considered essential in Ishii's method, was unnecessary in this study. The study revealed that utilising ligands with smaller bite angles is crucial for achieving high activity. Conversely, the application of ligands with broader bite angles, such as dppe (1,2-bis(diphenylphosphino)ethane) and dppp (1,3-bis(diphenylphosphino)propane), led to a significant decrease in ethanol conversion. The observed high reactivity of the dppm ligand is believed to be attributed to the hemilabile characteristic of the ligand, which facilitates the Guerbet reaction. Despite the attainment of satisfactory results, the effectiveness of this catalyst was hindered by its poor stability, as evidenced by the presence of ruthenium nanoparticles that exhibited no catalytic activity after a standard reaction.[87] The *trans*-$[RuCl_2(dppm)_2]$ complex, displayed in Scheme 1-13, exhibited improved stability, and yielded a remarkable 36% of 1-butanol.[32, 86a] However, obtaining this yield required a longer reaction duration of 24 hours, which caused a reduction in selectivity to 85% can be attributed to the increased production of alcohol.

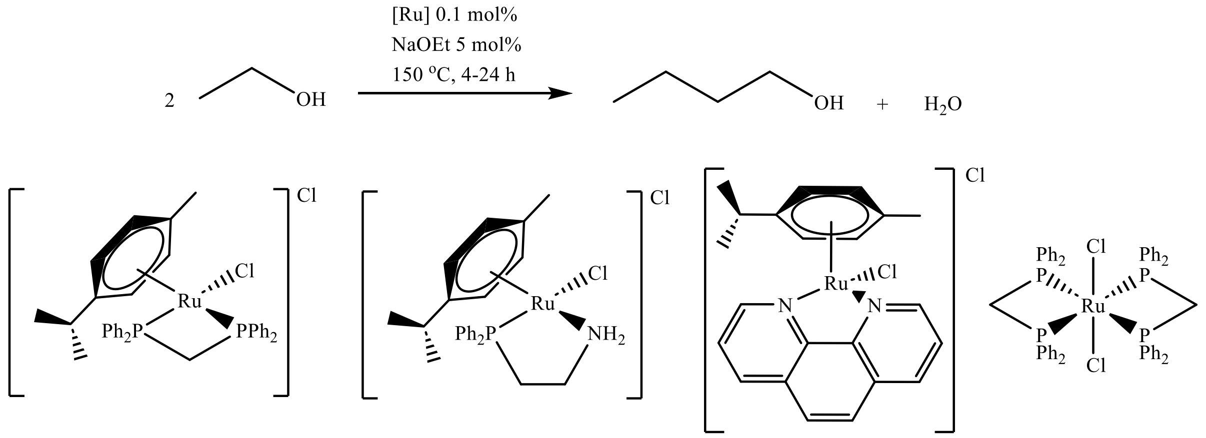

Scheme 1-12: Ruthenium catalysts developed by the Wass group for ethanol upgrading.

The research conducted by the Wass group has significantly broadened the current variety of catalysts utilised for ethanol upgrading. Two significant instances can be observed in Scheme 1-13, namely the utilisation of 2-(diphenylphosphino)ethylamine (PN) and 1,10-phenanthroline ligands (phen) ligands. The catalyst [RuCl(η^6 -*p*-cymene)(PN)]Cl was employed for ethanol upgrading, resulting in a 21% yield and 91% selectivity towards the production of 1-butanol. In contrast, the catalyst [RuCl(η^6 -*p*-cymene)(phen)]Cl exhibited a 17% yield with 90% selectivity for 1-butanol production.[32, 88] The addition of 5% v/v of water to the ethanol upgrading process led to the production of a 9.8% yield of 1-butanol (>99% selectivity) using [RuCl(η^6 -*p*-cymene)(PN)]Cl as the catalyst, similarly, using [RuCl(η^6 -*p*-cymene)(phen)]Cl as the catalyst resulted in a 15% yield of 1-butanol (90% selectivity).[32, 88] The high-water tolerance exhibited by this substance has significant technological benefits in industrial applications.

The Wass group has recently directed their attention towards converting ethanol/methanol mixtures into isobutanol, a topic that will be examined in this thesis. Once again, the utilisation of dppm and 2-(diphenylphosphino)ethylamine ligands has been seen (Scheme 1-14). The bis-chelate catalysts, [$RuCl_2(PX)_2$], have been preferred due to their enhanced stability and more significant activity compared to the mono chelate derivatives, [RuCl(η^6 -*p*-cymene)(PX)]Cl. The *trans*-[$RuCl_2(PN)_2$] catalyst exhibited a commendable performance, resulting in a 51% yield of isobutanol with a selectivity of 90%. On the other hand, *trans*-[$RuCl_2(dppm)_2$] demonstrated remarkable activity, giving 75% isobutanol with an exceptionally high selectivity of 99%.[89]

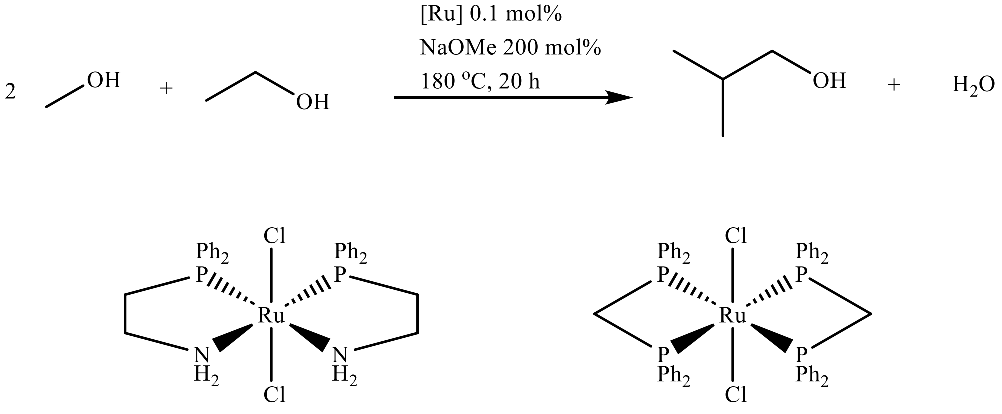

Scheme 1-13: Ruthenium catalysts developed by the Wass group for ethanol/methanol upgrading.[89]

1.8. Thesis Scope

Isobutanol as an environmentally friendly replacement for petrol is a highly reasonable course of action. Isobutanol possesses numerous advantages over bioethanol as a sustainable fuel; moreover, its widespread utilisation could be improved without sustainable manufacturing techniques. The Guerbet reaction has demonstrated efficacy in converting bioethanol feedstocks to biobutanol. However, this approach often needs to be improved, primarily in terms of inadequate ethanol conversions and notably low selectivity of the desired product. High temperatures and pressures are commonly utilised for severe reaction conditions. Specifically, homogeneous catalysis has demonstrated certain advantages over heterogeneous catalysis in achieving higher isobutanol selectivity due to better control over reaction pathways and active site uniformity. Homogeneous catalysts provide greater molecular-level interaction with reactants, enabling more precise reaction conditions and increasing selectivity. Additionally, homogeneous systems often operate under relatively milder reaction conditions, as the catalysts are typically more reactive and efficient in solution.

Nevertheless, there remains plenty of possibility for further advancement. The primary objective of the work outlined in this thesis is to develop innovative catalytic systems that provide higher yields and improved selectivity for isobutanol production compared to existing systems. This work aims to address key scientific questions, such as how to design catalysts with enhanced activity and stability and how to expand the repertoire of ligand sets within the established collection of Guerbet catalysts to achieve greater control over reaction selectivity and efficiency. Finally, the government of Saudi Arabia envisions green energy as the primary fuel source. By implementing this research, I aim to contribute to realising the envisioned goals and completing my academic pursuits in Saudi Arabia.

1.9. References

[1] BP p.l.c., *BP Statistical Review of World Energy 2022*, BP, London, UK, **2022**.

[2] International Energy Agency (IEA), *World Energy Outlook 2021*, IEA, Paris, France, **2021**.

[3] International Energy Agency (IEA), *Global Energy Review 2022*, IEA, Paris, France, **2022**.

[4] J. H. Gary, G. E. Handwerk and M. J. Kaiser, *Petroleum Refining: Technology and Economics*, CRC Press, Boca Raton, **2007**.

[5] J. G. Speight, *The Chemistry and Technology of Petroleum*, CRC Press, Boca Raton, **2014**.

[6] P. McKendry, *Bioresource Technology* **2002**, *83*, 37-46.

[7] U.S. Environmental Protection Agency, *Greenhouse Gas Emissions from a Typical Passenger Vehicle*, U.S. EPA, Washington, DC, USA, **2018**.

[8] A. K. Agarwal, *Progress in Energy and Combustion Science* **2007**, *33*, 233-271.

[9] G. N. Tiwari and R. K. Mishra, *Advanced Renewable Energy Sources*, Royal Society of Chemistry, Cambridge, **2012**.

[10] IPCC (Intergovernmental Panel on Climate Change), *Climate Change 2021: The Physical Science Basis*, Cambridge University Press, Cambridge, UK, **2021**.

[11] H. Schobert, *Chemistry of Fossil Fuels and Biofuels*, Cambridge University Press, **2013**.

[12] BP p.l.c., *BP Energy Outlook 2018*, BP, London, UK, **2018**.

[13] A. P. de Souza, A. Grandis, D. C. Leite and M. S. Buckeridge, *BioEnergy Research* **2014**, *7*, 24-35.

[14] A. Demirbas, *Progress in Energy and Combustion Science* **2007**, *33*, 1-18.

[15] a) J. Fargione, J. Hill, D. Tilman, S. Polasky and P. Hawthorne, *Science* **2008**, *319*, 1235-1238; b) K. Kohse-Höinghaus, P. Oßwald, T. A. Cool, T. Kasper, N. Hansen, F. Qi, C. K. Westbrook and P. R. Westmoreland, *Angewandte Chemie International Edition* **2010**, *49*, 3572-3597.

[16] D. M. Alonso, J. Q. Bond and J. A. Dumesic, *Green Chemistry* **2010**, *12*, 1493-1513.

[17] M. L. Lopes, S. C. D. L. Paulillo, A. Godoy, R. A. Cherubin, M. S. Lorenzi, F. H. C. Giometti, C. D. Bernardino, H. B. D. Amorim Neto and H. V. D. Amorim, *Brazilian Journal of Microbiology* **2016**, *47*, 64–76.

[18] G. M. Walker, *Bioethanol: Science and Technology of Fuel Alcohol*, Bookboon, London, **2010**.

[19] J. Goldemberg, *Science* **2007**, *315*, 808-810.

[20] P. Dziugan, K. G. Jastrzabek, M. Binczarski, S. Karski, I. A. Witonska, B. Kolesinska and Z. J. Kaminski, *Fuel* **2015**, *158*, 81-90.

[21] a) P. Dürre, *Biotechnology Journal: Healthcare Nutrition Technology* **2007**, *2*, 1525-1534; b) M. Gautam and D. W. Martin, *Proceedings of the Institution of Mechanical Engineers, Part A: Journal of Power and Energy* **2000**, *214*, 497-511; c) C. Jin, M. Yao, H. Liu, F. L. Chia-fon and J. Ji, *Renewable and sustainable energy reviews* **2011**, *15*, 4080-4106; d) S. Y. Lee, J. H. Park, S. H. Jang, L. K. Nielsen, J. Kim and K. S. Jung, *Biotechnology and bioengineering* **2008**, *101*, 209-228; e) S. Nanda, J. A Kozinski and A. K Dalai, *Current Biochemical Engineering* **2016**, *3*, 24-36; f) T. Riittonen, E. Toukoniitty, D. K. Madnani, A.-R. Leino, K. Kordas, M. Szabo, A. Sapi, K. Arve, J. Wärnå and J.-P. Mikkola, *Catalysts* **2012**, *2*, 68-84; g) Y. Xie, Y. Ben-David, L. J. Shimon and D. Milstein, *Journal of the American Chemical Society* **2016**, *138*, 9077-9080; h) F. Yüksel and B. Yüksel, *Renewable energy* **2004**, *29*, 1181-1191.

[22] M. Balat, H. Balat and C. Öz, *Progress in Energy and Combustion Science* **2008**, *34*, 551-573.

[23] J. Littlewood, L. Wang, C. Turnbull and R. J. Murphy, *Biotechnology for Biofuels* **2013**, *6*, 1-13.

[24] a) B. J. Khawla, M. Sameh, G. Imen, F. Donyes, G. Dhouha, E. G. Raoudha and N.-E. Oumèma, *Industrial Crops and Products* **2014**, *52*, 144-149; b) S. González-García, C. M. Gasol, X. Gabarrell, J. Rieradevall, M. T. Moreira and G. Feijoo, *Renewable Energy* **2010**, *35*, 1014-1023.

[25] G. W. Huber and A. Corma, *Angewandte Chemie International Edition* **2007**, *46*, 7184-7201.

[26] a) G. W. Huber, S. Iborra and A. Corma, *Chemical Reviews* **2006**, *106*, 4044-4098; b) M. Ni, D. Y. Leung and M. K. Leung, *International Journal of Hydrogen Energy* **2007**, *32*, 3238-3247.

[27] a) P. Dziugan, M. Balcerek, K. Pielech-Przybylska and P. Patelski, *Biotechnology for Biofuels* **2013**, *6*, 1-10; b) A. J. Ragauskas, C. K. Williams, B. H. Davison, G. Britovsek, J. Cairney, C. A. Eckert, W. J. Frederick Jr, J. P. Hallett, D. J. Leak and C. L. Liotta, *Science* **2006**, *311*, 484-489.

[28] a) S. H. M. Azhar, R. Abdulla, S. A. Jambo, H. Marbawi, J. A. Gansau, A. A. M. Faik and K. F. Rodrigues, *Biochemistry and Biophysics Reports* **2017**, *10*, 52–61; b) O. J. Sanchez and C. A. Cardona, *Bioresource Technology* **2008**, *99*, 5270-5295.

[29] K. J. Pellow, *Catalytic Upgrading of Ethanol to Advanced Biofuels*, Doctoral Dissertation, University of Bristol, UK, **2018**.

[30] T. W. Jeffries, *Nature Biotechnology* **2005**, *23*, 40-41.

[31] a) L. M. Vane, *Biofuels, Bioproducts and Biorefining* **2008**, *2*, 553-588; b) L. M. Vane, F. R. Alvarez, L. Rosenblum and S. Govindaswamy, *Industrial & Engineering Chemistry Research* **2013**, *52*, 1033-1041.

[32] J. Lee, *New Catalysts for the Upgrading of Ethanol to Butanol Biofuels*, Doctoral Dissertation, University of Bristol, UK, **2015**.

[33] a) L. D. Gomez, C. G. Steele-King and S. J. McQueen-Mason, *New Phytologist* **2008**, *178*, 473-485; b) A. F. Lee and K. Wilson, *Catalysis Today* **2015**, *242*, 3-18; c) T. Searchinger, R. Heimlich, R. A. Houghton, F. Dong, A. Elobeid, J. Fabiosa, S. Tokgoz, D. Hayes and T.-H. Yu, *Science* **2008**, *319*, 1238-1240.

[34] P. Azadi, O. R. Inderwildi, R. Farnood and D. A. King, *Renewable and Sustainable Energy Reviews* **2013**, *21*, 506-523.

[35] a) C. O. Tuck, E. Pérez, I. T. Horváth, R. A. Sheldon and M. Poliakoff, *Science* **2012**, *337*, 695-699; b) M.-L. Zhang, Y.-T. Fan, Y. Xing, C.-M. Pan, G.-S. Zhang and J.-J. Lay, *Biomass and Bioenergy* **2007**, *31*, 250-254.

[36] A. Cabiac, E. Guillon, F. Chambon, C. Pinel, F. Rataboul and N. Essayem, *Applied Catalysis A: General* **2011**, *402*, 1-10.

[37] N. Mosier, C. Wyman, B. Dale, R. Elander, Y. Lee, M. Holtzapple and M. Ladisch, *Bioresource Technology* **2005**, *96*, 673-686.

[38] B. Hahn-Hägerdal, M. Galbe, M.-F. Gorwa-Grauslund, G. Lidén and G. Zacchi, *Trends in Biotechnology* **2006**, *24*, 549-556.

[39] a) C. Cook and A. Devoto, *Journal of the Science of Food and Agriculture* **2011**, *91*, 1729-1732; b) T. Hasunuma and A. Kondo, *Biotechnology Advances* **2012**, *30*, 1207-1218.

[40] J. Singh and S. Gu, *Renewable and Sustainable Energy Reviews* **2010**, *14*, 2596-2610.

[41] P. P. Peralta-Yahya, F. Zhang, S. B. Del Cardayre and J. D. Keasling, *Nature* **2012**, *488*, 320-328.

[42] K. Nasirzadeh, D. Zimin, R. Neueder and W. Kunz, *Journal of Chemical & Engineering Data* **2004**, *49*, 607-612.

[43] K. W. Waldron, *Bioalcohol Production: Biochemical Conversion of Lignocellulosic Biomass*, Elsevier, **2010**.

[44] a) S. Atsumi, T. Hanai and J. C. Liao, *Nature* **2008**, *451*, 86-89; b) J. T. Moss, A. M. Berkowitz, M. A. Oehlschlaeger, J. Biet, V. Warth, P.-A. Glaude and F. Battin-Leclerc, *The Journal of Physical Chemistry A* **2008**, *112*, 10843-10855.

[45] a) M. Uyttebroek, W. Van Hecke and K. Vanbroekhoven, *Catalysis Today* **2015**, *239*, 7-10; b) X. Zhang, Z. Liu, X. Xu, H. Yue, G. Tian and S. Feng, *ACS Sustainable Chemistry & Engineering* **2013**, *1*, 1493-1497.

[46] G. M. Torres, R. Frauenlob, R. Franke and A. Börner, *Catalysis Science & Technology* **2015**, *5*, 34-54.

[47] T. Tsuchida, S. Sakuma, T. Takeguchi and W. Ueda, *Industrial & Engineering Chemistry Research* **2006**, *45*, 8634-8642.

[48] a) R. Herman, *Catalysis Today* **2000**, *55*, 233-245; b) H. T. Luk, C. Mondelli, D. C. Ferré, J. A. Stewart and J. Pérez-Ramírez, *Chemical Society Reviews* **2017**, *46*, 1358-1426; c) K. A. Verkerk, B. Jaeger, C.-H. Finkeldei and W. Keim, *Applied Catalysis A: General* **1999**, *186*, 407-431.

[49] T. L. Jordison, C. T. Lira and D. J. Miller, *Industrial & Engineering Chemistry Research* **2015**, *54*, 10991-11000.

[50] Y. S. Jang, J. Lee, A. Malaviya, D. Y. Seung, J. H. Cho and S. Y. Lee, *Biotechnology Journal* **2012**, *7*, 186-198.

[51] H. Aitchison, R. L. Wingad and D. F. Wass, *ACS Catalysis* **2016**, *6*, 7125-7132.

[52] a) Q. Liu, G. Xu, X. Wang and X. Mu, *Green Chemistry* **2016**, *18*, 2811-2818; b) J. Lu, C. J. Brigham, C. S. Gai and A. J. Sinskey, *Applied Microbiology and Biotechnology* **2012**, *96*, 283-297.

[53] a) K. M. Smith, K.-M. Cho and J. C. Liao, *Applied Microbiology and Biotechnology* **2010**, *87*, 1045-1055; b) Y. Tashiro, T. Yoshida, T. Noguchi and K. Sonomoto, *Engineering in Life Sciences* **2013**, *13*, 432-445.

[54] a) G. Jurgens, S. Survase, O. Berezina, E. Sklavounos, J. Linnekoski, A. Kurkijärvi, M. Väkevä, A. van Heiningen and T. Granström, *Biotechnology letters* **2012**, *34*, 1415-1434; b) M. Kumar, Y. Goyal, A. Sarkar and K. Gayen, *Applied Energy* **2012**, *93*, 193-204.

[55] a) Z. Chen, Y. Wu, J. Huang and D. Liu, *Bioresource Technology* **2015**, *197*, 260-265; b) P. Ghiaci, J. Norbeck and C. Larsson, *PLoS One* **2014**, *9*, e102774; c) R. A. G. Marusich, *New Strategies for the Production of Butanol and 1,3-Propanediol from Glycerol*, Doctoral Dissertation, Universidade do Minho, Portugal, **2012**; d) B.-R. Oh, S.-Y. Heo, S.-M. Lee, W.-K. Hong, J. M. Park, Y. R. Jung, D.-H. Kim, J.-H. Sohn, J.-W. Seo and C. H. Kim, *Biotechnology Letters* **2014**, *36*, 57-62; e) L. Zhang, R. Singh, D. Sivakumar, Z. Guo, J. Li, F. Chen, Y. He, X. Guan, Y. C. Kang and J.-K. Lee, *Green Chemistry* **2018**, *20*, 230-242.

[56] a) P. G. Andersson and I. J. Munslow, *Modern Reduction Methods*, John Wiley & Sons, **2008**; b) W. Bonrath, J. Medlock, J. Schütz, B. Wüstenberg, T. Netscher, B. Wüstenberg and T. Netscher, *Hydrogenation in the Vitamins and Fine Chemicals Industry–An Overview*, InTech Rijeka, **2012**.

[57] D. Wang and D. Astruc, *Chemical reviews* **2015**, *115*, 6621-6686.

[58] a) A. Corma, J. Navas and M. J. Sabater, *Chemical Reviews* **2018**, *118*, 1410-1459; b) T. Irrgang and R. Kempe, *Chemical Reviews* **2018**, *119*, 2524-2549; c) T. Kwok, O. Hoff, R. J. Armstrong and T. J. Donohoe, *Chemistry–A European Journal* **2020**, *26*, 12912-12926; d) B. G. Reed-Berendt, K. Polidano and L. C. Morrill, *Organic & Biomolecular Chemistry* **2019**, *17*, 1595-1607; e) K. Shimizu, *Catalysis Science & Technology* **2015**, *5*, 1412-1427.

[59] a) P. J. Black, M. G. Edwards and J. M. Williams, *European Journal of Organic Chemistry* **2006**, *2006*, 4367-4378; b) G. E. Dobereiner and R. H. Crabtree, *Chemical Reviews* **2010**, *110*, 681-703; c) M. G. Edwards, R. F. R. Jazzar, B. M. Paine, D. J. Shermer, M. K. Whittlesey, J. M. J. Williams and

D. D. Edney, *Chemical Communications* **2004**, 90-91; d) M. H. S. Hamid, P. A. Slatford and J. M. Williams, *Advanced Synthesis & Catalysis* **2007**, *349*, 1555-1575; e) F. Huang, Z. Liu and Z. Yu, *Angewandte Chemie International Edition* **2016**, *55*, 862-875; f) S. D. Lacroix, A. Pennycook, S. Liu, T. T. Eisenhart and A. C. Marr, *Catalysis Science & Technology* **2012**, *2*, 288-290; g) A. C. Marr, *Catalysis Science & Technology* **2012**, *2*, 279-287; h) T. D. Nixon, M. K. Whittlesey and J. M. Williams, *Dalton Transactions* **2009**, 753-762; i) Y. Obora, *ACS Catalysis* **2014**, *4*, 3972-3981; j) B. C. Roy, K. Chakrabarti, S. Shee, S. Paul and S. Kundu, *Chemistry–A European Journal* **2016**, *22*, 18147-18155.

[60] K. Chakrabarti, B. Paul, M. Maji, B. C. Roy, S. Shee and S. Kundu, *Organic & Biomolecular Chemistry* **2016**, *14*, 10988-10997.

[61] G. Guillena, D. J. Ramon and M. Yus, *Chemical Reviews* **2010**, *110*, 1611-1641.

[62] D. Gabriëls, W. Y. Hernández, B. Sels, P. Van Der Voort and A. Verberckmoes, *Catalysis Science & Technology* **2015**, *5*, 3876-3902.

[63] A. J. O'Lenick Jr, *Journal of Surfactants and Detergents* **2001**, *4*, 311-315.

[64] F. C. Meunier, J. Scalbert, F. Thibault-Starzyk, *Compet Rendus. Chimie* **2015**, *18*, 345–350.

[65] S. Veibel and J. Nielsen, *Tetrahedron* **1967**, *23*, 1723-1733.

[66] A. Messori, A. Gagliardi, C. Cesari, F. Calcagno, T. Tabanelli, F. Cavani and R. Mazzoni, *Catalysis Today* **2023**, *423*, 114003.

[67] a) M. Biermann, H. Gruß, W. Hummel and H. Gröger, *ChemCatChem* **2016**, *8*, 895-899; b) P. L. Burk, R. L. Pruett and K. S. Campo, *Journal of Molecular Catalysis* **1985**, *33*, 15-21; c) C. Carlini, A. Macinai, A. M. R. Galletti and G. Sbrana, *Journal of Molecular Catalysis A: Chemical* **2004**, *212*, 65-70; d) C. S. Cho, B. T. Kim, H.-S. Kim, T.-J. Kim and S. C. Shim, *Organometallics* **2003**, *22*, 3608-3610; e) C. S. Cho, B. T. Kim, T.-J. Kim and S. C. Shim, *The Journal of Organic Chemistry* **2001**, *66*, 9020-9022; f) D. Gnanamgari, C. H. Leung, N. D. Schley, S. T. Hilton and R. H. Crabtree, *Organic & Biomolecular Chemistry* **2008**, *6*, 4442-4445.

[68] a) J. Kozlowski and R. Davis, *ACS Catalysis* **2013**, *3*, 1588–1600; b) E. F. Pratt and D. G. Kubler, *Journal of the American Chemical Society* **1954**, *76*, 52-56.

[69] a) R. Miller and G. Bennett, *Industrial & Engineering Chemistry* **1961**, *53*, 33-36; b) A. Ndou and N. Coville, *Applied Catalysis A: General* **2004**, *275*, 103-110.

[70] G. Gregorio, G. Pregaglia and R. Ugo, *Journal of Organometallic Chemistry* **1972**, *37*, 385-387.

[71] P. L. Burk, R. L. Pruett and K. S. Campo, *Journal of Molecular Catalysis* **1985**, *33*, 1-14.

[72] T. Matsu-Ura, S. Sakaguchi, Y. Obora and Y. Ishii, *The Journal of Organic Chemistry* **2006**, *71*, 8306-8308.

[73] a) A. Galadima and O. Muraza, *Industrial & Engineering Chemistry Research* **2015**, *54*, 7181-7194; b) Q. Zhang, J. Dong, Y. Liu, Y. Wang and Y. Cao, *Journal of Energy Chemistry* **2016**, *25*, 907-910.

[74] a) A. Chistyakov, P. Zharova, M. Tsodikov, S. Nikolaev, I. Krotova and D. Ezzhelenko, *Kinetics and Catalysis* **2016**, *57*, 803-811; b) D. Jiang, X. Wu, J. Mao, J. Ni and X. Li, *Chemical Communications* **2016**, *52*, 13749-13752; c) G. Onyestyák, G. Novodárszki, Á. F. Wellisch, J. Valyon, A. J. Thakur and D. Deka, *Reaction Kinetics, Mechanisms and Catalysis* **2017**, *121*, 31-41; d) Z. Sun, A. C. Vasconcelos, G. Bottari, M. C. A. Stuart, G. Bonura, C. Cannilla, F. Frusteri, K. Barta, *ACS Sustainable Chemistry & Engineering* **2017**, *5*, 1738-1746; e) C. Yang and Z. Meng, *Journal of Catalysis* **1993**, *142*, 37-44.

[75] a) K. Kourtakis, M. B. D'Amore, L. E. Manzer, *Catalytic Conversion of Ethanol to a 1-Butanol-Containing Reaction Product Using a Thermally Decomposed Hydrotalcite Catalys*t, US Patent *7700810 B2*, Du Pont, United States, **2010**; b) F. Otto, Q. Wilhelm, *Process for the Production of Higher Alcohols, Particularly Butyl Alcohol, from Ethyl Alcohol*, US Patent *1992480 A*, Degussa, United States, **1935**; c) T. Tsuchida, A. Kiminori, S. Sakuma, T. Inui, *Synthesis Method of Chemical Industrial Raw Material and High-Octane Fuel, and High-Octane Fuel Composition*, US Patent *6323383 B1*, Sangi KK, United States, **2001**; d) J. P. Wibaut, *Process for the Manufacture of Butyl Alcohol*, US Patent *1910582 A*, Bataafsche Petroleum, United States, **1933**; e) J. H. Earley, R. A. Bourne, M. J. Watson and M. Poliakoff, *Green Chemistry* **2015**, *17*, 3018-3025; f) H. S. Ghaziaskar and C. C. Xu, *RSC Advances* **2013**, *3*, 4271-4280; g) C. R. Ho, S. Shylesh and A. T. Bell, *ACS Catalysis* **2016**, *6*, 939-948; h) T. L. Jordison, L. Peereboom and D. J. Miller, *Industrial & Engineering Chemistry*

Research **2016**, *55*, 6579-6585; i) T. Moteki and D. W. Flaherty, *ACS Catalysis* **2016**, *6*, 4170-4183; j) A. Ndou, N. Plint and N. Coville, *Applied Catalysis A: General* **2003**, *251*, 337-345; k) S. Ogo, A. Onda, Y. Iwasa, K. Hara, A. Fukuoka and K. Yanagisawa, *Journal of Catalysis* **2012**, *296*, 24-30; l) S. Ogo, A. Onda and K. Yanagisawa, *Applied Catalysis A: General* **2011**, *402*, 188-195; m) K. K. Ramasamy, M. Gray, H. Job, D. Santosa, X. S. Li, A. Devaraj, A. Karkamkar and Y. Wang, *Topics in Catalysis* **2016**, *59*, 46-54; n) K. K. Ramasamy, M. Gray, H. Job, C. Smith and Y. Wang, *Catalysis Today* **2016**, *269*, 82-87; o) T. Riittonen, K. Eränen, P. Mäki-Arvela, A. Shchukarev, A.-R. Rautio, K. Kordas, N. Kumar, T. Salmi and J.-P. Mikkola, *Renewable Energy* **2015**, *74*, 369-378; p) T. Tsuchida, J. Kubo, T. Yoshioka, S. Sakuma, T. Takeguchi and W. Ueda, *Journal of Catalysis* **2008**, *259*, 183-189; q) Z. Young, S. Hanspal and R. Davis, *ACS Catalysis* **2016**, *6*, 3193–3202.

[76] M. N. Dvornikoff and M. W. Farrar, *The Journal of Organic Chemistry* **1957**, *22*, 540-542.

[77] G. Xu, T. Lammens, Q. Liu, X. Wang, L. Dong, A. Caiazzo, N. Ashraf, J. Guan and X. Mu, *Green Chemistry* **2014**, *16*, 3971-3977.

[78] a) J. J. Bravo-Suárez, B. Subramaniam and R. V. Chaudhari, *Applied Catalysis A: General* **2013**, *455*, 234-246; b) J. I. Di Cosimo, C. R. Apesteguia, M. J. L. Ginés and E. Iglesia, *Journal of Catalysis* **2000**, *190*, 261-275; c) E. S. Olson, R. K. Sharma and T. R. Aulich, *Applied Biochemistry and Biotechnology* **2004**, *115*, 913-932.

[79] W. Ueda, T. Kuwabara, T. Ohshida and Y. Morikawa, *Journal of the Chemical Society, Chemical Communications* **1990**, 1558-1559.

[80] W. Ueda, T. Ohshida, T. Kuwabara and Y. Morikawa, *Catalysis Letters* **1992**, *12*, 97-104.

[81] a) C. Carlini, M. Di Girolamo, A. Macinai, M. Marchionna, M. Noviello, A. M. R. Galletti and G. Sbrana, *Journal of Molecular Catalysis A: Chemical* **2003**, *204*, 721-728; b) C. Carlini, M. Di Girolamo, M. Marchionna, M. Noviello, A. M. R. Galletti and G. Sbrana, *Journal of Molecular Catalysis A: Chemical* **2002**, *184*, 273-280; c) C. Carlini, C. Flego, M. Marchionna, M. Noviello, A. M. R. Galletti, G. Sbrana, F. Basile and A. Vaccari, *Journal of Molecular Catalysis A: Chemical* **2004**, *220*, 215-220; d) C. Carlini, A. Macinai, M. Marchionna, M. Noviello, A. M. R. Galletti and G. Sbrana, *Journal of Molecular Catalysis A: Chemical* **2003**, *206*, 409-418; e) C. Carlini, M. Marchionna, M. Noviello, A.

M. R. Galletti, G. Sbrana, F. Basile and A. Vaccari, *Journal of Molecular Catalysis A: Chemical* **2005**, *232*, 13-20.

[82] C. Carlini, M. Di Girolamo, A. Macinai, M. Marchionna, M. Noviello, A. M. R. Galletti and G. Sbrana, *Journal of Molecular Catalysis A: Chemical* **2003**, *200*, 137-146.

[83] R. Newland, M. F. Wyatt, R. Wingad and S. M. Mansell, *Dalton Transactions* **2017**, *46*, 6172-6176.

[84] K. Inui, T. Kurabayashi, S. Sato and N. Ichikawa, *Journal of Molecular Catalysis A: Chemical* **2004**, *216*, 147-156.

[85] I.-C. Marcu, D. Tichit, F. Fajula and N. Tanchoux, *Catalysis Today* **2009**, *147*, 231-238.

[86] a) G. R. Dowson, M. F. Haddow, J. Lee, R. L. Wingad and D. F. Wass, *Angewandte Chemie International Edition* **2013**, *52,* 9005-9008; b) G. R. M. Dowson, *Transformations of Ethanol by Homogeneous Catalysis for Creation of Advanced Biofuels.* University of Bristol, UK, **2012**.

[87] J. M. Thomas and W. J. Thomas, *Principles and Practice of Heterogeneous Catalysis*, Wiley-VCH, Weinheim, **1997**.

[88] R. L. Wingad, P. J. Gates, S. T. Street and D. F. Wass, *ACS Catalysis* **2015**, *5,* 5822-5826.

[89] R. L. Wingad, E. J. Bergström, M. Everett, K. J. Pellow and D. F. Wass, *Chemical Communications* **2016**, *52*, 5202-5204.

Chapter 2: Ruthenium Catalysis by Using Monodentate Phosphine Ligands

2.1. Background

The Wass group has made significant strides in the production of *n*-butanol and isobutanol through their dedicated research in biofuel production. The recent study led by Folasade J. Sama *et al.* aimed to develop ruthenium diphosphine complexes with enhanced value by incorporating functionalised backbones to catalytically convert ethanol and methanol into isobutanol.[1] The findings of this research underscore the crucial role of side chain functionalisation in boosting the catalytic activity of the backbone functionalised diphosphine ligands. This study aligns with previous research and sets the stage for the creation of more efficient catalysts for alcohol upgrading in terms of efficiency and selectivity. Consequently, it promises to significantly impact biofuel production and catalyst development, offering a bright future for the field.

As depicted in Scheme 2-1, the Wass group has effectively synthesised a new series of catalysts, 2.5-2.12, utilising ruthenium catalysts, building on previous research (Figure 2-1).[2] These catalysts were further analysed using X-ray crystallography, revealing fascinating details about their distinct structural features (Figure 2-2).[1] These structural profiles are frequently required to determine the impact of modifications in the ligand's backbones on the catalytic activity.

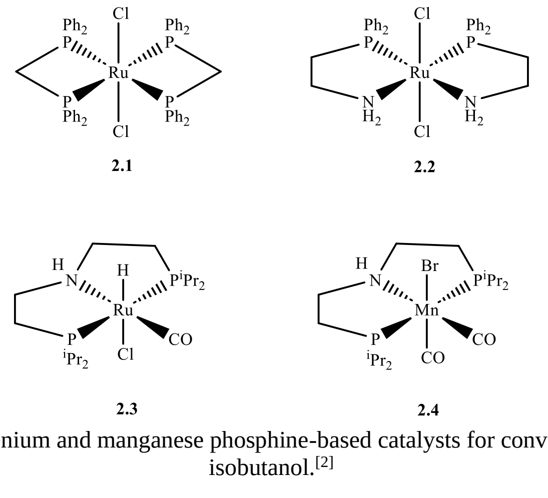

Figure 2-1: Previously used ruthenium and manganese phosphine-based catalysts for conversion of ethanol and methanol to isobutanol.[2]

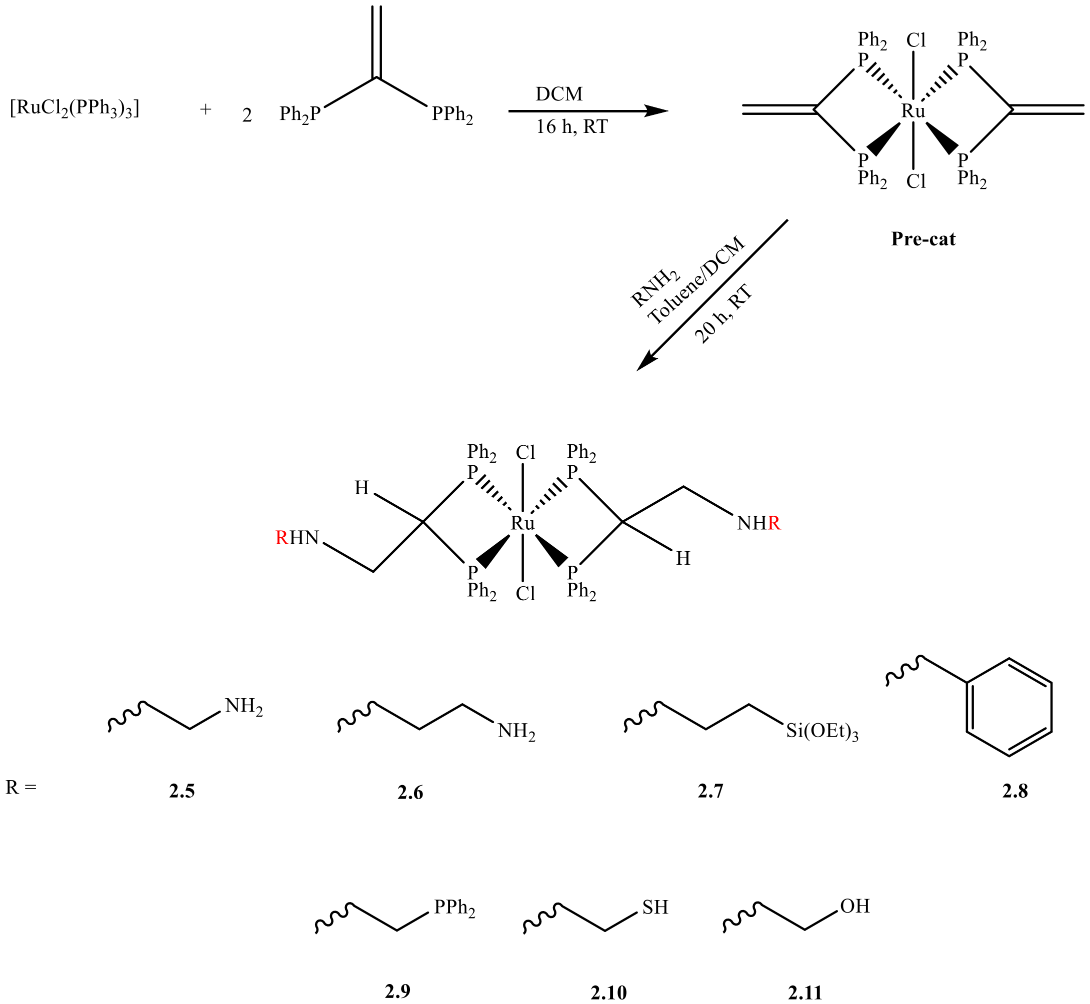

Scheme 2-1: Synthesis of complexes **2.5** to **2.11**

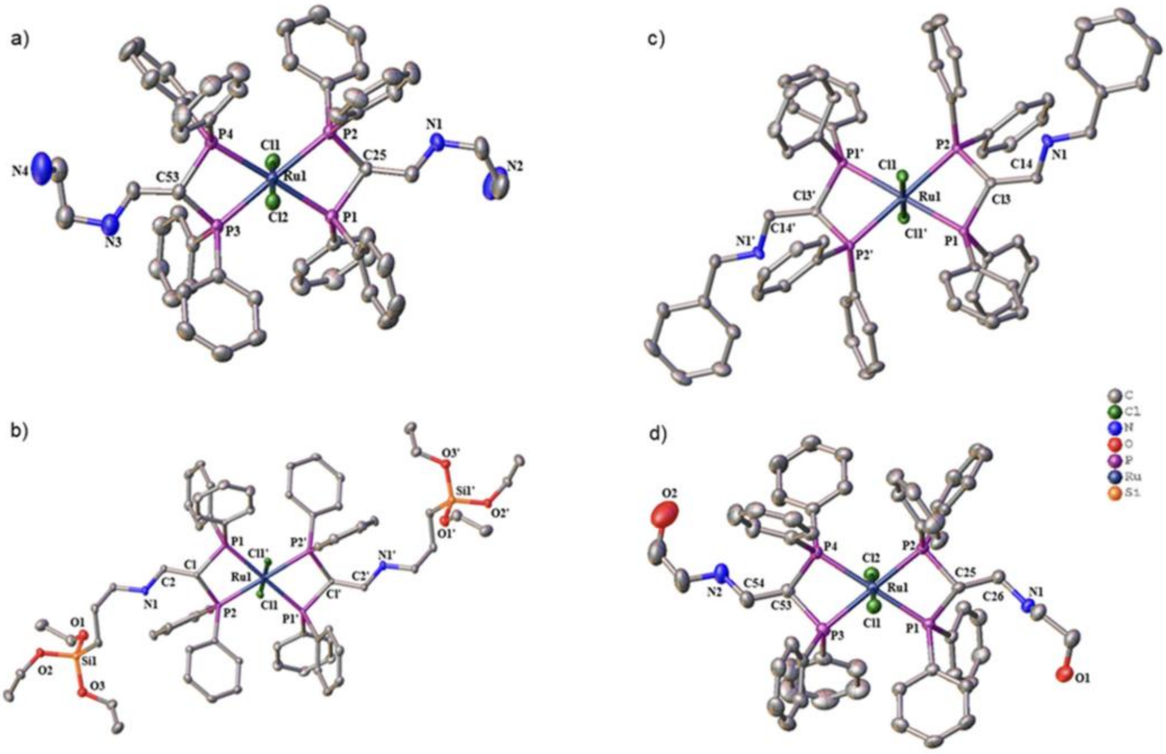

Figure 2-2: X-ray crystal structures of complexes **2.5** (a), **2.7** (b), **2.8** (c), and **2.11** (d) exhibiting *trans*-configurations. Hydrogen atoms and solvent molecules (where present) are omitted for clarity.[1]

The study elucidates the utilisation and catalytic mechanism of these compounds. Table 2-1 evaluates the catalytic efficiency in terms of yield and selectivity for isobutanol. The findings of the tests demonstrate that some changes to the backbone enhance both the catalytic activity and selectivity.

Table 2-1: Ruthenium catalysed conversion of ethanol and methanol to isobutanol.[1]

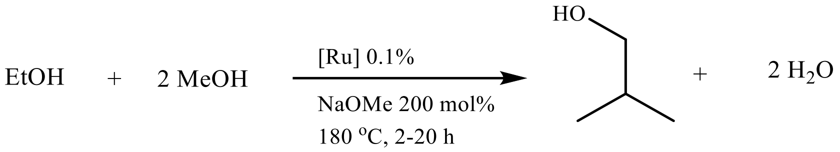

Run^a	**Catalyst**	**Time**	**EtOH Conversion (%)**^{b}	**Yield**^{c} **[Selectivity] (%)**		
				Isobutanol	***n*-Propanol**	***n*-Hexanol**
1	**2.5**	2	78	74 [94]	3 [4]	1 [1]
2	**2.5**	20	80	74 [94]	4 [5]	2 [1]
3	**2.6**	2	84	59 [97]	1 [2]	1 [1]
4	**2.6**	20	94	69 [94]	2 [2]	8 [4]
5	**2.7**	2	83	59 [97]	1 [2]	1 [1]
6	**2.7**	20	95	69 [96]	2 [2]	4 [2]
7	**2.8**	2	83	60 [98]	1 [2]	1 [1]
8	**2.8**	20	95	66 [96]	2 [2]	4 [2]
9	**2.9**	2	89	60 [94]	3 [5]	1 [1]
10	**2.9**	20	89	68 [94]	3 [4]	6 [3]
11	**2.10**	2	88	62 [100]	0 [0]	0 [0]
12	**2.10**	20	100	79 [100]	0 [0]	0 [0]
13	**2.11**	2	79	52 [97]	2 [3]	1 [1]
14	**2.11**	20	94	72 [96]	2 [2]	4 [2]
15	**Pre-cat**	2	48	46 [97]	1 [2]	1 [1]
16	**2.1**	2	88	65 [98]	1 [2]	0 [0]
17	**2.1**	20	90	75 [99]	1 [1]	0 [0]

^{a} Conditions: ethanol (1 mL, 17.13 mmol), methanol (10 mL, 247.13 mmol), [Ru] catalyst (0.01713 mmol, 0.1 mol%), NaOMe (34.26 mmol, 200 mol%), mol% is based on ethanol substrate, 180 °C. ^{b} Total ethanol conversion as determined by GC liquid phase analysis. ^{c} Total yield and selectivity of alcohol products in the liquid fraction as determined by GC.

The catalytic activity of complexes **2.5-2.11** in converting ethanol/methanol to isobutanol was evaluated using the established experimental procedures described by the Wass group. According to the data in Table 2-1, all catalysts exhibited satisfactory performance, achieving a yield of over 50% and a selectivity of over 90% within 2 hours. The catalyst containing diamine ethylene functionalities, referred to as catalyst **2.5**, achieved a yield of 74% and converted 78% of ethanol in a 2-hour reaction (entry 1). Compared to the previous best catalyst, *trans*-[$RuCl_2(dppm)_2$], this catalyst shows significant results. A 2-hour experiment achieved a 65% yield of isobutanol with 98% selectivity and an 88% ethanol conversion. Extending the reaction time to 20 hours enhanced performance, yielding 75% isobutanol with 99% selectivity and a 90% ethanol conversion.[2] This performance is comparable to the most exemplary existing instances. Catalyst **2.6**, which possesses the same amine functionality but a longer propylene linker, exhibited reduced activity towards isobutanol with a yield of 59%. Catalyst **2.10** exhibits remarkable selectivity in the liquid phase, as evidenced by the detection of only isobutanol by GC. In most cases, extending the run time to 20 hours resulted in almost complete ethanol conversion.[1]

To conclude, the performance of these complexes as catalysts in the Guerbet upgrading of methanol/ethanol to isobutanol is equal to or surpasses that of the original **2.1** catalyst, mostly because of their improved stability under typical reaction circumstances. This process for deriving catalysts can increase the diversity of ligand libraries and provide a potential pathway for catalyst heterogenisation.

2.2. Aims and Objectives

Despite recent advances that were reported by the Wass group, there is still wide scope for improvement. The use of expensive ligands could be a barrier to industrial uptake of Guerbet processes for the generation of long chain alcohols as replacements for petrochemical fuels. The primary aim of this chapter was to examine the impact of simple monodentate phosphine ligands with different ruthenium precursors to assess the potential for attaining enhanced yields and selectivity.

The overarching goals and objectives of the research conducted in this chapter were as follows:

- To explore how variations in well-known ruthenium catalysts (Figure 2-3) can further optimise the ethanol/methanol conversion processes, focusing on improving selectivity and yield for isobutanol production. While these catalysts are well-established, the study aims to investigate how modifications in ligand structure, reaction conditions, and catalyst loading can lead to enhanced catalytic performance, particularly under more sustainable and industrially relevant conditions.
- To investigate the impact of monodentate phosphine ligands on these ruthenium catalysts during the synthesis of isobutanol.

2.3. Ethanol and Methanol Upgrading to Isobutanol

The present study examined the utilisation of ruthenium precursors (Figure 2-3) in conjunction with monodentate phosphine ligands to enhance the conversion of ethanol and methanol into isobutanol. Before introducing any phosphine ligand, an assessment was conducted on the following ruthenium complexes to evaluate their impact on enhancing the conversion of isobutanol to achieve optimal yield and selectivity.

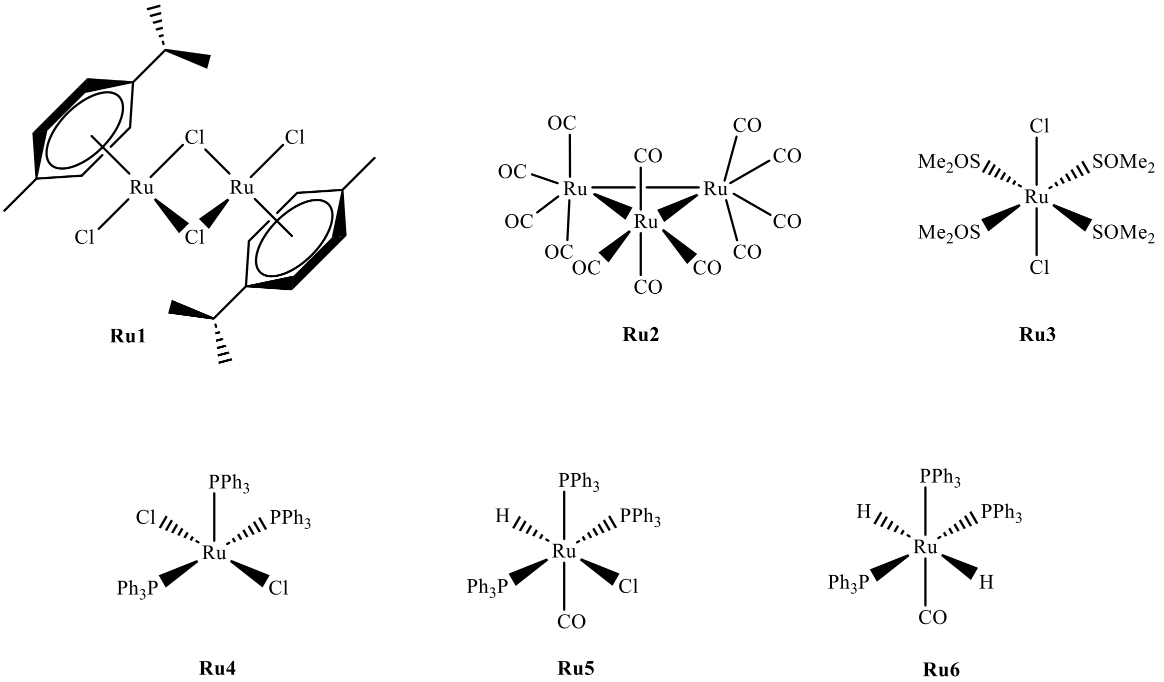

Figure 2-3: Well-known ruthenium catalysts used in this research.

Ru1 (Dichloro(*p*-cymene)ruthenium(II) dimer, [Ru(*p*-Cymene)Cl$_2$]$_2$): **Ru1** features two ruthenium centres, each coordinated to a p-cymene ligand and two chloride ions. The dual metal centres act as cooperative active sites, enhancing catalytic performance through interaction between the two ruthenium ions.

Ru2 (Ruthenium carbonyl, Ru$_3$(CO)$_{12}$): **Ru2** contains three ruthenium centres bridged by carbonyl ligands. The carbonyl groups facilitate electron back-donation, stabilising intermediates and promoting multi-centre substrate activation, which boosts overall catalytic efficiency.

Ru3 (Dichlorotetrakis(dimethylsulfoxide)ruthenium(II), [RuCl$_2$(DMSO)$_4$]): **Ru3** has a single ruthenium centre coordinated to two chloride and four DMSO ligands. Its mononuclear nature allows precise control over substrate interactions, enhancing selectivity, particularly in isobutanol formation.

Ru4 (Dichlorotris(triphenylphosphine)ruthenium(II), [RuCl$_2$(PPh$_3$)$_3$]): **Ru4**'s single ruthenium centre is coordinated with two chloride ions and three triphenylphosphine ligands. These phosphine ligands increase the electron density at the ruthenium centre, improving its ability to perform key catalytic steps such as oxidative addition and reductive elimination.

Ru5 (Carbonylchlorohydridotris(triphenylphosphine)ruthenium(II), [RuClH(CO)(PPh$_3$)$_3$]): **Ru5** includes a single ruthenium centre bound to chloride, hydride, carbonyl, and triphenylphosphine ligands. The hydride and carbonyl ligands facilitate hydrogen transfer, improving efficiency in hydrogenation steps, which is essential for isobutanol production.

Ru6 (Carbonyldihydridotris(triphenylphosphine)ruthenium(II), [RuH$_2$(CO)(PPh$_3$)$_3$]): **Ru6**, similar to **Ru5**, has a single ruthenium centre coordinated to two hydride ligands, carbonyl, and triphenylphosphine. The dual hydride ligands enhance hydrogenation, which is crucial for converting ethanol and methanol to isobutanol, while the triphenylphosphine ligands aid in maintaining high selectivity for C–C bond formation.

It should be noted that the present study focused exclusively on analysing liquid-phase products, and as such, potential gas-phase by-products or salts formed during the reactions were not collected or examined. The analysis concentrated primarily on the liquid products, specifically those derived from the conversion of ethanol and methanol to isobutanol, to assess the catalytic process's efficiency. This study's turnover number (TON) calculations were based on the mmol of ethanol conversion, providing a measure of the catalyst's effectiveness in the liquid-phase reaction. Future studies should incorporate a more thorough analysis of all reaction phases, including gas-phase products, to better understand the reaction outcomes and optimise the catalytic process further.

2.3.1. Catalytic Performance of Ruthenium Complexes in Guerbet Reactions for Isobutanol Production

This study performed in situ Guerbet reactions using ruthenium catalysts **Ru1-Ru6** under fixed reaction conditions, focusing on upgrading ethanol and methanol to isobutanol. The results demonstrated variability in ethanol conversion efficiencies and product selectivity, highlighting the influence of catalyst structure on biofuel production. Ethanol conversions ranged from 53.0% to 83.5%, with **Ru4**, **Ru5**, and **Ru6** showing notably higher conversions, surpassing 68.0%. The key findings of this study align with those from previous research that explored similar catalytic systems for alcohol upgrading, including using phosphine ligands to enhance catalytic performance.[3]

In addition, pre-catalysts **Ru4**, **Ru5**, and **Ru6**, containing the PPh_3 moiety, demonstrate significantly higher yields and selectivity for isobutanol than the other catalysts. Notably, pre-catalyst **Ru5** achieves an impressive isobutanol yield of 50.7%, underscoring the impact of specific structural features on product formation. However, the carbon balance for **Ru5** is 110.8%, indicating an analytical error calculated to be 37.7%, which may affect the accuracy of the reported yield.

A notable aspect of this study was the turnover number (TON) calculation, which is crucial in evaluating the number of catalytic cycles a catalyst can undergo before deactivation. For example, **Ru5** exhibited an outstanding TON of 367 for isobutanol production, significantly higher than those reported for similar systems using homogeneous catalysts. Comparatively, in earlier studies, catalyst systems utilising ruthenium complexes with phosphine ligands demonstrated TON values in the range of 200-300, depending on the reaction conditions and ligand choice .[4] The high TON observed in **Ru5** suggests it is one of the most efficient catalysts for isobutanol production, as it outperforms many previously reported systems under comparable conditions.[5]

The superior performance of **Ru5** can be attributed to the presence of the triphenylphosphine (PPh_3) ligand, which acts as a strong σ-donor. PPh_3 enhances the electron density at the ruthenium centre, stabilising key intermediates throughout the catalytic cycle. This stabilisation is crucial for facilitating oxidative addition and reductive elimination, key steps in hydrogenation and C–C bond-forming reactions essential for isobutanol production. Previous studies have shown that phosphine ligands like PPh_3 can significantly enhance catalytic activity by improving the coordination environment around the metal centre, leading to more efficient and selective reactions.[3b] The results from **Ru4** and **Ru6**, with TON values of 305 and 227, respectively, are consistent with findings from similar catalytic systems, where the use of PPh_3 ligands led to high catalytic efficiency and selectivity.[4]

Compared to studies using bidentate ligands, this research found that the bidentate nature of **Ru4**, **Ru5**, and **Ru6** provided significant advantages in stabilising reactive intermediates. For instance, studies on related ruthenium-based systems for ethanol conversion have reported lower TON values when monodentate ligands were used in place of bidentate ligands, indicating the stabilising effect of bidentate ligands on the catalytic cycle.[3a] The high selectivity observed in this study, particularly with **Ru5** achieving 95.2%, mirrors result from other studies using similar bidentate ligand systems, where selectivity remained high due to the controlled coordination environment provided by the phosphine ligands.[5b]

Furthermore, this study's analysis of the carbon balance revealed missing carbon, likely due to the formation of gas-phase by-products such as CO_2 and CO, or volatile intermediates. The missing carbon was particularly significant in catalysts **Ru1**, **Ru2**, and **Ru3**, where the carbon balance was as low as 14.0% for **Ru1**. Similar observations were made in studies by Cadierno et al. (2003), which also reported the formation of undetected gas-phase products in catalytic systems using ruthenium precursors. This highlights the importance of conducting comprehensive analyses of all reaction phases—liquid and gas—to understand the catalytic processes.[3a]

Equilibrium may have influenced the performance of these catalysts; however, without time-on-stream data, it is difficult to confirm whether equilibrium was reached or how rapidly it occurred. Catalysts such as **Ru1**, **Ru2**, and **Ru3** showed limited ethanol conversion and lower TON values, suggesting an early onset of equilibrium despite their potential for higher catalytic activity under extended reaction conditions. While similar trends have been reported in the literature, attributing reduced performance solely to equilibrium effects in this study remains speculative without detailed time-course data.[3b] For catalysts like **Ru5**, which achieved a high TON despite reaching equilibrium, continuous product removal or other strategies could further enhance its efficiency, as suggested by previous studies on equilibrium-shifting techniques in homogeneous catalysis.[5a]

In summary, this research presents significant advancements in the use of ruthenium catalysts for isobutanol production, with **Ru5** emerging as the most promising catalyst. The results are comparable to those from other studies on similar catalytic systems, particularly regarding TON, selectivity, and the role of phosphine ligands in enhancing catalytic performance.

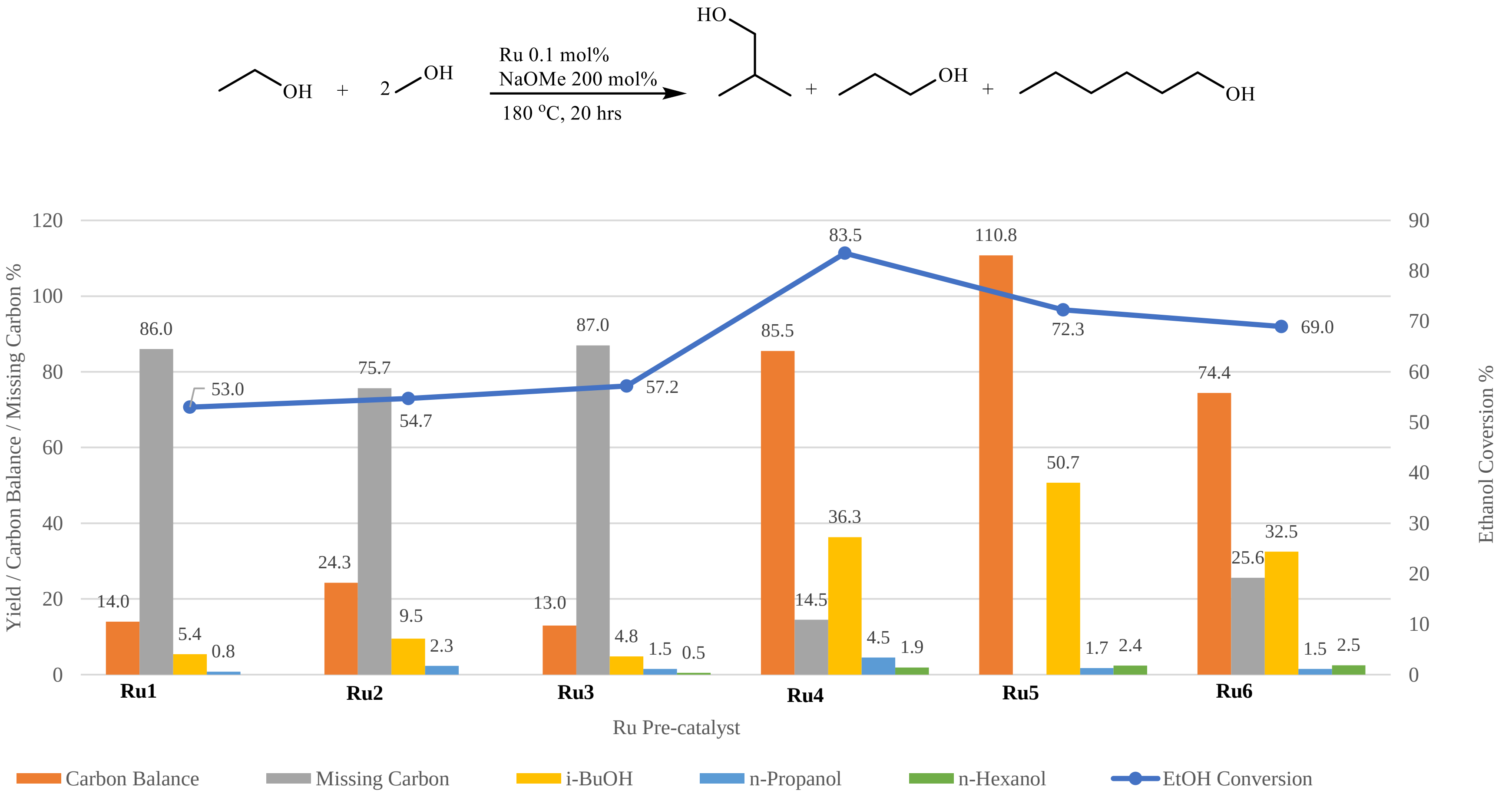

Figure 2-4: Yield of liquid products and ethanol conversion achieved with pre-catalysts **Ru1**-**Ru6**. **Conditions:** ethanol (0.75 mL, 12.8 mmol), methanol (7.5 mL, 185.15 mmol), **Ru** (0.0128 mmol, 0.1 mol%), NaOMe (34.26 mmol, 200 mol%), 20 hours, 180 °C, mol% relative to ethanol. **Carbon Balance (%)** represents the percentage of initial ethanol carbon detected in the products, ideally around 100% for complete accounting. **Missing Carbon (%)** indicates any unaccounted carbon potentially due to undetected side products, volatiles, or experimental loss. **EtOH Conversion %** (line) shows the percentage of ethanol converted to products. **Product Yields**: The bars represent the yields of individual products, including *i*-BuOH (isobutanol), *n*-propanol, and *n*-hexanol.

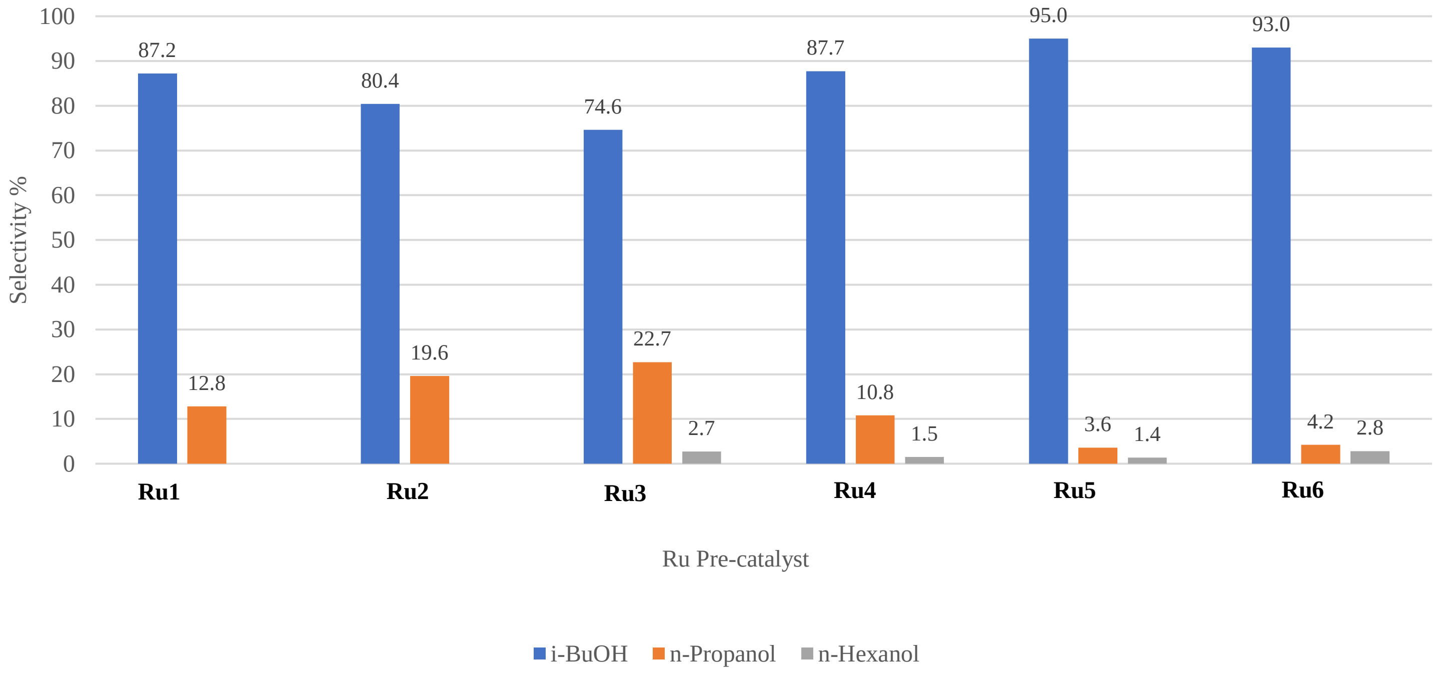

Figure 2-5: Selectivity of liquid products achieved with pre-catalysts **Ru1-Ru6**. Conditions: ethanol (0.75 mL, 12.8 mmol), methanol (7.5 mL, 185.15 mmol), **Ru** (0.0128 mmol, 0.1 mol%), NaOMe (34.26 mmol, 200 mol%), 20 hours, 180 °C, mol% relative to ethanol. **Product Selectivity %**: Bars represent selectivity percentages for each product—*i*-BuOH (isobutanol), *n*-propanol, and *n*-hexanol—across the different pre-catalysts. High selectivity for *i*-BuOH is observed with pre-catalysts **Ru4**, **Ru5**, and **Ru6**, indicating a strong preference for isobutanol production with these catalyst compositions, while lower selectivity for *n*-propanol and *n*-hexanol suggests limited formation of these products.

2.4. Monodentate Phosphine Ligands

The choice of ligands heavily influences homogeneous catalysts' electronic and steric properties in the Guerbet reaction. Substituting monodentate phosphorus-based ligands (P-ligands) can significantly alter the reaction's selectivity and efficiency, particularly in steps involving hydrogen borrowing and C–C bond formation.[6] P-ligands possess either electron-donating or electron-withdrawing properties, directly impacting the metal centre's electron density. Electron-rich ligands, such as triphenylphosphine (PPh_3), enhance the stability of the metal-hydride intermediate required for alcohol dehydrogenation.[7] However, excessively strong donor ligands can lead to over-reduction, causing catalyst deactivation. Conversely, electron-withdrawing ligands, such as tris(4-fluorophenyl)phosphine, stabilise reactive intermediates, improving step selectivity. Achieving the optimal balance of these electronic effects is crucial to fine-tuning the catalytic cycle for maximum performance.

The size and shape of the ligand also play a pivotal role by influencing substrate access and reaction pathways. Bulky ligands introduce steric constraints around the metal centre, which can restrict the positioning of alcohol substrates and intermediates. This steric hindrance can be advantageous, as it prevents unwanted side reactions such as aldol self-condensation during hydrogenation.[7] On the other hand, less crowded or smaller ligands allow easier substrate access but can reduce selectivity by diminishing steric protection around the reactive site.

Understanding the effects of ligand modifications on the reaction is critical to developing more efficient catalytic systems. These advancements can potentially significantly enhance biofuels' synthesis via the Guerbet reaction.

2.4.1. Electronic Effects of Monodentate Phosphine Ligands

Tolman has described the various electronic impacts of substituents on the phosphorus atom inside strained ring systems of diverse monodentate phosphine ligands. These influences have a substantial impact on altering the behaviour and selection of catalysts.[5a] Alkyl and aryl groups act as electron-donating substituents through their σ-bonding and π-interaction abilities, which help regulate the electron distribution around the metal centre in catalytic systems. Their electron-donating effects increase the electron density at the metal centre, thereby stabilising reactive intermediates and enhancing the catalyst's overall efficiency.[3] Increased electron density enhances the nucleophilic nature of the metal and its capacity to interact with and activate substrate molecules.[3a]

Conversely, electron-withdrawing substituents decrease the electron density at the metal centre compared to when electron-donating groups are present, as these substituents pull electron density away from the metal core, leading to a less nucleophilic metal centre.[8] A lower electron density at the metal centre results in decreased reactivity due to reduced nucleophilicity, which is critical for the activation of substrates in catalytic cycles such as the Guerbet reaction. In this mechanism, the metal centre must engage in oxidative addition and subsequent hydrogen transfer steps, where a nucleophilic metal centre facilitates the coordination and activation of substrates like ethanol or methanol. A reduction in nucleophilicity hinders the metal’s ability to donate electron density to these substrates, thereby slowing key steps such as dehydrogenation and aldol condensation, which are crucial for efficient isobutanol production.[3] The manipulation of electronic characteristics through electron-withdrawing groups can also influence the selectivity of the catalyst, guiding the reaction down specific pathways or towards specific products.[9] Understanding these electrical properties enables chemists to strategically construct catalysts for specific processes by choosing appropriate substituents on the phosphine ligands.

2.4.2. Steric Effects of Monodentate Phosphine Ligands

The steric effects of this ligand type are considered, considering the influence of steric hindrance on monodentate phosphine ligands in catalytic reactions.[10] Additionally, it is crucial to consider the length of the alkyl groups connected to the phosphorus atom, as they significantly influence the functioning of the catalyst. Once again, the presence of bulky substituents might obstruct the metal centre, impeding the access of substrates to their binding site and interfering with proper interaction.

Steric hindrance, a phenomenon explained by the bulky group effect, can be utilised in directing catalytic processes.[11] By isolating specific substrates from the metal core, it is possible to manipulate the parameters that determine selectivity, allowing for the design of customised catalysts to guide the production of desired products. Additionally, it provides opportunities to manipulate the spatial configuration surrounding the active site to govern the paths of chemical reactions. Chemists can optimise catalytic activity and achieve desired reaction outcomes with excellent selectivity by carefully choosing alkyl groups of appropriate size to adjust the steric factor.[12] Considering this, an understanding of steric effects is crucial in developing novel and effective catalysts in homogeneous catalysis.

2.4.3. The Effect of Monodentate Phosphine Ligands on 1-Butanol and Isobutanol Production

Phosphines are monodentate ligands employed in transition metal systems to convert lower-carbon alcohols, such as ethanol and methanol, into higher-carbon alcohols, like 1-butanol and isobutanol. Tolman's contributions to quantifying ligand steric and electronic characteristics, mainly through the development of the Tolman cone angle and Tolman electronic parameter (TEP), are essential for understanding the behaviour of phosphine ligands in catalytic reactions.[5b] For instance, ligands can exert electron-donating effects on the metal centre, thereby increasing the metal's nucleophilicity. This enhanced nucleophilicity is crucial because it allows the metal centre to more effectively donate electron density to the alcohol substrate, facilitating bond activation in reactions such as the Guerbet process; the increased nucleophilicity aids in the deprotonation and dehydrogenation of alcohols, critical steps in forming the desired higher alcohol products.[3]

The investigation of monodentate phosphine ligands for isobutanol production has yet to be extensively explored, mainly in catalysis. This chapter delves into this intriguing research area by closely analysing the interaction dynamics between monodentate phosphine ligands and well-established ruthenium catalysts. This work aims to conduct an extensive study to clarify the catalytic mechanisms and explore the capacity of monodentate phosphine ligands to impact the production of isobutanol. By utilising the established features of ruthenium catalysts as a foundation, this research aims to expand the understanding of catalytic processes, selectivity, and efficiency in isobutanol synthesis from methanol and ethanol.

2.4.4. Tolman Cone Angles and Electronic Parameters

In homogeneous catalysis, the steric and electronic properties of phosphine ligands play a pivotal role in tuning the reactivity and selectivity of metal complexes. Phosphine ligands can significantly impact the catalytic environment by influencing both the accessibility of the metal centre and the electron density it retains.

The Tolman cone angle (TCA) provides insight into the steric properties of phosphine ligands. For instance, PPh_3 (**PL1**) has a TCA of 145°, which is relatively moderate compared to **PL5** and **PL6**, whose TCAs are 166° and 165°, respectively. A larger cone angle, such as that seen in **PL5**, can create a greater steric bulk around the metal centre, which can help minimise unwanted side reactions by limiting the approach of extraneous species.[5b] However, the increased steric hindrance of larger cone angle ligands can sometimes restrict substrate access to the metal centre, potentially reducing the catalytic turnover in reactions where substrate proximity is essential.

In addition to steric effects, the electronic influence of phosphine ligands is characterised by the Tolman Electronic Parameter (TEP), which reflects the electron-donating or electron-withdrawing nature of the ligand. PPh_3 (**PL1**), with a TEP of 2069 cm^{-1}, is a relatively balanced electron donor. In contrast, **PL5** has a higher TEP of 2091 cm^{-1}, indicating more electron-withdrawing. This property renders **PL5** effective for reactions where an electrophilic metal centre is beneficial, enhancing interactions that depend on substrate polarisation or electron-deficient activation states.[5b] Conversely, **PL6**, with a TEP of 2071 cm^{-1}, exhibits moderate electron-withdrawing characteristics, positioning it between PPh_3 and PL5 in terms of electron density modulation.

Thus, while **PL1** (PPh_3) is well-suited to catalytic environments where a balanced electron-donating ligand is advantageous, **PL5** and **PL6** offer distinct electronic profiles that make them useful for more selective applications. **PL5**, being the most electron-withdrawing, stabilises electron-deficient catalytic intermediates, whereas **PL6**'s intermediate properties provide versatility across a range of reaction mechanisms.

Table 2-3 presents the cone angles and electronic parameters of the ligands illustrated in Figure 2-6. The balance between steric bulk and electronic effects, as represented by both cone angle and electronic parameters, plays a crucial role in adjusting the reactivity and selectivity of phosphine ligands in catalytic processes. By carefully choosing ligands with suitable steric and electronic properties, catalysts can be optimised for peak performance in specific reactions, such as the Guerbet process for alcohol upgrading. Unfortunately, the TCA and TEP values for **PL3** (Tris(2,4,6-trimethylphenyl)phosphine), **PL7** (Tris[3,5-bis(trifluoromethyl)phenyl]phosphine), and **PL8** (Tris[4-(trifluoromethyl)phenyl]phosphine) were unavailable and have not yet been reported in the literature. Nevertheless, the findings from this study are expected to advance our understanding of ligand-catalyst interactions and provide valuable insights into the broader field of biofuel catalysis.

Table 2-2: Tolman cone angles and electronic parameters for monodentate phosphine ligands.[5b, 13]

Phosphine Ligand (PL)	Tolman Cone Angle (Degree)	Tolman Electronic Parameter (cm^{-1})	Electron Donating/Withdrawing Effect
Triphenylphosphine (PL1)	145	2069	Moderate Donor
Tris(*o*-tolyl)phosphine (PL2)	194	2067	Weak Donor
Tris(4-methoxyphenyl)phosphine (PL4)	167	2066	Strong Donor
Tris(pentafluorophenyl)phosphine (PL5)	166	2091	Strong Withdrawing
Tris(4-fluorophenyl)phosphine (PL6)	165	2071	Moderate Withdrawing
Tri-*tert*-butylphosphine (PL9)	182	2056	Strong Donor
Triisopropylphosphine (PL10)	160	2059	Moderate Donor
Tricyclohexylphosphine (PL11)	170	2056	Strong Donor

Note: The Tolman cone angle (in degrees) represents the steric bulk of the phosphine ligand, with larger angles indicating greater spatial hindrance. The Tolman electronic parameter (TEP, cm^{-1}) reflects electron-donating or withdrawing capability, with lower values indicating stronger electron donation. The electron-donating/withdrawing effect provides a qualitative classification of each ligand's electronic properties.

2.5. Screening Ruthenium Catalysts with Monodentate Phosphine Ligands *In situ*

2.5.1. Screening Catalysts Ru1, Ru2 and Ru3 with PL1

The catalysts **Ru1**, **Ru2**, and **Ru3** lack phosphine groups, making them suitable for testing in the presence of 0.3 mol% of **PL1** (relative to ethanol) to assess the impact of the ligand on the catalytic process and the resulting yield. While **Ru1**, **Ru2**, and **Ru3** are binuclear, trinuclear, and mononuclear complexes, respectively, using 0.3 mol% **PL1** was based on the number of moles of each complex rather than the total number of ruthenium centres. This approach ensures a consistent ligand-to-complex ratio across all systems, allowing for a fair comparison of catalytic efficiency. Although this method does not normalise the different nuclearities of the ruthenium species, it provides a practical and consistent basis for evaluating the influence of phosphine ligands on ethanol conversion and isobutanol selectivity.

In this study, the use of 0.3 mol% **PL1** (relative to ethanol) resulted in ethanol conversions of 87.4%, 77.5%, and 86.0% for **Ru1**, **Ru2**, and **Ru3**, respectively. The catalyst **Ru1/PL1** achieved an isobutanol production yield of 42.8%, with a high overall selectivity of 96.7% (Table 2-4, Entry 1). Similarly, **Ru2/PL1** and **Ru3/PL1** exhibited isobutanol production yields of 49.7% (selectivity 92.7%) and 34.9% (selectivity 96.6%), respectively (Table 2-4, Entries 2 and 3). Additionally, GC analysis detected the presence of by-products, including *n*-propanol and *n*-hexanol, produced by all catalysts in low yields and selectivity. This highlights that the simple monodentate phosphine ligand PPh_3 (**PL1**) significantly enhances the catalytic activity of ruthenium precursors **Ru1-Ru3** in ethanol/methanol conversion to isobutanol.

While this study utilised 0.3 mol% **PL1** relative to ethanol, future work could explore optimising the ligand-to-metal ratio to account for the different nuclearities of the ruthenium precursors. Previous studies have shown that varying the ligand-to-metal ratio can significantly influence catalytic outcomes. For example, work by Behr *et al*. demonstrated that increasing the ligand-to-metal ratio enhanced both the selectivity and yield in Guerbet alcohol synthesis, suggesting that further optimisation could enhance the outcomes of the current study.[14] Similarly, Dixon *et al.* discussed the role of phosphine ligands in fine-tuning catalytic selectivity in C–C bond formation, showing that ligand steric and electronic effects can impact reaction mechanisms[15].

Table 2-3: Yield and selectivity of liquid products and ethanol conversion achieved with catalysts **Ru1**, **Ru2** and **Ru3** in the presence of **PL1**.

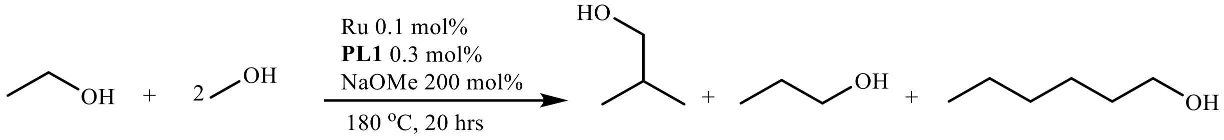

Entry [a]	Catalyst	EtOH Conversion (%) [b]	Yield [c] (TON) [d] [Selectivity] (%)			Carbon Balance (%) [e]	Missing Carbon (%) [f]	Error of Analysis (%) [g]
			Isobutanol	*n*-Propanol	*n*-Hexanol			
1	**Ru1/PL1**	87.4	42.8 (375) [96.7]	1.4 (12) [3.1]	0.3 (3) [0.2]	88.4	11.6	-
2	**Ru2/PL1**	77.5	49.7 (382) [92.7]	2.5 (19) [4.6]	1.8 (14) [2.9]	109.6	-	29.3
3	**Ru3/PL1**	86.0	34.9 (300) [96.6]	1.2 (10) [3.2]	0.2 (2) [0.2]	70.5	29.5	-

[a] Conditions: ethanol (0.75 mL, 12.8 mmol), methanol (7.5 mL, 185.15 mmol), **Ru** (0.0128 mmol, 0.1 mol%), **PL1** (0.0384 mmol, 0.3 mol%), NaOMe (34.26 mmol, 200 mol%), 20 hours, 180 °C, mol% relative to ethanol. [b] Total ethanol conversion as determined by GC liquid phase analysis. [c] Total yield and selectivity of alcohol products in the liquid fraction as determined by GC. [d] TON based on mmol of ethanol converted to products per mmol Ru. [e] **Carbon Balance %:** the percentage of initial carbon in ethanol detected in the products. Ideally close to 100%, indicating accurate accounting of all ethanol-derived carbon atoms. [f] **Missing Carbon:** any carbon discrepancy, indicating undetected carbon potentially due to side products, volatiles, or experimental losses. [g] **Analysis Error %:** an estimated measure of uncertainty in the analytical method, reflecting potential deviations from ideal values due to instrument limitations or procedural inaccuracies.

2.5.2. Hypothetical Coordination of Ruthenium Catalysts

2.5.2.1. Coordination of [RuCl$_2$(*p*-cymene)]$_2$ (Ru1) with Triphenylphosphine (PL1)

When [RuCl$_2$(*p*-cymene)]$_2$ reacts with three equivalents of triphenylphosphine (PPh$_3$), the coordination chemistry of ruthenium continues to favour a *pseudo*-octahedral geometry, typical of ruthenium(II) complexes.[16] The dimeric form of [RuCl$_2$(*p*-cymene)]$_2$ contains two ruthenium centres, each coordinated through the η^6-arene bonding of *p*-cymene (via its aromatic ring), with two bridging chloride ligands completing the coordination sphere. Each ruthenium centre utilises three coordination sites from the η^6-arene interaction with *p*-cymene, leaving two positions for chloride ligands. In the dimer, the two ruthenium atoms share the chloride ligands.[16-17]

When PPh_3 is introduced in a 3:1 molar ratio relative to the **Ru1**, the reaction likely dissociates the dimer into monomeric units. The expected resulting complex is [$RuCl_2$(*p*-cymene)(PPh_3)], with each ruthenium centre coordinating one PPh_3 molecule. The ruthenium centre adopts a *pseudo*-octahedral geometry, where three coordination sites are occupied by η^6-*p*-cymene, two by chloride ligands, and the sixth site by one PPh_3 ligand. However, with the introduction of three equivalents of PPh_3, only one equivalent of PPh_3 effectively coordinates to the metal centre because the remaining sites are occupied by *p*-cymene and chloride ligands.[16, 18] The excess PPh_3 molecules may play an important indirect role in the catalytic system. They could contribute to stabilising the catalytic environment by participating in equilibrium processes, influencing steric and electronic factors, or scavenging reactive by-products, thereby maintaining the overall efficiency of the catalyst.[17]

This coordination behaviour results from the steric bulk around the metal centre, particularly from the *p*-cymene and PPh_3 ligands. The PPh_3 ligand, acting as a strong σ-donor, increases the electron density at the metal centre, promoting the stabilisation of intermediates during catalytic processes.[17] However, the coordination of more than one PPh_3 ligand per ruthenium centre is unlikely due to steric hindrance and geometric constraints. The available coordination sites on ruthenium are limited, as the *p*-cymene ligand already occupies three of the six available sites, leaving only one site for PPh_3 and two for the chloride ligands.[17, 19]

The *cis*-chloride coordination in the expected resulting [$RuCl_2$(*p*-cymene)(PPh_3)] complex is also favoured due to steric and electronic effects. The bulky PPh_3 and *p*-cymene ligands create a spatially constrained environment around the metal centre, making the *cis* configuration of the chloride ligands more favourable. This geometry minimises steric clashes and provides easier access for substrates during catalytic reactions. The *cis*-chloride arrangement also helps stabilise intermediate complexes, improving the efficiency of C–C bond-forming reactions, which are vital for catalytic applications like biofuel synthesis.[20]

The following scheme, Scheme 2-2, illustrates the hypothetical process of [RuCl$_2$(*p*-cymene)]$_2$ dissociation, followed by the coordination of triphenylphosphine (PPh$_3$) to form the expected *pseudo*-octahedral complex [RuCl$_2$(*p*-cymene)(PPh$_3$)]. This process involves the dissociation of the dimer into monomeric units, creating a single active site for PPh$_3$ coordination.

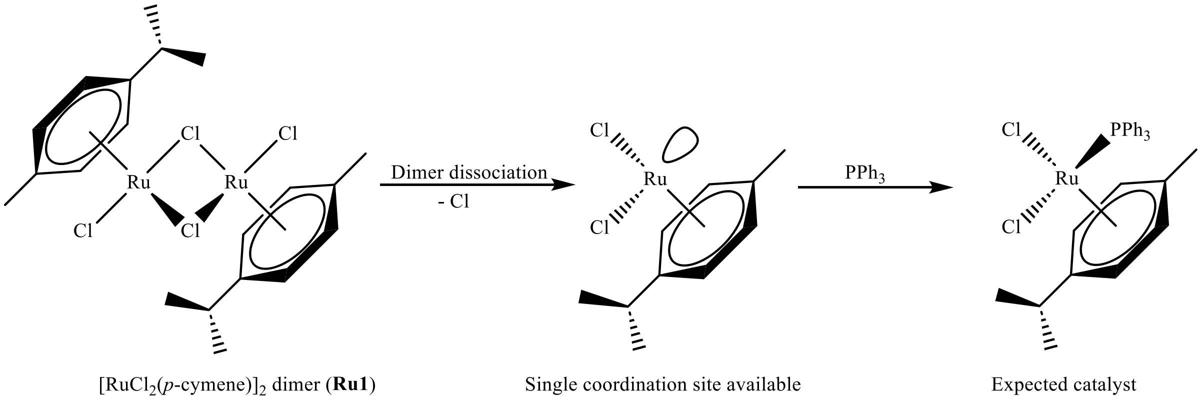

Scheme 2-2: Hypothetical process of **Ru1** dissociation followed by the coordination of PPh$_3$

In summary, when [RuCl$_2$(*p*-cymene)]$_2$ reacts with three equivalents of PPh$_3$, the dimer dissociates into monomeric [RuCl$_2$(*p*-cymene)(PPh$_3$)] units. Only one equivalent of PPh$_3$ coordinates to each ruthenium centre, with the remaining PPh$_3$ molecules remaining uncoordinated in the system. These excess PPh$_3$ ligands may play an indirect but crucial role by influencing equilibrium processes and scavenging reactive by-products. The complex retains a pseudo-octahedral geometry, favouring *cis*-chloride coordination, which stabilises the complex and enhances its catalytic efficiency in reactions such as hydrogenation and C–C bond formation.

2.5.2.2. Coordination of Ru_3CO_{12} (Ru2) with Triphenylphosphine (PL1)

When $Ru_3(CO)_{12}$ (**Ru2**) reacts with three equivalents of triphenylphosphine (PPh_3), the reaction significantly modifies the original ruthenium cluster. $Ru_3(CO)_{12}$ is characterised by a triangular arrangement of three ruthenium atoms, each bridged by carbonyl ligands, forming a stable metal cluster. When three equivalents of PPh_3 are introduced, the substitution of terminal carbonyl ligands by PPh_3 occurs, leading to the dissociation of the triangular cluster into monomeric species. This typically results in the formation of $[Ru(PPh_3)_3(CO)_2]$, a five-coordinate ruthenium complex with three PPh_3 ligands and two remaining carbonyl ligands.[17]

The expected structure of $[Ru(PPh_3)_3(CO)_2]$ adopts a trigonal bipyramidal geometry, with the two carbonyl ligands occupying the axial positions and the three PPh_3 ligands in the equatorial positions. Although five-coordinate complexes are less common than six-coordinate ones, this arrangement is stabilised by the steric and electronic properties of the ligands involved.[21] The strong σ-donor properties of PPh_3 significantly increase the electron density at the ruthenium centre, stabilising the metal complex and allowing for its catalytic applications.[18]

One of the primary stabilising factors in this complex is the back-donation between the ruthenium metal centre and the π-acceptor CO ligands. This backbonding effect helps delocalise electron density, making the complex more robust despite having fewer ligands than its octahedral counterparts.[17] The steric bulk of PPh_3 also plays a critical role by preventing over-coordination, limiting the number of additional ligands that can bind to the ruthenium centre and ensuring that the five-coordinate structure remains stable.[20]

In catalytic processes, the availability of a single coordination site in $[Ru(PPh_3)_3(CO)_2]$ can enhance its functionality. This open site provides space for the binding or activating substrates, crucial in reactions such as hydrogenation or C–C bond formation. The selective binding at this single active site helps improve the efficiency and selectivity of the catalytic process.[17-18]

In addition to the stabilising roles of the ligands, many five-coordinate metal complexes exhibit *fluxional behaviour,* where ligands rapidly exchange positions. This dynamic flexibility allows the complex to adapt to different coordination environments during catalytic cycles, contributing to its overall stability and efficiency as a catalyst.[21]

Scheme 2-3 illustrates the hypothetical process of $Ru_3(CO)_{12}$ (**Ru2**) dissociation, followed by the coordination of three equivalents of triphenylphosphine (PPh_3) to form the expected trigonal bipyramidal complex [$Ru(PPh_3)_3(CO)_2$]. During this process, the Ru3 cluster dissociates into monomeric units, each coordinating with three PPh3 ligands, leaving a single active site available for catalytic activity.

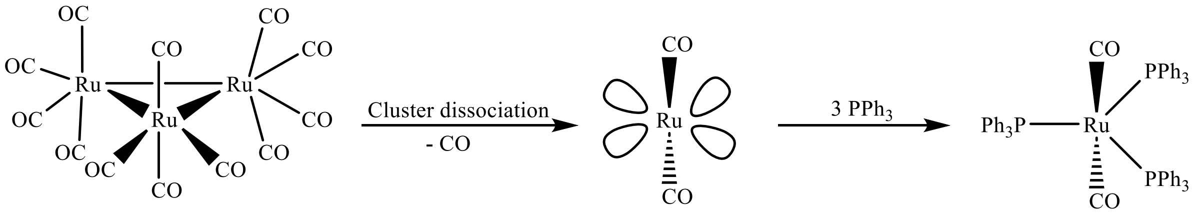

$Ru_3(CO)_{12}$ (**Ru2)**

Four coordination sites available

Expected catalyst

Scheme 2-3: Hypothetical process of **Ru2** dissociation followed by the coordination of three equivalents of PPh_3

To conclude, the expected complex [$Ru(PPh_3)_3(CO)_2$] remains stable due to the strong σ-donor and π-acceptor properties of PPh_3 and CO ligands, respectively, as well as the steric bulk of PPh_3, which limits over-coordination. The available single active site is critical in enhancing catalytic efficiency, making this complex highly useful in reactions requiring precise control over the coordination environment. This complex's stability and catalytic performance make it particularly effective in selective hydrogenation and C–C bond-forming reactions.[17-19]

2.5.2.3. Coordination of [$RuCl_2(DMSO)_4$] (Ru3) with Triphenylphosphine (PL1)

When [$RuCl_2(DMSO)_4$] reacts with three equivalents of triphenylphosphine (PPh_3), the expected resulting product is [$RuCl_2(DMSO)(PPh_3)_3$], where three PPh_3 ligands replace three DMSO ligands. This substitution significantly alters both the steric and electronic properties of the complex. The bulky nature of PPh_3, a strong σ-donor ligand, plays a vital role in stabilising the complex by occupying three coordination sites on the ruthenium centre. This steric bulk prevents over-coordination and reduces the likelihood of additional ligands attaching to the metal centre, which helps maintain the six-coordinate geometry of the complex. The two chloride ligands are forced into a *cis*-configuration to minimise steric repulsion between the large PPh_3 ligands and smaller chloride ions, stabilising the coordination environment.[21] The cis-configuration of the chlorides is also crucial for catalytic activity, as it allows substrates easier access to the active site, enhancing the complex's efficiency in reactions like hydrogenation and C–C bond formation.[18]

The PPh_3 ligands similarly influence the electronic properties of the complex. Being a strong σ-donor, PPh_3 increases the electron density at the ruthenium centre, stabilising catalytic intermediates and promoting reactivity in processes like the Guerbet reaction, which produces isobutanol. Additionally, the remaining DMSO ligand, coordinating via its sulfur atom, helps balance the strong donation from the PPh_3 ligands while also contributing to the overall stability of the complex.[17] This six-coordinate pseudo-octahedral structure is ideal for catalytic applications where selectivity is paramount. The steric protection provided by PPh_3 minimises side reactions, ensuring that only desired substrates can access the active site.[21] The strong electron-donating properties of PPh_3 also facilitate efficient hydrogen transfer, making [$RuCl_2(DMSO)(PPh_3)_3$] an excellent platform for selective catalytic transformations. This complex's unique balance of steric and electronic factors allows it to function efficiently in industrially relevant reactions, providing precise control over the coordination environment.[16]

Scheme 2-4 illustrates the hypothetical process involving the coordination of three equivalents of triphenylphosphine (PPh_3) with [$RuCl_2(DMSO)_4$], leading to the formation of the expected *pseudo*-octahedral complex [$RuCl_2(DMSO)(PPh_3)_3$].

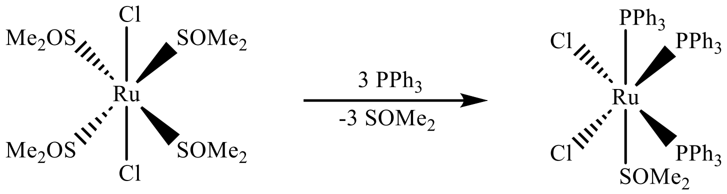

Scheme 2-4: Hypothetical process of the coordination of three equivalents of PPh_3 with **Ru3**

In conclusion, the reaction of $[RuCl_2(DMSO)_4]$ with three equivalents of triphenylphosphine (PPh_3) leads to the formation of the complex $[RuCl_2(DMSO)(PPh_3)_3]$, where the steric bulk and strong σ-donating properties of PPh_3 significantly influence the complex's geometry and catalytic activity. The steric hindrance introduced by the PPh_3 ligands ensures a *cis*-chloride configuration, facilitating effective substrate interaction at the active site. The electron-donating properties of PPh_3 enhance the electron density at the ruthenium centre, stabilising catalytic intermediates and promoting selective catalytic transformations. This *pseudo*-octahedral structure, combining steric protection and electronic stability, makes $[RuCl_2(DMSO)(PPh_3)_3]$ a highly effective catalyst for a variety of chemical processes, including hydrogenation and C–C bond formation.

2.5.3. Screening Ru1 on isobutanol Guerbet reactions with various PR_3 Ligands

Figures 2-7 and 2-8 present a thorough summary of the influence of different PR_3 ligands (Figure 2-6), when used together with catalyst **Ru1**, on the process of ethanol/methanol upgrading to isobutanol conversion. The ligands investigated span a spectrum of structural differences, which impact the catalytic results. The ligands employed in these catalytic reactions include PPh_3 (**PL1**), monodentate phosphine ligands with electron-donating groups **(PL2**, **PL3**, **PL4**), monodentate phosphine ligands with electron-withdrawing groups (**PL5**, **PL6**, **PL7**, **PL8**), and aliphatic monodentate phosphine ligands (**PL9**, **PL10**, **PL11**).

Ru1/PL1 and **Ru1/PL6** demonstrated the highest catalytic performance among the ligands tested. **Ru1/PL1** achieved a TON of 375 for isobutanol, 12 for n-propanol, and 3 for n-hexanol, coupled with an isobutanol yield of 42.8% and a selectivity of 96.7%. Similarly, **Ru1/PL6** showed comparable results, with a TON of 389 for isobutanol and n-propanol value similar to **Ru1/PL1**. Its isobutanol yield was slightly higher at 44.8%, with a selectivity of 97.0%. These values highlight the remarkable efficiency of PL1 and PL6 in enhancing the catalytic performance of the ruthenium pre-catalyst. The high carbon balances for both catalysts (88.4% for **Ru1/PL1** and 92.8% for **Ru1/PL6**) indicate that the majority of the ethanol converted was accounted for in the liquid products, with minimal formation of gas-phase by-products or other undetected intermediates.

In contrast, **Ru1/PL5** exhibited moderate performance, with a TON of 81 for isobutanol and 12 for *n*-propanol. The isobutanol yield was lower at 11.1%, with a selectivity of 87.4%. The significant steric bulk introduced by the fluorine-substituted ligand likely interfered with effective coordination at the metal centre, resulting in lower yields and a higher percentage of missing carbon, as reflected in the carbon balance of only 24.7%. The missing carbon (75.3%) suggests the formation of undetected by-products or gas-phase compounds.

Ru1/PL7 and **Ru1/PL8** also demonstrated mid-range TON values for isobutanol—172 and 188, respectively—while the n-propanol TON remained relatively consistent at 15. **Ru1/PL7** achieved an isobutanol yield of 22.1% and a selectivity of 91.3%, while **Ru1/PL8** yielded 26.7% isobutanol, with a selectivity of 92.6%. However, their carbon balances of 47.0% and 56.6%, respectively, indicated significant missing carbon, likely due to the formation of gas-phase by-products. These results suggest that equilibrium may have been reached earlier in the reaction, preventing further ethanol conversion and limiting the overall yield.

Ru1/PL2, **Ru1/PL3**, and **Ru1/PL4** exhibited the poorest performance among the tested ligands. Their ethanol conversions were relatively low, and the TON values for isobutanol were 56, 50, and 57, respectively. The isobutanol yields were also modest, ranging from 7.5% to 8.1%, with selectivity between 78.1% and 81.2%. These ligands are characterised by electron-donating groups, which may have increased electron density at the ruthenium centre, interfering with efficient hydrogen transfer and C–C bond formation. Their carbon balances were exceptionally low, with 19.3% for **Ru1/PL2**, 17.6% **for Ru1/PL3**, and 18.3% **for Ru1/PL4**, highlighting that a significant portion of the ethanol was either converted into gas-phase products or undetected due to incomplete recovery or side reactions.

The aliphatic ligands, including **Ru1/PL9**, **Ru1/PL10**, and **Ru1/PL11**, exhibited moderate performance. The ethanol conversions ranged from 60.8% to 77.7%, with isobutanol TON values of 66, 94, and 105, respectively. Despite modest isobutanol yields of 8.5% to 17.3%, the carbon balances were notably lower than the top-performing ligands, with 21.0% for **Ru1/PL9**, 27.8% for **Ru1/PL10**, and 35.3% for **Ru1/PL11**. The steric hindrance created by the bulky nature of these ligands likely reduced the efficiency of the catalytic site, contributing to the lower catalytic activity and the higher percentage of missing carbon, as evidenced by the relatively low carbon balances.

In conclusion, **Ru1/PL1** and **Ru1/PL6** emerged as the most efficient combinations for ethanol upgrading to isobutanol, as reflected in their high TON values, yields, and carbon balances. Catalytic systems such as **Ru1/PL5**, **Ru1/PL7**, and **Ru1/PL8** showed moderate performance but suffered from lower carbon balances, while **Ru1/PL2**, **Ru1/PL3**, and **Ru1/PL4** exhibited poor performance overall. These findings underscore the importance of selecting ligands with the appropriate electronic and steric properties to optimise catalytic activity and product yield in Guerbet reactions. Moreover, the differences in carbon balances and missing carbon highlight the need for further optimisation of experimental conditions to reduce the formation of by-products and improve overall reaction efficiency.

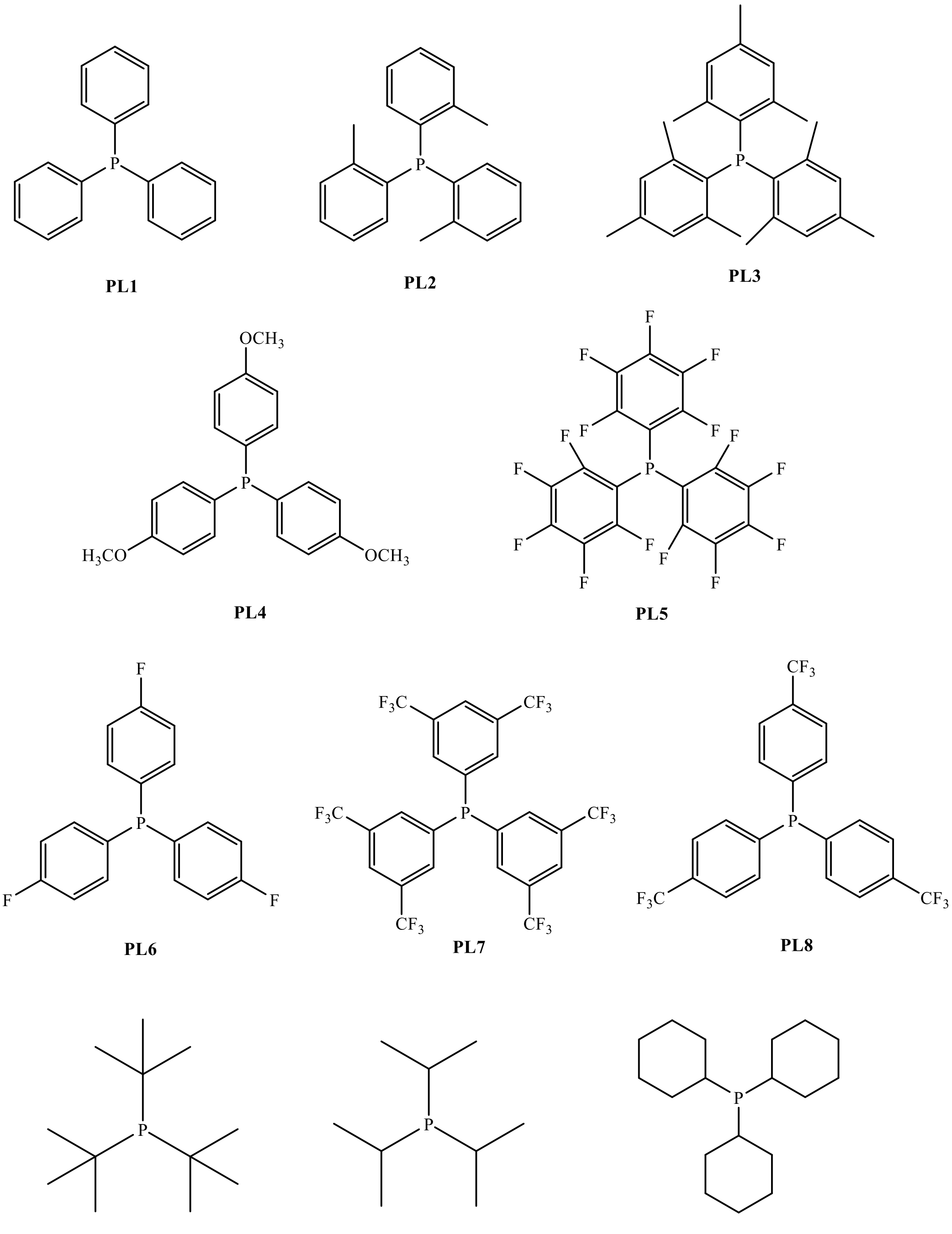

PL1 PL2 PL3

PL4 PL5

PL6 PL7 PL8

PL9 PL10 PL11

Figure 2-6: Monodentate phosphine ligands employed in combination with ruthenium catalysts.

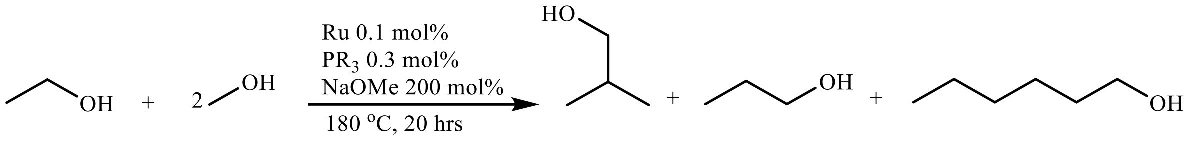

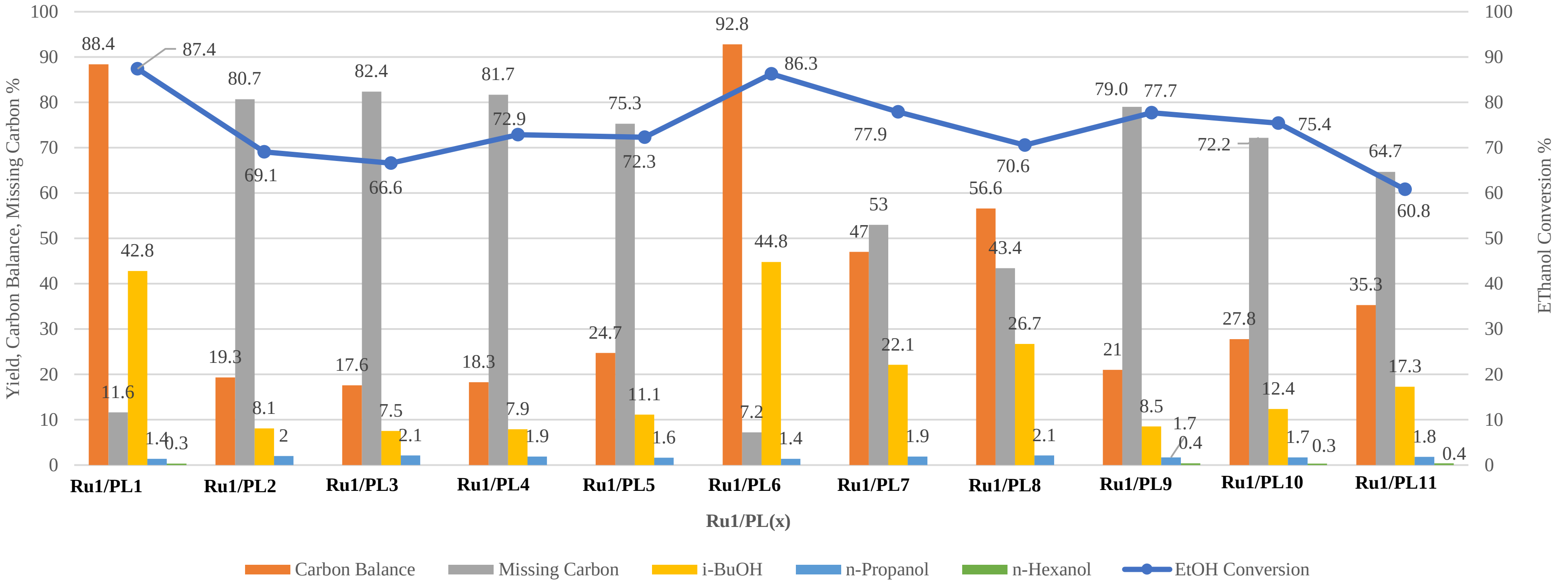

Figure 2-7: Yield of liquid products and ethanol conversion achieved with catalysts **Ru1**. in conjunction with various **PR₃**. Conditions: ethanol (0.75 mL, 12.8 mmol), methanol (7.5 mL, 185.15 mmol), **Ru1** (0.0128 mmol, 0.1 mol%), **PR₃** (0.0384 mmol, 0.3 mol%), NaOMe (34.26 mmol, 200 mol%), 20 hours, 180 °C, mol% relative to ethanol. **Carbon Balance (%)** represents the percentage of initial ethanol carbon detected in the products, ideally around 100% for complete accounting. **Missing Carbon (%)** indicates any unaccounted carbon potentially due to undetected side products, volatiles, or experimental loss. **EtOH Conversion %** (line) shows the percentage of ethanol converted to products. **Product Yields**: The bars represent the yields of individual products, including *i*-BuOH (isobutanol), *n*-propanol, and *n*-hexanol.

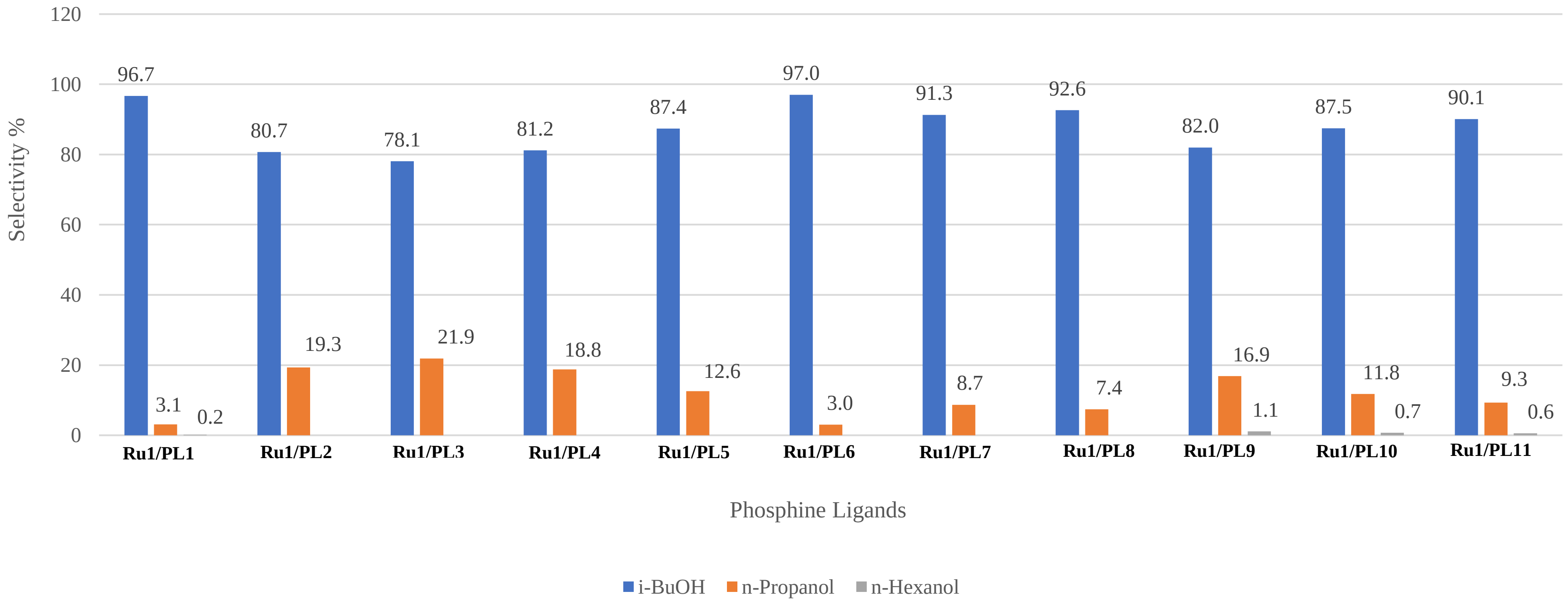

Figure 2-8: Selectivity of liquid products achieved with catalysts **Ru1** in conjunction with various **PR$_3$**. Conditions: ethanol (0.75 mL, 12.8 mmol), methanol (7.5 mL, 185.15 mmol), **Ru1** (0.0128 mmol, 0.1 mol%), **PR$_3$** (0.0384 mmol, 0.3 mol%) NaOMe (34.26 mmol, 200 mol%), 20 hours, 180 °C, mol% relative to ethanol. **Selectivity %**: Bars represent the selectivity percentages for each product—*i*-BuOH (isobutanol), *n*-Propanol, and *n*-Hexanol—with each PR$_3$ ligand. High selectivity towards *i*-BuOH is observed with several ligands, indicating a preference for isobutanol production across these catalyst-ligand combinations. Lower selectivity for *n*-propanol and *n*-hexanol suggests limited formation of these products under the specified conditions.

It is crucial to undertake a thorough analysis of the interaction between catalyst **Ru1** and ligands **PL1** and **PL6**, as these ligands have been found to produce the maximum amount of isobutanol. This experiment aims to determine the ideal response time that maximises isobutanol production. This chapter will undertake an extended exploration due to the abundant supply of ligand **PL1**. On the other hand, the investigation of ligand **PL6** will be restricted to time screening because of its limited availability. By employing this strategic approach, one can carefully analyse the temporal characteristics of the interaction between ligand **PL6** and catalyst **Ru1**. Valuable insights will be observed into the complex dynamics that affect the synthesis of isobutanol in this particular catalytic system.

2.5.4. Optimisation of Ru1 in the presence of PL1

The extended experimental run of 20 hours provided an understanding of the catalytic performance of ruthenium catalysts with monodentate phosphine ligands. However, conducting shorter experimental runs of 4 hours can save time while yielding valuable insights. These shorter experiments can effectively elucidate how variations in **PL1** concentration, temperature and base loading impact isobutanol production, allowing for more efficient optimisation of the catalytic process. Figures 2-9 and 2-10 display the results of testing catalyst **Ru1** with varying mol% of ligand **PL1** to determine the optimal concentration for maximising ethanol conversion and isobutanol production. Concentrations of **PL1** ranging from 0.1 mol% to 0.4 mol% were tested. The results show a clear trend: ethanol conversion increased from 54.3% at 0.1 mol% **PL1** to a peak of 77.0% at 0.4 mol% **PL1**. This data demonstrates a direct relationship between **PL1** concentration and ethanol conversion, indicating an enhanced interaction between the catalyst and the ligand, improving the conversion process's overall efficiency.

As the mol% of **PL1** increased, the yield and selectivity of isobutanol rose markedly up to a certain threshold. At 0.3 mol% **PL1**, the isobutanol yield reached 35.9%, with an impressive selectivity of 96.0%, and ethanol conversion stood at 74.8%. Interestingly, when the concentration of **PL1** was further increased to 0.4 mol%, the isobutanol yield remained nearly the same at 35.5%, with a consistent selectivity of 96.0%. Meanwhile, the ethanol conversion only increased slightly to 77.0%.

This suggests that increasing the concentration of **PL1** beyond 0.3 mol% does not significantly enhance isobutanol yield or selectivity. The levelling off in performance indicates that 0.3 mol% is the optimal concentration for this catalytic system.

It is also worth noting that while one PPh_3 molecule coordinates to the ruthenium centre in the $[RuCl_2(p\text{-cymene})(PPh_3)]$ expected complex, the additional equivalents of PPh_3 (beyond what directly binds) are not necessarily "wasted" in the system. These extra PPh_3 ligands may stabilise the catalytic environment by participating in equilibrium processes, influencing steric and electronic factors, or scavenging reactive by-products. Thus, the excess PPh_3 plays an indirect but crucial role in maintaining the overall efficiency of the catalyst.[17]

The near-identical yields and selectivity at 0.3 mol% and 0.4 mol% **PL1** suggest that 0.3 mol% represents the ideal balance where the catalyst and ligand fully interact, maximising efficiency without excess ligand. At the molecular level, this optimal ratio reflects the saturation point where all available active sites are effectively coordinated with **PL1**. Beyond this concentration, any additional ligand may not contribute to further improvements, as the active sites are already occupied, and the system has reached its maximum efficiency.

To summarise, Figures 2-9 and 2-10 illustrate that higher concentrations of **PL1** positively influence ethanol conversion and selectively enhance isobutanol production, but 0.3 mol% is the most effective concentration for optimising the performance of the **Ru1/PL1** system in isobutanol synthesis.

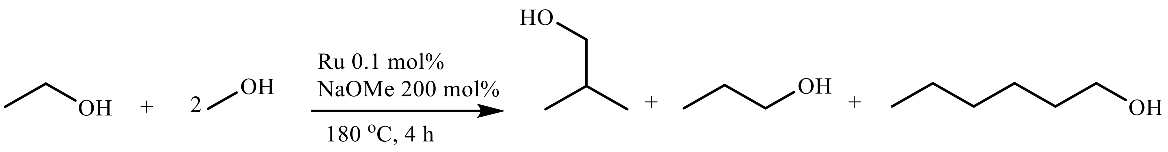

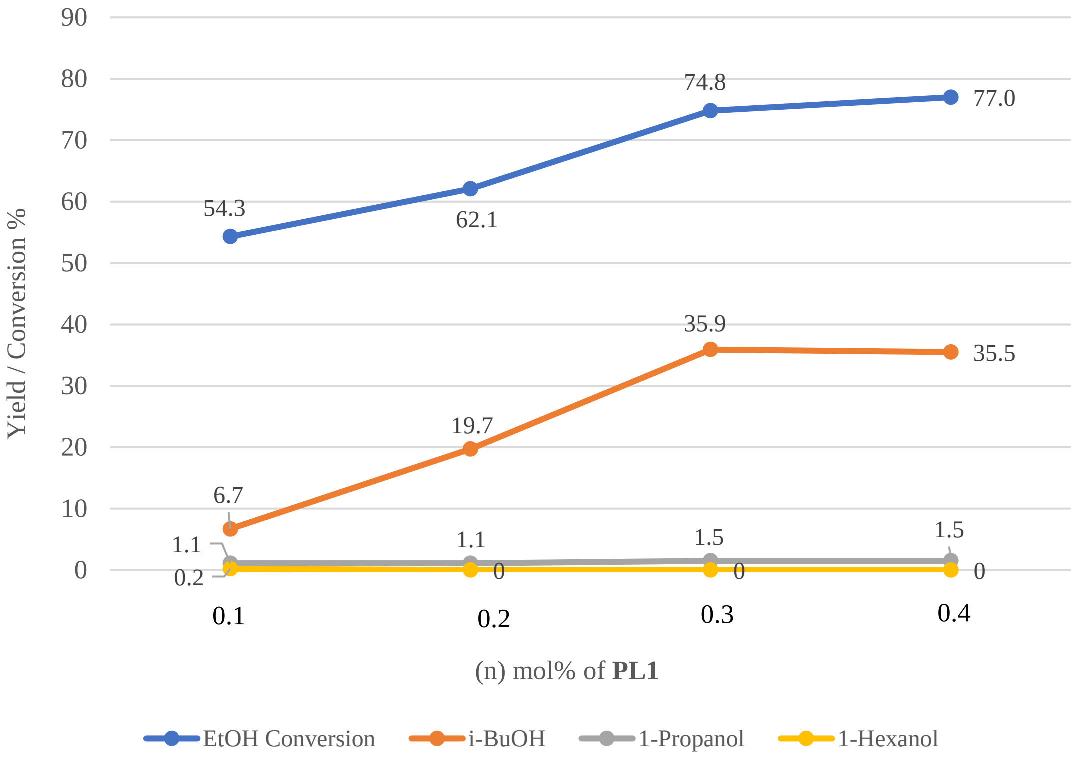

Figure 2-9: Yield of liquid products and ethanol conversion achieved with catalyst **Ru1** in the presence of different concentrations of **PL1**. Conditions: ethanol (0.75 mL, 12.8 mmol), methanol (7.5 mL, 185.15 mmol), Ru1 (0.0128 mmol, 0.1 mol%), NaOMe (34.26 mmol, 200 mol%), 4 hours, 180 °C, mol% relative to ethanol. **Ethanol Conversion %:** The line indicates the percentage of ethanol converted to products across different **PL1** concentrations. **Product Yields:** Lines for *i*-BuOH (isobutanol), *n*-propanol, and *n*-hexanol illustrate the yield percentages for each product. Higher **PL1** concentrations are associated with increased *i*-BuOH yields, indicating a strong influence of **PL1** concentration on isobutanol production.

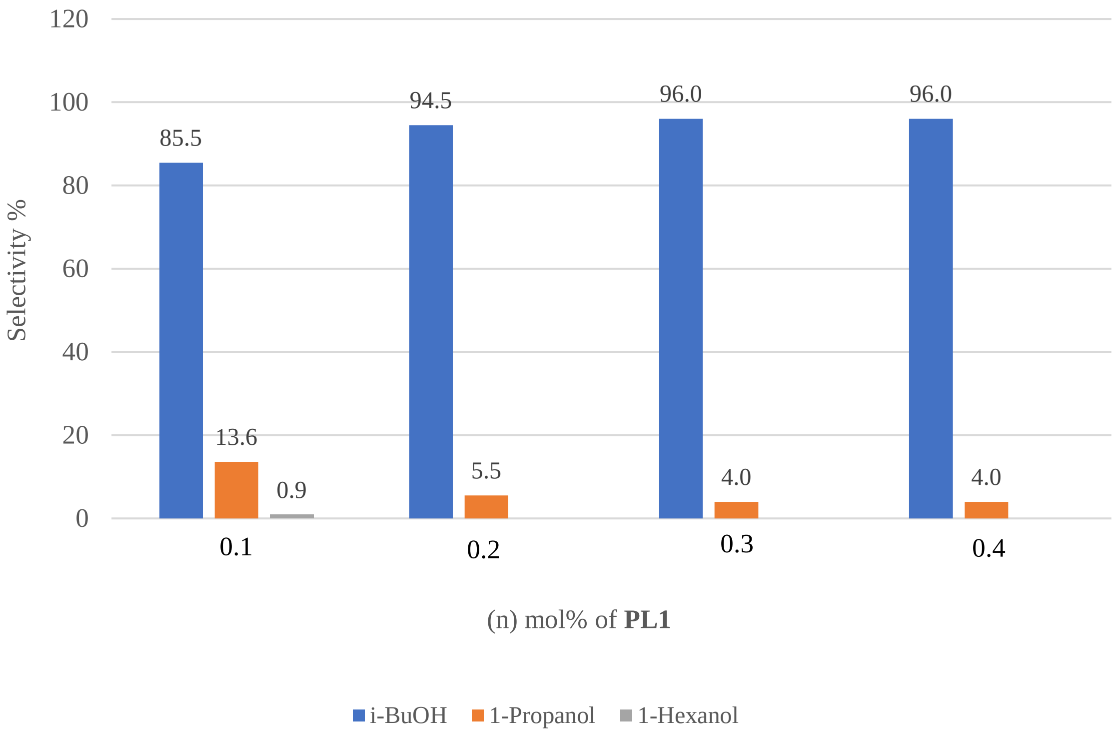

Figure 2-10: Selectivity of liquid products achieved with catalyst **Ru1** in the presence of different concentrations of **PL1**. Conditions: ethanol (0.75 mL, 12.8 mmol), methanol (7.5 mL, 185.15 mmol), **Ru1** (0.0128 mmol, 0.1 mol%), NaOMe (34.26 mmol, 200 mol%), 4 hours, 180 °C, mol% relative to ethanol. **Selectivity %**: Bars represent the selectivity of each product—*i*-BuOH (isobutanol), *n*-propanol, and *n*-hexanol—at different concentrations of **PL1**. High selectivity towards *i*-BuOH is maintained across all **PL1** concentrations, reaching up to 96%, indicating a strong preference for isobutanol production with this catalyst-ligand combination.

Figures 2-11 and 2-12 present the results of testing catalyst **Ru1** with 0.3 mol% of **PL1** at different temperatures to determine the most favourable conditions for maximising isobutanol production. Key metrics such as ethanol conversion, isobutanol yield and selectivity, *n*-propanol yield and selectivity, and the yield of other by-products are systematically recorded to illustrate the temperature dependence of the catalytic process.

The temperatures tested ranged from 120°C to 180°C, showing a significant increase in ethanol conversion, from 6.5% at 120°C to 74.8% at 180°C. This increase correlates with a rise in isobutanol yield, which reached a maximum of 35.9% at 180°C, with a selectivity of 96.0%. The yield and selectivity of *n*-propanol also increased slightly at 180°C. In comparison, the formation of other by-products was minimal but showed a slight rise at 150°C, indicating temperature plays a role in their formation.

To better understand these results, it is essential to consider the changing nature of the rate-determining step (RDS) as the temperature increases. At lower temperatures, the dehydrogenation (DH) step is likely the RDS, meaning the ethanol conversion is limited by the slow removal of hydrogen from the alcohol molecule. This explains the lower conversion and reduced yields of isobutanol at 120°C. However, As the temperature rises, the dehydrogenation step becomes more efficient, increasing ethanol conversion and isobutanol yield.

At higher temperatures, such as 180°C, the aldol condensation (AC) step becomes the new RDS. This step involves coupling intermediate products to form higher alcohols, such as isobutanol. The fact that isobutanol yields continue to rise with increasing temperature indicates that this step becomes increasingly efficient as the temperature increases. However, the selectivity of *n*-propanol and other by-products suggests that side reactions are also more likely at higher temperatures, which can lead to the formation of minor products.

In summary, Figures 2-11 and 2-12 demonstrate a strong relationship between temperature and the catalytic performance of **Ru1/PL1** in ethanol conversion and isobutanol production. The shift in the rate-determining step from dehydrogenation to aldol condensation as the temperature increases provides an understanding of optimising reaction conditions for maximum biofuel generation.

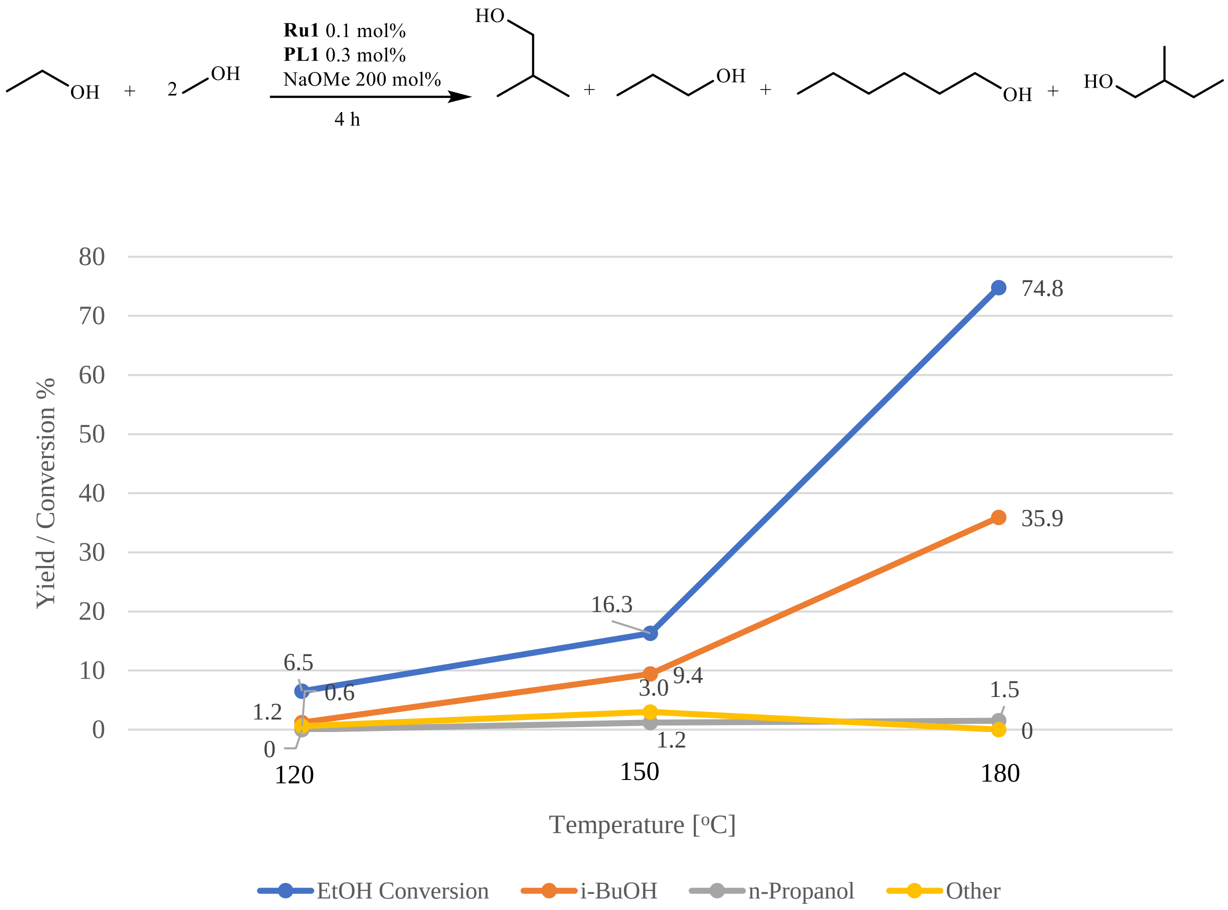

Figure 2-11: Yield of liquid products and ethanol conversion achieved with catalyst **Ru1** in the presence of **PL1** at different temperatures. Conditions: ethanol (0.75 mL, 12.8 mmol), methanol (7.5 mL, 185.15 mmol), **Ru1** (0.0128 mmol, 0.1 mol%), **PL1** (0.0384 mmol, 0.3 mol%) NaOMe (34.26 mmol, 200 mol%), 4 hours, mol% relative to ethanol. **EtOH Conversion %**: Line shows the percentage of ethanol converted to products as temperature increases, indicating enhanced conversion at higher temperatures. **Product Yields**: Lines represent the yields of *i*-BuOH (isobutanol) and *n*-propanol, as well as other by-products, which include a mixture of *n*-hexanol and 2-methylbutanol. Higher temperatures favour increased yields, especially for *i*-BuOH.

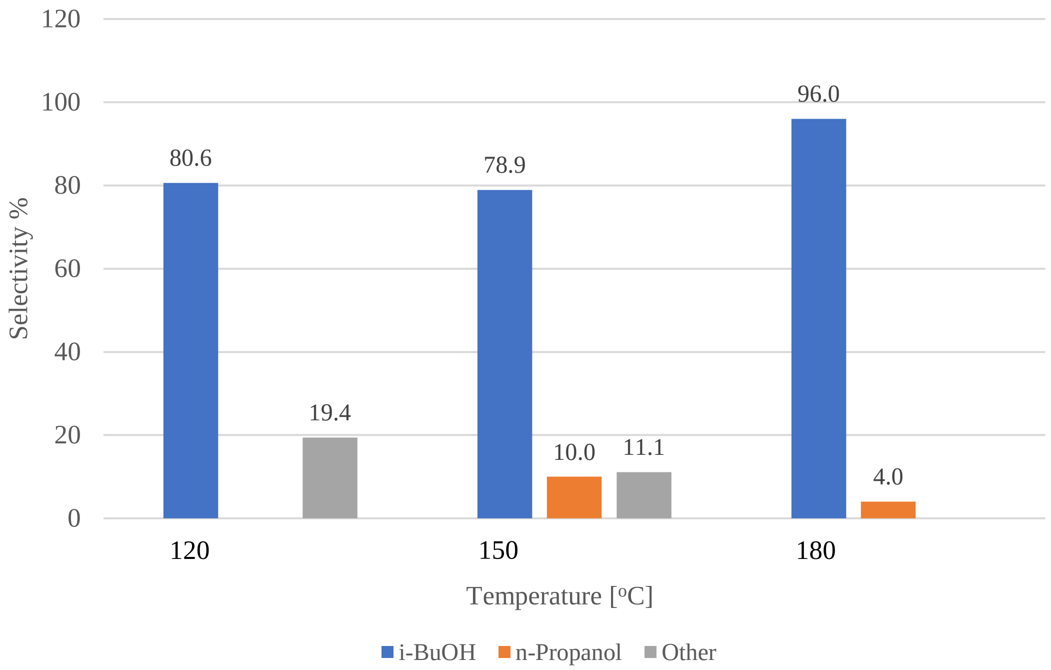

Figure 2-12: Selectivity of liquid products achieved with catalyst **Ru1** in the presence of **PL1** at different temperatures. Conditions: ethanol (0.75 mL, 12.8 mmol), methanol (7.5 mL, 185.15 mmol), **Ru1** (0.0128 mmol, 0.1 mol%), **PL1** (0.0384 mmol, 0.3 mol%), NaOMe (34.26 mmol, 200 mol%), 4 hours, mol% relative to ethanol. **Product Selectivity %**: Bars represent selectivity for *i*-BuOH (isobutanol), *n*-propanol, and other by-products, which include a mixture of *n*-hexanol and 2-methylbutanol. Increased temperatures lead to higher selectivity for *i*-BuOH, reaching up to 96% at 180 °C, while selectivity for *n*-propanol and other by-products decreases, highlighting the effect of temperature on product distribution.

Figures 2-13 and 2-14 present a detailed summary of the screening procedure for catalyst **Ru1** with a **PL1** concentration of 0.3 mol% at varying base concentrations (mol%) using sodium methoxide. This experiment aimed to identify the optimal base concentration for maximising ethanol conversion, isobutanol yield, and selectivity. Base concentrations ranging from 50 mol% to 200 mol% were tested, showing a consistent increase in ethanol conversion from 8.9% at 50 mol% to 74.8% at 200 mol% base concentration.

As the base concentration increased, the yield of isobutanol rose significantly, with the highest yield of 35.9% and selectivity of 96.0% observed at 200 mol% base concentration. The production of *n*-propanol and other by-products showed distinct patterns, with *n*-propanol peaking at 150 mol%, suggesting a relationship between base concentration and its formation.

It is important to note that sodium methoxide plays a direct and essential role in the reaction, particularly in the coupling process. Methanol, lacking an alpha hydrogen, does not undergo dehydrogenation like ethanol or other alcohols. Instead, the sodium methoxide added in large quantities is the active species facilitating key steps such as aldol condensation and C-C bond formation during the Guerbet reaction. The methoxide ion, formed from methanol, may still participate in the reaction. However, the added sodium methoxide acts as the primary base, driving the reaction forward by promoting the coupling steps and ensuring efficient ethanol conversion. This explains the consistent rise in ethanol conversion and isobutanol production with increasing sodium methoxide concentrations, as it ensures sufficient base is available to maintain the reaction's progress.

In conclusion, Figures 2-13 and 2-14 demonstrate that increasing the concentration of sodium methoxide enhances ethanol conversion and isobutanol production. Sodium methoxide plays a critical role in facilitating the coupling reactions rather than methanol itself. This insight helps to fine-tune the base concentration to maximise biofuel production in this catalytic system.

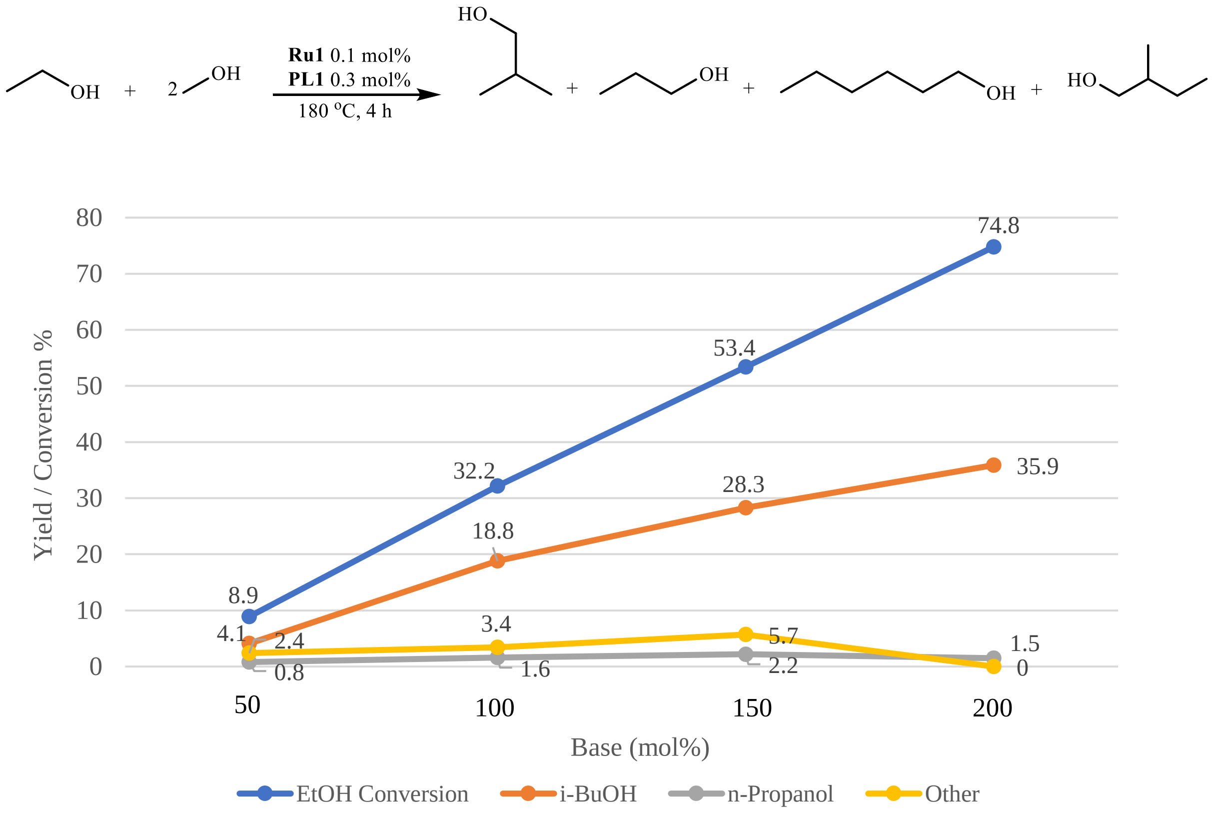

Figure 2-13: Yield of liquid products and ethanol conversion achieved with catalyst **Ru1** in the presence of **PL1** at different base concentrations. Conditions: ethanol (0.75 mL, 12.8 mmol), methanol (7.5 mL, 185.15 mmol), **Ru1** (0.0128 mmol, 0.1 mol%), **PL1** (0.0384 mmol, 0.3 mol%), 4 hours, 180 ºC mol% relative to ethanol. **EtOH Conversion %**: Line shows the ethanol conversions as base concentration increases, indicating a positive correlation with conversion efficiency. **Product Yields**: Lines represent yields of *i*-BuOH (isobutanol), *n*-propanol, and other by-products, which include a mixture of *n*-hexanol and 2-methylbutanol. Higher base concentrations favour increased yields of *i*-BuOH and improved ethanol conversion.

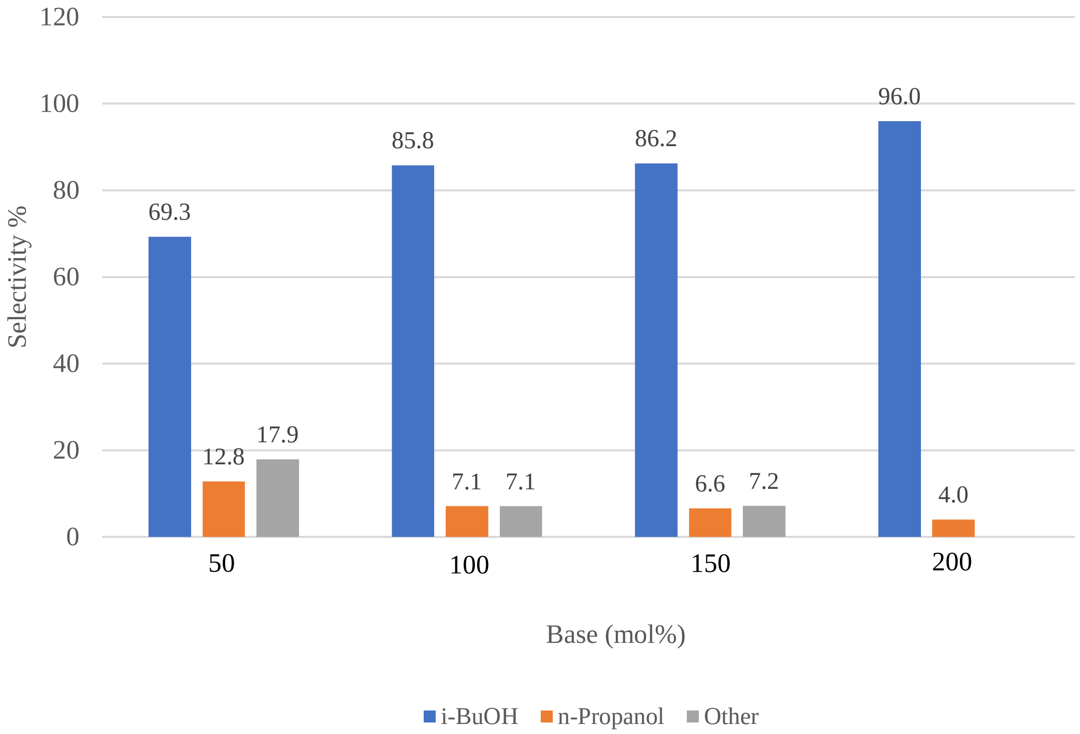

Figure 2-14: Selectivity of liquid products achieved with catalyst **Ru1** in the presence of **PL1** at different base concentrations. Conditions: ethanol (0.75 mL, 12.8 mmol), methanol (7.5 mL, 185.15 mmol), **Ru1** (0.1 mol%), **PL1** (0.3 mol%), 4 hours, mol% relative to ethanol. **Product Selectivity %**: Bars represent selectivity for *i*-BuOH (isobutanol), *n*-propanol, and other by-products, which consist of a mixture of *n*-hexanol and 2-methylbutanol. Increasing base concentration enhances the selectivity for *i*-BuOH, reaching up to 96% at 200 mol%, indicating a strong preference for isobutanol formation under higher base conditions, while selectivity for other products decreases.

2.5.5. Screening Ru1 with PL1 on isobutanol Guerbet reactions at different times

Figures 2-15 and 2-16 present the results of screening catalyst **Ru1** with ligand **PL1** over different reaction times, ranging from 2 to 20 hours, to identify the optimal time for maximum isobutanol production while considering other reaction parameters. Ethanol conversion and isobutanol yield were monitored alongside the formation of minor by-products, including *n*-propanol, *n*-hexanol, and 2-methyl-1-butanol.

The ethanol conversion increased from 24.8% after 2 hours to 77.0% after 4 hours, remaining steady between 8 and 16 hours and rising to 87.4% after 20 hours. This plateau between 4 and 16 hours may suggest that the reaction reached equilibrium, where the forward and reverse reaction rates were balanced. The increase in conversion after 16 hours likely indicates a shift in equilibrium, potentially due to slow catalyst activation or the depletion of intermediates, allowing further ethanol conversion.

Regarding the isobutanol yield, the data show a peak yield of 57.3% at 16 hours, which dropped to 42.8% at 20 hours. This reduction in isobutanol yield could be attributed to the onset of secondary reactions or the formation of by-products such as *n*-hexanol and 2-methyl-1-butanol after the 16-hour mark. These by-products could form through condensation reactions involving higher alcohols as intermediates in the Guerbet process. As the reaction time increases, these by-products can consume the intermediates or isobutanol, reducing its yield. Another explanation might be reversible reactions involving isobutanol or the formation of trace amounts of unidentified by-products. Given that the autoclave was cooled in ice, it is unlikely that product evaporation caused this decline in yield.

Despite this reduction, isobutanol selectivity remained high throughout the experiment, peaking at 96.7% at 20 hours. This indicates that the catalytic system consistently favoured isobutanol formation even as yield fluctuated.

The production of *n*-propanol remained minimal across all time intervals, with the highest yield of 2.4% observed at 16 hours, while selectivity varied between 3.1% and 7.3% over time. This variation in selectivity, despite relatively constant yields, suggests that as the reaction progresses, the overall conversion of ethanol increases, leading to higher amounts of isobutanol and other products. As a result, *n*-propanol remains a small but steady by-product, and its selectivity decreases as more ethanol is converted into the desired products. This explains why the yield of *n*-propanol appears constant while its selectivity fluctuates, reflecting its reduced significance as the reaction shifts towards the formation of isobutanol and other compounds.

However, an increase in *n*-hexanol and 2-methyl-1-butanol was observed at 16 hours, alongside an overall by-product yield of 8.1%. *n*-Hexanol likely forms through higher chain condensation reactions, whereas 2-methyl-1-butanol is a product of self-condensation of ethanol or mixed condensation involving ethanol and other intermediates. These by-products result from longer reaction times, which encourage side reactions that divert intermediates from forming isobutanol. This explains the decrease in isobutanol yield after 16 hours, as these by-products consume key intermediates.

The data indicate that 16 hours is the optimal reaction time for achieving the highest isobutanol yield. Beyond this point, secondary reactions lead to a decline in isobutanol production. Ethanol conversion increases steadily, with a plateau suggesting equilibrium, which shifts after 16 hours. While *n*-propanol production remains insignificant, the formation of other by-products underscores the need to minimise side reactions to maximise isobutanol production.

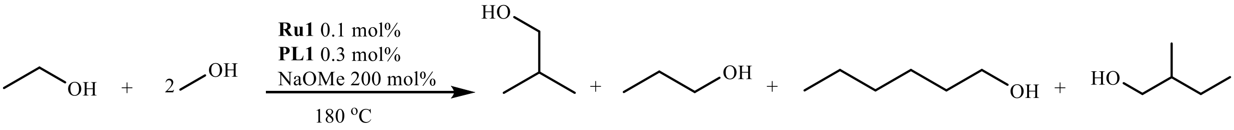

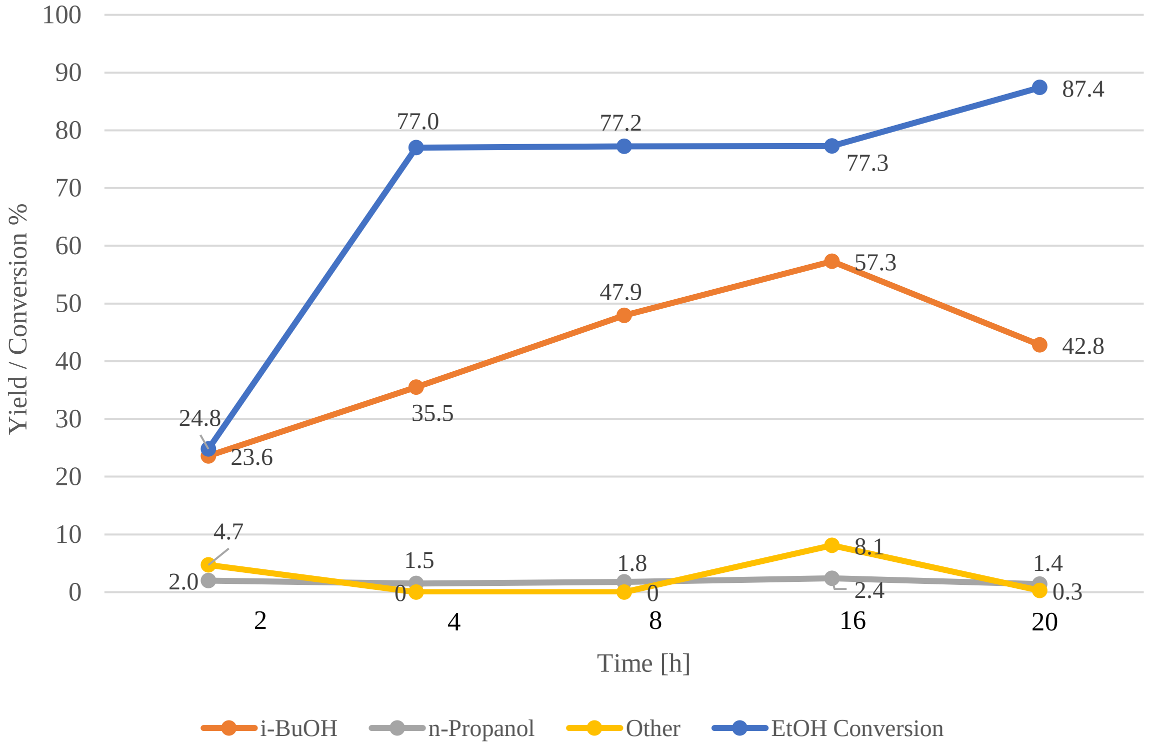

Figure 2-15: Yield of liquid products and ethanol conversion achieved with catalyst **Ru1** in the presence of **PL1** at different times. Conditions: ethanol (0.75 mL, 12.8 mmol), methanol (7.5 mL, 185.15 mmol), **Ru1** (0.0128 mmol, 0.1 mol%), **PL1** (0.0384 mmol, 0.3 mol%), NaOMe (34.26 mmol, 200 mol%), 180 °C, mol% relative to ethanol. **EtOH Conversion %**: The line indicates ethanol conversion over time, showing a significant increase within the first few hours, reaching 87.4% at 20 hours. **Product Yields**: Lines represent the yields of *i*-BuOH (isobutanol), *n*-propanol, and other by-products, which include a mixture of *n*-hexanol and 2-methylbutanol. *i*-BuOH yield rises initially, peaking at 16 hours before slightly declining, while other products remain at lower levels.

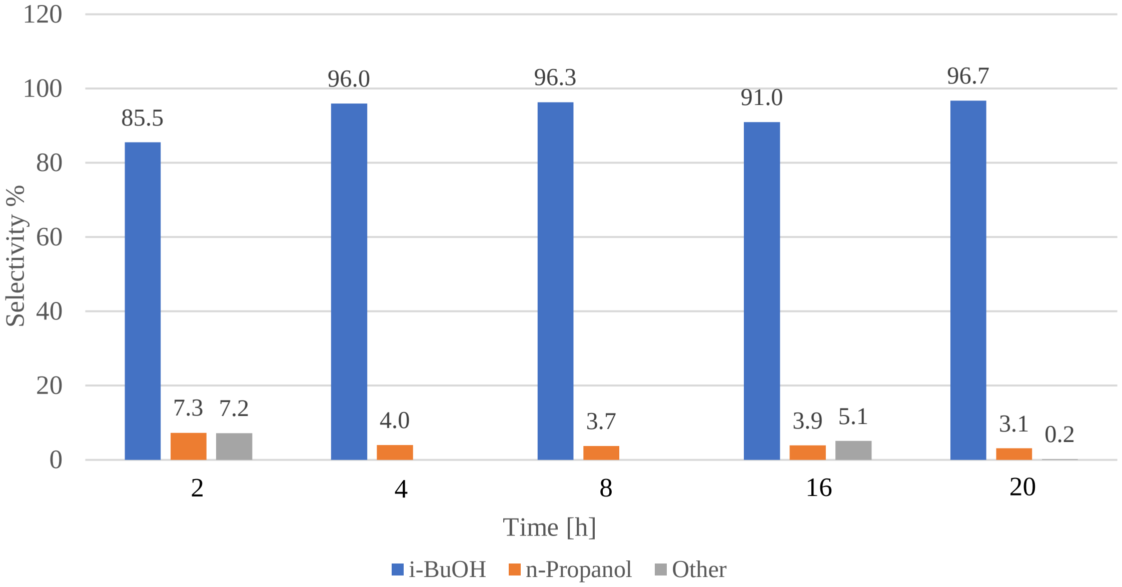

Figure 2-16: Selectivity of liquid products and ethanol conversion achieved with catalyst **Ru1** in the presence of **PL1** at different times. Conditions: ethanol (0.75 mL, 12.8 mmol), methanol (7.5 mL, 185.15 mmol), **Ru1** (0.0128 mmol, 0.1 mol%), **PL1** (0.0384 mmol, 0.3 mol%), NaOMe (34.26 mmol, 200 mol%), 180 °C, mol% relative to ethanol. **Product Selectivity %**: Bars indicate selectivity for *i*-BuOH (isobutanol), *n*-propanol, and other by-products, which include a mixture of *n*-hexanol and 2-methylbutanol. Selectivity for *i*-BuOH remains consistently high, reaching up to 96.7% at 20 hours, while selectivity for *n*-propanol and other by-products remains comparatively low, demonstrating a strong preference for isobutanol formation over time.

2.5.6. Screening Ru1 with PL6 on isobutanol Guerbet reactions at different times

Figures 2-17 and 2-18 present the results of testing catalyst **Ru1** with ligand **PL6** at various reaction times, ranging from 2 to 20 hours, to determine the optimal duration for maximising isobutanol production while considering ethanol conversion and by-product formation. Over time, ethanol conversion increased steadily from 23.3% at 2 hours to a maximum of 86.3% at 20 hours.

A plateau in ethanol conversion was observed at 8 hours (73.2%) and 16 hours (73.5%), suggesting the reaction reached equilibrium during these intervals. At equilibrium, the forward and reverse reactions proceed at equal rates, limiting further ethanol conversion until reaction conditions shift. The eventual increase in conversion to 86.3% at 20 hours indicates a shift in equilibrium, possibly due to changes in reaction dynamics or the depletion of intermediates, which allowed additional ethanol to convert.

The isobutanol yield followed a similar pattern. It increased from 15.2% at 2 hours to 39.6% at 8 hours before reaching a peak of 44.8% at 20 hours. This suggests that, despite the equilibrium state, isobutanol formation continued as more ethanol converted after the equilibrium shift. Notably, isobutanol selectivity remained high throughout, peaking at 95.6% at 8 hours and rising to 97.0% at 20 hours. This indicates that the catalytic system consistently favoured isobutanol production over by-products, even as the reaction approached equilibrium.

In contrast, *n*-propanol production remained minimal across all time points, with the highest yield of 2.2% at 4 hours and selectivity ranging from 3.0% to 6.6%. These low yields confirm *n*-propanol's insignificant role in the overall catalytic process. The formation of *n*-hexanol and 2-methyl-1-butanol fluctuated, with the highest yield of 5.4% observed at 16 hours. However, by 20 hours, no significant amounts of these by-products were detected, suggesting that the shift likely influenced their formation in equilibrium.

To conclude, the data from this study demonstrate that 20 hours is the most effective reaction time for maximising isobutanol yield while maintaining high selectivity. The catalytic system showed strong selectivity towards isobutanol, even as it approached equilibrium, with minimal formation of by-products such as *n*-hexanol and 2-methyl-1-butanol. The observed equilibrium behaviour played a role in determining the final ethanol conversion and product distribution, highlighting the importance of optimising reaction conditions to shift equilibrium in favour of isobutanol production.

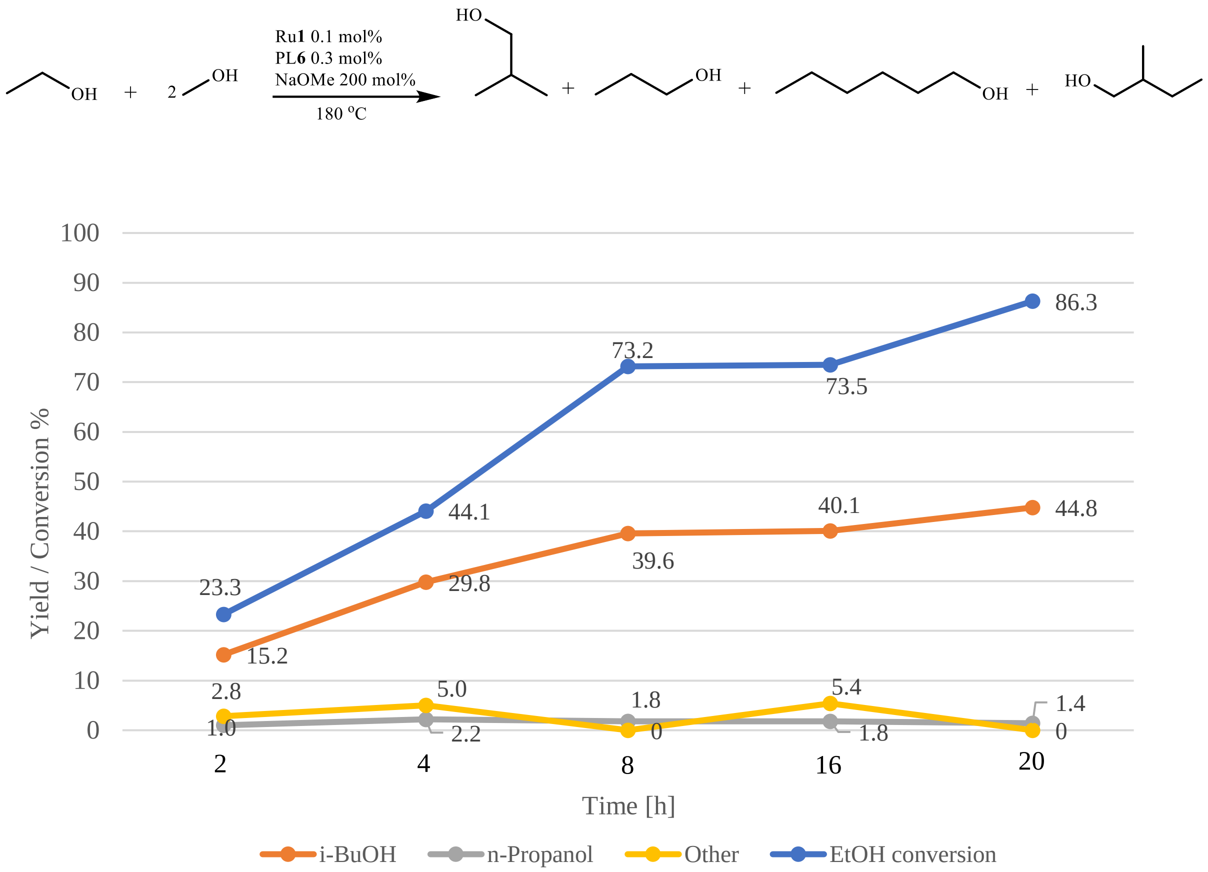

Figure 2-17: Yield of liquid products and ethanol conversion achieved at different times. Conditions: ethanol (0.75 mL, 12.8 mmol), methanol (7.5 mL, 185.15 mmol), **Ru1** (0.0128 mmol, 0.1 mol%), **PL6** (0.0384 mmol, 0.3 mol%), NaOMe (34.26 mmol, 200 mol%), 180 °C, mol% relative to ethanol. **EtOH Conversion %**: The line represents the ethanol conversion rate, showing a steady increase over time, reaching 86.3% at 20 hours. **Product Yields**: Lines indicate yields of *i*-BuOH (isobutanol), *n*-propanol, and other by-products, which consist of a mixture of *n*-hexanol and 2-methylbutanol. The yield of *i*-BuOH steadily increases with time, highlighting its dominance among the products, while *n*-propanol and other by-products remain at lower levels.

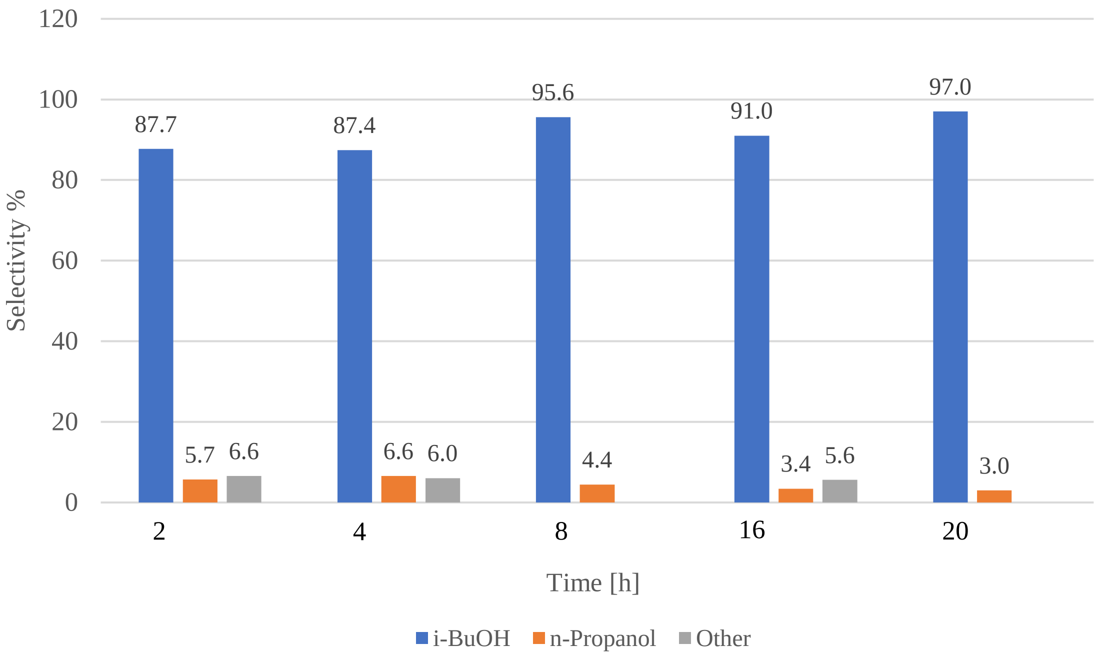

Figure 2-18: Selectivity of liquid products and ethanol conversion achieved at different times. Conditions: ethanol (0.75 mL, 12.8 mmol), methanol (7.5 mL, 185.15 mmol), **Ru1** (0.0128 mmol, 0.1 mol%), **PL6** (0.0384 mmol, 0.3 mol%), NaOMe (34.26 mmol, 200 mol%), 180 °C, mol% relative to ethanol. **Product Selectivity %**: Bars represent selectivity for *i*-BuOH (isobutanol), *n*-propanol, and other by-products (a mixture of *n*-hexanol and 2-methylbutanol) at different reaction times. High selectivity for *i*-BuOH is observed throughout, reaching 97.0% at 20 hours, indicating a strong preference for isobutanol formation, while *n*-propanol and other by-products maintain lower selectivity levels.

2.5.7. Screening Ru2 on isobutanol Guerbet reactions

2.5.7.1. The effect of electron withdrawing monodentate ligands

The limited availability of catalyst **Ru2** posed a challenge in thoroughly investigating isobutanol synthesis using this pre-catalyst. However, based on the findings in Section 2.4.2, ligands such as **PL1** and those containing electron-withdrawing functional groups (**PL6**, **PL7**, and **PL8**) demonstrated superior performance when paired with Ru1. Therefore, further exploration of these ligands' interactions with **Ru2** was essential to understand their impact on isobutanol production.

Given that **Ru2** contains three ruthenium centres compared to the binuclear structure of **Ru1**, the concentration of ligands had to be adjusted accordingly. The higher nuclearity of **Ru2** allows for greater interaction with ligand molecules, potentially increasing the number of active sites available for catalysis.

Table 2-6 illustrates that multiple experiments were conducted to test a range of **PL1** concentrations from 0.3 to 1.2 mol% with **Ru2** to identify the optimal ligand-to-metal ratio for maximising ethanol conversion and isobutanol yield. The results showed a strong correlation between ligand concentration and catalytic performance regarding ethanol conversion, yield, and carbon balance.

At 0.0384 mmol (0.3 mol%) of **PL1**, the ethanol conversion was 77.5%, producing an isobutanol yield of 49.7%. The calculated TON for isobutanol was 382, and the *n*-propanol and *n*-hexanol TONs were 19 and 14, respectively. Despite the relatively high yield, the carbon balance was 112.6%, with an error of 29.2%, suggesting an overestimation of liquid products in the analysis. This may be due to discrepancies in the quantification of gas-phase products, leading to an inflated carbon balance (Table 2-6, entry 1).

As the **PL1** concentration increased to 0.768 mmol (0.6 mol%), ethanol conversion improved significantly to 90.0%, with an isobutanol yield of 50.2%. The corresponding TON values were 451 for isobutanol, 16 for *n*-propanol, and 3 for *n*-hexanol. The carbon balance in this experiment was more reliable at 103.5%, with a reduced error of 11.3%, indicating more consistent measurements and reduced overestimation. Given the high ethanol conversion and improved measurement accuracy, this concentration emerged as the most effective for further testing with other ligands (Table 2-6, entry 2).

At 0.1152 mmol (0.9 mol%) of **PL1**, ethanol conversion decreased slightly to 88.1%, while the isobutanol yield increased to 52.3%, with TONs of 461 for isobutanol, 21 for *n*-propanol, and 3 for *n*-hexanol. However, the carbon balance rose to 108.4%, with a higher error of 23.0%, suggesting some inconsistency in the analysis. This could be attributed to side reactions or unquantified gas-phase by-products that affected the overall carbon accounting (Table 2-6, entry 3).

Further increasing the **PL1** concentration to 0.1536 mmol (1.2 mol%) resulted in an ethanol conversion of 86.0% and an isobutanol yield of 51.4%, with TON values of 442, 21, and 3 for isobutanol, *n*-propanol, and *n*-hexanol, respectively. The carbon balance in this experiment was 104.9%, with an error of 13.5%, indicating minor overestimation but generally accurate measurements. While higher concentrations of **PL1** provided slightly better yields, the ethanol conversion decreased, suggesting that increasing ligand concentration beyond a certain threshold may reduce catalytic efficiency (Table 2-6, entry 4).

Evaluating other ligands, 0.0768 mmol (0.6 mol%) of **PL6** demonstrated superior performance, with the highest ethanol conversion of 91.2% and an isobutanol yield of 54.1%. The TON for isobutanol was 495, and *n*-propanol TON was 11. The carbon balance was 109.0%, with a low error of 9.4%, making **PL6** the most efficient ligand tested in terms of ethanol conversion, yield, and analysis accuracy. This ligand's ability to enhance catalytic efficiency while maintaining a low error rate underscores its potential for maximising ethanol conversion and product selectivity (Table 2-6, entry 5).

In contrast, **PL7** exhibited a lower ethanol conversion of 82.0%, with an isobutanol yield of 30.6% and TON values of 251 for isobutanol, 18 for n-propanol, and 2 for n-hexanol. The carbon balance was 63.8%, with a significant 36.2% missing carbon, likely due to the formation of gas-phase by-products or incomplete ethanol conversion. The substantial carbon loss highlights the inefficiency of this system compared to **PL6** (Table 2-6, entry 6).

Similarly, **PL8** showed an ethanol conversion of 82.5%, with an isobutanol yield of 35.8% and TON values of 296 for isobutanol, 17 for n-propanol, and 2 for n-hexanol. The carbon balance of 74.5% and 25.5% missing carbon indicates that while this ligand performed slightly better than **Ru2/PL7**, significant carbon loss still occurred, reducing its overall efficiency (Table 2-6, entry 7).

The trend across these ligands highlights the influence of their electronic and steric properties on catalytic performance. **PL6**, with its electron-withdrawing fluorophenyl groups, stabilises intermediates during the reaction, leading to higher ethanol conversion and isobutanol selectivity while showing an overestimated carbon balance. On the other hand, **PL7** and **PL8**, though possessing electron-withdrawing characteristics, likely introduce significant steric hindrance, limiting their ability to facilitate the catalytic steps efficiently, resulting in lower yields and greater carbon loss.

It is also important to consider the role of equilibrium in these reactions. Given the higher nuclearity of **Ru2**, the reaction equilibrium may be reached at different stages compared to **Ru1**, complicating direct comparisons of their catalytic performance. For example, the lower yields observed with **Ru2/PL7** and **Ru2/PL8** may be due to equilibrium limitations rather than the intrinsic inefficiency of the catalysts. Therefore, reactions that exhibit high ethanol conversion and similar selectivity may obscure the actual differences in catalytic potential due to equilibrium dynamics.

Lastly, carbonyl ligands in **Ru2** introduce the potential for CO formation. Although CO was not directly detected in this study, its formation is likely due to the decomposition of these carbonyl ligands under reaction conditions. The release of CO could explain some of the missing carbon, as it may have escaped into the gas phase. Future studies should incorporate gas-phase analysis to accurately quantify CO and its contribution to the overall carbon balance.

In conclusion, the detailed evaluation of **PL1** at 0.0768 mmol (0.6 mol%) and its comparison with other ligands (**PL6**, **PL7**, and **PL8**) highlight the significant impact of ligand structure on catalytic efficiency. **PL6** showed the highest ethanol conversion and isobutanol yield, though equilibrium effects and the formation of CO and other by-products complicate the overall assessment. Comprehensive gas-phase analysis and further optimisation of the ligand-to-metal ratio could enhance the accuracy of these measurements and provide a more complete understanding of the catalytic dynamics involved.

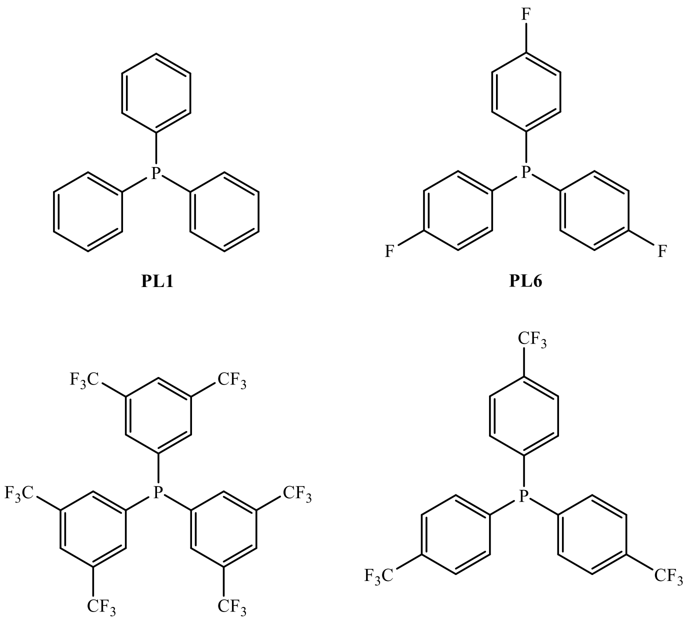

Figure 2-19: Monodentate phosphine ligands utilised with **Ru2**.

Table 2-4: Yield and selectivity of liquid products and ethanol conversion achieved with catalysts **Ru2** in presence of different concentrations of PR_3.

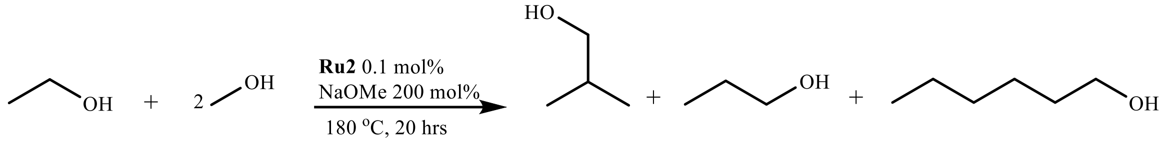

Entry [a]	PR_3	PR_3 mol%	Ethanol Conversion (%) [b]	Yield[c] (TON)[d] [Selectivity] (%)			Carbon Balance (%) [e]	Missing Carbon (%) [f]	Analysis Error (%) [g]
				Isobutanol	*n*-Propanol	*n*-Hexanol			
1	**PL1**	0.3	77.5	49.7 (382) [92.7]	2.5 (19) [4.6]	2.9 (14) [2.7]	112.6	-	29.2
2	**PL1**	0.6	90.0	50.2 (451) [96.4]	1.8 (16) [3.4]	0.3 (3) [0.2]	103.5	-	11.3
3	**PL1**	0.9	88.1	52.3 (461) [95.5]	2.4 (21) [4.3]	0.4 (3) [0.2]	108.4	-	23.0
4	**PL1**	1.2	86.0	51.4 (442) [95.4]	2.4 (21) [4.4]	0.4 (3) [0.2]	104.9	-	13.5
5	**PL6**	0.6	91.2	54.1 (495) [96.5]	1.2 (11) [3.5]	0 (0) [0]	109.0	-	9.4
6	**PL7**	0.6	82.0	30.6 (251) [92.9]	2.2 (18) [6.7]	0.3 (2) [0.4]	63.8	36.2	-
7	**PL8**	0.6	82.5	35.8 (296) [94.4]	2.0 (17) [5.4]	0.3 (2) [0.2]	74.5	25.5	-

[a] Conditions: ethanol (0.75 mL, 12.8 mmol), methanol (7.5 mL, 185.15 mmol), **Ru2** (0.0128 mmol, 0.1 mol%), NaOMe (34.26 mmol, 200 mol%), 20 hours, 180 °C, PR_3, mol% specified in the table. [b] Total ethanol conversion as determined by GC liquid phase analysis. [c] Total yield and selectivity of alcohol products in the liquid phase, as determined by GC. [d] TON calculated based on mmol of ethanol converted to products per mmol of Ru. [e] **Carbon Balance %:** the percentage of initial carbon in ethanol detected in the products. Ideally close to 100%, indicating accurate accounting of all ethanol-derived carbon atoms. [f] **Missing Carbon:** any carbon discrepancy, indicating undetected carbon potentially due to side products, volatiles, or experimental losses. [g] **Analysis Error %:** an estimated measure of uncertainty in the analytical method, reflecting potential deviations from ideal values due to instrument limitations or procedural inaccuracies.

2.5.8. Formation of Gas and Solid By-products in the Guerbet Reaction

A solid by-product was observed throughout all reaction runs, which was confirmed to be a mixture of sodium formate, sodium carbonate, and sodium acetate, as documented in our group's earlier work.[2] These solid by-products form through various side reactions involving methanol and ethanol during the Guerbet process, driven by the dehydrogenation of alcohols under basic conditions provided by sodium methoxide ($NaOCH_3$). Additionally, hydrogen gas (H_2) was produced, and its formation increased proportionally with the concentration of the phosphine ligand, the reaction temperature, and the base loading.

2.5.8.1. Formation of Hydrogen Gas (H_2)

Hydrogen gas is primarily formed during dehydrogenating alcohols (ethanol and methanol) in the Guerbet reaction. Dehydrogenation produces acetaldehyde in ethanol and formaldehyde in methanol. Both reactions release hydrogen gas (H_2) as a by-product.

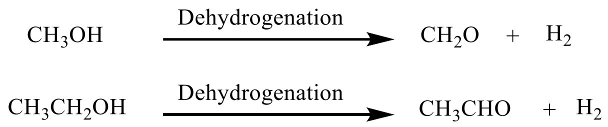

$$CH_3OH \xrightarrow{\text{Dehydrogenation}} CH_2O + H_2$$

$$CH_3CH_2OH \xrightarrow{\text{Dehydrogenation}} CH_3CHO + H_2$$

Scheme 2-5: The formation of H_2 gas by dehydrogenating methanol and ethanol.

As the reaction temperature, base concentration, and phosphine ligand concentration increase, the dehydrogenation steps become more efficient, producing greater amounts of hydrogen gas.

2.5.8.2. Formation of Sodium Formate (HCOONa)

The dehydrogenation of methanol (CH_3OH) forms formaldehyde (CH_2O). This formaldehyde can react with methoxide ions (OCH_3^-) from sodium methoxide to form sodium formate (HCOONa). The reaction steps are as follows:

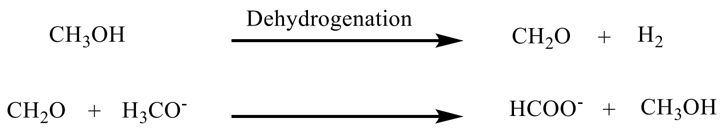

$$CH_3OH \xrightarrow{\text{Dehydrogenation}} CH_2O + H_2$$

$$CH_2O + H_3CO^- \longrightarrow HCOO^- + CH_3OH$$

Scheme 2-6: Formation of sodium formate.

Sodium formate forms from methanol via dehydrogenation and subsequent reaction with methoxide, a strong base provided by sodium methoxide.

2.5.8.3. Formation of Sodium Acetate (CH_3COONa)

Sodium acetate is formed through the dehydrogenation of ethanol (CH_3CH_2OH), producing acetaldehyde (CH_3CHO). The acetaldehyde can then be oxidised in the basic environment provided by sodium methoxide, forming acetic acid (CH_3COOH). This acetic acid reacts with sodium methoxide to produce sodium acetate.

$$CH_3CH_2OH \xrightarrow{\text{Dehydrogenation}} CH_3CHO + H_2$$

$$CH_3CHO + H_3CO^- \longrightarrow CH_3COO^- + CH_3OH$$

Scheme 2-7: Formation of sodium acetate.

Sodium acetate forms when acetaldehyde is oxidised in the presence of sodium methoxide, which acts as a strong base, supporting the reaction and producing acetate.

2.5.8.4. Formation of Sodium Carbonate (Na_2CO_3)

Sodium carbonate can form in two main ways:

- **Decomposition of Sodium Formate:** Under elevated temperatures, sodium formate can decompose into sodium carbonate (Na_2CO_3), releasing hydrogen gas (H_2) and carbon dioxide (CO_2).
- **The reaction of CO_2 with Sodium Methoxide:** The CO_2 produced during the reaction can react with sodium methoxide ($NaOCH_3$) to form sodium carbonate.

$$2HCOONa \xrightarrow{\text{Heat}} Na_2CO_3 + H_2 + CO_2$$

$$CO_2 + 2NaOCH_3 \longrightarrow Na_2CO_3 + 2CH_3OH$$

Scheme 2-8: Two ways for the formation of sodium carbonate.

Thus, sodium carbonate forms either through the thermal decomposition of sodium formate or by the reaction of CO_2 (generated in the reaction) with sodium methoxide.

Finally, these side reactions, resulting in the formation of sodium formate, sodium acetate, sodium carbonate, and hydrogen gas, are characteristic of the reaction conditions in the Guerbet process. While this study primarily focused on the liquid-phase products, the presence of these by-products has been confirmed in previous analyses conducted by our research group.[2] These findings provide valuable insights into the nature of the side reactions occurring under the catalytic conditions used.

2.6. Conclusion:

Chapter 2 evaluated the catalytic activity of widely used ruthenium pre-catalysts (**Ru1-Ru6**) in combination with various monodentate phosphine ligands for the conversion of ethanol and methanol to isobutanol. The primary aim of this work was to understand how these catalysts influence isobutanol production and to explore the effects of different ligands on catalyst efficiency, product yield, and selectivity.

The evaluation of catalysts **Ru4**, **Ru5**, and **Ru6** revealed significant catalytic performance. The triphenylphosphine ligand **PL1** is pivotal in stabilising the ruthenium centre, increasing electron density, and improving catalytic efficiency.

Conversely, pre-catalysts **Ru1-Ru3**, when used without phosphine ligands, showed poor conversion of ethanol and methanol into isobutanol. However, the introduction of **PL1** significantly increased isobutanol yield and selectivity. For instance, **Ru1** alone gave 5.4% isobutanol with 87.2% selectivity; however, it increased to 42.8% yield and 96.7% selectivity when combined with **PL1**. These results underscore the crucial role of phosphine ligands in improving catalytic activity.

The study of monodentate phosphine ligands with different steric and electronic properties demonstrated that ligands with electron-withdrawing groups (e.g., **PL6**) and lower steric hindrance delivered a significant catalytic performance. **PL6** exhibited the highest yield and selectivity of isobutanol, outperforming other ligands. Interestingly, ligands with electron-donating groups or more sterically encumbered structures (such as **PL7** and **PL8**) showed reduced efficiency, likely due to steric limitations affecting substrate interactions at the active site. This highlights the critical importance of ligand design, where balancing electronic and steric effects is essential for maximising catalyst efficiency—a topic should be further explored in future research.

Additionally, the metal-to-ligand molar ratio was investigated, and it was determined that 1:3 was the ideal ratio for maximising biofuel production, as observed in the **Ru1/PL1** system. This molar ratio ensured optimal catalyst-ligand interaction, directly impacting the conversion rate and product yield.

A detailed screening of reaction conditions using **Ru1** and **PL1** demonstrated that the standard conditions reported in the literature were optimal. Lower temperatures and decreased base co-catalyst concentrations led to reduced catalytic activity, reinforcing that maintaining optimal reaction conditions is as important as catalyst selection for achieving high conversion and selectivity in biofuel production. In addition, the research focused on examining **Ru2** with the most promising ligands, such as **PL1**, **PL6**, **PL7**, and **PL8**, at a uniform concentration of 0.6 mol% to ensure fair comparisons. The results confirmed that **PL6**, with its electron-withdrawing fluorophenyl groups, delivered the best performance with **Ru2**, achieving the highest ethanol conversion and isobutanol yield.

Recent research has increasingly focused on developing more complex phosphine ligands to create highly sophisticated catalytic systems for isobutanol production. These advanced ligands, with tailored steric and electronic properties, offer advantages such as improved catalyst stability and reactivity. However, this study highlights that simple monodentate phosphine ligands can also deliver high yields and selectivity for isobutanol when combined with simple ruthenium catalysts, which demonstrates the potential of straightforward catalyst-ligand systems in biofuel production, challenging the notion that only complex ligands can provide high performance in these reactions.

In conclusion, Chapter 2 has significantly advanced our understanding of the catalytic mechanisms involving simple ruthenium catalysts and monodentate phosphine ligands. The findings show that simple catalytic systems can achieve high efficiency and selectivity in biofuel production with the right combination of ligands and conditions. The results also establish a strong foundation for future catalyst development by emphasising the importance of ligand design (particularly the balance of electronic and steric effects) and optimised reaction conditions. These insights could lead to improved catalytic systems that enhance the production of isobutanol, by focusing on ligand efficiency, better catalyst-ligand ratios, and optimised reaction conditions.

2.7. Future Work:

Future research will deepen the understanding of how monodentate phosphine ligands influence the catalytic production of isobutanol. The next phase will address the limitations encountered in the current study, particularly regarding the scope of ligands and metal centres investigated. By broadening the range of ligands and exploring alternative catalytic systems, we seek to identify more effective and selective combinations for biofuel production.

A key aspect of this future work will be expanding the range of phosphine ligands studied. The current research primarily focused on ligands like triphenylphosphine (**PL1**) and those with electron-withdrawing functional groups (e.g., **PL6**, **PL7**, **PL8**). However, several other phosphine ligands with varying steric and electronic properties warrant investigation. For instance, ligands with stronger electron-withdrawing effects, such as Tris(4-cyanophenyl)phosphine ($P(C_6H_4CN)_3$) and Tris(4-chlorophenyl)phosphine ($P(C_6H_5Cl)$) could further enhance catalyst performance by increasing metal-ligand back-donation, stabilising reaction intermediates, and potentially promoting more efficient C–C bond formation. These ligands were not explored in the present work due to time and material constraints. However, they are promising candidate for future research based on their theoretical ability to fine-tune catalytic activity.

Alternative metal centres beyond ruthenium will also be explored to build on the current findings. Metals like iridium and manganese have been identified as promising candidates for catalytic systems due to their similar properties and coordination chemistries. Specifically, iridium is known for its exceptional hydrogenation and C–H activation capabilities, which could provide a distinct advantage in promoting hydrogen transfer and C–C bond formation in the Guerbet reaction. The inclusion of iridium complexes, such as $Ir_4(CO)_{12}$, $[Ir(PPh_3)_3COCl]$, and $[IrCp^*Cl_2]_2$, will allow for a direct comparison of iridium's catalytic performance against ruthenium. These complexes have demonstrated excellent activity in related catalytic processes, and investigating their behaviour in ethanol and methanol upgrading could yield important insights into the differences between iridium and ruthenium in biofuel production.

Similarly, manganese-based catalysts represent an exciting area for exploration. Manganese is a first-row transition metal that is more abundant and cost-effective than ruthenium or iridium, making it a desirable candidate for sustainable catalysis. Manganese complexes like $Mn_2(CO)_{10}$ and $Mn(CO)_5Br$ have shown catalytic activity in hydrogenation reactions and C–C bond-forming processes. Their ability to operate under mild conditions and diverse redox chemistry could provide alternative reaction pathways for isobutanol production, potentially offering economic and environmental benefits over ruthenium and iridium catalysts. By examining manganese, we aim to uncover whether this metal can serve as a viable, greener alternative to ruthenium while maintaining high selectivity and conversion efficiency in the Guerbet reaction.

A systematic evaluation of these new ligand-metal combinations will focus on optimising reaction conditions such as ligand-to-metal ratios, temperature, and base co-catalyst concentration. The outcomes of this work will provide a clearer understanding of how steric and electronic effects from both the ligands and metal centres contribute to catalytic performance. This will allow us to refine and expand the principles established in the current study, which showed that electron-withdrawing ligands generally promote better catalytic activity.

In addition, it will be essential to perform a detailed analysis of the solid by-products formed during the catalytic reactions to confirm their composition and understand their role in the reaction mechanism. Techniques such as X-ray diffraction (XRD) and Fourier-transform infrared spectroscopy (FTIR) can be employed to characterise the crystalline and chemical structure of the solids. Thermogravimetric analysis (TGA) may also help determine these by-products' thermal stability and composition, as it provides insights into the decomposition temperatures of any carbonates, formates, or acetates that might be present. Additionally, elemental analysis and solid-state NMR spectroscopy could help identify specific elements and molecular fragments within the solids. By using these analytical techniques, we can confirm the nature of suspected compounds like sodium carbonate, sodium formate, or sodium acetate, which were hypothesised in previous experiments. This detailed characterisation will not only validate the assumptions made in earlier studies but also help elucidate how these by-products are formed and whether they influence the catalytic cycle or inhibit the system's overall efficiency. Understanding the formation and composition of solid by-products will contribute to optimising the catalytic process and improving the overall yield of isobutanol.

The role of gas-phase products, such as hydrogen, carbon monoxide and other undetected side products, will be investigated. The detection of CO in future experiments will provide further insights into the carbon balance observed in this study, particularly in reactions involving metal carbonyl complexes like $Ru_3(CO)_{12}$ and the proposed iridium and manganese carbonyl systems. The formation of CO and its potential contribution to the missing carbon fraction will be more closely monitored using gas chromatography or other advanced analytical techniques. This will ensure a better evaluation of the catalytic processes and help address the carbon efficiency challenge encountered in this chapter.
In summary, the proposed future work will focus on:

- Expanding the range of monodentate phosphine ligands to include ligands with stronger electron-withdrawing or sterically bulky characteristics.
- Exploring alternative metal centres, such as iridium and manganese, to evaluate their effectiveness compared to ruthenium.
- Investigating the carbon balance and the formation of gas-phase by-products in more detail, particularly focusing on hydrogen and carbon monoxide production.
- Analysing the solid by-products formed during the reactions using techniques such as X-ray diffraction (XRD), Fourier-transform infrared spectroscopy (FTIR), thermogravimetric analysis (TGA), and NMR spectroscopy, which will confirm the composition of solids like sodium carbonate, formate, or acetate, which were hypothesised to form, and shed light on how these by-products may impact the catalytic cycle or overall reaction efficiency.
- Optimising ligand-to-metal ratios and reaction conditions to improve the efficiency and selectivity of biofuel production.

These avenues of research will build on the current findings and lead to the development of more efficient, sustainable, and cost-effective catalytic systems for isobutanol production, with broader implications for biofuel synthesis.

2.8. References:

[1] F. J. Sama, R. A. Doyle, B. M. Kariuki, N. E. Pridmore, H. A. Sparkes, R. L. Wingad and D. F. Wass, *Dalton Transactions* **2024**, *53*, 8005-8010.

[2] K. J. Pellow, R. L. Wingad and D. F. Wass, *Catalysis Science & Technology* **2017**, *7*, 5128-5134.

[3] a) R. H. Crabtree, *The Organometallic Chemistry of the Transition Metals*, John Wiley & Sons, **2005**; b) J. F. Hartwig, *Organotransition Metal Chemistry: from Bonding to Catalysis*, University Science Books, **2010**.

[4] V. Cadierno, P. Crochet, J. Díez, S. E. García-Garrido, J. Gimeno and S. García-Granda, *Organometallics* **2003**, *22*, 5226-5234.

[5] a) P. C. Kamer and P. W. van Leeuwen, *Phosphorus (III) Ligands in Homogeneous Catalysis: Design and Synthesis*, John Wiley & Sons, **2012**; b) C. A. Tolman, *Chemical Reviews* **1977**, *77*, 313-348.

[6] D. Gabriëls, W. Y. Hernández, B. Sels, P. Van Der Voort and A. Verberckmoes, *Catalysis Science & Technology* **2015**, *5*, 3876-3902.

[7] A. Chieregato, J. Velasquez Ochoa, C. Bandinelli, G. Fornasari, F. Cavani and M. Mella, *ChemSusChem* **2015**, *8*, 377-388.

[8] A. D. Procyk and D. F. Bocian, *Journal of the American Chemical Society* **1991**, *113*, 3765-3773.

[9] D. E. Fogg and E. N. dos Santos, *Coordination Chemistry Reviews* **2004**, *248*, 2365-2379.

[10] C. P. Lenges and M. Brookhart, *Angewandte Chemie International Edition* **1999**, *38*, 3533-3537.

[11] H.-U. Blaser, A. Indolese and A. Schnyder, *Current Science* **2000**, 1336-1344.

[12] C. Bolm and M. Beller, *Transition Metals for Organic Synthesis*, Wiley-VCH, Weinheim, **2004**.

[13] J. Jover and J. Cirera, *Dalton Transactions* **2019**, *48*, 15036-15048.

[14] A. Behr and G. Henze, *Green Chemistry* **2011**, *13*, 25-39.

[15] J. T. Dixon, M. J. Green, F. M. Hess and D. H. Morgan, *Catalysis Today* **2004**, *96*, 267-281.

[16] L. Ruiz-Ramírez, T. A. Stephenson and E. S. Switkes, *Journal of the Chemical Society, Dalton Transactions* **1973**, 1770-1782.

[17] G. Chelucci, *Coordination Chemistry Reviews* **2017**, *331*, 1-36.

[18] B. M. Trost, F. D. Toste and A. B. Pinkerton, *Chemical Reviews* **2001**, *101*, 2067-2096.

[19] C. Satheesh, P. N. Sathish Kumar, P. R. Kumara, R. Karvembu, A. Hosamani and M. Nethaji, *Applied Organometallic Chemistry* **2019**, *33*, e5111.

[20] F. Novio, D. Monahan, Y. Coppel, G. Antorrena, P. Lecante, K. Philippot and B. Chaudret, *Chemistry–A European Journal* **2014**, *20*, 1287-1297.

[21] M. A. Bennett, *Coordination Chemistry Reviews* **1997**, *166*, 225-254.

Chapter 3: Ethanol Upgrading Using Ruthenium Catalysts with dppf Ligand

3.1. Introduction

The discovery of ferrocene in 1951 by Pauson and Kealy marked a significant milestone in organometallic chemistry, owing to its intriguing sandwich-like structure.[1] Lithiation of ferrocene at the 1,1'-positions followed by reaction with a suitable electrophile enables the synthesis of functionalised and substituted ferrocenes.[2] One example of such a derivative is 1,1'-bis(diphenylphosphino)ferrocene (dppf).[3]

The compound dppf was first identified in 1965 by dilithiating ferrocene with *n*-butyllithium and subsequently reacting it with chlorodiphenylphosphine (Scheme 3-1).[4] Dppf is a very efficient ligand that is extensively used in a variety of transition metal-catalysed reactions. The increased use of dppf as a supporting ligand in catalysis can be attributed to several advantageous features. These include the simple synthesis of dppf from the more affordable ferrocene and its thermal and moisture stability.

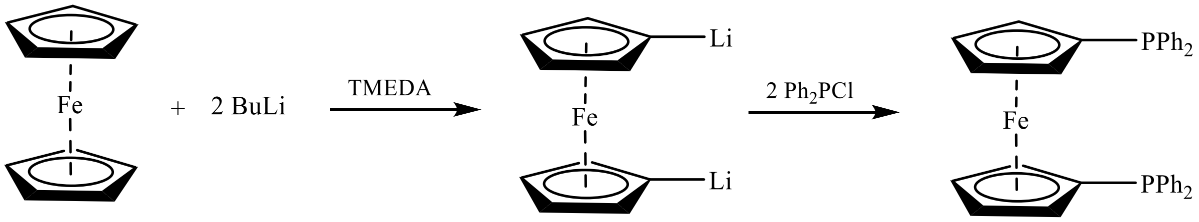

Scheme 3-1: Synthesis of dppf.

Additionally, the popularity of dppf arises from its straightforward synthesis using inexpensive ferrocene; it is easy to work with, can be dissolved in common solvents, and is stable under air, moisture, and heat; additionally, dppf is easy to work with and can be dissolved in common solvents, which allows for the relatively simple isolation of metal complexes with Group 6-12 metals; furthermore, it possesses functionality compatible with ESI-MS, NMR, and XRD techniques.[5]

Dppf is highly attractive in catalysis due to its ferrocene backbone, which provides a naturally large bite angle. This structural feature allows the ligand to easily accommodate different coordination geometries, including octahedral, compressed square planar, trigonal bipyramidal, and open planar trigonal, with minimal energetic penalty. Computational studies have determined that the average P–M–P angle, based on X-ray crystallography, is 98.74°, with the optimal bite angle reported to be 95.60°.[6]

This flexibility in bite angle enhances the ability of dppf to stabilise transition metal intermediates in various oxidation states and coordination geometries. For example, dppf stabilises both Pd(0) and Pd(II) oxidation states during key steps such as oxidative addition and reductive elimination in catalytic cycles. The adaptability of the ferrocene backbone supports the formation of catalytically relevant intermediates, enhancing the performance of transition metal catalysts across different catalytic reactions. This flexibility makes dppf a versatile ligand for a range of catalytic systems.[5]

3.1.1. Steric and Electronic Effects of dppf in Enhancing Ruthenium Catalysts:

In homogeneous catalysis, the steric and electronic properties of ligands such as dppf are essential for optimising the efficiency of ruthenium catalysts. These properties directly influence key steps in catalytic processes, particularly those involving transformations like hydrogenation, metathesis, oxidation reactions, and Guerbet reactions. Dppf's large bite angle [95.60°] and bulky diphenylphosphine groups create an optimal environment around the ruthenium centre by providing a controlled steric hindrance, which limits the access of unwanted molecules to the catalytic site, helping to stabilise reactive intermediates and prevents side reactions that could reduce efficiency. Such steric effects are particularly beneficial in selective binding and activation of substrates, allowing the catalyst to operate more effectively.[7]

In the specific context of the Guerbet reaction, the steric bulk provided by dppf ensures that the ruthenium catalyst is highly selective. This selectivity minimises the formation of by-products, a common challenge in such complex transformations. The bulky diphenylphosphine groups shield the ruthenium centre and allow the active site to favour desired reactions, ensuring a higher yield of the target alcohols. This protective environment is essential for maintaining the catalytic activity and preventing the catalyst's deactivation, which could occur if undesired molecules reach the active centre.

Electronically, the moderate electron-donating properties of dppf play a significant role in stabilising ruthenium in various oxidation states throughout the catalytic cycle. This electron donation is crucial during critical steps such as oxidative addition and reductive elimination, where the energy barrier needs to be minimised for efficient catalysis. In the Guerbet reaction, for instance, dppf's electronic effects facilitate the dehydrogenation of alcohols and the subsequent aldol condensation, two pivotal steps in the reaction mechanism.[8] By stabilising the metal centre, dppf allows the catalyst to perform these transformations more smoothly and with greater energy efficiency. The balance between electron donation and withdrawal also ensures that the catalyst remains active over prolonged periods, enhancing its durability and effectiveness.[9]

Moreover, the unique interplay between dppf's steric and electronic properties allows ruthenium-based catalysts to be highly adaptable in various catalytic environments. Combining steric hindrance and electronic tuning enables ruthenium to mediate various chemical transformations with high selectivity and yield efficiently. This makes dppf a valuable ligand in academic research and industrial applications where efficient, selective catalysis is crucial.[7, 10]

To conclude, the steric and electronic properties of dppf are considered potentially beneficial for enhancing the performance of ruthenium catalysts in homogeneous catalysis, including reactions such as the Guerbet process. These characteristics may contribute to improved catalytic efficiency and selectivity by facilitating more selective substrate binding, minimising side reactions, and stabilising reactive intermediates. Further investigation would be required to confirm these effects under Guerbet conditions.

3.1.2. The Role of dppf in Homogeneous Catalysis

Bianchini *et al.* demonstrated the effectiveness of palladium catalysts with dppf ligands in the methoxycarbonylation of alcohols.[11] The study revealed that dppf was crucial in stabilising the palladium centre, allowing the catalyst to facilitate the methoxycarbonylation reaction efficiently. The bulky phosphine groups in dppf created a protective environment around the metal centre, reducing side reactions and enhancing the selectivity for the desired product. The authors found that dppf improved the catalyst's activity, leading to higher yields and better control over the reaction than other phosphine ligands.

The study by Albrecht and van Koten provides valuable insights into the role of ligands, including dppf, in enhancing the performance of platinum and ruthenium complexes in homogeneous catalysis.[7] Although this study does not explicitly focus on the Guerbet reaction, it discusses the importance of steric and electronic effects of ligands such as dppf in various catalytic processes involving ruthenium complexes. The steric bulk and electronic properties of dppf are highlighted as critical factors in stabilising the metal centre and controlling reaction pathways, which are also crucial in Guerbet reactions. By stabilising the ruthenium centre and preventing undesired side reactions, dppf allows the catalyst to efficiently mediate alcohol dehydrogenation and aldol condensation—two essential steps in the Guerbet process. Therefore, while the study does not directly focus on the Guerbet reaction, the discussion of dppf's role in stabilising and enhancing ruthenium catalysis can be applied to understanding its significance in alcohol production reactions like the Guerbet process.

Another study by Štěpnička *et al.* explores the synthesis, coordination behaviour, and catalytic application of planar-chiral monocarboxylate dppf analogues, particularly 10,2-bis(diphenylphosphino)ferrocene-1-carboxylic acid (Hdpc), in homogeneous catalysis.[12] The research focuses on palladium-catalysed enantioselective allylic alkylation, where dppf derivatives played a vital role in improving both the selectivity and efficiency of the catalysts. The unique steric and electronic properties of the dppf ligands created an optimised environment around the palladium centre, contributing to higher yields and improved enantioselectivity of the reaction, which was attributed to dppf's ability to stabilise the metal complex and regulate the approach of reactants to the catalytic site, thus enhancing the control over the reaction pathway. While the study primarily focuses on asymmetric alkylation, the findings on the coordination behaviour and catalytic efficiency of dppf derivatives offer valuable insights into their broader application in similar catalytic systems, such as those involved in alcohol production.

Dppf is pivotal in enhancing homogeneous catalysis. Its ability to stabilise metal centres like palladium and ruthenium improves catalytic efficiency by reducing side reactions and increasing selectivity. Whether in methoxycarbonylation or enantioselective alkylation, the steric and electronic properties of dppf contribute to higher yields and better control of reaction pathways. These studies highlight dppf's versatility, making it an invaluable ligand in various catalytic processes, including sustainable alcohol production systems like the Guerbet reaction.

3.2. Aims and Objectives:

Despite its potential as a flexible ligand in transition metal catalysis, the use of dppf in Guerbet chemistry has yet to be investigated. This study aims to examine the suitability of dppf as a ligand in combination with different ruthenium catalyst precursors. The goal is to determine the practicality and effectiveness of this catalytic system in promoting the production of isobutanol from mixtures of ethanol and methanol with high yields and selectivity.

Isobutanol is a promising biofuel that has the potential to be a sustainable substitute for traditional fossil fuels. Hence, assessing the catalytic activity of new systems for the production of isobutanol is imperative. After an initial screen of dppf with a range of ruthenium precursors the catalytic process will be optimised, and the yields and selectivity of isobutanol will be precisely determined using advanced analytical techniques such as gas chromatography.

This study intends to provide valuable insights into the development of efficient and sustainable catalytic techniques for biofuel generation. It seeks to contribute to the transition towards a greener and more sustainable energy landscape by achieving the mentioned objectives.

3.3. Catalytic Performance of dppf in Isobutanol Production

3.3.1. Exploration of dppf with Ruthenium precursor complexes

This chapter details the investigation into isobutanol production, using dppf as a co-ligand. The role of dppf was explored in conjunction with various ruthenium precursors, **Ru1–Ru5** (Figure 3-1), to enhance the catalytic performance of these systems. In this context, dppf acts as a co-ligand by coordinating with the ruthenium centre, modulating its electronic and steric properties, thereby promoting selective catalysis in the Guerbet reaction.

The catalytic screening was performed under reaction conditions developed by Wass and co-workers. These conditions involved ethanol upgrading to isobutanol in a mixture containing 0.75 mL ethanol (12.8 mmol), 7.5 mL methanol (185.2 mmol), 0.1 mol% Ru catalyst loading, 0.1–0.3 mol% dppf, and 200 mol% NaOMe (34.26 mmol). The reaction proceeded for 20 hours at 180°C in a 65 mL Parr autoclave, with all mol% relative to ethanol.[13] By 'in-situ catalytic screening,' this study refers to evaluating the catalytic performance directly within the reaction mixture without isolating the catalyst or pre-ligated complex beforehand, providing a direct assessment of catalyst behaviour under operating conditions.

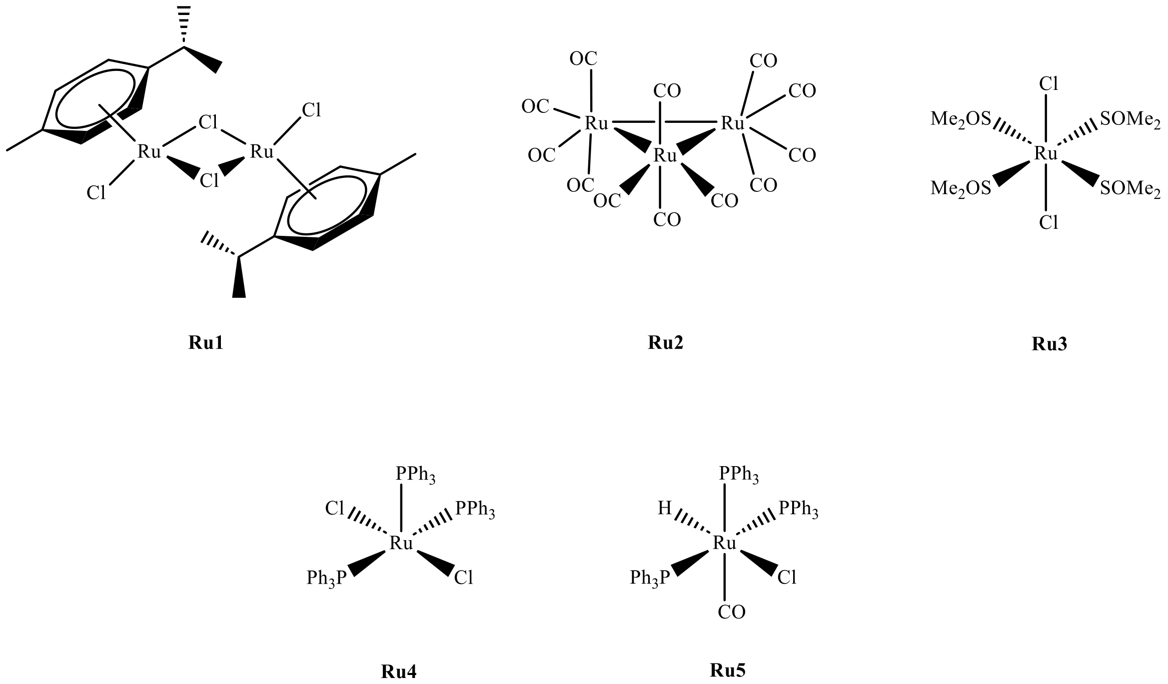

Ru1 **Ru2** **Ru3**

Ru4 **Ru5**

Figure 3-1: Typical ruthenium precursors used with dppf for ethanol/methanol upgrading to isobutanol.

Table 3-1 summarises the effect of different concentrations of dppf (0.1–0.3 mol%) on the catalytic performance of various ruthenium precursors (**Ru1–Ru5**) for isobutanol production. The analysis began by testing dppf alone at 0.2 mol%, which resulted in a minimal ethanol conversion of just 0.6% and no detectable isobutanol production (Table 3-1, entry 1). This confirmed that dppf has no significant catalytic activity, highlighting the necessity of combining it with active ruthenium catalysts for effective ethanol upgrading.

The study tested **Ru1** at 0.2 mol% and 0.3 mol% dppf, which showed similar isobutanol yields of 58.1% and 60.2%, with high selectivity above 98% (Table 3-1, entries 2 and 3). The TON values for isobutanol were 558 and 564, respectively, indicating efficient catalyst turnover. However, the results suggest that increasing the dppf concentration only marginally improved the yield. Notably, the carbon balance and error in analysis increased with the higher dppf concentration. For instance, in entry 3, the carbon balance reached 120%, with an error of 6.6%. This suggests that equilibrium effects may have influenced the reaction, as similar selectivity and high ethanol conversion were observed in both runs, making direct catalyst comparisons challenging when equilibrium has been reached.

Ru2 followed a similar trend at 0.2 mol% and 0.3 mol% dppf concentrations. Ethanol conversion remained high, and the isobutanol yield improved from 60.8% to 64.4%, with selectivity consistently above 98% (Table 3-1, entries 4 and 5). The TON for isobutanol increased from 584 to 609, showing better catalytic performance with higher dppf concentration. However, the carbon balance also increased significantly, peaking at 131.4% for 0.3 mol% dppf, suggesting that **Ru2** may have reached equilibrium earlier than **Ru1**, leading to a potential overestimation of the liquid products. This equilibrium effect complicates direct comparisons, as the higher carbon balance and analysis errors indicate potential inconsistencies in product quantification.

In the case of **Ru3**, which utilised lower dppf concentrations due to its monometallic nature, distinct results were observed. At 0.1 mol% dppf, **Ru3** achieved a 66.8% isobutanol yield (Table 3-1, entry 6), with a TON of 579 for isobutanol. Increasing the concentration to 0.2 mol% led to an impressive 80% isobutanol yield and a higher TON of 775 (Table 3-1, entry 7), with complete selectivity. However, the carbon balance was notably high at 159.7%, suggesting potential overestimation and measurement errors. With an analysis error of 3.3%, **Ru3** may have reached equilibrium faster than Ru1 and Ru2, making it challenging to compare catalytic efficiency at this reaction stage.

Compared to entry 7, which exhibited one of the highest isobutanol production results, the Wass group investigated the impact of the dppm ligand in the catalyst [RuCl2(dppm)2] on isobutanol production, achieving similar results. The [RuCl2(dppm)2] catalyst rapidly affected isobutanol production, reaching a 65% yield within 2 hours. After 20 hours, the yield increased to 75%, with selectivity reaching 98%. These findings are comparable to the performance of **Ru3/dppf**, reinforcing the effectiveness of phosphine ligands in ruthenium-based catalytic systems for isobutanol synthesis.

In contrast, **Ru4** and **Ru5**, which contain triphenylphosphine, responded differently to dppf. Adding 0.1 mol% dppf to **Ru4** increased the isobutanol yield from 36.3% (without dppf) to 46.5% (refer to Chapter 2, Section 2.3.1), with a TON of **407** for isobutanol and complete selectivity at 100% (Table 3-1, entry 8). The carbon balance was relatively stable at 92.9%, with a missing carbon percentage of 7.1%, suggesting **Ru4** effectively converted ethanol without significant side reactions. However, Ru5 performed poorly with 0.1 mol% dppf, with the isobutanol yield dropping from 50.7% to 15.4% (refer to Chapter 2, Section 2.3.1), a TON of 112, and a missing carbon percentage of 69.9% (Table 3-1, entry 9). This drastic drop in performance suggests that adding dppf might have disrupted the active site or altered the reaction pathway for **Ru5**, leading to poor catalytic activity and substantial missing carbon. It is crucial to note that equilibrium effects and diminishing returns were observed when moving from 0.2 mol% to 0.3 mol%. For instance, increasing dppf concentration from 0.2 mol% to 0.3 mol% in **Ru1** and **Ru2** yielded only a marginal improvement in isobutanol production, while the carbon balance and analysis error increased disproportionately. This suggests that going beyond 0.3 mol% dppf would likely result in excessive ligand loading, potentially disrupting the reaction equilibrium without significant gains in yield or selectivity. Thus, 0.3 mol% represents an optimal threshold for maximising catalytic performance without destabilising the system.

In conclusion, catalysts **Ru3** and **Ru2** demonstrated the highest productivity for producing isobutanol under the tested conditions, with **Ru3** achieving the highest yield at 80%. However, it is important to consider that equilibrium might have been reached in several reactions, complicating direct comparisons. Catalysts that reached equilibrium faster showed higher carbon balances, making it challenging to assess their full potential.

Table 3-1: Yield and selectivity of liquid products and ethanol conversion achieved with pre-catalysts Ru**1**-Ru**5** in the presence of dppf.

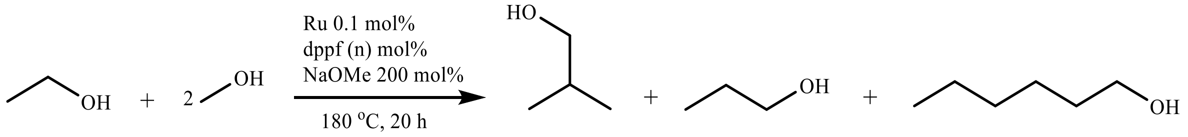

Entry [a]	**Catalyst**	**dppf (n) mol%**	**EtOH Conversion (%)** [b]	**Yield** [c] **(TON)** [d] **[Selectivity] (%)**			**Carbon Balance (%)** [e]	**Missing Carbon (%)** [f]	**Error of Analysis (%)** [g]
				Isobutanol	***n*-Propanol**	***n*-Hexanol**			
1	-	0.2	0.6	0 [0]	0 [0]	0 [0]	-	-	-
2	**Ru1**	0.2	95.9	58.1 (558) [98.2]	1.1 (11) [1.8]	0 [0]	116.6	-	4.8
3	**Ru1**	0.3	93.5	60.2 (564) [98.5]	1.6 (15) [1.5]	0 [0]	120.0	-	6.6
4	**Ru2**	0.2	95.9	60.8 (584) [98.4]	1.0 (10) [1.6]	0 [0]	123.2	-	3.9
5	**Ru2**	0.3	94.6	64.4 (609) [98.1]	1.3 (12) [1.9]	0 [0]	131.4	-	5.7
6	**Ru3**	0.1	86.7	66.8 (579) [97.2]	1.4 (12) [1.9]	1.8 (16) [0.8]	141.4	-	15.3
7	**Ru3**	0.2	96.5	80.0 (775) [100]	0 [0]	0 [0]	159.7	-	3.3
8	**Ru4**	0.1	87.4	46.5 (407) [100]	0 [0]	0 [0]	92.9	7.1	-
9	**Ru5**	0.1	72.6	15.4 (112) [100]	0 [0]	0 [0]	30.1	69.9	-

[a] Conditions: ethanol (0.75 mL, 12.8 mmol), methanol (7.5 mL, 185.15 mmol), Ru (0.0128 mmol, 0.1 mol%), dppf (0.0128–0.0384 mmol, 0.1-0.3 mol%), NaOMe (34.26 mmol, 200 mol%), 20 hours, 180 °C, mol% relative to ethanol. [b] Conversion of ethanol based on total number of liquid products obtained as determined by GC analysis. [c] Total yield and selectivity of Guerbet products in the liquid fraction as determined by GC analysis. [d] TON based on mmol of ethanol converted to products per mmol Ru. [e] **Carbon Balance %:** the percentage of initial carbon in ethanol detected in the products. Ideally close to 100%, indicating accurate accounting of all ethanol-derived carbon atoms. [f] **Missing Carbon:** any carbon discrepancy, indicating undetected carbon potentially due to side products, volatiles, or experimental losses. [g] **Analysis Error %:** an estimated measure of uncertainty in the analytical method, reflecting potential deviations from ideal values due to instrument limitations or procedural inaccuracies.

3.3.2. Exploring the Influence of Monodentate Phosphine Ligands (PL1 and PL6) on Isobutanol Production in Conjunction with dppf

The significant role of monodentate phosphine ligands, specifically **PL1** and **PL6** (Figure 3-2), in isobutanol production prompted an investigation into their interaction with dppf to explore whether a synergistic enhancement of catalytic activity could be achieved. **PL1** and **PL6** were selected due to their previously demonstrated high isobutanol yields compared to other monodentate phosphine ligands (see Chapter 2, Section 2.5.2).

From an electronic structure perspective, **PL1** and **PL6** differ from dppf regarding their donating and withdrawing abilities. **PL1** is a strong σ-donor with minimal electronic modulation, which makes it effective in stabilising metal complexes by enhancing electron density at the metal centre.[14] In contrast, **PL6** incorporates electron-withdrawing fluorine substituents, which reduce the electron density around the phosphorus atom and the metal centre, affecting overall reactivity.[15] Dppf acts as a bidentate ligand with a relatively large bite angle, and its ferrocene backbone offers electronic flexibility and the ability to stabilise different metal oxidation states and geometries.[16]

Structurally, dppf provides a bidentate coordination framework, whereas **PL1** and **PL6** are monodentate, allowing for more flexible coordination to metal centres.[17] Dppf forms stable chelate rings, enhancing the catalyst's ability to form and stabilise intermediates in catalytic cycles. By combining dppf with monodentate phosphines like **PL1** and **PL6**, an exciting interplay between structural flexibility and electronic effects is introduced: dppf's chelation stabilises the metal centre, while the monodentate ligands can fine-tune the electronic environment, either increasing (**PL1**) or decreasing (**PL6**) the electron density. This interaction enhances the potential for catalytic efficiency, particularly for processes such as oxidative addition and reductive elimination.[18]

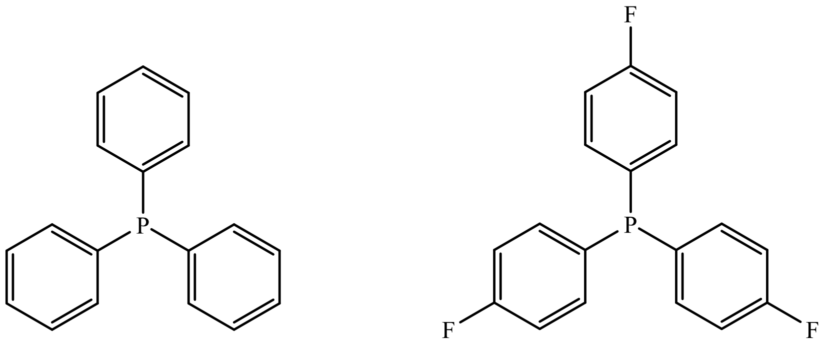

PL1 **PL6**

Figure 3-2: Monodentate phosphine ligands used in this chapter.

Table 3-2 presents the impact of adding phosphine ligands **PL1** and **PL6** to ruthenium catalysts combined with dppf for ethanol upgrading to isobutanol. The results demonstrate that both ligands enhance catalytic performance, though differences in isobutanol yield reflect how each ligand interacts with the various ruthenium precursors.

For **Ru1**, the combination of 0.1 mol% **PL1** with 0.1 mol% dppf resulted in an isobutanol yield of 70.4%, with high selectivity (97.9%) (Table 3-2, entry 1). The TON for isobutanol in this run was 638, with a TON of 15 for n-propanol, indicating efficient catalyst turnover with minimal by-product formation. However, replacing **PL1** with 0.1 mol% **PL6** further increased the isobutanol yield to 76.2% while maintaining high selectivity (98.4%) (Table 3-2, entry 2). The TON for isobutanol, in this case, was 708, with a slightly lower TON of 11 for n-propanol, highlighting **PL6**'s superior efficiency in facilitating ethanol conversion. The higher yield with **PL6** can be attributed to its electron-withdrawing nature, which likely enhances ethanol activation, promoting a more efficient catalytic cycle than **PL1**.

When **Ru2** was tested with 0.1 mol% of either **PL1** or **PL6** and 0.2 mol% dppf, both combinations produced similar isobutanol yields of 72.9% (Table 3-2, entries 3 and 4). The TON values for isobutanol were 683 for **Ru2/PL1** and 678 for **Ru2/PL6**, suggesting that both ligands perform comparably in this catalytic system. The TON for n-propanol was **9** for **Ru2/PL1** and 20 for **Ru2/PL6**, indicating a higher formation of n-propanol with **PL6**. These results suggest that, for **Ru2**, the choice between **PL1** and **PL6** has a less significant impact on overall isobutanol yield, likely due to **Ru2**'s trimetallic nature, which provides sufficient catalytic sites for ethanol activation regardless of ligand choice. The carbon balance in both cases was also comparable (147.9% for **PL1** and 148.3% for **PL6**), with minimal analysis errors, confirming the robustness of the reaction conditions.

In contrast, the combination of **Ru3** with 0.1 mol% **PL1** and 0.2 mol% dppf led to a reduced isobutanol yield of 68.4% (Table 3-2, entry 5), down from 80% when only dppf was used with **Ru3** (Table 3-1, entry 7). Although slightly lower, the TON for isobutanol in this run was 657, which still demonstrates efficient catalytic turnover.

The monometallic nature of **Ru3** can explain this decrease. Unlike **Ru1** and **Ru2**, **Ru3** has fewer active sites, and adding **PL1** may have caused "site blockage," preventing dppf from effectively coordinating with the ruthenium centre. Consequently, fewer active sites were available for ethanol conversion, resulting in a lower isobutanol yield. The diagram in Figure 3-3 illustrates this potential blockage effect when combining monometallic **Ru3** with **PL1**.

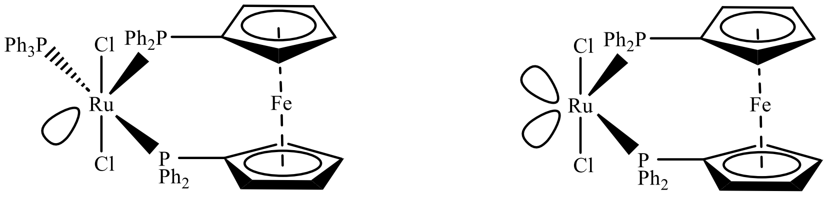

Single coordination site available

Double coordination sites available

Figure 3-3: Schematic representation of potential site blockage in **Ru3**/**PL1**/dppf system.

Additionally, *n*-propanol was detected as a by-product in small amounts across all runs, ranging from 1.0% to 2.2%, with negligible yields of other by-products. The high selectivity towards isobutanol in each case (97.1%–100%) underscores the effectiveness of the catalytic system in minimising undesired side products.

The decision not to increase the dppf concentration beyond 0.3 mol% was based on achieving a balance between catalytic activity and efficiency. Excessive amounts of dppf could lead to over coordination at the metal centre, reducing available active sites and potentially causing unwanted side reactions, as seen with **Ru3** and **PL1**. Additionally, higher concentrations of dppf could increase steric hindrance, hindering the efficient binding of ethanol. Therefore, the analysis was limited to a maximum of 0.3 mol% to maintain a functional balance between ligand coordination and catalytic activity.

To conclude, the study illustrates the crucial role of phosphine ligands **PL1** and **PL6** in enhancing catalytic performance when combined with ruthenium precursors and dppf for ethanol upgrading to isobutanol. Both ligands showed high selectivity towards isobutanol, with **PL6** yielding slightly better results due to its electron-withdrawing nature. **Ru1** and **Ru2** showed robust catalytic activity, while **Ru3** experienced site blockage when **PL1** was added, highlighting the importance of optimising ligand-to-metal ratios based on the number of active sites available. Ultimately, the primary objective was to extend this particular study by exploring various concentrations of dppf and investigating other monodentate phosphine ligands to determine their potential impact on isobutanol production. However, time constraints prevented further experimentation.

Table 3-2: Yield and selectivity of liquid products and ethanol conversion achieved with catalysts **Ru1-Ru3** in the presence of dppf and 0.1 mol% of PR$_3$.

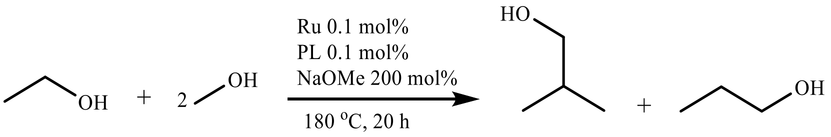

Entry [a]	**Catalyst**	**PR$_3$**	**dppf (n) mol%**	**EtOH Conversion (%)** [b]	**Yield** [c] **(TON)** [d] **[Selectivity] %**		**Carbon Balance (%)** [e]	**Error of Analysis (%)** [f]
					Isobutanol	***n*-Propanol**		
1	**Ru1**	**PL1**	0.1	90.7	70.4 (638) [97.9]	1.6 (15) [2.1]	144.0	10.5
2	**Ru1**	**PL6**	0.1	92.7	76.2 (708) [98.4]	1.2 (11) [1.6]	154.2	7.6
3	**Ru2**	**PL1**	0.2	93.8	72.9 (683) [98.6]	1.0 (9) [1.4]	147.9	6.8
4	**Ru2**	**PL6**	0.2	92.7	72.9 (678) [97.1]	2.2 (20) [2.9]	148.3	7.6
5	**Ru3**	**PL1**	0.2	96.4	68.4 (657) [100]	0 (0) [0]	136.6	4.2

[a] Conditions: ethanol (0.75 mL, 12.8 mmol), methanol (7.5 mL, 185.15 mmol), Ru (0.0128 mmol, 0.1 mol%), dppf (0.0128-0.0256 mmol, 0.1-0.2 mol%), PR$_3$ (0.0128 mmol, 0.1 mol%) NaOMe (34.26 mmol, 200 mol%), 20 hours, 180 °C, mol% relative to ethanol. [b] Conversion of ethanol based on total number of liquid products obtained as determined by GC analysis. [c] Total yield and selectivity of Guerbet products in the liquid fraction as determined by GC analysis. [d] TON based on mmol of ethanol converted to products per mmol Ru. [e] **Carbon Balance %:** the percentage of initial carbon in ethanol detected in the products. Ideally close to 100%, indicating accurate accounting of all ethanol-derived carbon atoms. [f] **Analysis Error %:** an estimated measure of uncertainty in the analytical method, reflecting potential deviations from ideal values due to instrument limitations or procedural inaccuracies.

3.3.3. Catalyst System Optimisation

The initial screening of dppf with various ruthenium precursors demonstrated that dppf acts as an effective ligand for ethanol upgrading to isobutanol. The most notable result was achieved using 0.2 mol% of dppf in combination with 0.1 mol% of **Ru3**, which yielded an impressive 80% isobutanol with complete selectivity (Table 3-1, entry 7). This represents one of the highest isobutanol yields reported using a homogeneous catalyst.

To check the accuracy of these findings, the experiment was repeated four times, resulting in an average isobutanol yield of 79.2% and an ethanol conversion of 94.5%. The standard deviation (SD) for these repetitions was calculated at 1.1%, while the standard error of the mean (SEM) was 0.5%. The standard deviation (SD) indicates the variability or dispersion of the yield results from the mean value, providing insight into how consistently the catalyst system performed across multiple runs. A low SD of 1.1% suggests that the system is relatively stable, and the variation between experimental runs is minimal, which is promising for the reproducibility of the catalyst's performance.

The standard error of the mean (SEM) reflects the precision of the average yield estimate. With an SEM of 0.5%, the uncertainty in the reported mean yield is relatively low, further supporting the reliability of the results. The combination of a high yield, low SD, and small SEM reinforces the conclusion that this catalyst system is effective and consistent across different experimental conditions.

In addition to achieving high yields, the study also emphasises the importance of selectivity, with particular runs reaching 100% selectivity towards isobutanol (Figure 3-5). Overall, the results are promising, as they not only demonstrate high ethanol conversions but also exceptional selectivity, making this catalyst system a strong candidate for further development in biofuel production.

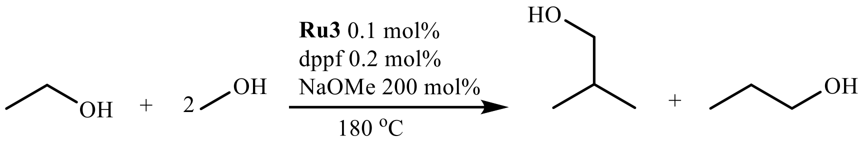

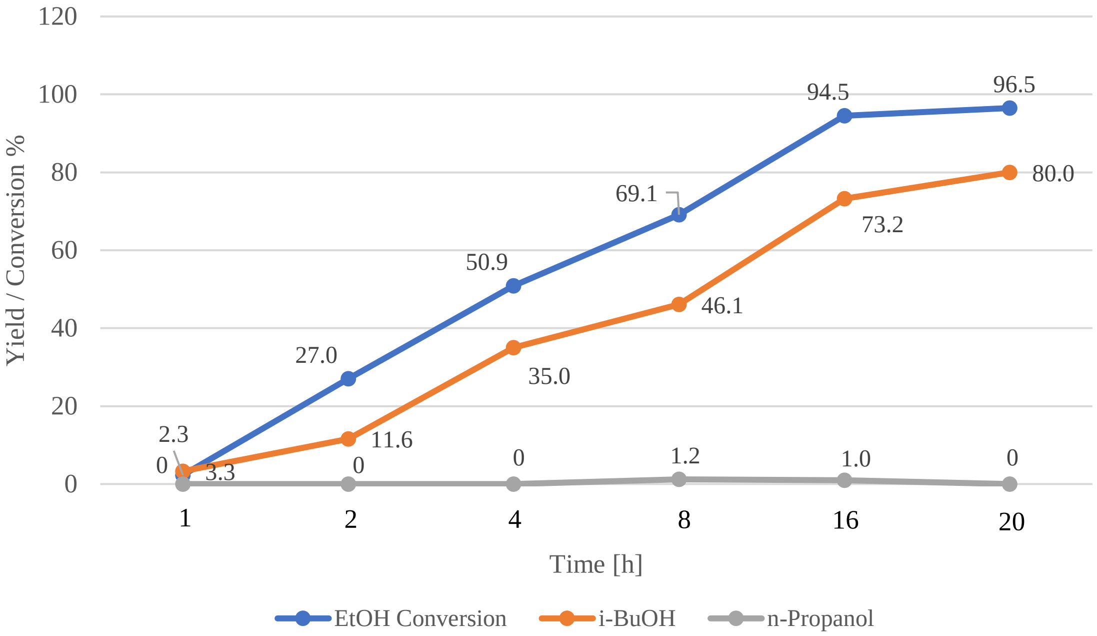

Figure 3-4: Yield of liquid products and ethanol conversion achieved with catalyst **Ru3** in the presence of dppf at different reaction times. Conditions: ethanol (0.75 mL, 12.8 mmol), methanol (7.5 mL, 185.15 mmol), **Ru3** (0.0128 mmol, 0.1 mol%), dppf (0.0256 mmol, 0.2 mol%), NaOMe (34.26 mmol, 200 mol%), 180 °C, mol% relative to ethanol. **EtOH Conversion %**: The line shows the conversion of ethanol over time, reaching a maximum of 96.5% at 20 hours. **Product Yields**: Lines represent yields of *i*-BuOH (isobutanol) and *n*-propanol over time, with *i*-BuOH yield steadily increasing to 80.0%, indicating it as the dominant product in the reaction.

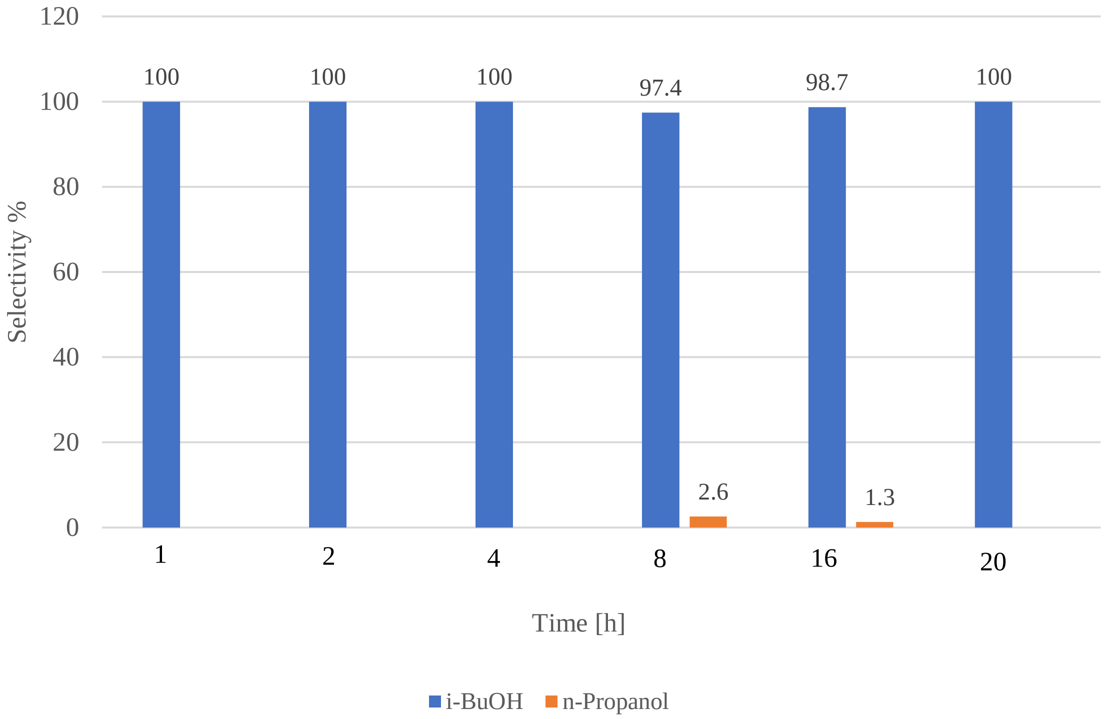

Figure 3-5: Selectivity of liquid products achieved with catalyst **Ru3** in the presence of dppf at different reaction times. Conditions: ethanol (0.75 mL, 12.8 mmol), methanol (7.5 mL, 185.15 mmol), **Ru3** (0.0128 mmol, 0.1 mol%), dppf (0.0256 mmol, 0.2 mol%), NaOMe (34.26 mmol, 200 mol%), 180 °C, mol% relative to ethanol. **Product Selectivity %**: Bars show selectivity for *i*-BuOH (isobutanol) and *n*-propanol over time. Selectivity remains consistently high for *i*-BuOH, achieving 100% selectivity at multiple time points, with a brief dip allowing *n*-propanol formation at 8 and 16 hours.

The impact of varying reaction temperature (Figure 3-6) and base loading (Figure 3-7) was thoroughly investigated to understand how these parameters influence isobutanol production. The gradual increase in isobutanol yield as temperatures rose highlights the importance of optimising these reaction conditions. Shorter experimental runs of 4 hours were conducted to provide clear insights into how temperature and base concentration changes impact the production process.

The results revealed that lower temperatures and reduced base concentrations had a significant detrimental effect on isobutanol yield, which is likely related to how temperature influences the reaction's rate-determining step (RDS), as discussed in Chapter 2, Section 2.5.3. At lower temperatures, the RDS tends to be the dehydrogenation of ethanol and methanol, a process that requires sufficient thermal energy to proceed efficiently. As the temperature increases, the RDS may shift towards other steps in the reaction, such as the coupling process or hydrogenation. This transition enables greater conversion efficiency, resulting in higher isobutanol yields. The optimal yields were observed under standard reaction conditions, where temperature and base concentration were adjusted to balance the RDS effectively.

In addition to temperature, base loading is critical to the overall reaction efficiency. Sodium methoxide acts as the base in this process, driving the dehydrogenation of ethanol and methanol. As previously highlighted in Chapter 2, Section 2.5.3, when sodium methoxide is used in large amounts, it supports the dehydrogenation and actively participates in the coupling reaction. Although methanol undergoes dehydrogenation, the excess sodium methoxide is the primary driver of the coupling reaction, thanks to its abundance and strong basicity. This ensures that there is always enough base available to facilitate both reaction steps, which is crucial for achieving high selectivity and yield of isobutanol. Therefore, temperature and base loading must be optimised to enhance the overall catalytic performance and prevent any limiting effects on the rate-determining step.

To conclude, the optimised reaction conditions for **Ru3** in combination with dppf have been identified as follows: 0.75 mL ethanol (12.8 mmol), 7.5 mL methanol (185.2 mmol), 0.1 mol% **Ru3**, 0.2 mol% dppf, and 200 mol% sodium methoxide (34.26 mmol), conducted for 20 hours at 180°C in a 65 mL Parr autoclave. These conditions resulted in the highest isobutanol yield of 80% with complete selectivity (Table 3-1, Entry 7). The excess sodium methoxide played a crucial role in the dehydrogenation and coupling steps, ensuring efficient conversion of ethanol to isobutanol. This set of optimised conditions has demonstrated a balanced and highly efficient catalytic process for the selective production of isobutanol.

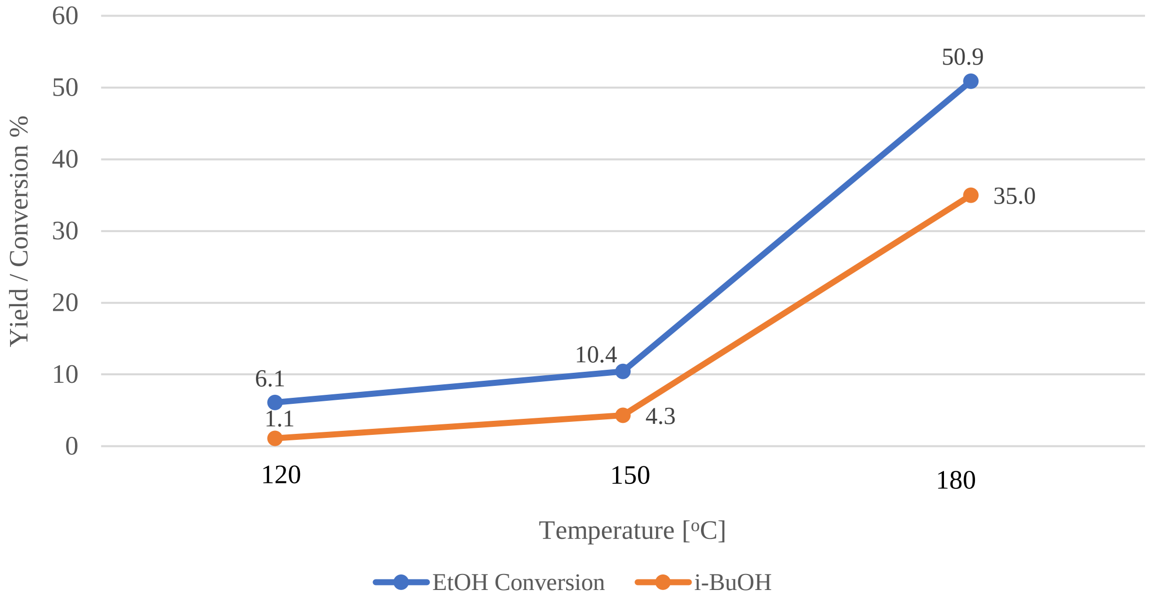

Figure 3-6: Yield of liquid products and ethanol conversion achieved with catalyst **Ru3** in the presence of dppf at different reaction temperatures. Conditions: ethanol (0.75 mL, 12.8 mmol), methanol (7.5 mL, 185.15 mmol), **Ru3** (0.0128 mmol, 0.1 mol%), dppf (0.0256 mmol, 0.2 mol%), NaOMe (34.26 mmol, 200 mol%), 4 hours, temperature as stated, mol% relative to ethanol. **EtOH Conversion %**: The line shows ethanol conversion, which increases significantly with temperature, reaching 50.9% at 180 °C. ***i*-BuOH Yield %**: The line indicates the yield of *i*-BuOH (isobutanol), which also rises with temperature, reaching a maximum of 35.0% at 180 °C, demonstrating a positive temperature effect on product formation.

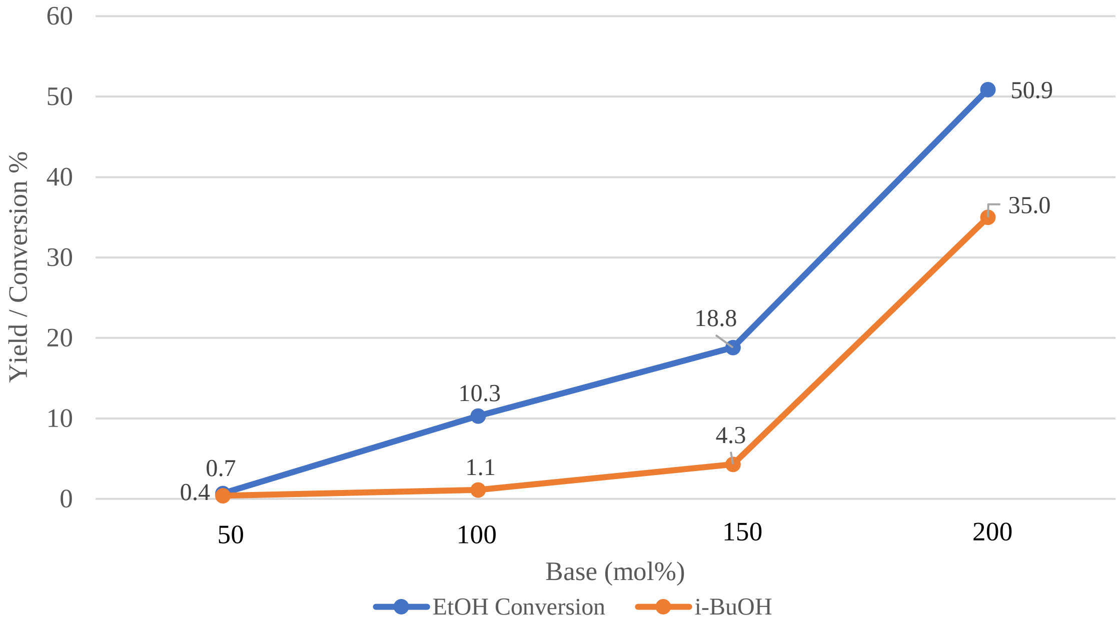

Figure 3-7: Yield of liquid products and ethanol conversion achieved with catalyst **Ru3** in the presence of dppf at various base loadings. Conditions: ethanol (0.75 mL, 12.8 mmol), methanol (7.5 mL, 185.15 mmol), **Ru3** (0.0128 mmol, 0.1 mol%), dppf (0.0256 mmol, 0.2 mol%), NaOMe (mol% as stated), 4 hours, 180 °C, mol% relative to ethanol. **EtOH Conversion %**: The line shows the conversion of ethanol, which increases significantly with higher base concentrations, reaching 50.9% at 200 mol%. ***i*-BuOH Yield %**: The line indicates the yield of *i*-BuOH (isobutanol), which also rises with increasing base concentration, achieving a maximum yield of 35.0% at 200 mol%.

3.3.4. Attempted Isolation of a Pre-formed Catalyst from dppf and Ru3

All of the catalytic runs so far had been performed by generating the catalytic species in situ by addition of dppf to the ruthenium precursor **Ru3**; therefore, we attempted to pre-form a catalyst for comparison (Scheme 3-10).

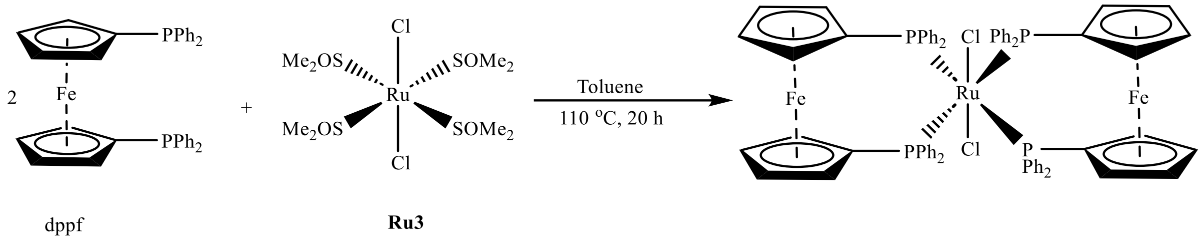

Scheme 3-2: Reaction scheme showing the expected product.

A reaction combined 1.08 mmol of dppf ligand with 0.54 mmol of **Ru3**. The suitability of the solvents dichloromethane (DCM) and toluene for the reactants was investigated individually to determine the optimal solvent system. Upon suitable heating, it was discovered that the reactants had superior solubility in toluene than DCM. The process was carried out under a nitrogen (N_2) atmosphere to protect any products formed from oxidation, even though dppf and **Ru3** are stable in air. An oil bath maintained a temperature of 110 °C, and the reaction continued throughout the night. Afterwards, the solvent was removed by evacuation, and the resultant product was rinsed three times with 20 mL of pentane, resulting in a brownish-orange solid weighing 0.27 g.

The ^1H NMR and ^{13}C NMR spectra were inconclusive, providing little valuable information for identifying the desired product. Consequently, they will not be further considered in this analysis. However, the $^{31}P\{^1H\}$ NMR spectrum (Figure 3-8) provided significant insights into the reaction between $[RuCl_2(DMSO)_4]$ and dppf, shedding light on the nature of the products formed.

A prominent peak at -17.5 ppm corresponds to free dppf, indicating that a significant amount of the ligand remained unreacted. As observed in previous studies, free dppf typically appears in this chemical shift range due to the shielding effects from the ferrocene backbone.[19] This suggests that not all the dppf ligands coordinated to the ruthenium centre, which may have resulted in the incomplete formation of the expected $[RuCl_2(dppf)_2]$ complex.

Two additional singlets were observed at 27.5 ppm and 28.8 ppm. These peaks may correspond to phosphine oxide species formed due to partial oxidation of the phosphine ligands, or they may indicate different coordination geometries of dppf in a ruthenium complex. Phosphine oxides typically appear in this region due to the deshielding effects of oxygen atoms.[18b] Alternatively, these shifts could represent ruthenium-dppf coordination environments, reflecting subtle changes in the complex's electronic structure. Such variations may arise from differences in ligand coordination or interactions with other species present in the reaction mixture.

A significant peak at 37.9 ppm may suggest the presence of a Ru-H species. As Morris et al. (1994) reported, hydride signals in $^{31}P\{^{1}H\}$ NMR spectra are typically observed in this region when associated with ruthenium complexes.[20] The formation of such a species could imply that the reaction conditions allowed for some hydrogenation or hydride transfer processes, even though these were not the primary goals of the experiment.

Further signals were observed at 44.3 ppm, 54.3 ppm, and 57.8 ppm, which can be attributed to the diphenylphosphino groups within the dppf ligand. These peaks are consistent with known chemical shifts for coordinated dppf, particularly when interacting with transition metals like ruthenium.[19] The presence of multiple peaks suggests that the dppf ligands in this system adopt different coordination environments, possibly due to variations in the geometry of the resulting complexes or partial coordination of dppf to ruthenium centres.

Ideally, one signal should be observed in the $^{31}P\{^{1}H\}$ NMR spectrum. This would occur if the two dppf ligands were symmetrically coordinated to the ruthenium centre, resulting in chemically equivalent phosphorus environments. However, deviations from this idealised structure, such as asymmetric coordination or different ligand interactions (e.g., varying chloride interactions or partial oxidation), could lead to the appearance of additional signals, as observed in the spectrum. These deviations often occur in coordination chemistry, where complexation can be influenced by steric and electronic factors, leading to a mixture of species or coordination isomers.

In conclusion, the $^{31}P\{^{1}H\}$ NMR spectrum revealed a complex mixture of species in the reaction. While free dppf suggests incomplete coordination, the other signals indicate the formation of ruthenium-dppf complexes with varying coordination environments. The multiple peaks observed for coordinated dppf likely result from differences in ligand binding and the presence of possible side products or intermediates. Further purification or modification of reaction conditions would be necessary to isolate the desired $[RuCl_2(dppf)_2]$ complex with higher purity.

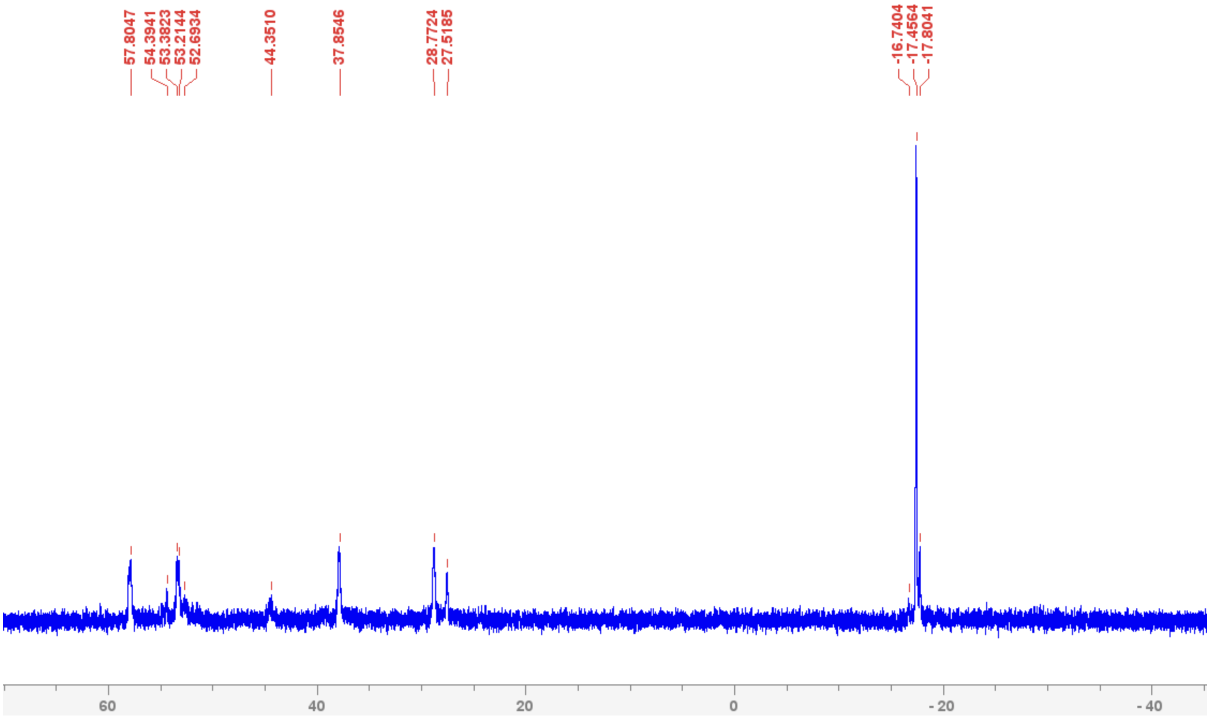

Figure 3-8: $^{31}P\{^{1}H\}$ NMR spectrum for the solid obtained from the reaction of dppf with $[RuCl_2(dmso)_4]$.

Figure 3-9 displays the mass spectrometric analysis of the expected complex $[RuCl_2(dppf)_2]$ reveals several critical peaks that align with the anticipated structure. Notably, the prominent signals observed at *m/z* 771.13 and *m/z* 773.03 correspond to the isotopic pattern of the ruthenium-containing species. These peaks reflect the natural isotopic distribution of ruthenium, particularly its stable isotopes ^{99}Ru and ^{101}Ru, contributing to the isotopic splitting evident in the spectrum. Additional peaks observed around *m/z* 1180–1181 likely indicate fragment ions involving the two dppf ligands or fragments related to the ferrocene backbone. Furthermore, a peak at *m/z* 553.11 suggests a possible fragment resulting from partial cleavage of one of the dppf ligands or a ruthenium-centred fragment with the loss of phosphine ligands, which is typical in the mass spectrometry of coordination complexes. The smaller peaks around m/z 734–735 likely correspond to further isotopic fragments from the dppf ligand or lower-order fragments from the complex. Ruthenium's isotopic distribution is well-represented by these multiple peaks, as it contains seven stable isotopes (^{96}Ru, ^{98}Ru, ^{99}Ru, ^{100}Ru, ^{101}Ru, ^{102}Ru, and ^{104}Ru), which collectively contribute to the characteristic isotopic pattern. The data indicate that the expected [RuCl$_2$(dppf)$_2$] complex may have been successfully synthesised, though additional structural confirmation could be achieved through techniques such as X-ray crystallography or elemental analysis.

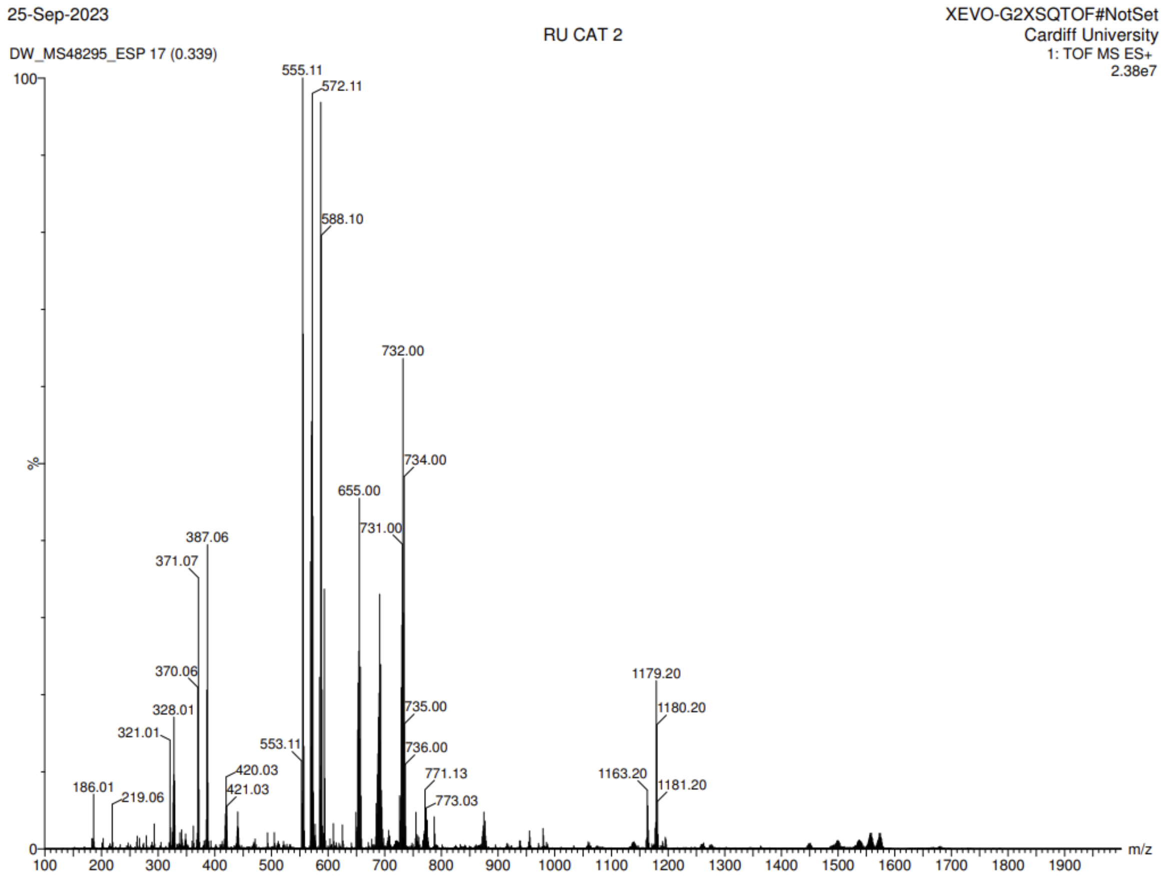

Figure 3-9: Mass Spectrometry for the solid obtained from the reaction of dppf with [RuCl$_2$(dmso)$_4$].

Finally, several efforts were undertaken to acquire the crystal structure, utilising different solvent systems, including DCM/hexane and toluene/pentane but all were unsuccessful.

3.3.5. Effect of Bidentate Phosphine Ligand Bite Angles on Isobutanol Synthesis

Due to the success of dppf as a ligand for the upgrading of ethanol to isobutanol, different bidentate phosphine ligands with bite angles similar to dppf were investigated. The purpose was to investigate whether such ligands would also yield good catalysts for the synthesis of isobutanol in the presence of **Ru3**. The dppf ligand has a bite angle of 98.60°, dpephos and dppb ligands have bite angles of 102.3° and 94° respectively, which makes them ideal candidates for study (Figure 3-10).

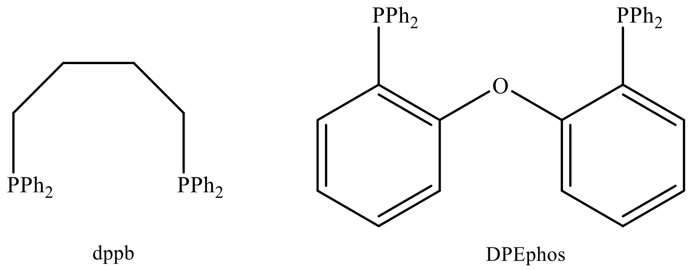

Figure 3-10: Bidentate ligands used in this section.

For this study, the optimised conditions for the dppf system were applied: 0.75 mL ethanol (12.8 mmol), 7.5 mL methanol (185.2 mmol), 0.1 mol% **Ru3**, 0.2 mol% of either dpephos or dppb and 200 mol% NaOMe (34.26 mmol), with a reaction time of 20 hours at 180°C in a 65 mL Parr autoclave (mol% relative to ethanol).

Figures 3-11 and 3-12 illustrate the comparative yields of isobutanol when different bidentate ligands were tested with **Ru3** under standardised conditions. The reaction with 0.2 mol% dppb resulted in a 64.3% yield of isobutanol, corresponding to a TON of 593. Using the same molar concentration of dpePhos produced a slightly lower isobutanol yield of 54.2%, with a corresponding TON of 462. In contrast, dppf demonstrated the highest efficiency, achieving an impressive 80% yield of isobutanol, with a TON of 775 under identical conditions.

These results highlight the significant role of dppf in enhancing isobutanol production compared to other bidentate ligands. The superior TON for dppf suggests it promotes a more efficient catalytic turnover, making it the most effective ligand in driving the Guerbet reaction towards higher

isobutanol yields. Meanwhile, dppb and dpePhos, while effective, show comparatively lower TONs and yields, indicating that they may facilitate a different level of catalytic efficiency than dppf.
It is worth noting, however, that none of these ligands can rival the rapid isobutanol production achieved with dppm in the [$RuCl_2(dppm)_2$] catalyst system. As previously discussed, this catalyst reached a 65% yield of isobutanol in just 2 hours, which further increased to 75% after extending the reaction time to 20 hours under the same conditions.

Gas Chromatography (GC) analysis confirmed substantial ethanol conversion with these ligands. Specifically, ethanol conversion was 84.9% with dpephos and 92.5% with dppb. The selectivity for isobutanol was also notably high, reaching 95.6% with dppb and 88.8% with dpephos, demonstrating that these ligands promote efficient conversion with minimal by-product formation.
Further GC results revealed negligible amounts of *n*-propanol, *n*-hexanol, and 2-methyl-1-butanol, highlighting the specificity of the reaction conditions and the efficiency of the catalysts in promoting the desired transformation.

In conclusion, while [$RuCl_2(dppm)_2$] remains superior in reaction speed and efficiency, dppf and dppb are particularly promising among the bidentate ligands tested, delivering higher yields and selectivity in isobutanol production. The negligible by-products and impressive ethanol conversion underscore the fine performance of these ligands, with dppf showing particular promise for extended reaction runs aimed at maximising isobutanol yield.

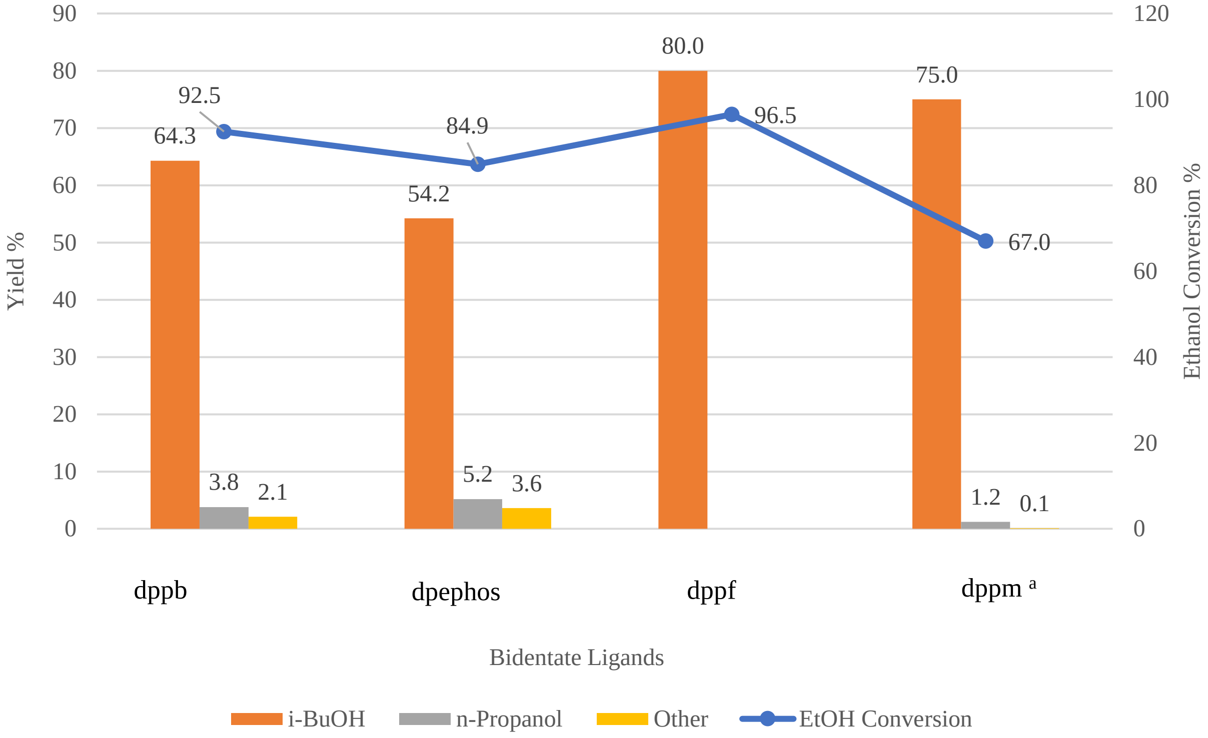

Figure 3-11: Yield of liquid products and ethanol conversion achieved with catalyst **Ru3** in the presence of dppb & dpephos. Conditions: ethanol (0.75 mL, 12.8 mmol), methanol (7.5 mL, 185.15 mmol), **Ru3** (0.0128 mmol, 0.1 mol%), ligand (0.0256 mmol, 0.2 mol%), NaOMe (34.26 mmol, 200 mol%), 180 °C, 20 hours, mol% relative to ethanol. **EtOH Conversion %**: The line indicates ethanol conversion across different ligands, showing a peak with dppf (96.5%) and a decline with dppm (67.0%). **Product Yields**: Bars represent yields of i-BuOH (isobutanol), *n*-propanol, and other by-products (a mixture of *n*-hexanol and 2-methylbutanol). The highest *i*-BuOH yield (80.0%) is observed with dppf. [a] Data for dppm was reported by the Wass group.[21]

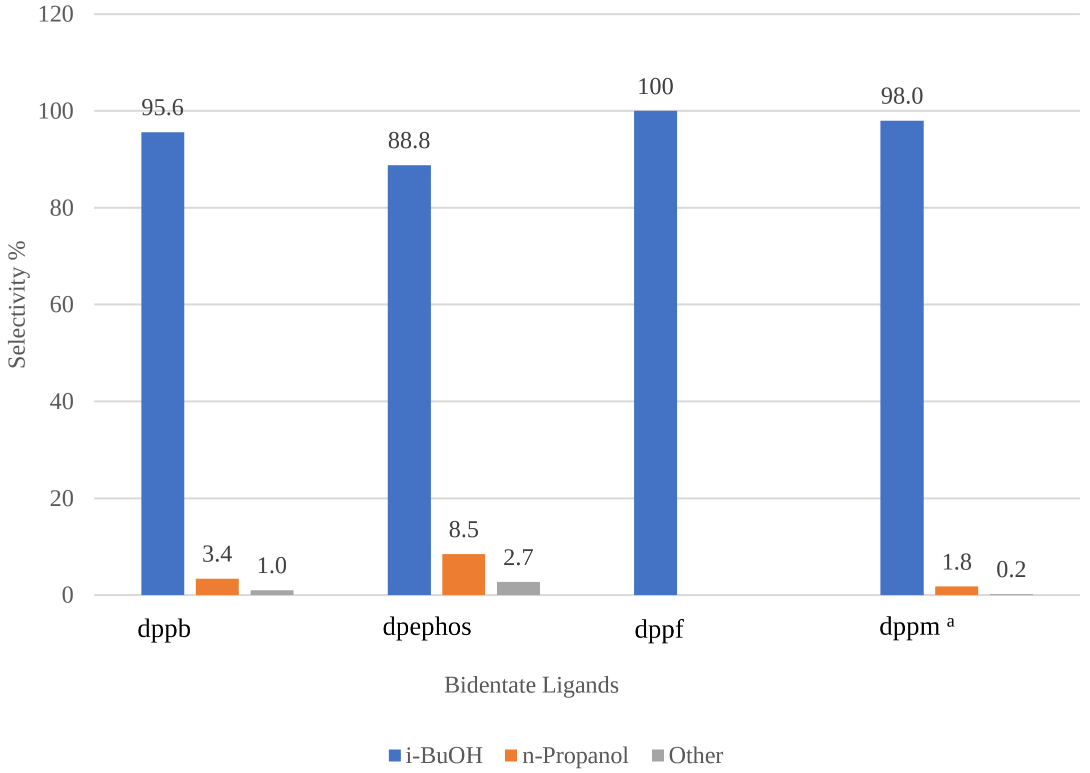

Figure 3-12: Selectivity of liquid products achieved with catalyst **Ru3** in the presence of dppb & dpephos. Conditions: ethanol (0.75 mL, 12.8 mmol), methanol (7.5 mL, 185.15 mmol), **Ru3** (0.0128 mmol, 0.1 mol%), Ligand (0.0256 mmol, 0.2 mol%), NaOMe (34.26 mmol, 200 mol%), 180 °C, 20 hours, mol% relative to ethanol. **Product Selectivity %**: Bars indicate selectivity for *i*-BuOH (isobutanol), *n*-propanol, and other by-products (*n*-hexanol and 2-methylbutanol) across different ligands. Maximum selectivity for *i*-BuOH (100%) is observed with dppf, while dppb and dppm also show high selectivity (95.6% and 98.0%, respectively). [a] Data for dppm was reported by the Wass group.[21]

These findings prompted further investigation into the isobutanol yield obtainable with dppb over varying reaction durations. As illustrated in Figure 3-13, extending the reaction time led to a steady increase in isobutanol production, while selectivity remained consistently high, between 92% and 95% (Figure 3-14).

A comparative analysis shows that dppf, like dppb, operates as a relatively slower ligand in promoting isobutanol production. In contrast, dppm has shown significantly greater efficiency, facilitating faster isobutanol synthesis than dppf and dppb. The slower catalytic activity observed with dppf and dppb highlights the need for extended reaction times to maximise yields.

Despite their slower kinetics, dppf generally performs more effectively than dppb. Experimental data suggests that dppf provides more favourable coordination and catalytic properties, particularly under prolonged reaction conditions. Therefore, dppf and dppb warrant further exploration through extended reaction times to fully assess their catalytic potential. Detailed kinetic and mechanistic studies would provide valuable insights into their catalytic behaviours, helping to fine-tune reaction conditions for enhanced efficiency.

While dppm currently stands out as the most efficient ligand for rapid isobutanol production, the promising attributes of dppf and dppb should be considered. With further experimentation, especially with longer reaction times, these ligands may demonstrate improved catalytic performance, thereby expanding the range of effective ligands available for optimising isobutanol synthesis.

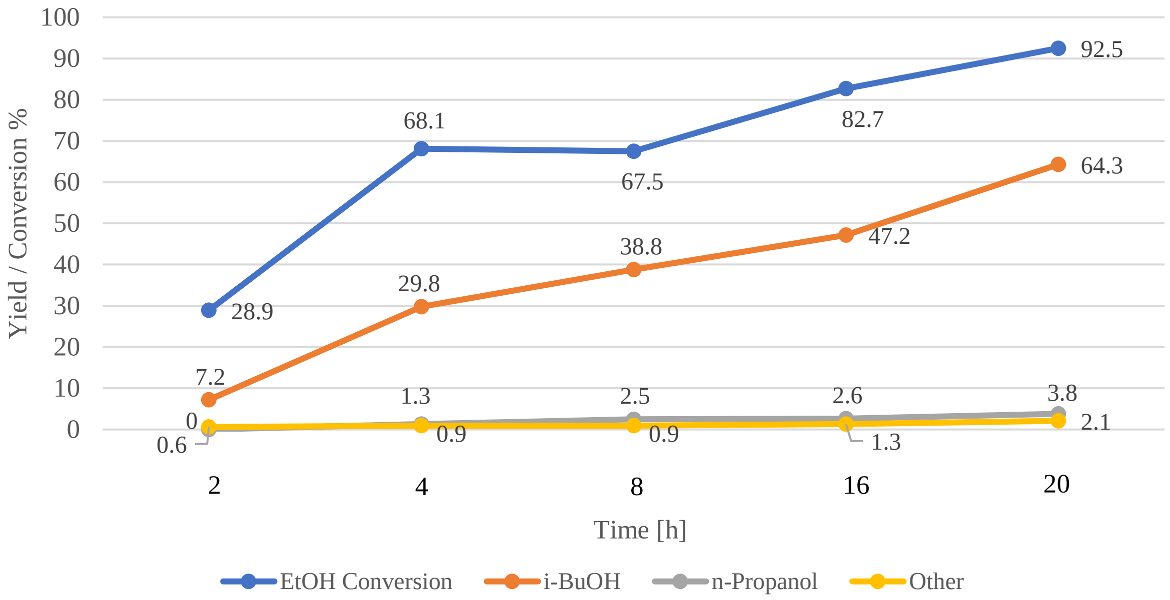

Figure 3-13: Yield of liquid products and ethanol conversion achieved with catalyst **Ru3** in the presence of dppb at different reaction times. Conditions: ethanol (0.75 mL, 12.8 mmol), methanol (7.5 mL, 185.15 mmol), **Ru3** (0.0128 mmol, 0.1 mol%), dppb (0.0256 mmol, 0.2 mol%), NaOMe (34.26 mmol, 200 mol%), 180 °C, mol% relative to ethanol. **EtOH Conversion %**: The line shows the conversion of ethanol, increasing significantly over time and reaching 92.5% at 20 hours. **Product Yields**: Lines represent yields of *i*-BuOH (isobutanol), *n*-propanol, and other products (a mixture of *n*-hexanol and 2-methylbutanol). The yield of *i*-BuOH steadily increases over time, peaking at 64.3% at 20 hours.

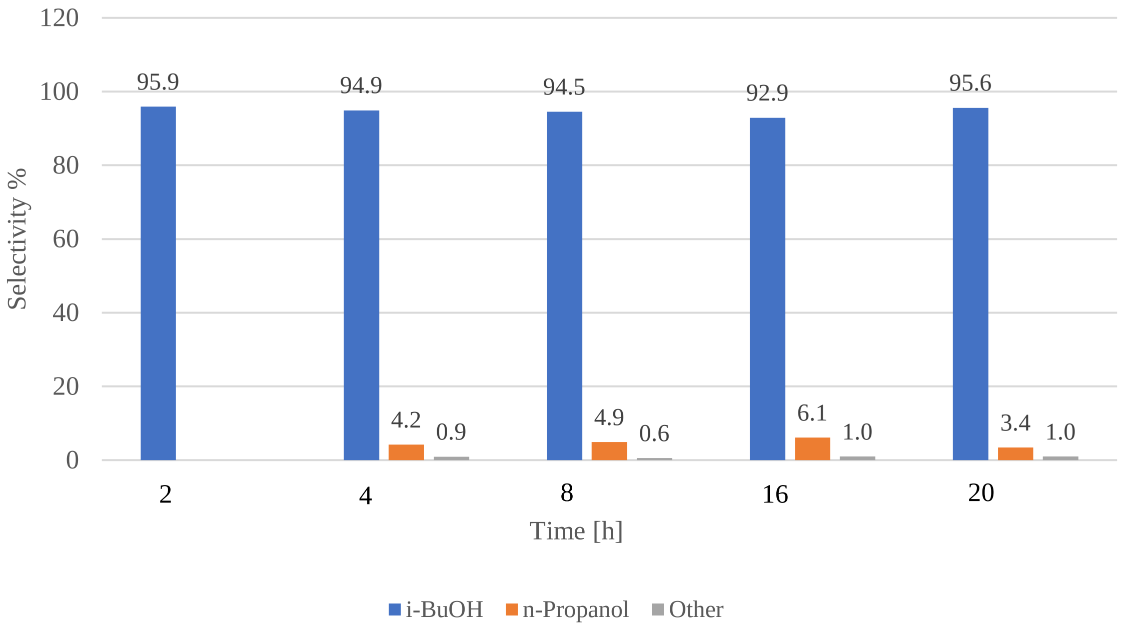

Figure 3-14: Selectivity of liquid products achieved with catalyst **Ru3** in the presence of dppb at different reaction times. Conditions: ethanol (0.75 mL, 12.8 mmol), methanol (7.5 mL, 185.15 mmol), **Ru3** (0.0128 mmol, 0.1 mol%), dppb (0.0256 mmol, 0.2 mol%), NaOMe (34.26 mmol, 200 mol%), 180 °C, mol% relative to ethanol. **Product Selectivity** %: Bars indicate selectivity for *i*-BuOH (isobutanol), *n*-propanol, and other by-products (a mixture of *n*-hexanol and 2-methylbutanol) at different reaction times. Selectivity for *i*-BuOH remains consistently high, averaging around 95%, while *n*-propanol and other by-products exhibit low selectivity percentages.

Finally, solid and gas by-products were consistently observed across this chapter's experiments. Chapter 2, Section 2.5.7 provides a more detailed discussion of these observations, including their implications and potential origins. These findings are important for understanding the overall reaction mechanisms and will help inform future optimisations of the catalytic system.

3.4. Conclusion:

This chapter explored isobutanol production using dppf as a ligand with various ruthenium pre-catalysts. The investigation focused on how dppf interacts with pre-catalysts Ru1-Ru5 to enhance isobutanol synthesis through the Guerbet reaction. Table 3-1 shows that dppf alone did not catalyse the ethanol upgrading reaction. However, when combined with specific ruthenium pre-catalyst, significant improvements in yield and selectivity were observed. The optimal combination was Ru3 with two equivalents of dppf, which delivered an exceptional isobutanol yield of 80% with complete selectivity. Further, the chapter examined the synergistic effects of adding monodentate phosphine ligands, specifically PL1 and PL6, to dppf and ruthenium systems. While adding PL1 to Ru3 and dppf reduced yield, both PL1 and PL6 positively impacted when paired with other catalysts, achieving yields of up to 76% with excellent selectivity.

The study also investigated the performance of other bidentate phosphine ligands with bite angles similar to dppf, such as dppb and dpephos. While dppb led to higher isobutanol production than dpephos, neither outperformed dppf, indicating that bite angle alone cannot fully predict catalytic activity. It was also observed that extending the reaction duration led to increased yields while maintaining high selectivity.

The differing efficiencies of dppm and dppf in isobutanol production present a fascinating area of study, particularly considering their contrasting bite angles—73° for dppm and 99° for dppf. This variation suggests that spatial arrangements and the electronic environments surrounding the central metal play crucial roles in catalytic performance. It is hypothesised that the presence of the iron centre in the dppf backbone contributes to the enhanced yield of isobutanol, potentially by facilitating electronic interactions and providing structural stability that optimises coordination with ruthenium catalysts.

Further research into these ligands' electronic and steric properties, alongside in-depth mechanistic studies, is necessary to fully understand the role of the iron centre and the impact of bite angles on catalytic performance. This understanding could lead to developing more effective catalysts that offer higher yields and selectivity in isobutanol production.

In conclusion, this chapter provides valuable insights into the catalytic efficiency of dppf and its interaction with ruthenium catalysts in isobutanol production, laying the groundwork for further research and advancements in this field.

3.5. Future Work:

Given the promising results obtained in this chapter, the research will continue with further exploration and experimentation. The following avenues will be pursued:

1. Stoichiometric Reactions:

Future work will involve stoichiometric reactions to identify the specific Ru-dppf complexes formed during typical catalytic reactions, which will aid in understanding the mechanistic pathways and the nature of the active catalytic species.

2. Synthesis and Isolation:

The synthesis and isolation of pre-formed analogues of Ru-dppf and other promising systems will be a priority. By isolating these complexes, it will be possible to study their properties in more detail and evaluate their catalytic performance in a controlled manner.

3. Expanded Investigation of PR_3 Ligands:

The study will expand as detailed in section 3.3.2 to investigate further the effects of different types of PR_3 ligands in the presence of varying concentrations of dppf. This investigation will help elucidate these ligands' role in the catalytic process and their impact on isobutanol yields.

4. Analysis of Solid and Gaseous Products:

Analysing the solid and gaseous by-products formed during the reactions will be essential. Understanding the nature and composition of these by-products will provide insights into the reaction pathways and help to optimise the reaction conditions for better selectivity and yield.

5. n-Butanol Production:

Future work will also explore the production of n-butanol using the most effective catalytic systems identified for isobutanol production. This will extend the catalysts' applicability and provide a broader understanding of their potential in alcohol production.

6. Investigation of Other Ferrocenylphosphines:

The study will also investigate other ferrocenylphosphines, such as 1,1'-bis(diisopropylphosphino)ferrocene (dippf) and 1,1'-bis(di-t-butylphosphino)ferrocene (dtbpf) (Figure 3-14), in isobutanol production. These ligands may offer different electronic and steric properties that could enhance catalytic performance.

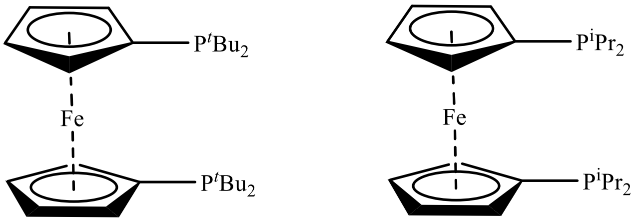

Figure 3-15: Other ferrocenylphosphine ligands to be investigated.

7. Exploring Alternative Metals:

Finally, changing the metal in the backbone from Fe to Ru or Co will be investigated to determine the possibility of enhancing isobutanol production. Substituting different metals may lead to new catalytic behaviours and improved efficiency. These future research directions aim to deepen our understanding of the catalytic processes and optimise the systems for higher yields and selectivity in isobutanol and n-butanol production. This continued research holds significant potential for advancements in green chemistry and sustainable biofuel production.

3.6. References:

[1] T. J. Kealy and P. L. Pauson, *Nature* **1951**, *168*, 1039-1040.

[2] R. Gómez Arrayás, J. Adrio and J. C. Carretero, *Angewandte Chemie International Edition* **2006**, *45*, 7674-7715.

[3] C. Nataro and S. M. Fosbenner, *Journal of Chemical Education* **2009**, *86*, 1412.

[4] P. Štěpnička, *Ferrocenes: Ligands, Materials and Biomolecules*, John Wiley & Sons, **2008**.

[5] D. J. Young, S. W. Chien and T. A. Hor, *Dalton Transactions* **2012**, *41*, 12655-12665.

[6] P. Dierkes and P. W. van Leeuwen, *Journal of the Chemical Society, Dalton Transactions* **1999**, 1519-1530.

[7] M. Albrecht and G. van Koten, *Angewandte Chemie International Edition* **2001**, *40*, 3750-3781.

[8] S. Koller, *Applications of Dehydrogenative and Borrowing Hydrogen Catalysis and Investigation of the Menthyl Grignard Reagent for the Synthesis of Chiral Phosphine Ligands*, Doctoral Dissertation, Technical University of Munich, **2019**.

[9] a) G. Centi and R. A. van Santen, *Catalysis for Renewables: from Feedstock to Energy Production*, John Wiley & Sons, **2007**; b) O. Kühl, *Phosphorus-31 NMR Spectroscopy: A Concise Introduction for the Synthetic Organic and Organometallic Chemist*, Springer Science & Business Media, **2008**.

[10] T. J. Colacot and S. Parisel, *Ferrocenes: Ligands, Materials and Biomolecules* **2008**, 117-140.

[11] C. Bianchini, A. Meli, W. Oberhauser, P. W. van Leeuwen, M. A. Zuideveld, Z. Freixa, P. C. Kamer, A. L. Spek, O. V. Gusev and A. M. Kal'sin, *Organometallics* **2003**, *22*, 2409-2421.

[12] M. Lamač, I. Císařová and P. Štěpnička, *New Journal of Chemistry* **2009**, *33*, 1549-1562.

[13] K. J. Pellow, R. L. Wingad and D. F. Wass, *Catalysis Science & Technology* **2017**, *7*, 5128-5134.

[14] J. F. Hartwig, *Organotransition Metal Chemistry: from Bonding to Catalysis*, University Science Books, **2010**.

[15] P. C. Kamer and P. W. van Leeuwen, *Phosphorus (III) Ligands in Homogeneous Catalysis: Design and Synthesis*, John Wiley & Sons, **2012**.

[16] C. Bruneau and P. H. Dixneuf, *Ruthenium in Catalysis*, Springer, **2014**.

[17] H. Colquhoun, J. Holton, D. Thompson and M. Twigg, *New Pathways for Organic Synthesis: Practical Applications of Transition Metals*, Springer Science & Business Media, **2012**.

[18] a) R. H. Crabtree, *The Organometallic Chemistry of the Transition Metals*, John Wiley & Sons, **2009**; b) C. A. Tolman, *Chemical Reviews* **1977**, *77*, 313-348.

[19] V. Cadierno, P. Crochet, J. Díez, S. E. García-Garrido, J. Gimeno and S. García-Granda, *Organometallics* **2003**, *22*, 5226-5234.

[20] B. Chin, A. J. Lough, R. H. Morris, C. T. Schweitzer and C. D'Agostino, *Inorganic Chemistry* **1994**, *33*, 6278-6288.

[21] R. L. Wingad, E. J. Bergström, M. Everett, K. J. Pellow and D. F. Wass, *Chemical Communications* **2016**, *52*, 5202-5204.

Chapter 4: Catalysis with Palladium Frustrated Lewis Pairs

4.1. Introduction

4.1.1. Lewis Acids and Bases

The Brønsted-Lowry theory categorises acids as substances that donate protons and bases as substances that absorb protons.[1] In 1923, Lewis proposed a novel categorisation of acids and bases, classifying them as electron pair acceptors and donors, respectively to provide a more comprehensive identification.[2] The LUMO of a Lewis acid interacts with the HOMO of a Lewis base by forming a bond with the lone pair of electrons. When a Lewis acid and a Lewis base are combined, they create a Lewis adduct (Figure 4-1A). For example, ammonia-borane (Figure 4-1B) is a well-known example of a Lewis adduct, where the lone pair on the nitrogen atom of ammonia is donated to the empty orbital on the boron atom of borane.[3]

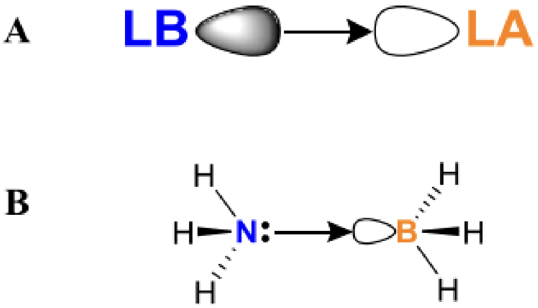

Figure 4-1: A) A schematic representation of a Lewis acid-base adduct; **B)** one of the simplest Lewis adducts ammonia-borane.

Since its original definition in 1923, reported systems have departed from Lewis's classification. In 1942, Brown *et al*. discovered that 2,6-lutidine can create a stable Lewis adduct with boron trifluoride (Scheme 4-1A).[4] Nevertheless, there was no discernible reaction when 2,6-lutidine was combined with trimethylboron, likely due to unfavourable steric interactions between the *ortho*-methyl groups of 2,6-lutidine and the methyl groups of trimethylborane. Wittig *et al*. documented the chemical reaction between triphenylphosphine and triphenylborane with benzyne, produced *in situ*, resulting in phosphonium borate **4.1** (Scheme 4-1B) about twenty years later.[5] While investigating organic ate-complexes, Tochtermann noted the occurrence of the trapping product **4.2** instead of the synthesis of polybutadiene.[6] Tochtermann used the term "antagonistiches paar" (translated as “antagonistic pair or couple”) to refer to a chemical that does not form traditional Lewis adducts. This study predates later work on so-called “frustrated” Lewis pairs by some 50 years.

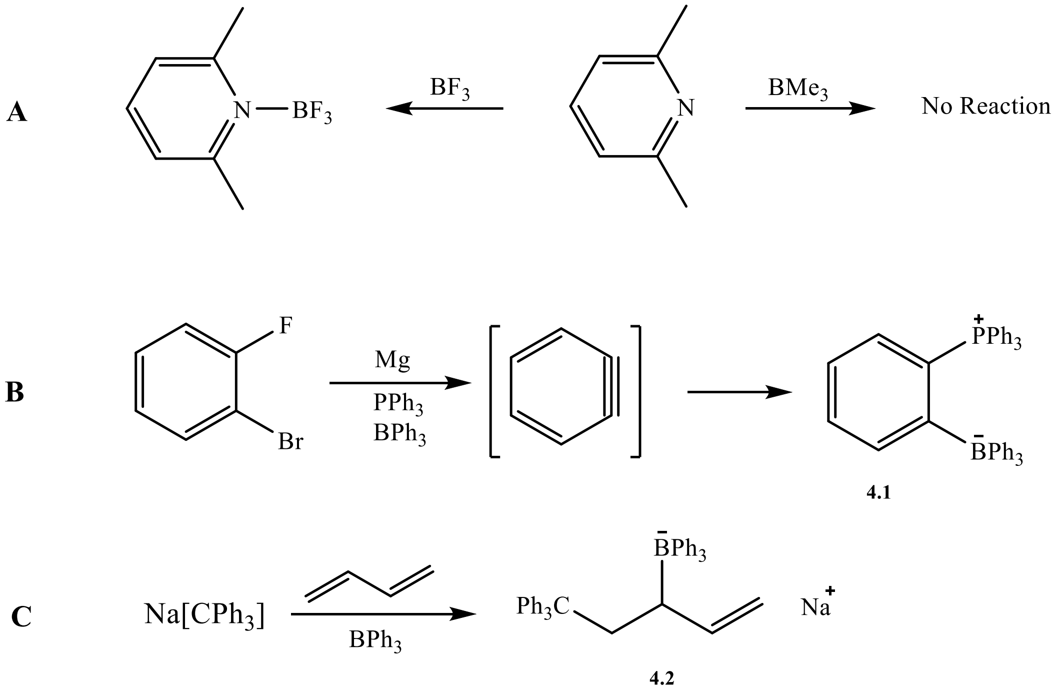

Scheme 4-1: A) Reaction of 2,6-lutidine with boranes reported by Brown *et al.*; B) Reaction of in situ generated benzyne with a phosphine and borane reported by Wittig; C) Formation of trapping product **4.2** by Tochtermann.

4.1.2. Frustrated Lewis Pairs

In 2006, Stephan *et al.* discovered the unexpected creation of zwitterion **4.3** during their investigation of phosphine-borane interactions. This synthesis occurred through the aromatic nucleophilic substitution of $B(C_6F_5)_3$ at the *para* position with the highly bulky phosphine Mes_2PH (Mes = 2,4,6-trimethylphenyl) (Scheme 4-2).[7] Erker *et al.* also made a similar observation in a related phosphine-borane system.[8] When compound **4.3** was treated with Me_2SiHCl, it formed zwitterion **4.4**, which consists of both hydridic and protic fragments. By subjecting **4.4** to heat, a significant alteration in the solution's colour occurred, changing it from colourless to orange-red. Additionally, the removal of H_2 was detected, resulting in the formation of species **4.5**. Significantly, this reaction exhibited reversibility, as the interaction between H_2 and **4.5** at ambient temperature resulted in the regeneration of **4.4**, representing the initial documented instance of reversible dihydrogen activation achieved exclusively by synthesising a system composed only of main group elements.

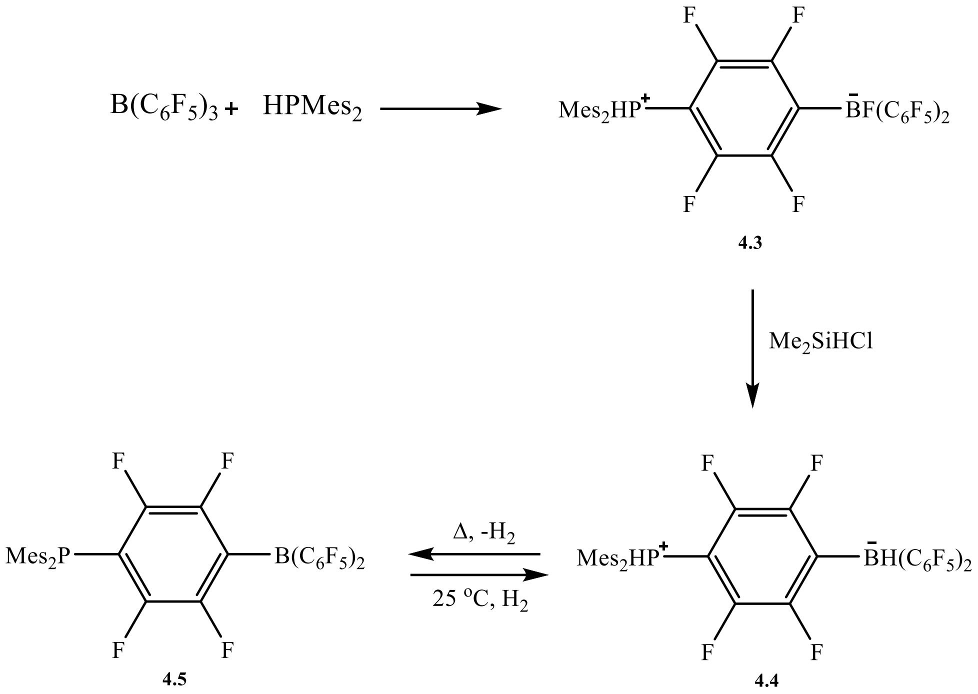

Scheme 4-2: Synthesis of zwitterion **4.4** and the reversible reaction with H_2.

Experimental evidence confirmed that phosphine-borane **4.5** exists as individual molecules in a solution, and the absence of aggregation can be attributed to the hindered spatial arrangement around the boron and phosphorus atoms.[7] Later on, this was identified as the initial instance of a 'frustrated Lewis pair' (FLP), a name coined in 2007 by Stephan while examining the reactivity of similar intermolecular phosphine-borane complexes with olefins.[9]

A frustrated Lewis pair is a type of Lewis pair that cannot engage in the typical donor-acceptor interactions because of the steric constraints surrounding the Lewis acidic and basic centres. This leads to a dormant, unfulfilled chemical reactivity of the Lewis pair that can be employed for various other reactions.[10]

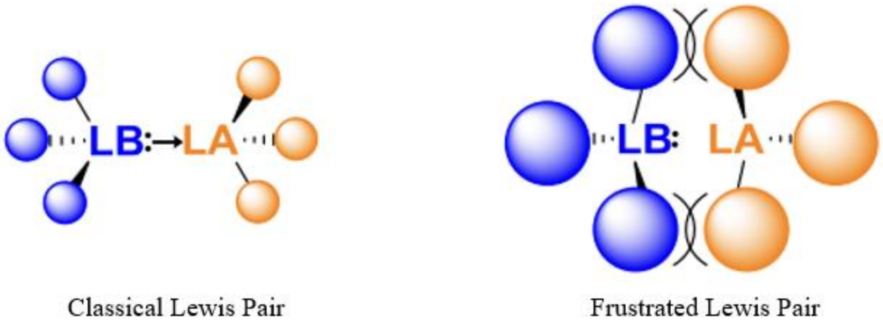

Figure 4-2: Schematic representation of a classical Lewis pair (left) and a frustrated Lewis pair (right).

4.1.3. Main Group FLPs and Small Molecule Activation

Initially, research on small molecule activation by FLPs mainly investigated systems of sterically hindered, electron-rich phosphines (such as P^tBu_3 and $PMes_3$) combined with a strongly Lewis acidic fragment, mainly $B(C_6F_5)_3$. These systems have demonstrated the ability to activate a range of small molecules under relatively mild conditions (Scheme 4-3).

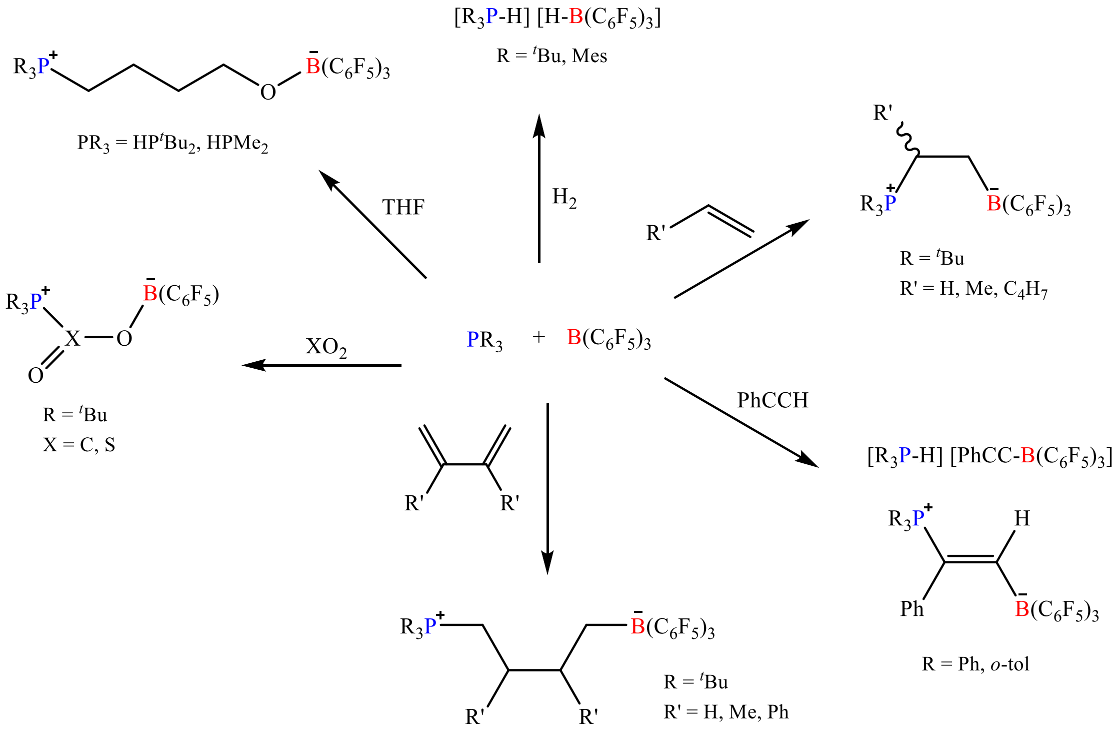

Scheme 4-3: Summary of small molecules activations by intermolecular FLP $PR_3/B(C_6F_5)_3$.

Following the first identification of reversible dihydrogen activation using phosphino-borane **4.5,** subsequent research efforts were directed towards studying a more straightforward intermolecular system involving $PR_3/B(C_6F_5)_3$. There was no apparent evidence of Lewis adduct formation for $PR_3/B(C_6F_5)_3$ (R = ^{t}Bu, Mes). However, the activation of H_2 at room temperature was facile.[11] Regrettably, it has been determined that this activation cannot be reversed. Various combinations of phosphines and boranes with lower Lewis acidity and basicity were tested, but these yielded limited effectiveness in activating dihydrogen. Dihydrogen activation was seen using P^tBu_3/BPh_3, although the H_2 heterolytic cleavage product yield was only 33%. Additionally, this reaction required much longer reaction durations than $PR_3/B(C_6F_5)_3$ (R = ^{t}Bu, Mes). This preliminary investigation showed that the needed reactivity could only be achieved by finding the optimal balance between sterics and electronics. The $PR_3/B(C_6F_5)_3$ system exhibited significant reactivity towards alkenes, forming 1,2-addition products with simple terminal alkenes[9] and 1,4-addition products with 1,3-dienes (Scheme 4-3).[12] Notably, the combination of $CH_2{=}(CH_2)_3PR_2$ (R = ^{t}Bu, Mes) and $B(C_6F_5)_3$ demonstrated the activation of an intermolecular alkene.[9] The reaction of $PR_3/B(C_6F_5)_3$ with alkynes is slightly more complex, as it involves two competing routes for the activation of PhCCH.[13] When P^tBu_3 is employed, deprotonation of the terminal alkyne is noticed. However, when PPh_3 and P(*o*-tol)$_3$ are utilised, the formation of the 1,2-addition product occurs, which was attributed to the relatively high basicity of P^tBu_3, which facilitates deprotonation rather than 1,2-addition. Similar reactivity was observed when substituting $B(C_6F_5)_3$ with $Al(C_6F_5)_3$.

The secondary phosphines $^tBu_2PH$ and Mes_2PH were demonstrated to initiate the opening of THF by attacking the activated α-carbon of the cyclic ether, following their first coordination to $B(C_6F_5)_3$ (Scheme 4-3).[14] The $PR_3/B(C_6F_5)_3$ system has demonstrated the ability to capture CO_2, requiring heating to 80 °C (with R = ^{t}Bu) to release the CO_2.[15] $PR_3/B(C_6F_5)_3$ underwent a fast reaction with SO_2, resulting in the formation of a product resembling the product obtained by CO_2 activation.[16] Nevertheless, the molecular structure analysis showed a deformed trigonal pyramidal geometry at the sulfur atom, which suggests the presence of chirality focused on the sulfur atom.

The intramolecular FLP $Mes_2P(CH_2)_2B(C_6F_5)_3$, connected by an ethylene bond, possesses Lewis acidic and Lewis basic centres, identical to the intermolecular system depicted in Scheme 4-3. Erker *et al*.

have thoroughly investigated the synthesis and reactivity of this interconnected P/B FLP, as shown in Scheme 4-4. The FLP is present in the solution as a suppressed four-membered cyclic intramolecular phosphine-borane,[17] which coexists in a condition of equilibrium with its 'open' form, which can then undergo further reactivity with small molecules.

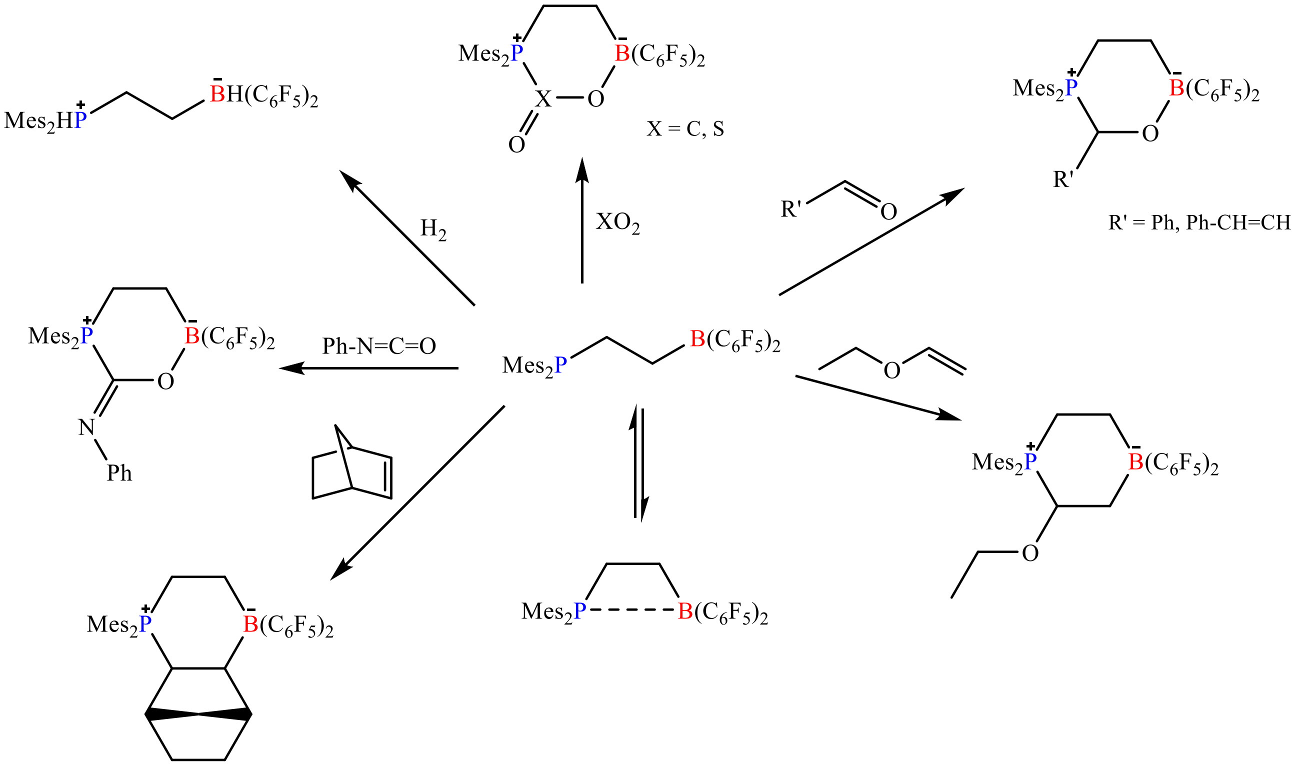

Scheme 4-4: Summary of small molecule activations by intramolecular FLP $Mes_2P(CH_2)_2B(C_6F_5)_2$.

This intramolecular FLP undergoes an irreversible reaction with H_2 at ambient temperature.[17] The activation of CO_2 was discovered to exhibit high reversibility, with the resulting product being relatively stable in solid form. However, in solution, CO_2 rapidly dissociates at temperatures over -20 °C.[15] The reaction with SO_2 at −78 °C resulted in a chiral product similar to the intermolecular FLP system.[16] The system underwent reactions between alkenes[18] and carbonyl compounds,[19] forming new P-C and B-O bonds in the products. The regiochemistry of these reactions followed the trend of bond formation. An intriguing finding was the activation of the carbonyl group in *trans*-cinnamic aldehyde relative to the alkene bond.

4.1.4. Transition Metal FLPs and Small Molecule Activation

Recent advancements in frustrated Lewis pair chemistry have involved substituting transition metals for main group elements as either the Lewis acidic or Lewis basic component. One advantage of utilising transition metals in FLP systems is the simplicity with which the characteristics of the metal system can be altered through straightforward synthetic ligand modification, which contrasts the complex techniques to alter the fluorinated boranes utilised in main group FLP chemistry. The reactivity of conventional transition metal complexes plays a crucial role in homogeneous catalysis and encompasses processes such as oxidative addition, reductive elimination, and migratory insertion. The possibility of creating new activation catalysts was anticipated by combining the reactivity of this transition metal with FLP systems.

Titanium and zirconium-based transition metal complexes have been extensively employed in homogeneous catalysis as Lewis acids to facilitate various synthetic reactions.[20] In 2011, Stephan *et al*. discovered a Lewis acidic zirconocene complex, $[Zr(Cp^*)_2(OMe)][B(C_6F_5)_4]$ (Cp* = pentamethylcyclopentadienyl), while studying Lewis acid exchange processes. They also found that when combined with the Lewis base P^tBu_3, this complex could activate N_2O.[21] This study did not test any additional small molecule activation.

In 2011, the Wass research group published a study on creating and using a range of intramolecular Zr^+/P FLP systems.[22] The systems utilised a zirconocene alkoxide complex that incorporated a Lewis basic phosphine group attached to the complex through a tether. The variations in the systems were achieved by altering either the cyclopentadienyl (Cp) rings or the substituents on the phosphine group (**4.6**, Scheme 4-5). There was no interaction between Zr and P in either the solution or the solid state. The complex was obtained as a chlorobenzene solvate, which was readily dissociated. This system demonstrated a range of small molecule activations, including common reactions in FLP chemistry (such as H_2, CO_2, and ethene) and more unusual activations such as alkyl halide linkages (Scheme 4-5).

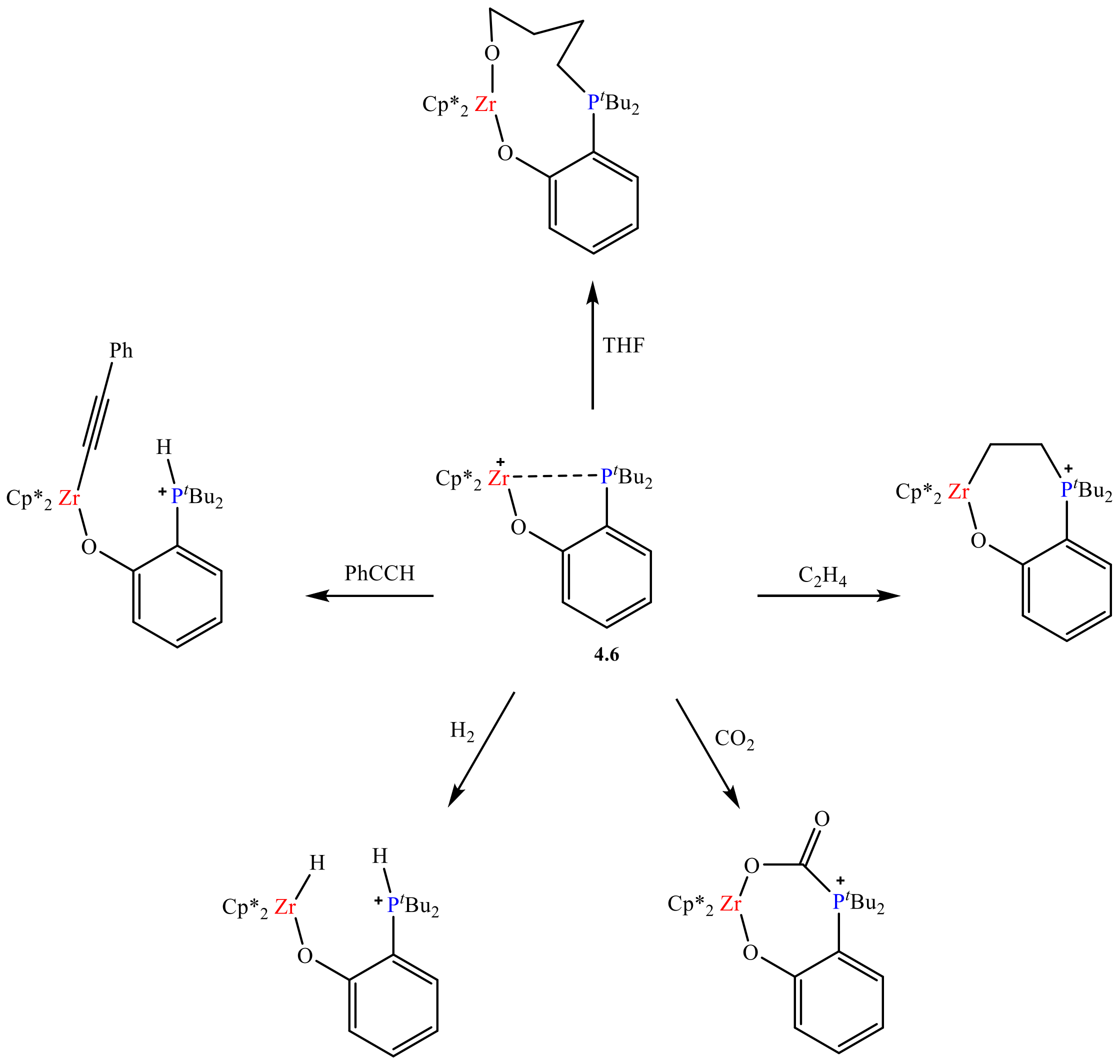

Scheme 4-5: Small molecule activations by intramolecular Zr^+/P Lewis pair **4.6**. $[B(C_6F_5)_4]^-$ omitted for clarity.

A noteworthy discovery was discovered regarding the activation of H_2. FLP **4.6** had a simple and permanent H_2 activation, but the Cp counterpart did not exhibit any reaction. A proposal was made to utilise ligands with higher electron density to boost the electron density at the Zr centre. This would facilitate the first binding of H_2, a required but temporary intermediary in the mechanism. The mixed Cp/Cp* analogue of **4.6** resulted in the reversible breaking of H_2 through heterolytic cleavage. The Zr^+/P FLP systems have also demonstrated activity in catalysing the dehydrogenation of certain amine-boranes.[22] The titanium analogue of **4.6** was synthesised and treated with hydrogen gas, reducing titanium(IV) to titanium(III). It was also demonstrated to work as a catalyst for dehydrogenating dimethylamine borane.[23]

4.1.5. Frustration vs. Cooperation

The phrase 'frustrated Lewis pair' refers to systems where the two Lewis components cannot form a traditional Lewis adduct. It is this unquenched reactivity that is utilised in the activation of small molecules. Nevertheless, numerous papers have shown the existence of both main group and transition metal systems called 'FLPs' that effectively activate small molecules. However, these systems also interact with the Lewis acidic and basic components. Figure 4-3 displays some instances of FLP systems in which an interaction between the Lewis centres has been detected.[17, 24]

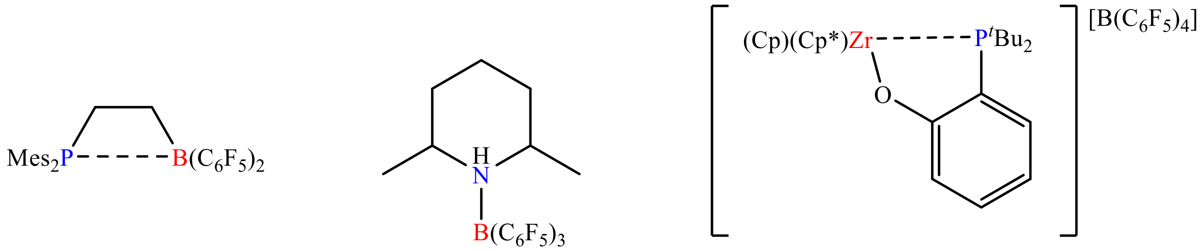

Figure 4-3: Selected examples of FLPs which shown an interaction between the Lewis centres.

The ability of a Lewis acid-base adduct to exhibit FLP reactivity was suggested to depend on the balance between the "open" and "closed" states of the system. Although a Lewis pair interaction is observed in these systems, they nonetheless display reactivity that aligns with the FLP paradigm. This raises doubts about the notion of a frustrated Lewis pair, leading to adopting a more appropriate term: 'cooperative Lewis pairs'. The synergistic interaction between the Lewis pair in activating small molecules was acknowledged, as the absence of either component would result in either a cessation of reactivity or the formation of different activation products.

4.2. Aims and Objectives

This research aims to deepen our understanding of Frustrated Lewis Pair (FLP) systems, a burgeoning field that has garnered significant interest among researchers. FLP systems, characterised by their unique reactivity and potential for catalysis, hold promise for advancing various chemical processes, particularly in small molecule activation.

A secondary objective of this study is to explore the activation of small molecules using FLP systems to gain an understanding of essential catalytic processes. However, this objective faced significant logistical challenges, notably the absence of the necessary gas system infrastructure at our research facility, which impeded our progress.

Research Objectives:

1. **Preparation of Bidentate Imine Ligands and Palladium Precursors:**
    - **Objective:** To prepare well-known bidentate imine ligands and palladium precursors to serve as foundational components for our research.
    - **Approach:** Employ established synthetic methods to produce these ligands and precursors, ensuring their purity and suitability for subsequent catalytic studies.
2. **Synthesis and Characterisation of Palladium Complexes:**
    - **Objective:** To synthesise palladium complexes and characterise them comprehensively.
    - **Approach:** Utilise a combination of Nuclear Magnetic Resonance (NMR) spectroscopy, Mass Spectrometry (MS), and X-ray crystallography to determine the structure and properties of these complexes.
3. **Application in Guerbet Reaction:**
    - **Objective:** To investigate the efficacy of the synthesised palladium complexes in the Guerbet reaction, focusing on their impact on isobutanol production.
    - **Approach:** Conduct a series of Guerbet reactions using the novel palladium complexes, systematically varying reaction conditions to optimise isobutanol yield and selectivity.

4.3. FLP-Mediated Catalysis in Guerbet Alcohol Production

In recent years, FLPs have gained significant attention for their ability to activate small molecules, including hydrogen and carbon dioxide, and their role in various catalytic transformations. Within Guerbet alcohol production, FLPs play a pivotal role by activating key molecules such as hydrogen, facilitating this process's essential steps.

The first stage of the Guerbet reaction involves dehydrogenating an alcohol to form an aldehyde. This transformation can be catalysed by an FLP system, where the Lewis base accepts a proton from the alcohol. At the same time, the Lewis acid coordinates with the oxygen atom, aiding in the cleavage of the O–H bond. This interaction leads to the formation of an aldehyde and the release of hydrogen. Subsequently, the aldehyde undergoes aldol condensation, a process catalysed by the base component of the FLP, forming a larger intermediate. Finally, the intermediate is hydrogenated into an alcohol, completing the Guerbet cycle. FLPs, mainly those adept at hydrogen activation, are vital in this final hydrogenation step, promoting the addition of hydrogen to the unsaturated intermediate and yielding the desired longer-chain alcohol.[25]

The FLP mechanism is highly promising due to its ability to activate hydrogen under mild conditions, eliminating the need for transition metal catalysts, which are conventionally employed in such reactions. The metal-free nature of FLPs offers a more sustainable and environmentally friendly alternative in catalytic processes like the Guerbet reaction.[26] Additionally, the steric and electronic flexibility of FLPs allows for fine-tuning to optimise performance in specific catalytic cycles, which may further enhance the selectivity and efficiency of Guerbet alcohol production.[27]

In conclusion, FLPs present a novel, metal-free approach to facilitating key steps in the Guerbet reaction, from alcohol dehydrogenation to the final hydrogenation. Their unique ability to activate hydrogen and other small molecules under mild conditions positions them as a promising alternative for sustainable alcohol upgrading.[26-27]

4.4. Preparation of Organic Ligand & Well-Known Palladium Precursors

Preparing well-established bidentate imine ligands, **L1** and **L2** (Figure 4-4), alongside palladium precursors forms a cornerstone of our research objectives. These components are essential for synthesising novel catalysts, as their extensive documentation in the literature provides a reliable foundation for ensuring experimental reproducibility.

The synthesis of **L1** and **L2** followed established protocols, fully supported by existing studies, to produce high-purity ligands suitable for complex formation. Similarly, standardised methods were be applied to prepare the palladium precursors, ensuring their effectiveness in catalytic applications.
Incorporating these ligands and precursors into our research enables the design and synthesis of new catalytic systems, enhancing synthetic efficiency and contributing to a deeper understanding of catalyst behaviour and performance.

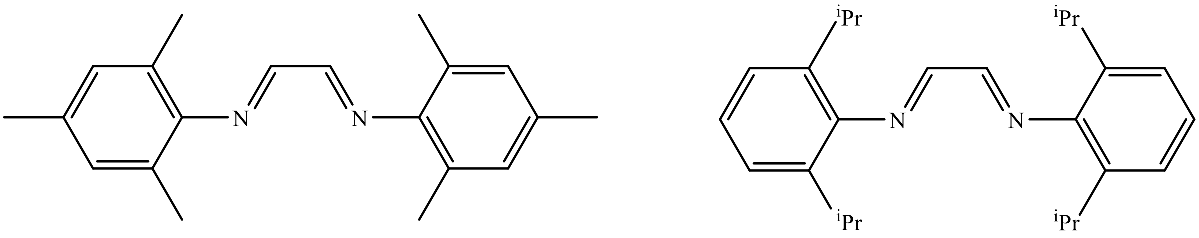

L1 **L2**

Figure 4-4: Organic ligands used in this chapter

Careful preparation of these organic ligands and well-known palladium precursors, with attention to detail and guidance from the literature, supports our goal to develop novel complexes. The insights gained from this work will offer valuable contributions to the evolving field of catalysis research.

4.4.1. Preparation of Ligands L1 and L2:

Scheme 4-6 details Ligands **L**1 and **L2** synthesis, following a protocol well-documented in the literature.[28] For **L1**, the synthesis employed 2,4,6-trimethylaniline (2 equivalents) and glyoxal in a 40% aqueous solution (1 equivalent) as starting materials. These reagents contributed to a stable reaction environment due to their air stability, enhancing the reliability of the synthesis. The reaction was conducted in a round-bottom flask at room temperature. A solvent mixture of methanol and water in a 2:1 volume ratio facilitated solubility and reaction kinetics. After a three-hour reaction time, the product was purified and recrystallised from pentane, achieving a high yield of 82.2%. Detailed NMR analysis of Ligand **L1**, which verifies its chemical structure and purity, is available in Chapter 5, Section 5.8.1.1. Ligand **L2** was synthesised using a similar procedure with minor adjustments to accommodate different starting materials: 2,6-diisopropylaniline (2 equivalents) and glyoxal (40% in H_2O). Reaction conditions and solvent systems remained consistent with those used for L1 to ensure reproducibility. After the reaction period, Ligand **L2** was purified, resulting in a yield of 72.4%. This methodical approach confirmed the synthesis process's reliability and provided ligands suitable for further catalytic applications. Chapter 5, Section 5.8.1.2 presents a comprehensive NMR analysis of Ligand **L2**, affirming its structure and purity.

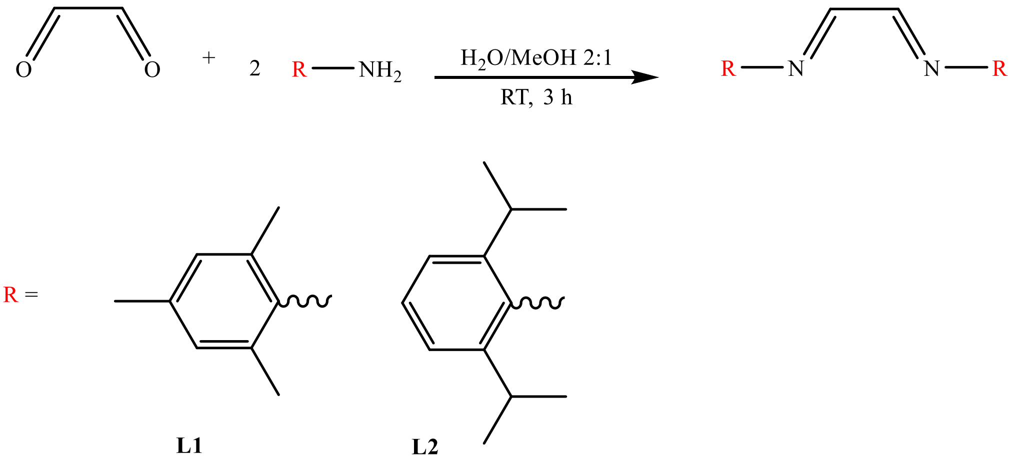

Scheme 4-6: Preparation of **L1** and **L2**

4.4.2. Synthesis of Pallidum Precursors:

4.4.2.1. Synthesis of [(COD)PdCl$_2$] (Pd1):

To develop a palladium precursor capable of effective coordination with the previously described organic ligands, the synthesis of [(COD)PdCl$_2$] (**Pd1**) was undertaken following a well-established protocol from the literature.[29] This approach involves the direct coordination of the palladium atom with the cyclooctadiene (COD) ligand. The materials selected for this reaction are notably air-stable, eliminating the need for a nitrogen atmosphere, thus simplifying the procedure.

The synthesis began by dissolving PdCl$_2$ in hydrochloric acid (HCl) while cooling the solution in an ice bath. Absolute ethanol was then introduced as a solvent, and the mixture was stirred for 15 minutes to ensure complete dissolution of the solid. After filtration, 1,5-cyclooctadiene (2.4 equivalents) was added to the filtrate, stirring for 20 minutes. The reaction mixture gradually changed colour to a characteristic orange, signalling the formation of the desired **Pd1** complex. After final filtration, the complex was obtained in a satisfactory yield of 81.2% (Scheme 4-7).

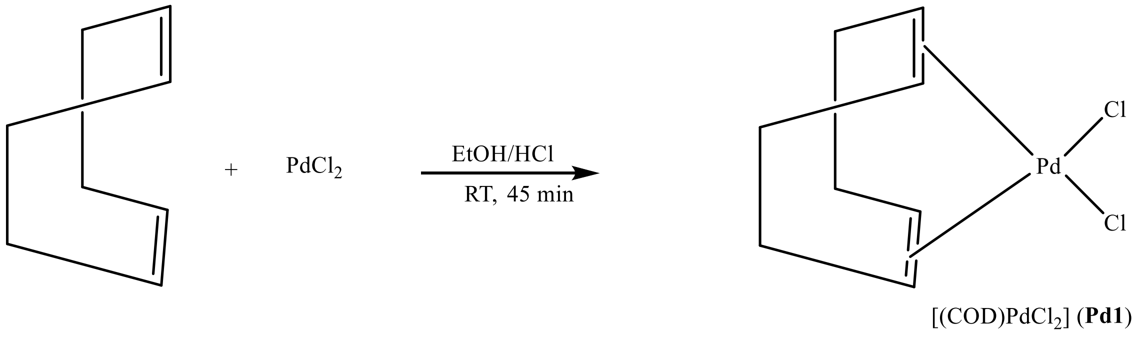

Scheme 4-7: Synthesis of **Pd1**

This straightforward synthesis method provides a practical, air-stable precursor for subsequent coordination studies and catalytic applications.

4.4.2.2. Synthesis of [(COD)PdMe]Cl (Pd2):

Rulke *et al*. established the following synthesis of [(COD)PdMe]Cl (Pd2).[30] This method began by dissolving 1 g of [(COD)PdCl$_2$] (**Pd1**) in dichloromethane (DCM) under a nitrogen atmosphere, ensuring an inert environment for the reaction. Tetramethyltin (1.2 equivalents) was added to the solution, gradually decolourising the mixture—a clear indicator of complex formation. The reaction was allowed to proceed overnight, followed by filtration through Celite to remove any by-products. After filtration, the solvent was removed under vacuum at 0°C, isolating the final product. The complex was then washed with diethyl ether (Et$_2$O) to purify it further, resulting in a high yield of 91.5%. For long-term stability and to prevent contamination, the final product should be stored in a freezer (Scheme 4-8).

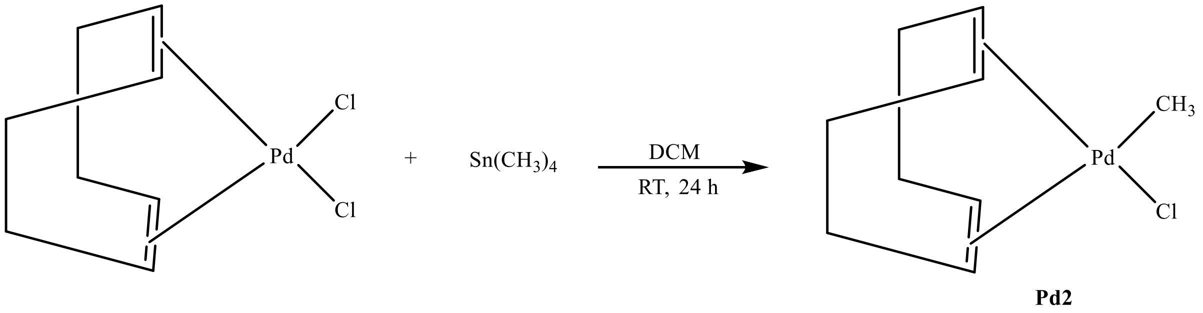

Scheme 4-8: Synthesis of [(COD)PdMe]Cl (**Pd2**)

The successful synthesis of **Pd2** was confirmed by the appearance of a distinct NMR signal at 1.12 ppm (s, 3H, Pd-CH$_3$), corresponding to the methyl protons directly bonded to the palladium centre. This signal is characteristic of the target complex and provides strong evidence of the methylation reaction's success. Chapter 5, Section 5.3.2.2. details the nuclear magnetic resonance (NMR) spectra.

The Celite filtration effectively removed unreacted tetramethyltin and tin-based by-products from the reaction mixture. Additionally, the purity of the product was further confirmed by the absence of tin-related signals in the NMR spectrum, which aligns with previously established methods for purifying palladium-tin complexes.[29] These steps ensured that the final **Pd2** complex was free from residual tin, supporting the synthesis's integrity and the final product's quality.

4.5. Synthesis of Palladium Complexes:

4.5.1. Synthesis of Complex 4.7

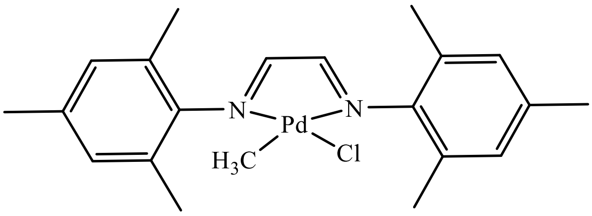

4.7

Complex **4.7** was synthesised following a procedure reported in Brookhart's patent, where its catalytic properties were documented, but no crystal structure was previously provided.[31] This synthesis aimed to confirm and characterise the structure of **4.7** by determining the metal coordination environment, including bond lengths, angles, and the identities of the coordinating moieties.

The synthesis involved reacting a palladium precursor **Pd2** with an excess of the bidentate diimine ligand **L1** under nitrogen in a well-prepared Schlenk flask to prevent contamination. After allowing the reaction to proceed overnight, the product was isolated by filtration, followed by washing with diethyl ether, yielding the final complex in a satisfactory 69.7% yield. The solvent choice proved crucial; dichloromethane (DCM) improved both solubility and yield compared to diethyl ether, enhancing the overall efficiency of the synthesis.

To elucidate the molecular structure of complex **4.7**, X-ray diffraction (XRD) analysis was performed. The crystal structure was obtained through a slow diffusion technique, where a concentrated solution of the product in dichloromethane (DCM) was carefully layered with hexane as a co-solvent. This setup allowed gradual crystallisation over a week at -18 °C. The single crystals produced were then analysed by X-ray diffraction (XRD), offering valuable details on the complex's molecular structure and coordination environment. The crystal structure revealed a square planar geometry around the palladium centre, coordinated by two nitrogen atoms from the diimine ligand, one methyl group, and one chloride ligand.

The PdN_2ClC coordination environment in Complex **4.8** is defined by notable bond lengths and angles characteristic of square planar palladium(II) complexes. The Pd–N bonds show slight asymmetry, with lengths of 2.183 Å and 2.044 Å, which is typical in such complexes and reflects subtle variations in ligand coordination. The Pd–Cl bond length measures 2.296 Å, while the Pd–C bond to the methyl group is slightly shorter at 2.020 Å, consistent with each coordinating ligand's steric and electronic demands.

The bond angles provide further insight into the geometry and strain within the complex. The N(1)–Pd–N(2) angle of 77.7° highlights the constraints imposed by the chelating diimine ligand, resulting in a deviation from the ideal 90° angle expected in an unstrained square planar environment. This bite angle reinforces the rigidity of the coordination sphere. The near-linear N(2)–Pd–Cl bond angle of 177.2° indicates a stable square planar arrangement, minimising steric interactions. The other angles within the coordination sphere, including N(1)–Pd–C at 173.1° and C–Pd–Cl at 87.3°, further support the overall stability of the complex.

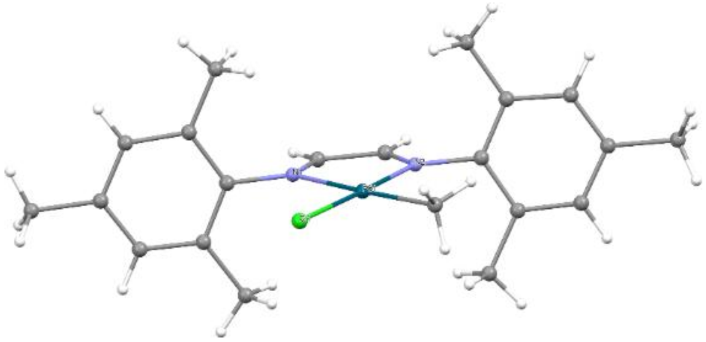

Figure 4-5: Crystal structure of Complex **4.7.** Selected bond lengths (Å) and angles (°): **Bond Lengths:** Pd–C 2.020(4); Pd–N(1) 2.183(3); Pd–N(2) 2.044(3); Pd–Cl 2.296(12). **Bond Angles:** N(1)-Pd-C 173.1(15); N(2)-Pd-Cl 177.2(9); N(1)-Pd-N(2) 77.7(11); C-Pd-Cl 87.3(14); C-Pd-N(2) 95.4(16); N(1)-Pd-Cl 99.5(8).

The X-ray analysis also confirmed the complex's calculated molecular mass of 449.9 g/mol. However, the mass spectrometry analysis did not observe a peak corresponding to the expected molecular mass. Instead, the presence of a base peak at *m/z* 397 suggests possible fragmentation during ionisation, with a stable fragment dominating the spectrum. Such fragmentation patterns are common in palladium complexes and indicate that the base peak does not necessarily represent the molecular ion but rather a stable ion generated from the complex.

The ^{1}H NMR data provided further structural insights, particularly regarding the coordination environment. The spectrum displayed two distinct singlets at δ 8.18 and 8.02 ppm, each corresponding to an HC=N proton. This splitting occurs because the complex's chelating diimine ligand lacks perfect symmetry around the palladium centre, leading to slightly different environments for each imine proton. Additionally, a singlet at δ 0.69 ppm corresponds to the Pd–CH_3 group, confirming the coordination of a methyl group to palladium.

The $^{13}C\{^1H\}$ NMR spectrum showed resonances at δ 162.8 and 158.6 ppm, corresponding to the C=N carbons of the diimine ligand, further confirming the ligand's coordination in the complex. Another notable peak at δ 2.2 ppm was observed, consistent with the Pd–CH_3 carbon. Chapter 5, Section 5.8.3.1. details the NMR spectra.

In summary, complex **4.7**, as originally synthesised following Brookhart's protocol, was successfully isolated and characterised with a previously unreported crystal structure. The structural confirmation via XRD, along with ^{1}H and ^{13}C NMR data and mass spectrometry, validates the coordination environment and molecular composition. These data affirm the successful synthesis of a stable palladium complex with a square planar geometry, further solidifying its potential as a robust precursor for catalytic applications.

4.5.2. Synthesis of Complex 4.8

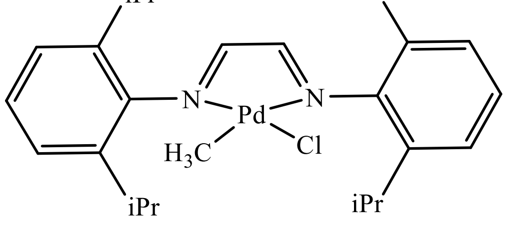

4.8

Complex **4.8** was synthesised following the protocol used for complex **4.7**, as described in the relevant literature.[31] In this synthesis, the precursor **Pd2** reacted with an excess of ligand **L2** under the same reaction conditions and the solvent system as previously used, ensuring consistency and enabling a direct comparison between the complexes. The yield of the final product was 67.1%, indicating a successful reaction under these optimised conditions.

The crystal structure of complex **4.8** was determined using the slow diffusion method, following a procedure similar to that of complex **4.7**. A concentrated product solution in dichloromethane (DCM) was layered with hexane as a co-solvent, allowing slow crystallisation over a week at -18 °C. X-ray diffraction (XRD) analysed the resulting single crystals, providing crucial insights into the complex's molecular arrangement and coordination environment. The structure revealed a square planar geometry around the palladium(II) centre, with coordination to two nitrogen atoms from the diimine ligand, one chloride ion, and one methyl group.

Key bond lengths and angles derived from the crystal data confirm complex **4.8**'s structural integrity. The Pd–N bonds were observed at 2.050 Å and 2.122 Å, highlighting the strong chelation offered by the diimine ligand, effectively stabilising the palladium centre. The Pd–Cl bond was measured at 2.356 Å, while the Pd–C (methyl) bond was 2.106 Å, consistent with typical bond lengths observed in palladium(II) complexes with comparable ligands.

The bond angles also reveal significant aspects of the coordination environment. The N(1)–Pd–N(2) bond angle of 79.5° reflects the structural constraints introduced by the chelating diimine ligand, slightly narrowing the angle due to the ligand's bite angle. The nearly linear bond angles, N(1)–Pd–Cl at 173.9° and C–Pd–N(2) at 176.1°, further support the stability of the square planar geometry, as they are close to the ideal 180°. Additionally, the Pd coordination sphere includes N(1)–Pd–C at 96.8° and N(2)–Pd–Cl at 95.5°, which are typical for square planar palladium complexes and contribute to the structure's overall stability.

These measured bond lengths and angles corroborate the coordination geometry expected for palladium(II) complexes, where the structural parameters align closely with similar reported complexes, enhancing the understanding of their stability and ligand interactions.

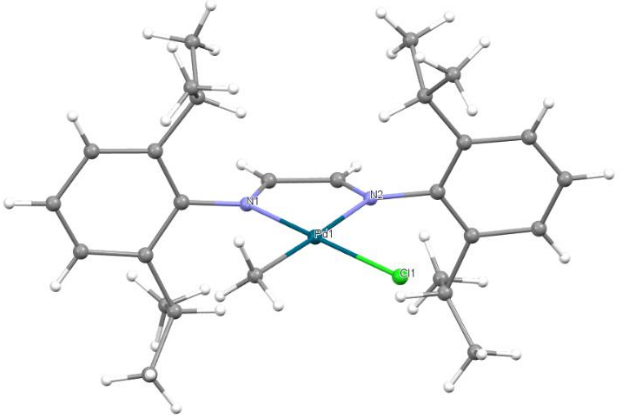

Figure 4-6: Crystal structure of Complex **4.8**. Selected bond lengths (Å) and angles (°): **Bond Lengths:** Pd–C 2.106(8); Pd–N(1) 2.050(6); Pd–N(2) 2.122(6); Pd–Cl 2.356(3). **Bond Angles (º):** N(1)-Pd-C 96.8(3); N(2)-Pd-Cl 95.5(18); N(1)-Pd-N(2) 79.5(2); C-Pd-Cl 88.1(3); C-Pd-N(2) 176.1(3); N(1)-Pd-Cl 173.9(2).

The mass spectrometry analysis, however, did not yield a peak corresponding to the expected molecular ion mass of 579.52 g/mol. Instead, the mass spectrum exhibited a prominent peak at approximately *m/z* 538.24, which suggests fragmentation during the ionisation process. This peak could result from losing specific ligands, producing a stable fragment ion that dominates the spectrum. Fragmentation of this nature is common in palladium(II) coordination complexes and suggests that the base peak may represent a stable ion generated from the complex rather than the intact molecular ion.

Further confirmation of the successful synthesis comes from NMR spectroscopy. In the ^{1}H NMR spectrum, two distinct peaks for the imine protons were observed at δ 8.20 and 8.04 ppm, corresponding to the HC=N groups. The presence of two separate peaks, rather than one, indicates a slight difference in the chemical environment of each HC=N proton, likely due to the cis configuration of the nitrogen atoms around the palladium centre. This asymmetry arises from the coordination geometry, where the nitrogen atoms are not equivalent due to their spatial arrangement relative to the other ligands. The methyl group attached to the palladium also appeared as a singlet at δ 0.77 ppm, a chemical shift consistent with a Pd–CH_3 moiety. In the $^{13}C\{^{1}H\}$ NMR spectrum, the Pd–CH_3 carbon was observed at δ 3.0 ppm, further supporting the presence of the methyl-palladium bond. Peaks at δ 162.8 and 158.6 ppm for the C=N carbons confirm the presence of the imine functionality and provide additional verification of the complex's identity. A thorough NMR examination is presented in Chapter 5, Section 5.3.3.2.

In summary, the structural and spectroscopic data confirm the successful synthesis of Complex **4.8**, with a square planar palladium(II) centre coordinated to a diimine ligand, a chloride, and a methyl group. The bond lengths and angles observed in the XRD analysis support the expected coordination environment, while the NMR data corroborate the structural assignment. Despite the absence of the exact molecular ion in mass spectrometry, the stable fragment ion at *m/z* 538.24 provides evidence of the complex's identity and typical fragmentation behaviour for palladium(II) complexes.

4.5.3. Synthesis of Complex 4.9

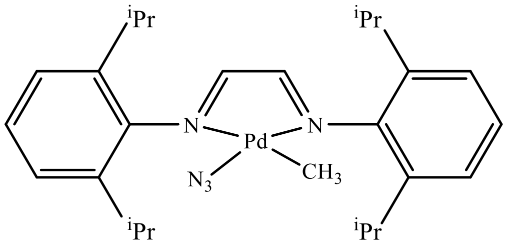

4.9

The synthesis of complex **4.9** represents a novel approach to modifying the coordination environment of the palladium centre by replacing the chloride ligand in complex **4.8** with a bulkier azide group. This substitution introduces steric and electronic modifications to the complex, potentially enhancing its stability and reactivity. The reaction was performed by treating complex **4.8** (1 equivalent) with sodium azide (1.3 equivalents) in dichloromethane (DCM) as a solvent. After an overnight reaction, complex **4.9** was successfully isolated with a moderate yield of 43.1%.

To confirm the molecular structure and coordination environment of complex **4.9**, identical crystallographic methodologies and solvent systems were employed to characterise complexes **4.7** and **4.8**. X-ray diffraction (XRD) analysis provided precise details of the coordination geometry, bond lengths, and bond angles, confirming the successful substitution of the chloride ligand with an azide group. The crystal structure for complex **4.9** revealed a molecular weight of 540.03 g/mol, aligning well with the theoretical expectations.

Key bond lengths and angles from the XRD analysis further characterise the coordination environment in complex **4.9**. The Pd–C bond to the methyl group measures 2.028 Å, while the Pd–N(1) and Pd–N(2) bonds in the diimine ligand measure 2.171 Å and 2.037 Å, respectively, indicating strong chelation by the diimine ligand. The Pd–N(3) bond length (from the azide group) is 2.025 Å, aligning with typical Pd–N bond lengths and confirming the azide's successful integration.

The bond angles around the palladium centre further support a square planar geometry, characteristic of palladium(II) complexes. The N(1)–Pd–C and N(2)–Pd–N(3) bond angles are 172.7° and 174.1°, respectively, reflecting a nearly linear arrangement that supports the stability of the square planar structure. The N(1)–Pd–N(2) angle of 77.8° indicates the expected strain introduced by the chelating diimine ligand. Additional angles, such as C–Pd–N(3) at 90.7°, C–Pd–N(2) at 95.1°, and N(1)–Pd–N(3) at 96.3°, contribute to the slightly distorted square planar geometry, shaped by the steric demands of the coordinated ligands.

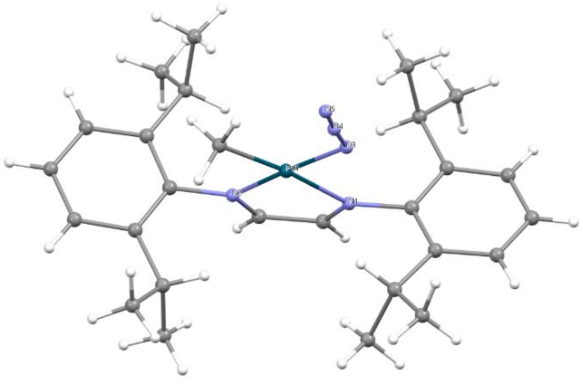

Figure 4-7: Crystal Structure of complex **4.9**. Selected bond lengths (Å) and angles (°): **Bond Lengths:** Pd–C 2.028(6); Pd–N(1) 2.171(4); Pd–N(2) 2.037(4); Pd–N(3) 2.025(5). **Bond Angles:** N(1)-Pd-C 172.7(2); N(2)-Pd-N(3) 174.1(2); N(1)-Pd-N(2) 77.8(16); C-Pd-N(3) 90.7(2); C-Pd-N(2) 95.1(2); N(1)-Pd-N(3) 96.3(19).

In the mass spectrometry analysis, the base peak observed at *m/z* 540.24 corresponds closely to the formula mass of complex **4.9**, supporting the successful synthesis of this complex. The presence of this peak, closely matching the calculated molecular weight, validates the composition and purity of the sample. The clear observation of *m/z* 540.24 in the spectrum provides strong evidence that complex **4.9** was synthesised as intended, further confirmed by the structural data.

The successful synthesis of complex **4.9** is further confirmed by ^{1}H and ^{13}C{^{1}H} NMR data. In the ^{1}H NMR spectrum, two singlets appear at δ 8.17 and 8.01 ppm, corresponding to the two HC=N protons in the diimine ligand. The observation of two distinct peaks for HC=N, rather than a single peak, suggests a slight asymmetry in the coordination environment, likely due to the presence of the bulky azide group, which influences the electronic environment around the palladium centre. The methyl group attached to the palladium is also seen as a singlet at δ 0.66 ppm, confirming its coordination. The ^{13}C{^{1}H} NMR spectrum shows a signal at δ 3.0 ppm for the Pd-CH3 carbon, further substantiating the coordination of the methyl group to palladium. Chapter 5, Section 5.3.3.3. contains a detailed examination of the NMR spectra for complex **4.9**.

The FTIR spectrum of complex **4.9** further supports the successful synthesis and coordination of the azide group. A sharp and intense absorption band observed at 2019 cm^{-1} corresponds to the N_3 stretch, characteristic of the azide functionality. The C=N stretch is seen at 1612 cm^{-1}, indicative of the diimine ligand. Additionally, a lower frequency band at 692 cm^{-1} is attributed to Pd–N bonding interactions, affirming the coordination of the azide and diimine ligands to the palladium centre.

In conclusion, combining crystallographic, NMR, MS, and FTIR data supports the successful synthesis and structural integrity of novel complex **4.9**. The substitution of chloride with an azide group is confirmed through XRD data, where bond lengths and angles are consistent with the expected square planar geometry. The NMR data reflect slight asymmetries in the coordination environment, consistent with a bulky azide group. The MS peak at *m/z* 540.24 aligns with the formula weight, while FTIR spectroscopy provides further evidence of the successful incorporation of the azide group. This comprehensive analysis underscores the novel and structurally sound synthesis of complex **4.9**.

4.5.4. Synthesis of Complex 4.10

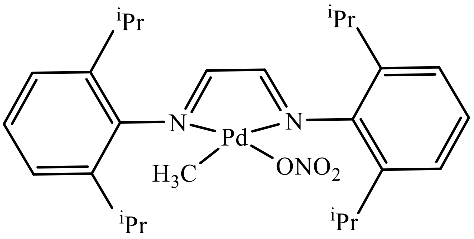

4.10

This synthesis demonstrates a novel approach, building upon the methodology used for complex **4.9**. In this experiment, complex **4.8** underwent an extended reaction with 1.3 equivalents of silver nitrate in dichloromethane (DCM) as the solvent, yielding complex **4.10** with a final product yield of 42.85%. The molecular structure and properties of complex **4.10** were characterised using X-ray diffraction (XRD) analysis, which provided crucial insights into its crystal structure, following the same methodologies and techniques in analysing the preceding complexes.

The crystal data reveal a complex with a Pd(II) centre coordinated with two nitrogen atoms from a diimine ligand, a methyl group, and a nitrate group. While the expected molecular formula, $C_{27}H_{39}N_3O_3Pd$, suggests a molecular weight of 560 g/mol, the crystallographic data indicated a different formula: $C_{30.5}H_{43}Cl_{0.56}N_{2.43}O_{1.3}Pd$, corresponding to a 590.1 g/mol molecular weight. This discrepancy suggests that some variability or inclusions were present in the crystal lattice, potentially involving co-crystallised starting materials or solvent molecules that might contribute additional weight.

The selected bond lengths and angles clearly show the unique coordination environment around the palladium centre in complex **4.10**, highlighting its structural characteristics. The Pd–C bond to the methyl group, measured at 2.098 Å, aligns well with typical palladium–carbon bonds in similar complexes, indicating a stable interaction between the metal centre and the alkyl group. The Pd–N bond lengths to the diimine ligand, recorded at 2.036 Å and 2.128 Å, suggest slight asymmetry within the coordination. This asymmetry is often observed in chelating ligands where the strain of the bidentate interaction creates subtle differences in bond distances, balancing electronic and steric demands at each nitrogen atom.

The Pd–O bond length of 2.035 Å, connecting palladium to the nitrate group, further illustrates the stability and strength of this interaction. The relatively short Pd–O bond suggests a strong coordination between palladium and nitrate oxygen, critical for maintaining the complex's square-planar geometry. This bond also indicates effective electronic donation from the nitrate oxygen to the palladium centre, stabilising the metal and supporting its catalytic potential.

An intriguing observation in the crystal structure of complex **4.10** is the presence of a Pd–Cl bond with a bond length of 2.345 Å. This suggests possibly including residual starting material, specifically complex **4.8**, within the crystal lattice. This Pd–Cl interaction implies that complex **4.8** may have co-crystallised with complex **4.10**, potentially stabilising the crystal lattice or affecting the molecular packing. Such inclusion could result from partial substitution or incomplete exchange of chloride for nitrate during synthesis. This phenomenon is common in metal-organic frameworks where crystal lattice stabilisation occurs through residual components.

The bond angles observed provide significant insights into its square-planar geometry, albeit with minor distortions influenced by ligand strain and steric factors. The nearly linear C–Pd–N(2) bond angle of 175.2° and the slightly bent O–Pd–N(1) angle of 163.1° support a predominantly planar coordination environment around the palladium centre, which is characteristic of its d^8 electronic configuration. The N(1)–Pd–N(2) bond angle of 78.7° reflects the strain exerted by the chelating diimine ligand, deviating from the ideal 90° expected in a square planar configuration and highlighting the rigidity inherent in the bidentate coordination. Additional angles, such as O–Pd–N(2) at 103.4° and O–Pd–C at 81.3°, indicate slight deviations from planarity, likely due to the bulkiness and spatial demands of the coordinated ligands. The N(1)–Pd–C bond angle of 96.8° illustrates the spatial adjustments needed to accommodate all ligands within the square planar framework. This demonstrates how steric factors and ligand rigidity contribute to the overall geometry.

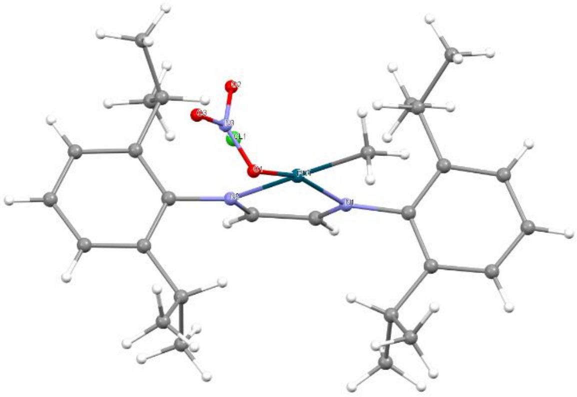

Figure 4-8: Crystal Structure of complex **4.10**. Selected bond lengths (Å) and angles (°): **Bond Lengths:** Pd-C 2.098(6); Pd-N(1) 2.036(4); Pd-N(2) 2.128(4); Pd-O 2.035(12); Pd-Cl 2.345(4). **Bond Angles:** O-Pd-N(1) 163.1(4); C-Pd-N(2) 175.2 (2); N(1)-Pd-N(2) 78.7(17); O-Pd(-N(2) 103.4(4); O-Pd-C 81.3(5); N(1)-Pd-C 96.8(2).

Mass spectrometry analysis provided further insights into the complex's structural composition. A prominent peak at *m/z* 540.24 was observed rather than the theoretical mass, indicating potential fragmentation during ionisation. The difference between the calculated and observed molecular weights could be due to fragmentation or the partial loss of coordinated ligands, which often occurs with palladium complexes. The discrepancy between the expected and crystallographic formulas suggests that residual starting materials or solvent molecules may be present within the crystal lattice, influencing the overall composition and mass distribution.

Further confirmation of the synthesis was obtained through NMR spectroscopy. In the ^{1}H NMR spectrum, two singlets at 8.19 and 8.04 ppm correspond to the two imine protons (HC=N), each integrating for one proton, indicative of the asymmetry introduced by the nitrate group. The presence of two distinct HC=N peaks rather than a single peak is attributed to the coordinating nitrate's subtle electronic and steric influences, which affect the chemical environment around each imine. Additionally, the signal at 0.77 ppm represents the Pd–CH_3 group, confirming the presence of the methyl ligand attached to palladium. The $^{13}C\{^{1}H\}$ NMR spectrum also shows a signal at 3.0 ppm, corresponding to the Pd–CH_3 carbon, further substantiating the successful incorporation of the methyl group. Chapter 5, Section 5.3.3.4 contains an in-depth examination of the NMR spectra.

The FTIR spectrum of complex **4.10** complements the structural and NMR analyses, providing additional insight into ligand coordination. The nitrate group (ONO_2) displays a characteristic stretch at

1273 cm^{-1}, indicating the N=O bond. N-O's bending or wagging modes were also observed at 795 cm^{-1}. The C=N stretch, representing the diimine ligand, was detected between 1616 cm^{-1}, while the Pd–O and Pd–N stretching vibrations appeared at 395 cm^{-1} and 480 cm^{-1}, respectively. These frequencies align with expected values for similar coordination environments, confirming the presence of nitrate and the diimine ligand around the palladium centre.

In summary, complex **4.10** demonstrates a successful chloride-to-nitrate substitution on a palladium centre, confirmed through a combination of XRD, NMR, FTIR, and MS analyses. The structural data reveal a Pd(II) centre coordinated in a square planar geometry, with the nitrate group and diimine ligand providing stabilising interactions. A Pd–Cl bond in the crystal structure implies partial retention of the starting material, complex **4.8**, possibly contributing to lattice stability. This study of complex **4.10** adds to the growing body of research on palladium complexes, showcasing their structural versatility and potential for functional modification through ligand substitution.

4.5.5. Synthesis of Complex 4.11

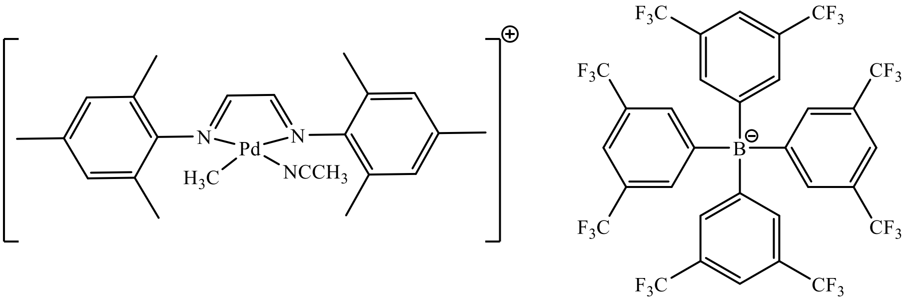

4.11

Complex **4.11**, although synthesised and mentioned in Brookhart's patent, lacked any previously reported crystal structure data.[31] This work aimed to modify complex **4.7** by substituting its chloride ligand with an acetonitrile moiety. The synthesis was done by reacting one equivalent of complex **4.7** with one equivalent of NaBArF$_{24}$ in a 1:1 mixture of diethyl ether (Et$_2$O) and dichloromethane (DCM). Subsequently, 1 mL of acetonitrile was introduced to the mixture, and the reaction proceeded for 3 hours. After completing the reaction, the solvent was removed, and the product was washed with 50 mL of pentane, resulting in a 69.9% yield. The BArF24 anion also contributed to the enhanced stability of the complex by providing steric protection.

The crystal structure of complex **4.11** was determined using X-ray diffraction (XRD) analysis, following the same procedures used for the previous complexes. Selected bond lengths and angles are consistent with the anticipated coordination environment. The methyl group's Pd–C bond length was observed at 2.037 Å, while the Pd–N distances to the diimine ligand were 2.017 Å and 2.133 Å, indicative of slight asymmetry often seen in such palladium complexes. The Pd–N bond to acetonitrile was measured at 2.010 Å, confirming effective coordination.

Bond angles further confirm the square planar geometry, albeit with minor distortions due to ligand strain. The N(3)–Pd–N(1) angle is close to linear at 172.2°, while the C–Pd–N(2) angle is similarly linear at 172.3°. The N(3)–Pd–N(2) angle of 92.9° and the N(1)–Pd–N(2) angle of 79.4° reflect the chelating nature of the diimine ligand, inducing slight deviations from ideal angles.

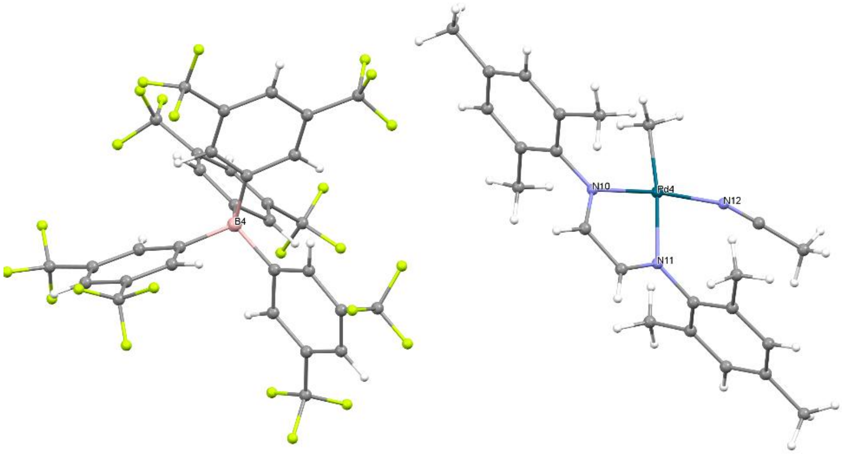

Figure 4-9: Crystal Structure of complex **4.11**. Selected bond lengths (Å) and angles (°): **Bond Lengths:** Pd-C 2.037(5); Pd-N(1) 2.017(4); Pd-N(2) 2.133(4); Pd-N(3) 2.010(4). **Bond Angles:** N(3)-Pd-N(1) 172.2(17); C-Pd-N(2) 172.3(2); N(3)-Pd-C 93.2(2); N(1)-Pd-C 94.5(19); N(3)-Pd-N(2) 92.9(17); N(1)-Pd-N(2) 79.4(16).

The NMR analysis corroborates the successful synthesis of complex **4.11**. The ^{1}H NMR spectrum shows singlet peaks at 8.13 and 7.63 ppm corresponding to the HC=N protons and the aromatic protons of the BArF$_{24}$ counterion, respectively. The methyl group on the Pd centre resonates at 0.62 ppm, confirming its presence. In the ^{13}C{^{1}H} NMR spectrum, the acetonitrile CH$_3$ appears at 29.8 ppm, and the Pd-CH$_3$ carbon at 6.8 ppm, further confirming the complex's structure. The ^{11}B NMR at 11 ppm and ^{19}F NMR at -62.6 ppm are consistent with the presence of the $BArF_{24}$ anion. To obtain an analysis of the NMR spectra for complex **4.11**, please see Chapter 5, Section 5.3.3.5.

Mass spectrometry analysis showed peaks corresponding to the expected molecular mass values for the palladium complex at *m/z* 454.15 and the counterion $BArF_{24}$ at *m/z* 863.07, validating the composition and confirming the integrity of both the cationic palladium species and the stabilising $BArF_{24}$ anion.

Complex **4.11** was synthesised by substituting the chloride in complex **4.7** with an acetonitrile ligand, achieving a 69.9% yield. The $BArF_{24}$ counterion enhanced stability, and X-ray diffraction confirmed the expected square planar geometry around palladium with slight distortions. NMR and mass spectrometry analyses verified the structure, with signals matching the methyl, acetonitrile, and $BArF_{24}$ components. Together, these results confirm the successful synthesis and stability of complex **4.11**.

4.5.6. Synthesis of Complex 4.12

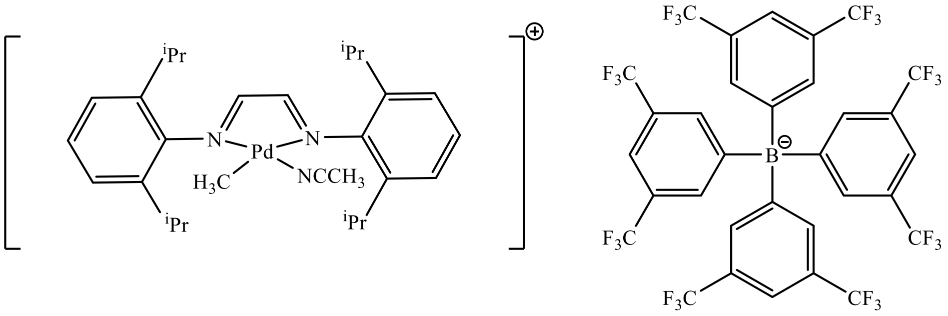

4.12

Complex **4.12** was synthesised based on the methodology outlined in Brookhart's patent, which describes using palladium complexes with $BArF_4^-$ counterions.[31] Although the specific crystal structure for this complex was not previously reported, it was prepared by reacting one equivalent of complex 4.8 with an equimolar amount of $NaBArF_4$ in 1 mL of acetonitrile, yielding a crystalline product with a moderate yield of 72.8%.

The crystal structure of complex **4.12** was obtained using the same solvent system and analytical methods applied to previous complexes. Critical structural data, such as bond lengths and angles, confirmed the coordination environment around the palladium centre and provided insight into the molecular geometry. The Pd–C bond to the methyl group measured 2.009 Å, while the Pd–N distances to the diimine ligand were observed at 2.030 Å and 2.135 Å. Additionally, the Pd–N bond to the acetonitrile was measured at 2.004 Å, supporting the successful incorporation of this ligand. The nearly linear angles N(3)–Pd–N(1) at 174.2° and C–Pd–N(2) at 173.6° reflect a square planar geometry around the palladium centre, with slight deviations due to ligand constraints. The smaller N(1)–Pd–N(2) angle at 78.1° highlights the strain introduced by the chelating diimine ligand. Additional bond angles, such as N(3)–Pd–C at 89.7°, N(1)–Pd–C at 95.6°, and N(3)–Pd–N(2) at 96.6°, further illustrate the spatial arrangement and minor distortions within the square planar coordination. These deviations likely result from steric interactions among the ligands, contributing to the overall stability of the complex.

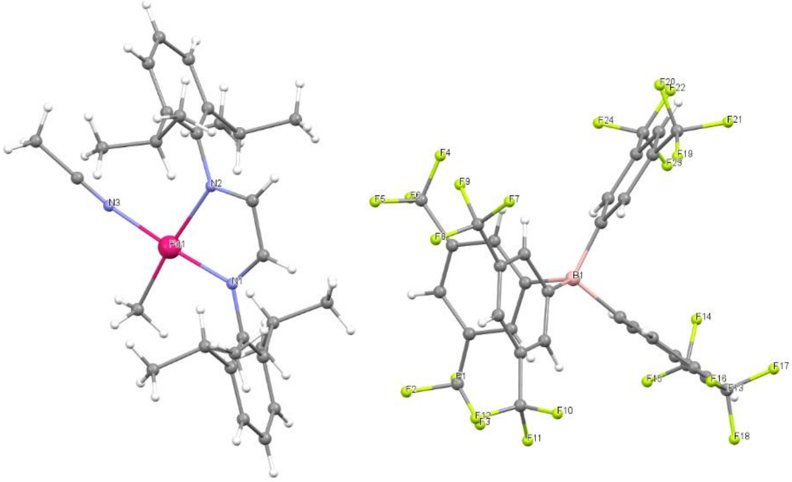

Figure 4-10: Crystal Structure of complex **4.12**. Selected bond lengths (Å) and angles (°): **Bond Lengths:** Pd(1)-C 2.009(3); Pd-N(1) 2.030(2); Pd-N(2) 2.135(2); Pd-N(3) 2.004(3). **Bond Angles:** N(3)-Pd-N(1) 174.2(11); C-Pd-N(2) 173.6(13); N(3)-Pd-C 89.7(14); N(1)-Pd-C 95.6(13); N(3)-Pd-N(2) 96.6(11); N(1)-Pd-N(2) 78.1(10).

NMR analysis further confirmed the successful synthesis of complex **4.12**. The ^{1}H NMR spectrum showed a doublet peak for the diimine backbone at 8.18 ppm, alongside resonances for the aromatic protons of $BArF4^{-}$ counterion at 7.63 and 7.47 ppm. The Pd-CH_3 signal appeared as a singlet at 0.74 ppm, indicating its coordination with the palladium centre. In the $^{13}C\{^{1}H\}$ NMR spectrum, the Pd-CH_3 resonance was found at 8.4 ppm, while the acetonitrile methyl group appeared at 30.0 ppm. Furthermore, the ^{11}B and ^{19}F NMR spectra displayed signals at 11 ppm and -62.6 ppm, respectively, consistent with the presence of the $BArF4^{-}$ counterion. The NMR spectra for complex **4.12** are thoroughly analysed in Chapter 5, Section 5.3.3.6.

Mass spectrometry analysis corroborated the expected structure, with peaks at *m/z* 538.24 for the palladium complex and *m/z* 863.07 for the BArF4$^-$ counterion, which aligned well with the calculated masses. These findings confirm the successful synthesis, stability, and structural integrity of complex **4.12**, underscoring its potential suitability for further applications.

4.5.7. Synthesis of Complex 4.13

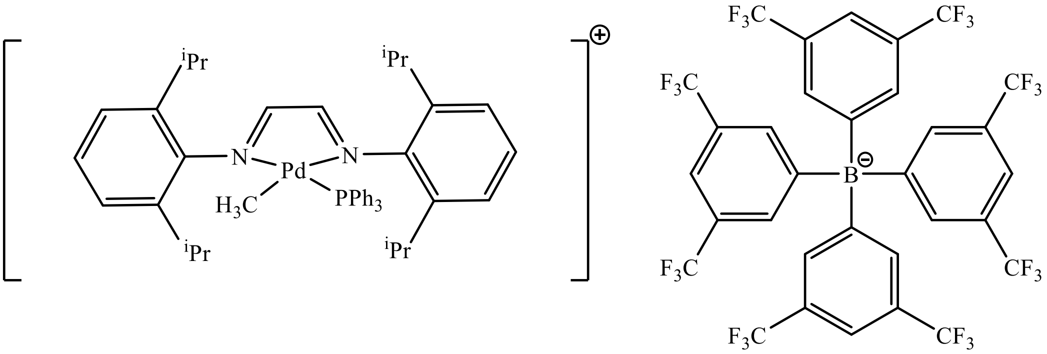

4.13

Complex **4.13** represents a novel synthesis, where an acetonitrile ligand from previous complexes is successfully replaced by the monodentate phosphine ligand, triphenylphosphine (PPh_3). This substitution was prompted by the weak coordination of acetonitrile, which is easily displaced, enabling the coordination of more robust ligands. Numerous attempts were made to incorporate other phosphine ligands into related complexes. However, stable coordination with palladium was uniquely achieved using PPh3, which resulted in a stable, novel coordination complex with complex **4.12**, giving rise to complex **4.13**.

The synthesis involved reacting complex **4.12** (1 equivalent) with PPh_3 (1.2 equivalents) in dichloromethane (DCM) at room temperature, allowing the reaction to proceed overnight. The solvent was removed Post-reaction, and the product was washed with 50 mL of pentane to eliminate impurities, yielding 69.1%. The structure of complex **4.13** was confirmed through X-ray diffraction (XRD) analysis, using consistent methodologies and solvent conditions as those applied to the previous complexes.

The crystal structure (Figure 4.12) of complex **4.13** exhibits a square planar geometry around the palladium centre, indicative of its d8 electronic configuration. Key bond lengths provide insights into the ligand interactions with palladium. The Pd–C bond, linking palladium to the methyl group, was measured at 2.037 Å, typical of palladium-methyl interactions. The Pd–N bonds to the diimine ligand show slight asymmetry, with Pd–N(1) at 2.122 Å and Pd–N(2) at 2.205 Å, revealing the constraints imposed by the chelating ligand. The Pd–P bond length of 2.248 Å reflects the successful coordination of the PPh3 ligand, consistent with known palladium-phosphine interactions.

The bond angles further characterise the geometry, indicating minor deviations due to steric influences from the coordinated ligands. The nearly linear P–Pd–N(1) angle of 172.9° and C–Pd–N(2) angle of 166.9° reflect a largely planar arrangement around palladium. The smaller N(1)–Pd–N(2) angle of 76.3° results from the chelation of the diimine ligand, imposing a degree of strain on the coordination sphere. Other angles, including P–Pd–C at 83.3°, N(1)–Pd–C at 90.6°, and P–Pd–N(2) at 109.8°, illustrate slight distortions, likely due to steric bulk from the phosphine and diimine ligands.

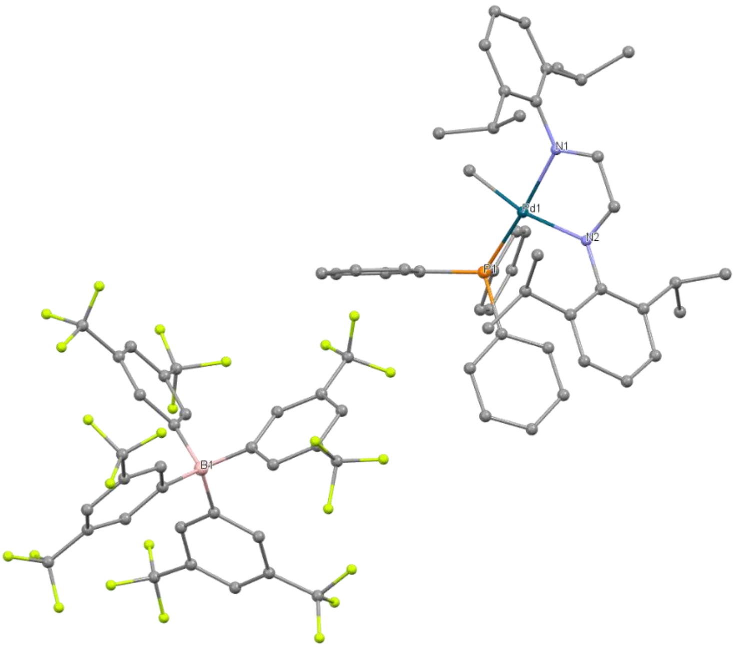

Figure 4-11: Crystal Structure of complex **4.13**. Selected bond lengths (Å) and angles (°): **Bond Lengths:** Pd-C 2.037(3); Pd-N(1) 2.122(18); Pd-N(2) 2.205(18); Pd-P 2.248(6). **Bond Angles:** P-Pd-N(1) 172.9(6); C-Pd-N(2) 166.9(9); P-Pd-C 83.3(8); N(1)-Pd-C 90.6(10); P-Pd-N(2) 109.8(5); N(1)-Pd-N(2) 76.3(7).

NMR data provides additional verification of the successful synthesis and stability of complex **4.13**. The ^{1}H NMR spectrum displays signals at 8.40 and 8.18 ppm, corresponding to the imine protons (HC=N) in the diimine ligand, while a singlet at 0.74 ppm confirms the presence of the Pd–CH_3 group. The $^{13}C\{^1H\}$ NMR spectrum corroborates this with a Pd–CH_3 carbon signal at 9.0 ppm. In the $^{31}P\{^1H\}$ NMR spectrum, a singlet at 37.8 ppm verifies the coordination of PPh_3 to palladium. Additional peaks in the ^{11}B NMR at 7 ppm and ^{19}F NMR at -62.6 ppm confirm the presence of the $BArF_{24}^-$ counterion, which is consistent with the structure and formulation of the complex. Complete results of the NMR examination can be found in Chapter 5, Section 5.3.3.7.

Mass spectrometry (MS) analysis further supports the composition of complex **4.13**. The expected molecular ion peak for the palladium complex appeared at *m/z* 759.31, while the $BArF_{24}^-$ counterion peaked at *m/z* 863.07. These peaks align with the anticipated mass-to-charge ratios, confirming the formulation and stability of complex **4.13**.

In summary, complex **4.13** is a novel palladium complex with acetonitrile replaced by PPh_3, yielding a stable square planar geometry. Key bond lengths and NMR data confirm the expected coordination environment. Mass spectrometry verified the structure with peaks at *m/z* 759.31 for the complex and *m/z* 863.07 for the $BArF_{24}^-$ counterion, affirming successful synthesis and structural integrity.

4.6. Investigating Isobutanol Production with Palladium FLP Complexes

Table 4-1 provides an overview of the performance of the complexes synthesised in the previous section (refer to Section 4.4). Each complex was tested for its efficacy in upgrading methanol and ethanol to isobutanol. The data indicate that all entries exhibited excellent selectivity for isobutanol; however, the yield was lower than anticipated.

The gas chromatography (GC) analysis revealed the presence of minor by-products, such as *n*-propanol and *n*-hexanol, albeit in minimal quantities. In contrast, no solid or gaseous by-products were detected across all tested entries.

The observed high ethanol conversion alongside low isobutanol yield and minimal detection of by-products can be attributed to a combination of factors inherent to the Guerbet reaction and catalytic process. First, confident intermediates, like acetaldehyde, may decompose or volatilise under reaction conditions, leading to their loss before progressing to isobutanol. Additionally, the Guerbet pathway includes reversible steps, such as alcohol dehydrogenation and aldol condensation, which, if favoured in reverse, could limit the overall progression towards the target product. Catalyst deactivation may further reduce reaction efficiency, causing incomplete transformation of intermediates. Some by-products, being volatile or in low concentrations, may escape detection via GC analysis, while "recycling" of ethanol and intermediates without efficient progression can create the appearance of high ethanol consumption with low isobutanol yield. Thus, a combination of intermediate volatility, reaction equilibria, potential catalyst deactivation, and analytical limitations likely contributes to the observed results.

Table 4-1: Yield and selectivity of liquid products and ethanol conversion achieved with complexes **4.7** to **4.13**.

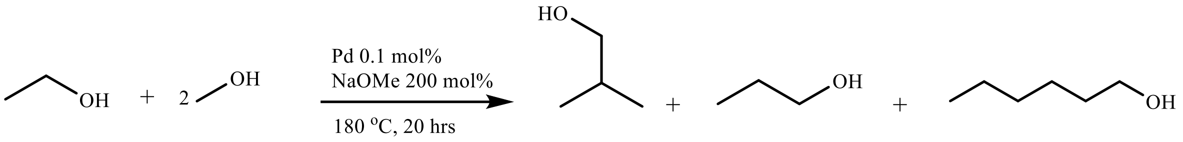

Entry[a]	**Complex**	**Ethanol Conversion (%)**[b]	**Yield**[c] **(TON)**[d] **[Selectivity] (%)**			**Carbon Balance (%)**[e]	**Missing Carbon (%)**[f]
			Isobutanol	***n*-Propanol**	***n*-Hexanol**		
1	**4.7**	33.5	6.4 (21.5) [96.5]	0 [0]	0.7 (2.3) [3.5]	16.3	83.7
2	**4.8**	48.3	4.9 (23.7) [100]	0 [0]	0 [0]	9.7	90.3
3	**4.9**	42.7	6.7 (28.8) [98.7]	0 [0]	0.3 (1.3) [1.3]	15.5	84.5
4	**4.10**	39.7	4.6 (18.3) [100]	0 [0]	0 [0]	7.8	92.2
5	**4.11**	44.3	1.8 (8.0) [93.1]	0.4 (1.8) [6.9]	0 [0]	4.4	95.6
6	**4.12**	38.1	3.1 (11.9) [95.2]	0 [0]	0.5 (1.9) [4.8]	9.9	90.1
7	**4.13**	57.4	8.2 (46.8) [96.4]	0 [0]	0.4 (2.3) [3.6]	9.6	90.4

[a] Conditions: ethanol (0.75 mL, 12.8 mmol), methanol (7.5 mL, 185.15 mmol), Pd (0.0128 mmol, 0.1 mol%), NaOMe (34.26 mmol, 200 mol%), 20 hours, 180 °C, mol% relative to ethanol. [b] Conversion of ethanol based on total number of liquid products obtained as determined by GC analysis. [c] Total yield and selectivity of Guerbet products in the liquid fraction as determined by GC analysis. [d] TON based on mmol of ethanol converted to products per mmol Ru. [e] **Carbon Balance %:** the percentage of initial carbon in ethanol detected in the products. Ideally close to 100%, indicating accurate accounting of all ethanol-derived carbon atoms. [f] **Missing Carbon:** any carbon discrepancy, indicating undetected carbon potentially due to side products, volatiles, or experimental losses.

Table 4-2 illustrates the impact of introducing the palladium complexes **4.9** and **4.13** to **Ru1** and **Ru3** in the presence of dppf and **PL1** (Figure 4-12). This section will delve into the different insights garnered from the production of isobutanol using these catalytic systems.

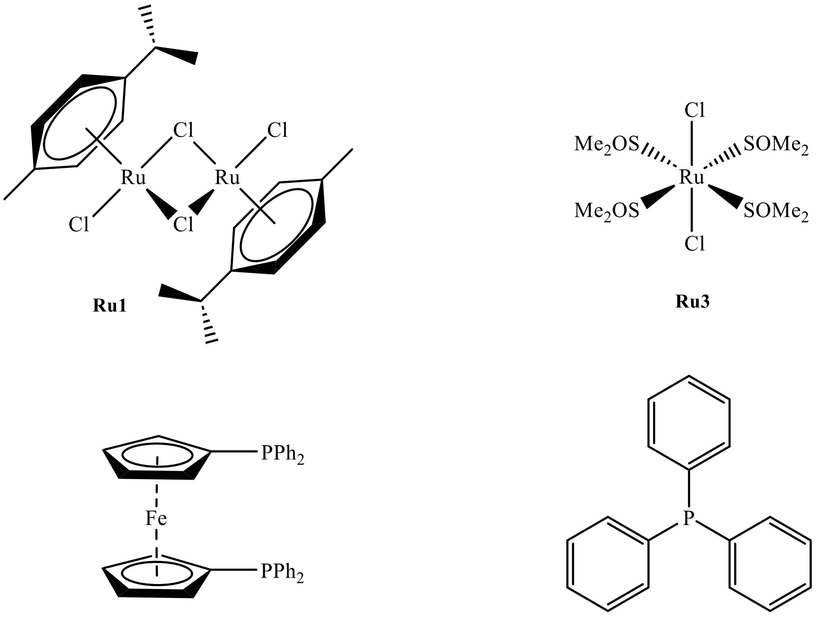

Ru1

Ru3

dppf

PL1

Figure 4-12: Ligands and Ru catalysts used in this chapter.

The rationale for selecting complexes **4.9** and **4.13**, alongside **Ru1** and **Ru3**, stems from the availability constraints encountered during the research. Most of the synthesised palladium complexes (refer to Section 4.4) were utilised via the slow diffusion method in the crystallisation process. Consequently, **4.9** and **4.13** were the most readily available for this test. Additionally, **Ru1** and **Ru3** were chosen due to the depletion of **Ru2** during earlier stages of the research and subsequent supply issues.

In this study, the introduction of 0.1 mol% of complexes **4.9** and **4.13** separately to 0.1 mol% of **Ru1** in the presence of 0.3 mol% of **PL1** (entries 1 and 2) enhanced isobutanol yield, increasing from 42.8% to 50.5% and 58.1%, respectively (refer to Chapter 2, Section 2.5.1). The notable increase in yield observed in entry two is likely attributed to the presence of the PPh_3 group in complex **4.13**.

Further experimentation involved testing 0.1 mol% of **Ru1** with 0.1 mol% of complexes **4.9** and **4.13** separately in the presence of 0.2 mol% of dppf. Compared to previous studies (refer to Chapter 3, Section 3.3.1), complexes **4.9** and **4.13** reduced the isobutanol yield from 58.1% to 36.9% and 42.6%, respectively (entries 3 and 4). Similarly, when 0.1 mol% of complexes **4.9** and **4.13** were added separately to 0.1 mol% of Ru**3** in the presence of 0.2 mol% dppf, a significant reduction in isobutanol yield was observed, dropping from 80% to 55.6% and 57%, respectively (entries 5 and 6).

Entries 3 through 6 exhibited high isobutanol selectivity, potentially due to the influence of dppf, while entries 1 and 2 demonstrated lower isobutanol selectivity. The GC analysis revealed the presence of minor by-products such as *n*-propanol and *n*-hexanol, with entries 1 and 2 displaying a slight, unusual increase in these by-products; however, no solid or gaseous by-products were detected across all entries. This study highlights the nuanced effects of combining various palladium complexes with Ru-based systems in the presence of different ligands. The results underscore the potential for tuning catalytic systems to optimise isobutanol production, though further research is needed to fully understand the underlying mechanisms and enhance yield and selectivity.

Table 4-2: Yield and selectivity of liquid products and ethanol conversion achieved with catalysts **Ru1** and **Ru3**, and complexes **4.9** and **4.13** in the presence of dppf and **PL1**

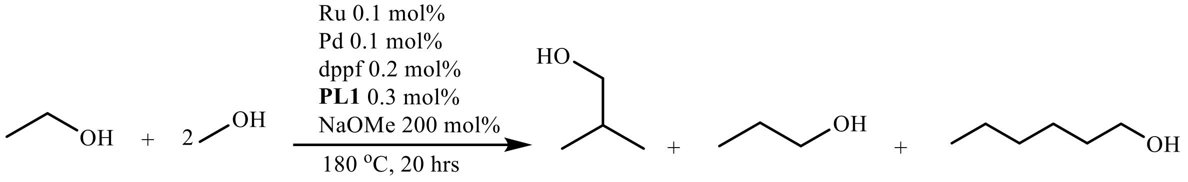

Entry [a]	**Ru/Pd**	**Ligand (n) mol%**	**Ethanol Conversion (%)** [b]	**Yield** [c] **(TON)** [d] **[Selectivity] (%)**			**Carbon Balance (%)** [e]	**Analysis Error (%)** [f]
				Isobutanol	***n*-Propanol**	***n*-Hexanol**		
1	**Ru1 & 4.9**	(3) **PL1**	71.6	50.5 (180) [85.4]	4.1 (16) [6.9]	10.6 (39) [7.7]	139.1	39.1
2	**Ru1 & 4.13**	(3) **PL1**	75.1	58.1 (219) [89.2]	3.1 (12) [4.7]	9.8 (35) [6.1]	150.0	33.4
3 [g]	**Ru1 & 4.9**	(2) dppf	69.2	36.9 (129) [95.3]	1.5 (4) [4.0]	0.9 (4) [0.8]	79.2	-
4 [h]	**Ru1 & 4.13**	(2) dppf	82.8	42.6 (176) [96.8]	1.1 (4) [2.6]	0.9 (4) [0.6]	89.2	-
5	**Ru3 & 4.9**	(2) dppf	89.8	55.6 (250) [93.8]	2.5 (12) [4.2]	3.2 (16) [2.0]	125.7	11.4
6	**Ru3 & 4.13**	(2) dppf	90.7	57.0 (258) [94.1]	2.3 (12) [3.8]	3.3 (16) [2.0]	128.0	10.4

[a] Conditions: ethanol (0.75 mL, 12.8 mmol), methanol (7.5 mL, 185.15 mmol), Pd (0.0128 mmol, 0.1 mol%), Ru (0.0128 mmol, .0.1 mol%) dppf (0.0256 mmol, 0.2 mol%), **PL1** (0.0384 mmol, 0.3 mol%), NaOMe (34.26 mmol, 200 mol%), 20 hours, 180 °C, mol% relative to ethanol. [b] Conversion of ethanol based on total number of liquid products obtained as determined by GC analysis. [c] Total yield and selectivity of Guerbet products in the liquid fraction as determined by GC analysis. [d] TON based on the mmol of ethanol converted to products per total mmol of metal complexes (Ru and Pd), not per individual metal centres. [e] **Carbon Balance %:** the percentage of initial carbon in ethanol detected in the products. Ideally close to 100%, indicating accurate accounting of all ethanol-derived carbon atoms. [f] **Analysis Error %:** an estimated measure of uncertainty in the analytical method, reflecting potential deviations from ideal values due to instrument limitations or procedural inaccuracies. [g, h] **Missing Carbon %** = 20.8 and 10.8 respectively.

4.7. Conclusion

In conclusion, Chapter 4 has explored the synthesis, characterisation, and structural analysis of various novel palladium complexes, demonstrating innovative modifications to enhance their stability, coordination environments, and potential catalytic applications. Using a range of ligands, including imines, phosphines, and nitriles, the chapter elucidates how different coordinating moieties influence the geometry and electronic properties of the palladium centre. The structural data, supported by crystal structures and spectroscopic analysis (NMR, MS, and FTIR), confirm the successful synthesis of each complex, showcasing diverse coordination behaviours such as square-planar geometry.

The investigation reveals that ligand bulk and electronic properties significantly affect the complexes' bond lengths, angles, and stability. Additionally, the results highlight the impact of certain counterion, such as $BArF_4^-$, in stabilising the structures and maintaining structural integrity. The high ethanol conversions observed in catalytic studies, albeit with low isobutanol yields and minimal by-products, underscore the need to optimise catalytic conditions further to maximise product yield and selectivity. This chapter lays a robust foundation for future exploration of these complexes in catalytic transformations, contributing valuable insights to organometallic chemistry.

4.8. Future Work

Future work will build on this research by deepening the investigation into palladium complexes with several key objectives. First, a systematic purification of all synthesised palladium complexes will be undertaken, wherever needed, followed by comprehensive analysis using advanced techniques such as High-Resolution Mass Spectroscopy (HRMS) to clarify molecular structures and ensure high purity. Additionally, this research will expand into the catalytic upgrading of other alcohols, such as propanol and methanol, to explore the potential of these complexes in biofuel synthesis, extending their applicability beyond isobutanol production.

Furthermore, in light of current limitations in gas-handling capabilities, efforts will focus on exploring palladium-phosphine complexes' small molecule activation potential. This will provide critical insights into these systems' catalytic mechanisms and fundamental reaction pathways. This multifaceted approach aims to refine the synthesis and characterisation of palladium complexes and uncover valuable applications in sustainable catalysis and energy solutions, advancing the field of catalytic research.

4.9. References

[1] a) J. N. Brønsted, *Recueil des Travaux Chimiques des Pays-Bas* **1923**, *42*, 718-728; b) T. Lowry, *Journal of the Society of Chemical Industry* **1923**, *42*, 43-47.

[2] Pauling, L. *Valence and the Structure of Atoms and Molecules*; Cornell University Press: Ithaca, NY, **1960**.

[3] S. G. Shore and R. W. Parry, *Journal of the American Chemical Society* **1955**, *77*, 6084-6085.

[4] a) H. C. Brown and B. Kanner, *Journal of the American Chemical Society* **1966**, *88*, 986-992; b) H. C. Brown, H. Schlesinger and S. Z. Cardon, *Journal of the American Chemical Society* **1942**, *64*, 325-329.

[5] G. Wittig and E. Benz, *Chemische Berichte* **1959**, *92*, 1999-2013.

[6] W. Tochtermann, *Angewandte Chemie International Edition in English* **1966**, *5*, 351-371.

[7] G. C. Welch, R. R. S. Juan, J. D. Masuda and D. W. Stephan, *Science* **2006**, *314*, 1124-1126.

[8] S. Döring, G. Erker, R. Fröhlich, O. Meyer and K. Bergander, *Organometallics* **1998**, *17*, 2183-2187.

[9] J. S. McCahill, G. C. Welch and D. W. Stephan, *Angewandte Chemie International Edition* **2007**, *46*, 4968-4971.

[10] a) D. W. Stephan and G. Erker, *Angewandte Chemie International Edition* **2010**, *49*, 46-76; b) D. W. Stephan and G. Erker, *Angewandte Chemie International Edition* **2015**, *54*, 6400-6441.

[11] G. C. Welch and D. W. Stephan, *Journal of the American Chemical Society* **2007**, *129*, 1880-1881.

[12] M. Ullrich, K. S.-H. Seto, A. J. Lough, D. W. Stephan, *Chemical Communications* **2009**, 2335–2337.

[13] M. A. Dureen and D. W. Stephan, *Journal of the American Chemical Society* **2009**, *131*, 8396-8397.

[14] G. C. Welch, J. D. Masuda and D. W. Stephan, *Inorganic Chemistry* **2006**, *45*, 478-480.

[15] C. M. Mömming, E. Otten, G. Kehr, R. Fröhlich, S. Grimme, D. W. Stephan and G. Erker, *Angewandte Chemie International Edition* **2009**, *48*, 6643-6646.

[16] M. Sajid, A. Klose, B. Birkmann, L. Liang, B. Schirmer, T. Wiegand, H. Eckert, A. J. Lough, R. Fröhlich and C. G. Daniliuc, *Chemical Science* **2013**, *4*, 213-219.

[17] P. Spies, G. Erker, G. Kehr, K. Bergander, R. Fröhlich, S. Grimme and D. W. Stephan, *Chemical Communications* **2007**, 5072-5074.

[18] C. M. Mömming, S. Frömel, G. Kehr, R. Fröhlich, S. Grimme and G. Erker, *Journal of the American Chemical Society* **2009**, *131*, 12280-12289.

[19] C. M. Mömming, G. Kehr, B. Wibbeling, R. Fröhlich and G. Erker, *Dalton Transactions* **2010**, *39*, 7556-7564.

[20] a) T. K. Hollis, W. Odenkirk, N. Robinson, J. Whelan and B. Bosnich, *Tetrahedron* **1993**, *49*, 5415-5430; b) H, Yamamoto, *Lewis Acids in Organic Synthesis*, Wiley-VCH: Weinheim, Germany, **2000**, Vols. 1–2.

[21] R. C. Neu, E. Otten, A. Lough and D. W. Stephan, *Chemical Science* **2011**, *2*, 170-176.

[22] A. M. Chapman, M. F. Haddow and D. F. Wass, *Journal of the American Chemical Society* **2011**, *133*, 8826-8829.

[23] A. M. Chapman and D. F. Wass, *Dalton Transactions* **2012**, *41*, 9067-9072.

[24] a) A. M. Chapman, M. F. Haddow and D. F. Wass, *Journal of the American Chemical Society* **2011**, *133*, 18463-18478; b) C. Jiang, O. Blacque, T. Fox and H. Berke, *Organometallics* **2011**, *30*, 2117-2124.

[25] G. Chelucci, *Coordination Chemistry Reviews* **2017**, *331*, 1-36.

[26] D. W. Stephan, *Dalton Transactions* **2009**, 3129-3136.

[27] D. W. Stephan, *Journal of the American Chemical Society* **2015**, *137*, 10018-10032.

[28] G. Pampaloni, G. Ricci, A. Sommazzi, M. Guelfi, G. Leone, F. Masi, *Bis-Imine Titanium Complex, Catalytic System Comprising Said Bis-Imine Titanium Complex and Process for the (Co) Polymerisation of Conjugated Dienes*, US Patent *11299505 B2*, **2022**.

[29] R. S. Erami, D. Díaz-García, S. Prashar, A. Rodríguez-Diéguez, M. Fajardo, M. Amirnasr and S. Gómez-Ruiz, *Catalysts* **2017**, *7*, 76.

[30] R. E. Rulke, J. M. Ernsting, A. L. Spek, C. J. Elsevier, P. W. van Leeuwen and K. Vrieze, *Inorganic Chemistry* **1993**, *32*, 5769-5778.

[31] M. S. Brookhart, L. K. Johnson, C. M. Killian, E. F. McCord, S. J. McLain, K. A. Kreutzer, S. D. Ittel and D. J. Tempel, *Highly Branched Olefin Polymers and Their Uses*. US Patent *5880241*, **1999**.

Chapter 5: Experimental

5.1. General Experimental Considerations:

All procedures were carried out under an inert atmosphere (N_2) using standard Schlenk line techniques or in an inert atmosphere glovebox (N_2) unless otherwise stated. All glassware was either flame dried or dried in an oven at 200 °C for at least two hours before use. All chemicals were sourced from standard suppliers and used as received, without additional purification unless explicitly specified otherwise. Solvents were purified using an Anhydrous Engineering Grubbs-type solvent system or an mBraun solvent purification system except anhydrous ethanol and methanol which were purchased from Sigma-Aldrich. All solvents were degassed before use through at least three freeze/pump/thaw cycles. NMR spectra were recorded on a Bruker Avance Neo 400 NMR spectrometer, Bruker 400 Ultrasheild or Bruker AscendTM 500 NMR spectrometer. ^{1}H and $^{13}C\{^{1}H\}$ NMR chemical shifts were referenced relative to the residual solvent resonances in the deuterated solvent. $^{11}B\{^{1}H\}$, ^{19}F, and $^{31}P\{^{1}H\}$ were referenced to $BF_3.OEt_2$, $CFCl_3$ and 85% H_3PO_4 as external standards respectively. Mass spectra (ESI) were recorded on a Waters Xevo G2-XS QTof Quadrupole Time-of-Flight Mass Spectrometer. Relative intensities are reported according to the following intervals: weak (w, 0–33%), medium (m, 33–66%), strong (s, 66–100%). Infrared spectra were recorded using an ATR (Attenuated Total Reflectance) method on an Agilent Technologies Cary 630 FTIR spectrometer, with solid samples analysed in air. Single-crystal XRD data were collected by Dr Benson Kariyuki on an Agilent SupaNova Dual Atlas diffractometer with a mirror monochromator [using either Cu (λ = 1.5418 Å) or Mo (λ = 0.7107 Å) radiation], equipped with an Oxford Cryosystems cooling apparatus. Crystal structures were solved and refined using SHELX.[1] Non-hydrogen atoms were refined with anisotropic displacement parameters. Hydrogen atoms were inserted in idealised positions, and a riding model was used with Uiso set at 1.2 or 1.5 times the value of Ueq for the atom to which they are bonded. Unless otherwise stated, catalytic reactions were carried out in a 65 mL Parr stainless steel autoclave equipped with a PTFE sleeve and stirrer bar, under a nitrogen atmosphere. The assembled autoclave was placed in a pre-heated aluminium heating block and the reaction mixture was stirred at 500 rpm. The reactions were timed from when the autoclave was placed in the heated block. Mol% is relative to ethanol. Ethanol conversion in this study was determined directly by quantifying the residual ethanol in the reaction mixture using GC analysis. This approach provides an absolute measure of conversion by comparing the amount of ethanol added with the amount remaining after the reaction. Unlike methods that estimate conversion based solely on product yields, this technique ensures a more accurate and rigorous assessment. While the yields of detectable products (e.g. C_4, C_6 and C_8 compounds) offer insight into selectivity, minor discrepancies between ethanol conversion and total product yield may arise due to the formation of undetected or trace by-products and analytical limitations. GC Analysis of all catalytic samples was performed by GC-FID using an Agilent 7820A GC, fitted with a CARBOWAX/20M capillary column 30 m x 0.320 mm, I.D. 0.25 μm. Method: starting oven temp 60 °C, hold for 5 min, heat to 220 °C at 40 °C min^{-1}, hold at 220 °C for 5 min. Calibration included a range of compounds relevant to both n-butanol and isobutanol chemistries. For n-butanol chemistry, the calibrated compounds were ethanol, n-butanol, 2-butanol, octanol, ethyl acetate, n-hexanol, 2-ethyl butanol, and 2-ethyl hexanol. For isobutanol chemistry, the compounds included ethanol, n-propanol, isobutanol, and 2-methyl butanol, each prepared in diethyl ether. Given the project's focus on isobutanol production, compounds specific to n-butanol chemistry may be excluded from the retention times table unless relevant to isobutanol production. Table 5-1 provides the retention times for all calibrated compounds.

Table 5-1: Retention Times of Calibrated Compounds for GC Analysis

Compound	Retention Times
Diethyl ether	3.623
Methanol	4.640
Ethyl acetate	4.668
Ethanol	5.024
2-BuOH	6.154
***n*-Propanol**	6.316
***i*-BuOH**	6.957
***n*-BuOH**	7.573
2-Ethyl butanol	9.115
2-Methyl butanol	8.234
***n*-Hexanol**	9.432
2-Ethylhexanol	10.234
Octanol	10.568
Hexadecane (Standard)	10.866

5.1.1. Yield and Selectivity of Guerbet Products:

The yield and selectivity of Guerbet products in the liquid fraction was calculated as follows. *n* is the number of mmol.

$$\text{Yield (\%)} = \frac{(X \times nProduct)}{nEtOH} \times 100$$

where:

- *X* = number of ethanol equivalents of product e.g. when calculating the yield of butanol, X = 2.
- *nProduct* is the amount (mmol) of the specific product.
- *nEtOH* is the amount (mmol) of ethanol initially added.

$$\text{Selectivity (\%)} = \frac{(nProduct)}{nAll\ Liquid\ Products} \times 100$$

where:

- *nAll Liquid Products* is the total amount (mmol) of all products detected in the liquid phase.

The amount of product (*nProduct*, in mmol) was determined from GC peak areas using a calibration curve based on external standards. The GC instrument response factor for each compound was used as follows:

$$nProduct = \frac{\boldsymbol{A}\ Product}{\boldsymbol{R}\ Product}$$

where:

- ***A** Product* = GC peak area of the product
- ***R** Product* = response factor (area per mmol) obtained from a calibration curve for that compound

5.1.2. Additional Calculations:

Carbon Balance (%):

This measures the consistency of carbon in the initial ethanol against all detected carbon in products.

$$\text{Carbon Balance (\%)} = \left(\frac{\text{Total Carbon in Products}}{\text{Total Carbon in Initial Ethanol}}\right) \times 100$$

where:

- *Total Carbon in Products* is the sum of carbon atoms in each detected product multiplied by its amount.
- *Total Carbon in Initial Ethanol* is the total carbon in the initial ethanol used.

Missing Carbon (%):

This calculates the percentage of initial ethanol’s carbon not accounted for in the detected products.

$$\text{Missing Carbon (\%)} = 100 - \text{Carbon Balance (\%)}$$

Error of the Analysis (%)

This estimates the accuracy of the analysis by comparing detected to expected values of carbon.

$$\text{Error of Analysis (\%)} = \left|\frac{\text{Experimental Value} - \text{Theoritical Value}}{\text{Theoritical Value}}\right| \text{ x } 100$$

Standard Deviation (SD):

This provides a measure of variability in the repeated measurements or experimental results.

$$\text{Standard Deviation (SD)} = \sqrt{\frac{1}{N-1}\sum_{i=1}^{N}(x_i - \bar{x})^2}$$

where:

- x_i is each individual measurement,
- $\bar{x}$ is the mean of all measurements, and
- N is the number of measurements.

Standard Error of Mean (SEM):

This indicates the precision of the mean value, especially useful for comparing repeated measurements.

$$\text{Standard Error of Mean (SEM)} = \frac{SD}{\sqrt{N}}$$

5.2. Experimental for Chapters 2 and 3

5.2.1. Example Procedure for Catalytic Upgrading of Ethanol and Methanol to Isobutanol:

In a glovebox, a PTFE sleeve was charged with a Ru catalyst (0.0128 mmol, 0.1 mol%), PR_3 ligand (0.3 mol%), NaOMe (1.38 g, 25.6 mmol, 200 mol%) and a stirrer bar. The PTFE sleeve was sealed within the autoclave. The autoclave was then attached to a Schlenk line and was put under a nitrogen atmosphere by evacuating the autoclave and re-filling with nitrogen three times. Against a flow of nitrogen, methanol (7.5 mL, 185.4 mmol) and ethanol (0.75 mL, 12.8 mmol) were injected into the autoclave. The autoclave was sealed and placed in a pre- heated aluminium heating block (180 °C) for 20 h. After the reaction time was complete, the autoclave was cooled to room temperature in an ice-water bath and the residual pressure was released.

5.2.2 Post-Reaction Procedure:

A portion of the post-reaction solution was passed through a 1 cm plug of acidic alumina and analysed by GC-FID (100 μL sample, 10 μL hexadecane standard, 1.7 mL Et_2O). Each liquid product was calibrated against hexadecane which was used as the standard.

5.2.2. Reaction of 1,1-bis(diphenylphosphino)ferrocene with dichlorotetrakis(dimethylsulfoxide)ruthenium(II) :

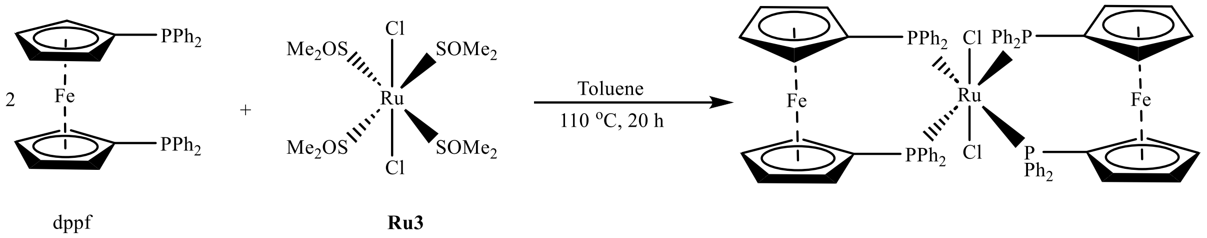

Scheme 5-1: Reaction scheme depicting the synthesis of the expected complex between 1,1'-bis(diphenylphosphino)ferrocene (dppf) and [$RuCl_2(DMSO)_2(Me_2SO)_2$] (**Ru3**) in toluene at 110 °C over 20 hours. The reaction results in the coordination of two dppf ligands to the ruthenium centre, replacing the DMSO ligands and forming a stabilised product with bridging chlorides.

In a Schlenk flask charged with a stirrer bar, 600 mg (1.08 mmol) of 1,1-bis(diphenylphosphino)ferrocene was added to 262 mg (0.54 mmol) of dichlorotetrakis(dimethylsulfoxide)ruthenium(II) chloride. The flask was evacuated and re-filled with nitrogen three times, then 50 mL of dry toluene was added to dissolve the mixture. The reaction mixture was heated to 100 °C for 20 hours. After cooling to room temperature, the solvent was removed by evacuation and the resultant solid was washed with 50 mL of dry pentane and dried by evacuation to give an orange solid (0.269 g).

$^{31}P\{^1H\}$ NMR (202 MHz, CD_2Cl_2): δ_P 57.8, 53.4, 44.4, 37.9, 28.8, 25.5 (P=O), -17.5 (Free dppf) ppm.

5.3. Experimental for Chapter 4

5.3.1. Synthesis of Bidentate Ligands:

5.3.1.1. Synthesis of L1:

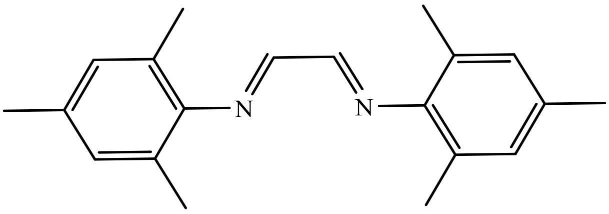

L_1 was synthesised by a modification of a literature method.[2] An air-stable reaction mixture was prepared by adding 100 mmol of 2,4,6-trimethylaniline to a combination of 25 mL H_2O and 50 mL methanol in a 250 mL round-bottom flask. Then, 50 mmol of glyoxal (40% in H_2O) was added dropwise while vigorously agitating the mixture. The mixture was heated to 50 °C for 3 hours. After cooling to room temperature, the resultant yellow solid was collected by filtration, washed with methanol, and recrystallized from pentane to give L_1 as a yellow solid (6.0 g, 82.2 %).

^{1}H NMR (400 MHz, $CDCl_3$): δ_H 8.02 (s, 2H, *H*C=N), 6.84 (s, 4H, *m*-C_{Ar}*H*), 2.22 (s, 6H, *p*-C*H*$_3$-C_{Ar}), 2.08 (s, 12H, *o*-C*H*$_3$-C_{Ar}) ppm.

^{13}C{^{1}H} NMR (101 MHz, $CDCl_3$): δ_C 163.5 (C=N), 147.4 (C-N), 134.2 (*m*-*C*$_{Ar}$), 128.9 (*p*-*C*$_{Ar}$), 126.6 (*o*-*C*$_{Ar}$) 20.8 (*p*-*C*H_3-C_{Ar}), 18.2 (*o*-*C*H_3-C_{Ar}) ppm.

5.3.1.2. Synthesis of L_2:

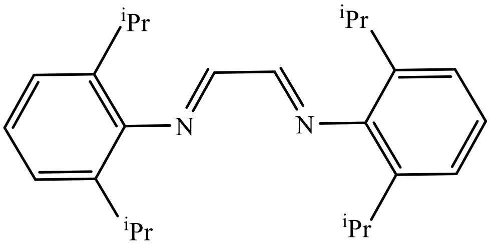

L_2 was synthesised by a modification of the same literature method used for L_1.[2] An air-stable reaction was set up by dissolving 100 mmol of 2,6-diisopropylaniline in 25 mL of H_2O and 50 mL of methanol in the presence of 50 mmol of glyoxal (40% in H_2O). Following recrystallisation from methanol, the reaction yielded L2 as a yellow solid (7.0 g, 74.4%).

^{1}H NMR (400 MHz, $CDCl_3$): δ_H 8.03 (s, 2H, *H*C=N), 7.13–7.08 (m, 6H, C_{Ar}-*H*), 2.85 (sept, 4H, *iso*-CH, J_{HH} = 6.87 Hz), 1.14 (d, 24H, *iso*-C*H*$_3$, J_{HH} = 8.60 Hz) ppm.

^{13}C{^{1}H} NMR (101 MHz, $CDCl_3$): δ_C 163.1 (*C*=N), 148.0 (*C*$_{Ar}$-N), 136.7 (*o*-*C*$_{Ar}$), 125.1 (*m*-*C*$_{Ar}$), 123.2 (*p*-*C*$_{Ar}$), 28.1 (*iso*-*C*H), 23.4 (*iso*-*C*H_3) ppm.

5.3.2. Synthesis of Palladium Precursors:

5.3.2.1. Synthesis of dichloro(1,5-cyclooctadiene)palladium(II):

This precursor was synthesised by a literature method.[3] 1.53 g (8.6 mmol) of $PdCl_2$ was dissolved in 6 mL of concentrated HCl, then chilled with an ice bath. The chilled solution was diluted with 150 mL of absolute ethanol, stirred for fifteen minutes, and then filtered to remove insoluble residue. The residue was washed with 2 x 10 mL ethanol. After transferring the filtrate to a new round-bottom flask, 2.5 mL (20.4 mmol) of 1,5-cyclooctadiene was added to the solution while stirring. The colour of the solution changed from brown to orange, and a solid product immediately formed. After stirring for a further 30 min, the yellow-orange solid was collected by filtration and washed with 3 x 10 mL of diethyl ether. The final product was dried by evacuation overnight to give a yellow-orange solid (2.0 g, 81.2%).

^{1}H NMR (500 MHz, $CDCl_3$): δ_H 6.24 (s, 4H, C*H*), 2.85 (d, 4H, CH_2, J_{HH} = 9.33 Hz), 2.50 (d, 4H, CH_2, J_{HH} = 9.51) ppm.

^{13}C{^{1}H} NMR (101 MHz, $CDCl_3$): δ_C 128.7, 125.6 (H*C*=*C*H), 23.5, 20.2 (*C*H_2) ppm.

5.3.2.2. Synthesis of Chloro(1,5-cyclooctadiene)methylpalladium(II) (Pd1):

This precursor was synthesised by a literature method.[4] After dissolving 2.0 g (7.0 mmol) of (COD)$PdCl_2$ in 50 mL of dichloromethane, 1.16 mL (1.2 equivalent, 8.4 mmol) of tetramethyl tin was added, and the mixture was stirred at room temperature for 48 hours until the vivid yellow colour of the precursor had disappeared. The colourless solution was filtered through Celite to remove any insoluble residues, including potential tin impurities. The solvent was then removed under reduced pressure, maintaining the temperature at 0 °C with an ice bath to prevent decomposition. The resulting off-white powder was thoroughly washed with 50 mL of diethyl ether to eliminate any remaining organotin species and dried by evacuation overnight to yield a white solid (1.7 g, 91.5%).

^{1}H NMR (500 MHz, $CDCl_3$): δ_H 5.65 (s, 2H, C*H*), 5.10 (d, 2H, C*H*, J_{HH} = 2.04 Hz), 2.60–2.40 (m, 8H, CH_2), 1.12 (s, 3H, Pd-CH_3) ppm.

^{13}C{^{1}H} NMR (101 MHz, $CDCl_3$): δ_C 124.9, 101.5 (H*C*=*C*H), 32.8, 28.6 (*C*H_2), 13.1 (Pd-*C*H_3) ppm.

5.3.3. Synthesis of Palladium Catalysts:

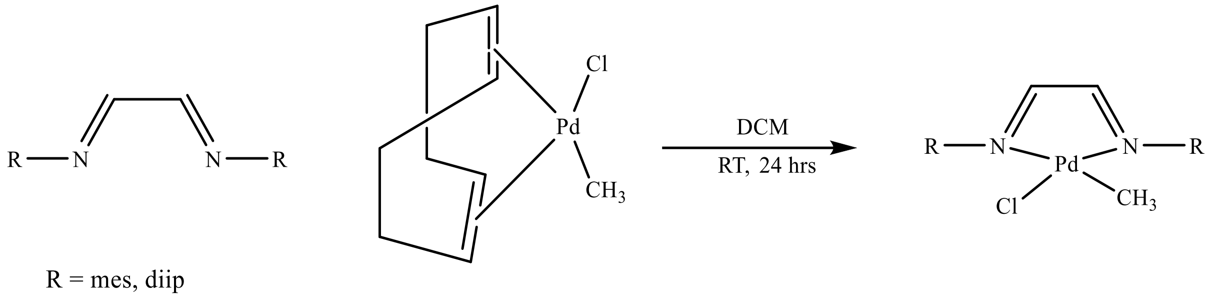

Scheme 5-2: General reaction for Pd catalysts synthesis.

5.3.3.1. Synthesis of Complex 4.7:

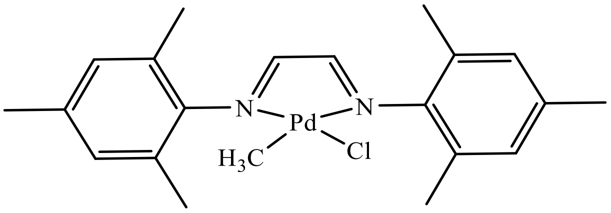

This precursor was synthesised by a literature method.[5] In a Schlenk flask, 3.64 g (12.44 mmol) of L_1 was added to 3 g (11.32 mmol) of Chloro(1,5-cyclooctadiene)methylpalladium(II). 30 mL of dried dichloromethane was added. The mixture was stirred at ambient temperature for 20 hours. The solvent was removed under reduced pressure; the solid product was washed with 30 mL of diethyl ether and dried overnight under reduced pressure to give an orange solid (3.55g, 69.7%).

^{1}H NMR (500 MHz, $CDCl_3$): δ_H 8.18 (s, 1H, *H*C=N), 8.02 (s, 1H, *H*C=N), 6.91 (s, 2H, *m*-C_{Ar}-*H*), 6.87 (s, 2H, *m*-C_{Ar}-*H*), 2.25 (s, 3H, *p*-CH_3-C_{Ar}), 2.24 (s, 12H, *o*-CH_3-C_{Ar}), 2.17 (s, 3H, *p*-CH_3-C_{Ar}), 0.69 (s, 3H, Pd-CH_3) ppm.

^{13}C{^{1}H} NMR (126 MHz, $CDCl_3$): δ_C 162.8 (*C*=N), 158.6 (*C*=N), 143.0 (C_{Ar}-N), 136.0 (*o*-C_{Ar}), 129 (*m*-C_{Ar}), 127.5 (*p*-C_{Ar}), 19.8 (*p*-*C*H_3-C_{Ar}), 16.8 (*o*-*C*H_3-C_{Ar}), 2.2 (Pd-*C*H_3) ppm.

5.3.3.2. Synthesis of Complex 4.8:

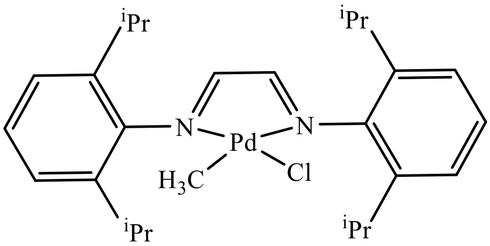

Complex **4.8** was synthesised and reported by the same literature method used for complex **4.7**.[6] 3g (11.32 mmol) of Chloro(1,5-cyclooctadiene)methylpalladium(II) reacted with 4.69g (12.44 mmol) of L_2 to give an ochre solid (4.4g, 67.1%).

^{1}H NMR (500 MHz, $CDCl_3$): δ_H 8.20 (s, 1H, *H*C=N), 8.04 (s, 1H, *H*C=N), 7.28–7.21 (m, 6H, C_{Ar}-*H*), 3.18 (sept, 4H, *iso*-C*H*, J_{HH} = 11.77 Hz), 1.34 (d, 6H, *iso*-CH_3, J_{HH} = 6.74 Hz), 1.28, (d, 6H, *iso*-CH_3, J_{HH} = 6.77 Hz), 1.10 (d, 12H, *iso*-CH_3, J_{HH} = 6.88 Hz), 0.77 (s, 3H, Pd-CH_3) ppm.

^{13}C{^{1}H} NMR (126 MHz, $CDCl_3$): δ_C 162.0, 158.2 (*C*=N), 143.3, 142.4 (C_{Ar}-N), 138.6, 137.7 (*o*-C_{Ar}), 127.0 (*m*-C_{Ar}), 122.4 (*p*-C_{Ar}), 28.7 (*iso*-*C*H), 27.6, 23.7, 22.1, 21.5 (*iso*-*C*H_3), 3.0 (Pd- *C*H_3) ppm.

5.3.3.3. Synthesis of Complex 4.9:

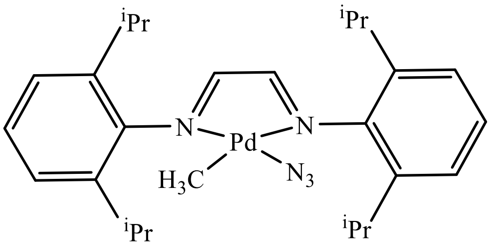

A novel complex was synthesised by adding 500 mg (0.94 mmol) of complex **4.8** to 79.2 mg (1.22 mmol) of sodium azide in a Schlenk flask, followed by adding 30 mL of dry dichloromethane. The mixture was stirred for 20 hours at room temperature. Subsequently, it was filtered through a cannula fitted with a filter stick into a clean Schlenk flask. The solvent was then removed under reduced pressure, and the product was washed with 30 mL of diethyl ether, yielding a dark red solid (220 mg, 43.1%).

^{1}H NMR (500 MHz, CDCl$_3$): δ_H 8.17 (s, 1H, *H*C=N), 8.01 (s, 1H, *H*C=N), 7.29–7.21 (m, 6H, C$_{Ar}$-*H*), 3.12 (sept, 4H, *iso*-C*H*, J_{HH} = 6.79 Hz), 1.33 (d, 6H, *iso*-CH_3, J_{HH} = 6.76 Hz), 1.29 (d, 6H, *iso*-CH_3, J_{HH} = 6.77 Hz), 1.15–1.10 (d, 12H, *iso*-CH_3 J_{HH} = 6.70), 0.66 (s, 3H, Pd-CH_3) ppm.

^{13}C{^{1}H} NMR (101 MHz, CDCl$_3$): δ_C 162.1, 158.2 (*C*=N), 143.0 (C_{Ar}-N), 138.0 (*o*-C_{Ar}), 127.0 (*m*-C_{Ar}), 122.5 (*p*-C_{Ar}), 28.7 (*iso*-*C*H), 27.5, 23.5, 22.9, 21.6 (*iso*-*C*H$_3$), 3.0 (Pd-*C*H$_3$) ppm.

FTIR:

- 2019 cm^{-1}: N$_3$ stretching
- 612 cm^{-1}: C=N stretching
- 692 cm^{-1}: Pd–N stretching

5.3.3.4. Synthesis of Complex 4.10:

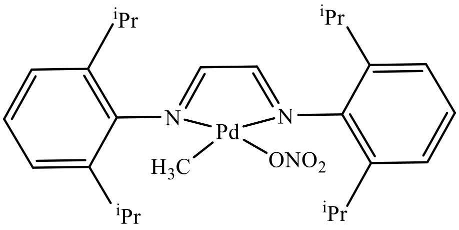

The novel complex **4.10** was synthesised by the same method used for complex **4.9**. 500 mg (0.94 mmol) of complex **4.8** with 207 mg (1.22 mmol) of silver nitrate to give an orange solid (240 mg, 42.9%).

^{1}H NMR (500 MHz, CDCl$_3$): δ_H 8.19 (s, 1H, *H*C=N), 8.04 (s, 1H, *H*C=N), 7.31–7.21 (m, 6H, C$_{Ar}$-*H*), 3.16 (sept, 4H, *iso*-C*H*, J_{HH} = 4.93 Hz), 1.34 (d, 6H, *iso*-CH$_3$, J_{HH} = 6.70 Hz), 1.28 (d, 6H, *iso-CH$_3$*, J_{HH} = 6.72 Hz), 1.11 (d, 12H, *iso*-CH_3, J_{HH} = 6.81 Hz), 0.77 (s, 3H, Pd-CH_3) ppm.

^{13}C{^{1}H} NMR (101 MHz, CDCl$_3$): δ_C 162.1, 158.2 (C=N), 143.3, 142.4 (C_{Ar}-N), 138.6, 137.7 (*o*-C_{Ar}), 127.0 (*m*-C_{Ar}), 122.4 (*p*-C_{Ar}), 28.7 (*iso*-*C*H), 27.5, 23.7, 22.1, 21.5 (*iso*-*C*H$_3$), 3.0 (Pd-*C*H$_3$) ppm.

FTIR:

- 1273 cm^{-1}: ONO_2 stretching, indicating N=O
- 795 cm^{-1}: N–O stretching
- 1616 cm^{-1}: C=N stretching
- 395 cm^{-1}: Pd–O stretching
- 480 cm^{-1}: Pd–N stretching

5.3.3.5. Synthesis of Complex 4.11:

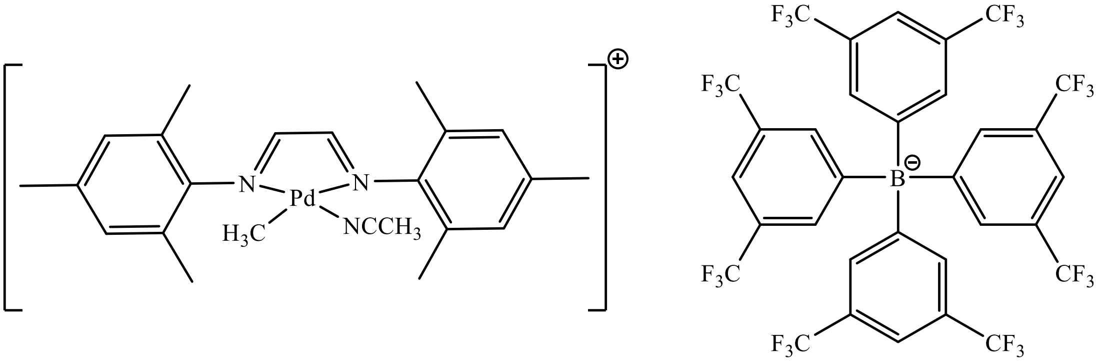

In a Schlenk flask, 450 mg (0.51 mmol) of sodium tetrakis-3,5-bis(trifluoromethyl)phenyl borate and 228 mg (0.51 mmol) of complex **4.7** were dissolved by adding 25 mL of Et_2O and 25 mL of DCM. Then, 3 mL of Acetonitrile was added to the mixture, which was left for 1.5 h at room temperature. After that, the solvent was removed by reduced pressure, and the product was washed with 50 mL of *n*-hexane to produce a red solid (470 mg, 69.9%).

^{1}H NMR (500 MHz, CD_2Cl_2): δ_H 8.13 (d, 2H, *H*C=N, J_{HH} = 8.35 Hz), 7.63 (s, 8H, *o*-C_{Ar}-*H* BAF), 7.47 (s, 4H, *p*-C_{Ar}-*H* BAF), 6.93 (s, 4H, *m*-C_{Ar}-*H*), 2.22 (s, 6H, *o*-CH_3-C_{Ar}), 2.20 (s, 6H, *o*-CH_3-C_{Ar}), 2.11 (s, 6H, *p*-CH_3-C_{Ar}), 1.87 (s, 3H, NC-CH_3), 0.62 (s, 3H, Pd-CH_3) ppm.

^{13}C{^{1}H} NMR (101 MHz, CD_2Cl_2): δ_C 169.2 (*C*=N), 163.2, 162.5, 162.0, 161.3 (*C*-B), 160.6 (N*C* Acetonitrile), 142.5 (C_{Ar}-N), 138.7 (*o*-C_{Ar}), 134.9 (*C*F_3 BAF), 129.5 (*m*-C_{Ar} BAF), 129.1, 128.8 (*m*-C_{Ar}), 128.0 (*m*-C_{Ar} BAF), 127.9, 125.8, 123.6, 121.5 (*o*-C_{Ar}, *p*-C_{Ar} BAF), 117.53 (*p*-C_{Ar}-H), 29.8 (*C*H_3 Acetonitrile), 20.7 (*p*-*C*H_3-C_{Ar}), 17.9 (*o*-*C*H_3-C_{Ar}), 6.8 (Pd-*C*H_3) ppm.

^{11}B NMR (160 MHz, CD_2Cl_2): δ_B 11 ppm.

^{19}F NMR (470 MHz, CD_2Cl_2): δ_F -62.6 ppm.

LRMS (ES$^+$): *m/z* calcd. for $C_{23}H_{30}N_3Pd$: 454.15, Found: 454.15

LRMS (ES$^-$): *m/z* calcd. for $C_{32}H_{12}BF_{24}$: 863.07, Found: 863.07

5.3.3.6. Synthesis of Complex 4.12:

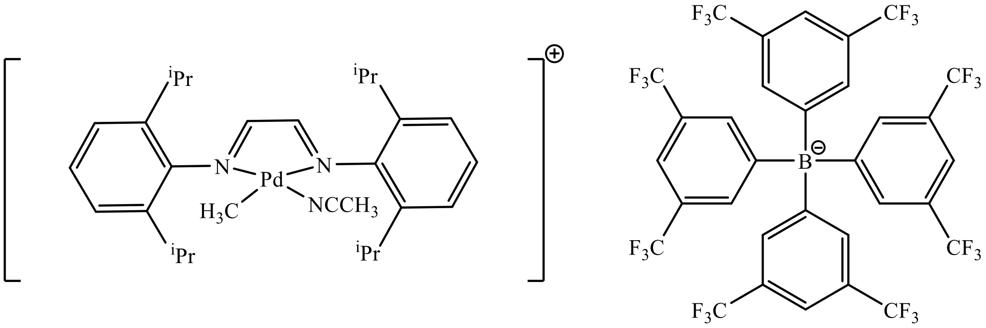

Complex **4.12** was synthesised using the same method as complex **4.11**. 381 mg (0.43 mmol) of sodium tetrakis-3,5-bis(trifluoromethyl)phenyl borate with 250 mg (0.43 mmol) complex **4.8** to give an orange solid (440 mg, 72.8%).

^{1}H NMR (500 MHz, CD_2Cl_2): δ_H 8.18, (d, 2H, *H*C=N, J_{HH} = 3.6247 Hz), 7.63 (s, 8H, *o*-C_{Ar}-*H* BAF), 7.47 (s, 4H, Ar *p*-C_{Ar}-*H* BAF), 7.25–7.23 (m, 6H, C_{Ar}-*H*), 3.07, 2.90 (d sept, 4H, *iso*-C*H*, J_{HH} = 6.44 Hz), 1.85 (s, 3H, NC-C*H₃*) 1.27 (dd, 12H, *iso*-C*H₃*, J_{HH} = 3.61 Hz), 1.16 (d, 6H, *iso*-C*H₃*, J_{HH} = 6.85 Hz), 1.12 (d, 6H, *iso*-C*H₃*, J_{HH} = 6.85 Hz), 0.74 (s, 3H, Pd-C*H₃*) ppm.

^{13}C{^{1}H} NMR (101 MHz, CD_2Cl_2): δ_C 168.1 (*C*=N), 163.2, 162.5, 161.9, 161.3 (C-B), 160.2 (N*C* Acetonitrile), 142.4 (C_{Ar}-N), 139.3, 138.3 (*o*-C_{Ar}), 134.9 (*C*F₃), 129.5 (*m*-C_{Ar} BAF), 125.8, 123.6 (*o*-C_{Ar} BAF), 124.2 (*p*-C_{Ar} BAF), 121.8 (*m*-C_{Ar}), 117.5 (*p*-C_{Ar}), 30.0 (*C*H₃ Acetonitrile), 29.0 (*iso*-*C*H), 26.3, 24.0, 23.4, 22.5 (*iso*-*C*H₃), 8.4 (Pd-*C*H₃) ppm.

^{11}B NMR (160 MHz, CD_2Cl_2): δ_B 11 ppm.

^{19}F NMR (470 MHz, CD_2Cl_2): δ_F -62.6 ppm.

LRMS (ES$^+$): *m/z* calcd. for $C_{29}H_{42}N_3Pd$: 538.24, Found: 538.24

LRMS (ES$^-$): *m/z* calcd. for $C_{32}H_{12}BF_{24}$: 863.07, Found: 863.07

5.3.3.7. Synthesis of Complex 4.13:

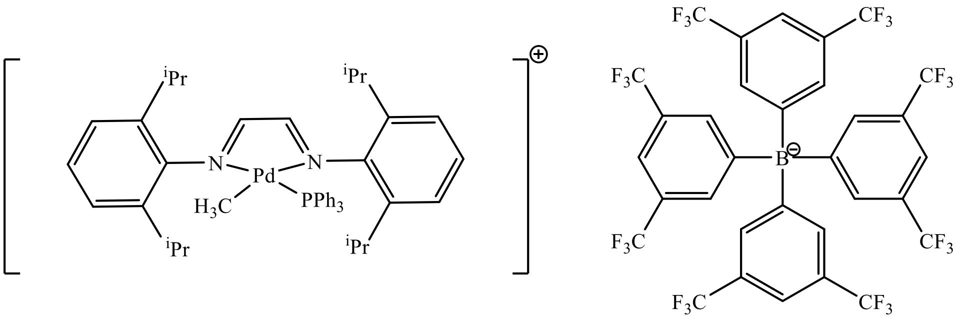

In a Schlenk flask, 200 mg (0.14 mmol) of complex 4.12 and 48.6 mg (0.18 mmol, 1.3 equivalent) of complex **4.7** were dissolved by adding 30 mL of DCM; then, the mixture was left for 20 hours at room temperature. After that, the solvent was removed by reduced pressure, and the product was washed with 50 mL of *n*-pentane to produce a red solid (160 mg, 69.1%).

^{1}H NMR (500 MHz, CD_2Cl_2): δ_H 8.40 (s, 1H, *H*C=N), 8.18 (s, 1H, *H*C=N), 7.65 (s, 8H, *o*-C_{Ar}-*H* BAF), 7.45 (s, 4H, *p*-C_{Ar}-*H* BAF), 7.34–7.25 (m, 6H, C_{Ar}-*H*), 7.17–7.08 (m, 9H, *m*-C_{Ar}-*H*, *p*-C_{Ar}-*H* PPh_3), 6.86, (d, 4H, *o*-CH PPh_3, J_{HH} = 5.88 Hz), 3.03, 2.93 (d sept, 4H, *iso*-CH J_{HH} = 6.51 Hz), 1.34 (d, 6H, *iso*-C*H*$_3$, J_{HH} = 6.77 Hz), 1.28 (d, 6H, *iso*-C*H*$_3$, J_{HH} = 6.68 Hz), 1.01 (d, 6H, *iso*-C*H*$_3$, J_{HH} = 6.74 Hz), 0.85, (d, 6H, *iso*-C*H*$_3$, J_{HH} = 6.72 Hz), 0.36, (d, 3H, Pd-C*H*$_3$) ppm.

^{13}C{^{1}H} NMR (101 MHz, CD_2Cl_2): δ_C 165.4 (*C*=N), 162.3, 162.0, 161.6, 161.3 (*C*-B), 145.4, 141.2 (C_{Ar}-N), 139.2, 137.9 (*p*-C_{Ar}), 134.9 (*C*F_3), 133.8 (C_{Ar}-P), 130.0 (*m*-C_{Ar} BAF), 129.0 (*m*-C_{Ar} PPh_3), 128.5, 126.4 (*p*-C_{Ar}, *o*-C_{Ar} PPh_3), 127.9, 125.8, 123.6, 121.5 (*p*-C_{Ar}, *o*-C_{Ar} BAF), 124.2, (*m*-C_{Ar}), 117.54 (*p*-C_{Ar}), 29.8 (*C*H_3 Acetonitrile), 29.0 (*iso*-*C*H), 27.2, 24.5, 22.3, 21.6 (*iso*-*C*H_3), 0.9 (Pd-CH_3) ppm.

^{11}B NMR (160 MHz, CD_2Cl_2): δ_B -7 ppm

^{19}F NMR (470MHz, CD_2Cl_2): δ_F -62.6 ppm

$^{31}P\{^1H\}$ NMR (202 MHz, CD_2Cl_2): δ_P 37.8 (s, Pd-P) ppm.

LRMS (ES^+): *m/z* calcd. for $C_{45}H_{54}N_2PPd$: 759.31, found: 759.31

LRMS (ES^-): *m/z* calcd. for $C_{32}H_{12}BF_{24}$: 863.07, Found: 863.07

5.4. Guerbet Reactions Full Results Tables:

5.4.1. Chapter 2: Catalytic Upgrading of Ethanol/Methanol – Full Results:

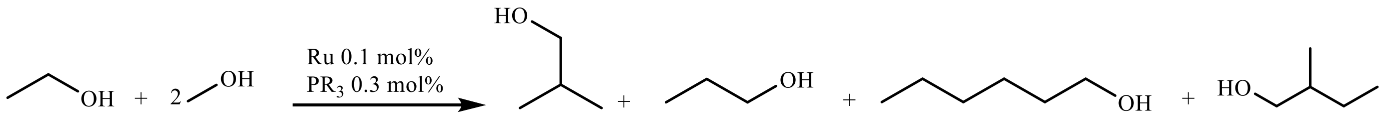

Table 5-2: Full results of catalytic upgrading of ethanol/methanol in Chapter 2.

Run [a]	Catalyst	PR_3	Time	Temperature	NaOMe (mol%)	EtOH Conversion (%) [b]	Yield [c] (TON) [d] [Selectivity] (%)			
							Isobutanol	***n*-Propanol**	***n*-Hexanol**	**2-Methyl-butanol**
1	**Ru1**	-	20	180	200	53.0	5.4 (29) [87.3]	0.8 (4) [12.8]	0 (0) [0]	0 (0) [0]
2	**Ru2**	-	20	180	200	54.7	9.5 (52) [80.4]	2.3 (13) [19.6]	0 (0) [0]	0 (0) [0]
3	**Ru3**	-	20	180	200	57.2	4.8 (27) [74.6]	1.5 (9) [22.7]	0.5 (3) [2.7]	0 (0) [0]
4	**Ru4**	-	20	180	200	83.5	36.3 (303) [87.7]	4.5 (38) [10.9]	1.9 (16) [1.5]	0 (0) [0]
5	**Ru5**	-	20	180	200	72.3	50.7 (367) [95.2]	1.7 (12) [3.3]	2.4 (17) [1.5]	0 (0) [0]
6	**Ru6**	-	20	180	200	69.0	32.5 (224) [93.0]	1.5 (10) [4.2]	2.5 (17) [2.8]	0 (0) [0]
7	**Ru1**	**PL1**	20	180	200	87.4	42.8 (375) [96.7]	1.4 (12) [3.1]	0.3 (3) [0.2]	0 (0) [0]
8	**Ru2**	**PL1**	20	180	200	77.5	49.7 (382) [92.7]	2.5 (19) [4.6]	1.8 (14) [2.9]	0 (0) [0]
9	**Ru3**	**PL1**	20	180	200	86.0	34.9 (300) [96.6]	1.2 (10) [3.2]	0.2 (2) [0.2]	0 (0) [0]
10	**Ru1**	**PL2**	20	180	200	69.1	8.1 (56) [80.7]	2.0 (14) [19.3]	0 (0) [0]	0 (0) [0]
11	**Ru1**	**PL3**	20	180	200	66.6	7.5 (50) [78.1]	2.1 (14) [21.9]	0 (0) [0]	0 (0) [0]

12	**Ru1**	**PL4**	20	180	200	72.8	7.9 (58) [81.2]	1.8 (13) [18.8]	0 (0) [0]	0 (0) [0]
13	**Ru1**	**PL5**	20	180	200	72.3	11.1 (80) [87.4]	1.6 (12) [12.6]	0 (0) [0]	0 (0) [0]
14	**Ru1**	**PL6**	20	180	200	86.3	44.8 (387) [97.0]	1.4 (12) [3.0]	0 (0) [0]	0 (0) [0]
15	**Ru1**	**PL7**	20	180	200	77.9	22.1 (172) [91.9]	1.9 (15) [8.7]	0 (0) [0]	0 (0) [0]
16	**Ru1**	**PL8**	20	180	200	70.7	26.7 (189) [92.6]	2.1 (15) [7.4]	0 (0) [0]	0 (0) [0]
17	**Ru1**	**PL9**	20	180	200	77.7	8.5 (66) [82.0]	1.7 (13) [16.9]	0.4 (3) [1.1]	0 (0) [0]
18	**Ru1**	**PL10**	20	180	200	75.4	12.4 (94) [87.5]	1.7 (13) [11.8]	0.3 (2) [0.7]	0 (0) [0]
19	**Ru1**	**PL11**	20	180	200	60.8	17.3 (105) [90.1]	1.8 (11) [9.2]	0.4 (2) [0.6]	0 (0) [0]
20[e]	**Ru1**	**PL1**	4	180	200	54.3	6.7 (36) [85.5]	1.1 (6) [13.6]	0.2 (1) [0.9]	0 (0) [0]
21[f]	**Ru1**	**PL1**	4	180	200	62.1	19.7 (122) [94.5]	1.1 (7) [5.5]	0 (0) [0]	0 (0) [0]
22	**Ru1**	**PL1**	4	180	200	74.8	35.9 (269) [96.0]	1.5 (11) [4.0]	0 (0) [0]	0 (0) [0]
23[g]	**Ru1**	**PL1**	4	180	200	77.0	35.5 (273) [96.0]	1.5 (12) [4.0]	0 (0) [0]	0 (0) [0]
24	**Ru1**	**PL1**	4	120	200	6.5	1.2 (1) [80.6]	0 (0) [0]	0 (0) [0]	0.6 (0.4) [19.4]
25	**Ru1**	**PL1**	4	150	200	16.3	9.4 (15) [78.9]	1.2 (2) [10.0]	1.1 (2) [2.9]	1.9 (3) [8.2]
26	**Ru1**	**PL1**	4	180	50	8.9	4.1 (4) [69.3]	0.8 (1) [12.8]	0.8 (1) [4.2]	1.6 (1) [13.7]
27	**Ru1**	**PL1**	4	180	100	32.2	18.8 (61) [85.8]	1.6 (5) [7.1]	0.9 (3) [1.4]	2.5 (8) [5.7]
28	**Ru1**	**PL1**	4	180	150	53.4	28.3 (151) [86.2]	2.2 (12) [6.6]	3.1 (17) [3.1]	2.7 (14) [4.1]
29	**Ru1**	**PL6**	2	180	200	23.3	15.2 (35) [87.7]	1.0 (2) [5.7]	1.2 (3) [2.6]	1.4 (3) [4.0]
30	**Ru1**	**PL6**	4	180	200	44.1	29.8 (131) [87.4]	2.2 (10) [6.6]	2.6 (12) [2.5]	2.4 (11) [3.6]
31	**Ru1**	**PL6**	8	180	200	73.2	39.6 (290) [95.6]	1.8 (13) [4.4]	0 (0) [0]	0 (0) [0]
32	**Ru1**	**PL6**	16	180	200	73.5	40.1 (295) [91.0]	1.8 (13) [4.2]	3.3 (24) [2.5]	2.1 (15) [2.3]
33	**Ru1**	**PL1**	2	180	200	24.8	23.6 (59) [85.8]	2.0 (5) [7.3]	2.2 (5) [2.7]	2.5 (6) [4.6]
34	**Ru1**	**PL1**	8	180	200	77.2	47.9 (370) [96.3]	1.8 (14) [3.7]	0 (0) [0]	0 (0) [0]
35	**Ru1**	**PL1**	16	180	200	77.3	57.3 (443) [91.1]	2.4 (19) [3.9]	5.0 (39) [2.7]	3.1 (24) [2.4]
36	**Ru2**	**PL1**	20	180	200	77.5	49.7 (382) [92.7]	2.5 (19) [4.6]	2.9 (14) [2.7]	0 (0) [0]
37[h]	**Ru2**	**PL1**	20	180	200	90.0	50.2 (451) [96.4]	1.8 (16) [3.4]	0.3 (3) [0.2]	0 (0) [0]
38[i]	**Ru2**	**PL1**	20	180	200	88.1	52.3 (461) [95.5]	2.4 (21) [4.3]	0.4 (3) [0.2]	0 (0) [0]
39[j]	**Ru2**	**PL1**	20	180	200	86.0	51.4 (442) [95.4]	2.4 (21) [4.4]	0.4 (3) [0.2]	0 (0) [0]
40[h]	**Ru2**	**PL6**	20	180	200	91.2	54.1 (495) [96.5]	1.2 (11) [3.5]	0 (0) [0]	0 (0) [0]

41[h]	**Ru2**	**PL7**	20	180	200	82.0	30.6 (251) [92.9]	2.2 (18) [6.7]	0.3 (2) [0.4]	0 (0) [0]
42[h]	**Ru2**	**PL8**	20	180	200	82.5	35.8 (296) [94.4]	2.0 (17) [5.4]	0.3 (2) [0.2]	0 (0) [0]

[a] Conditions, methanol (7.5 mL, 185.35 mmol), ethanol (0.75 mL, 12.85 mmol), Ru (0.0128 mmol, 0.1 mol%), PR_3 (0.0384 mmol, 0.3 mol%), mol% is relative to ethanol, 500 rpm stirring, 65 mL autoclave. [b] Total conversion of ethanol to liquid products as determined by GC analysis of the liquid phase. [c] Total yield and selectivity of Guerbet products in the liquid fraction as determined by GC analysis. [d] TON based on mmol of ethanol converted to products per mmol of Ru. [e] **PL1** (0.0128 mmol, 0.1 mol%). [f] 0.2 mol% **PL1** (0.0256 mmol, 0.2 mol%). [g] **PL1** (0.0512 mmol, 0.4 mol%). [h] PR_3 (0.0768 mmol, 0.6 mol%). [i] **PL1** (0.1152 mmol, 0.9 mol%). [j] **PL1** (0.1536 mmol, 1.2 mol%).

5.4.2. Chapter 3: Catalytic Upgrading of Ethanol/Methanol – Full Results:

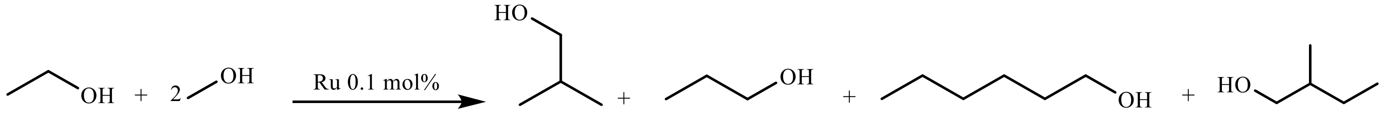

Table 5-3: Full results of catalytic upgrading of ethanol/methanol in Chapter 3.

Run[a]	**Catalyst**	**Ligand (mol%)**	**dppf (mol%)**	**Time**	**Temperature**	**NaOMe (mol %)**	**EtOH Conversion (%)**[b]	**Yield**[c] **(TON)** [d] **[Selectivity] (%)**			
								Isobutanol	***n*-Propanol**	***n*-Hexanol**	**2-Methyl-butan-1-ol**
1	-	-	0.2	20	180	200	0.6	0 (0) [0]	0 (0) [0]	0 (0) [0]	0 (0) [0]
2	**Ru1**	-	0.2	20	180	200	95.9	58.1 (558) [98.2]	1.1 (11) [1.8]	0 (0) [0]	0 (0) [0]
3	**Ru1**	-	0.3	20	180	200	93.5	60.2 (564) [98.5]	1.6 (15) [1.5]	0 (0) [0]	0 (0) [0]
4	**Ru2**	-	0.2	20	180	200	95.9	60.8 (584) [98.4]	1.0 (10) [1.6]	0 (0) [0]	0 (0) [0]
5	**Ru2**	-	0.3	20	180	200	94.6	64.4 (609) [98.1]	1.3 (12) [1.9]	0 (0) [0]	0 (0) [0]
6	**Ru3**	-	0.1	20	180	200	86.7	66.8 (579) [97.2]	1.4 (12) [1.9]	1.8 (16) [0.8]	0 (0) [0]
7	**Ru3**	-	0.2	20	180	200	96.5	80.0 (775) [100]	0 (0) [0]	0 (0) [0]	0 (0) [0]
8	**Ru4**	-	0.1	20	180	200	87.4	46.5 (407) [100]	0 (0) [0]	0 (0) [0]	0 (0) [0]
9	**Ru5**	-	0.1	20	180	200	72.6	15.4 (112) [100]	0 (0) [0]	0 (0) [0]	0 (0) [0]
10	**Ru1**	**PL1** (0.1)	0.1	20	180	200	90.7	70.4 (638) [97.9]	1.6 (15) [2.1]	0 (0) [0]	0 (0) [0]
11	**Ru1**	**PL6** (0.1)	0.1	20	180	200	92.7	76.2 (708) [98.4]	1.2 (11) [1.6]	0 (0) [0]	0 (0) [0]
12	**Ru2**	**PL1** (0.1)	0.2	20	180	200	93.8	72.9 (683) [98.6]	1.0 (9) [1.4]	0 (0) [0]	0 (0) [0]
13	**Ru2**	**PL6** (0.1)	0.2	20	180	200	92.7	72.9 (678) [97.1]	2.2 (20) [2.9]	0 (0) [0]	0 (0) [0]
14	**Ru3**	**PL1** (0.1)	0.2	20	180	200	96.4	68.4 (657) [100]	0 (0) [0]	0 (0) [0]	0 (0) [0]
15	**Ru3**	-	0.2	1	180	200	2.3	3.3 (1) [100]	0 (0) [0]	0 (0) [0]	0 (0) [0]

16	**Ru3**	-	0.2	2	180	200	27.0	11.6 (31) [100]	0 (0) [0]	0 (0) [0]	0 (0) [0]
17	**Ru3**	-	0.2	4	180	200	50.9	35.0 (178) [100]	0 (0) [0]	0 (0) [0]	0 (0) [0]
18	**Ru3**	-	0.2	8	180	200	69.1	46.1 (319) [97.4]	1.2 (8) [2.6]	0 (0) [0]	0 (0) [0]
19	**Ru3**	-	0.2	16	180	200	94.5	73.2 (692) [98.7]	1.0 (9) [1.3]	0 (0) [0]	0 (0) [0]
20	**Ru3**	-	0.2	4	120	200	6.1	1.1 (7) [100]	0 (0) [0]	0 (0) [0]	0 (0) [0]
21	**Ru3**	-	0.2	4	150	200	10.4	4.3 (4) [100]	0 (0) [0]	0 (0) [0]	0 (0) [0]
22	**Ru3**	-	0.2	4	180	50	0.7	0.4 (0.03) [100]	0 (0) [0]	0 (0) [0]	0 (0) [0]
23	**Ru3**	-	0.2	4	180	100	10.3	1.1 (1) [100]	0 (0) [0]	0 (0) [0]	0 (0) [0]
24	**Ru3**	-	0.2	4	180	150	18.8	4.3 (8) [100]	0 (0) [0]	0 (0) [0]	0 (0) [0]
25	**Ru3**	Dppb (0.2)	-	20	180	200	92.5	64.3 (595) [95.6]	3.8 (35) [3.4]	2.1 (19) [1.0]	0 (0) [0]
26	**Ru3**	Dpephos (0.2)	-	20	180	200	84.9	54.2 (460) [88.8]	5.2 (44) [8.5]	0.9 (7) [0.5]	2.7 (23) [2.2]
27	**Ru3**	Dppb (0.2)	-	2	180	200	28.9	7.2 (21) [95.9]	0 (0) [0]	0 (0) [0]	0.6 (2) [4.1]
28	**Ru3**	Dppb (0.2)	-	4	180	200	68.1	29.8 (203) [94.9]	1.3 (9) [4.2]	0.9 (6) [0.9]	0 (0) [0]
29	**Ru3**	Dppb (0.2)	-	8	180	200	67.5	38.8 (262) [94.5]	2.5 (17) [4.9]	0.9 (6) [0.6]	0 (0) [0]
30	**Ru3**	Dppb (0.2)	-	16	180	200	82.7	47.2 (390) [92.9]	2.6 (22) [6.1]	1.3 (11) [1.0]	0 (0) [0]

[a] Conditions, methanol (7.5 mL, 185.35 mmol), ethanol (0.75 mL, 12.85 mmol), Ru (0.0128 mmol, 0.1 mol%), mol% is relative to ethanol, 500 rpm stirring, 65 mL autoclave. [b] Total conversion of ethanol to liquid products as determined by GC analysis of the liquid phase. [c] Total yield and selectivity of Guerbet products in the liquid fraction as determined by GC analysis. [d] TON based on mmol of ethanol converted to products per mmol of Ru.

5.4.3. Chapter 4: Catalytic Upgrading of Ethanol/Methanol – Full Results:

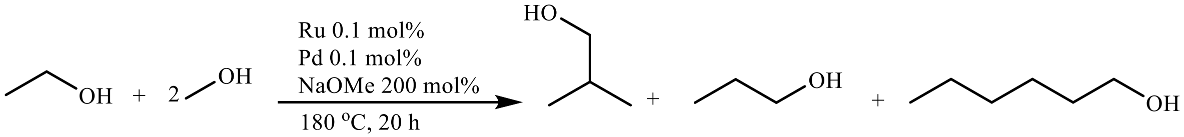

Table 5-4: Full results of catalytic upgrading of ethanol/methanol in Chapter 4.

Run [a]	**Pd Catalyst**	**Ru Catalyst**	**Ligand (mol%)**	**EtOH Conversion (%)** [b]	**Yield** [c] **(TON)** [d] **[Selectivity] (%)**		
					Isobutanol	***n*-Propanol**	***n*-Hexanol**
1	**4.7**	-	-	33.5	6.4 (21.5) [96.5]	0 (0) [0]	0.7 (2.3) [3.5]
2	**4.8**	-	-	48.3	4.9 (23.7) [100]	0 (0) [0]	0 (0) [0]
3	**4.9**	-	-	42.7	6.7 (28.8) [98.7]	0 (0) [0]	0.3 (1.3) [1.3]
4	**4.10**	-	-	39.7	4.6 (18.3) [100]	0 (0) [0]	0 (0) [0]
5	**4.11**	-	-	44.3	1.8 (8.0) [93.1]	0.4 (1.8) [6.9]	0 (0) [0]
6	**4.12**	-	-	38.1	3.1 (11.9) [95.2]	0 (0) [0]	0.5 (1.9) [4.8]
7	**4.13**	-	-	57.4	8.2 (46.8) [96.4]	0 (0) [0]	0.4 (2.3) [3.6]
8	**4.9**	**Ru1**	**PL1** (0.3)	71.6	50.5 (180) [85.4]	4.1 (16) [6.9]	10.6 (39) [7.7]
9	**4.13**	**Ru1**	**PL1** (0.3)	75.1	58.1 (219) [89.2]	3.1 (12) [4.7]	9.8 (35) [6.1]
10	**4.9**	**Ru1**	dppf (0.2)	69.2	36.9 (129) [95.3]	1.5 (4) [4.0]	0.9 (4) [0.8]
11	**4.13**	**Ru1**	dppf (0.2)	82.8	42.6 (176) [96.8]	1.1 (4) [2.6]	0.9 (4) [0.6]
12	**4.9**	**Ru3**	dppf (0.2)	89.8	55.6 (250) [93.8]	2.5 (12) [4.2]	3.2 (16) [2.0]
13	**4.13**	**Ru3**	dppf (0.2)	90.7	57.0 (258) [94.1]	2.3 (12) [3.8]	3.3 (16) [2.0]

[a] Conditions, methanol (7.5 mL, 185.35 mmol), ethanol (0.75 mL, 12.85 mmol), Pd (0.0128 mmol, 0.1 mol%), Ru (0.0128 mmol, 0.1 mol%), NaOMe (34.26 mmol, 200 mol%), mol% relative to ethanol, 180 °C, 20h, 500 rpm stirring, 65 mL autoclave. [b] Total conversion of ethanol to liquid products as determined by GC analysis of the liquid phase. [c] Total yield and selectivity of Guerbet products in the liquid fraction as determined by GC analysis. [d] TON based on mmol of ethanol converted to products per mmol of catalyst.

5.5. X-ray Crystallographic Data:

Table 5-5: Crystal data and structure refinement for **4.7**

Identification Code	**4.7**
Empirical Formula	$C_{21}H_{27}ClN_2Pd$
Formula Weight	449.9
Temperature/K	200(2)
Wavelength/Å	0.71073
Crystal System	Orthorhombic
Space Group	Pbca
a/Å	12.7191(5)
b/Å	15.6100(6)
c/Å	21.2859(8)
α/°	90
β/°	90
γ/°	90
Volume/$Å^3$	4226.2(3)
Z	8
Density (Calculated)/Mg/cm^3	1.412
Absorption Coefficient/mm^{-1}	1.010
F(000)	1840
Crystal Size mm^3	0.210 x 0.180 x 0.110
Theta Range for Data Collection	3.459 to 29.915°
Index Ranges	-17<=h<=12, -21<=k<=20, -17<=l<=28
Reflections collected	18646
Independent reflections	5306 [R(int) = 0.0264]
Completeness of Theta = 25.242°	99.8%
Absorption Correction	Gaussian
Max. and Min. Transition	1.000 and 0.783
Refinement Method	Full-matrix least-squares on F^2
Data/Restraints/Parameters	5306 / 0 / 233
Goodness-of-fit on F^2	1.097
Final R indexes [I>=2σ (I)]	R1 = 0.0416, wR2 = 0.1018
Final R indexes [all data]	R1 = 0.0652, wR2 = 0.1168
Extension Coefficient	n/a
Largest diff. peak/hole / e $Å^{-3}$	0.815 and -0.665

Table 5-6: Crystal data and structure refinement for **4.8**

Identification Code	**4.8**
Empirical Formula	$C_{30.5}H_{43}ClN_2Pd$
Formula Weight	579.52
Temperature/K	200(2)
Wavelength/Å	1.54184
Crystal System	Monoclinic
Space Group	P 21/c
a/Å	15.6107(9)
b/Å	15.2712(5)
c/Å	14.9934(9)
α/°	90
β/°	118.634
γ/°	90
Volume/$Å^3$	3137.2(4)
Z	4
Density (Calculated)/Mg/cm^3	1227
Absorption Coefficient/mm^{-1}	5.681
F(000)	1212
Crystal Size mm^3	0.290 x 0.240 x 0.030
Theta Range for Data Collection	4.335 to 72.437°
Index Ranges	-19<=h<=18, -18<=k<=18, -18<=l<=15
Reflections collected	8365
Independent reflections	5341 [R(int) = 0.0360]
Completeness of Theta = 67.684°	99.8%
Refinement Method	Full-matrix least-square F^2
Data/Restraints/Parameters	5341 / 7 / 319
Goodness-of-fit on F^2	1.053
Final R indexes [I>=2σ (I)]	R1 = 0.0758, wR2 = 0.2072
Final R indexes [all data]	R1 = 0.0865, wR2 = 0.2240
Extension Coefficient	n/a
Largest diff. peak/hole / e $Å^{-3}$	1.143 and -1.162

Table 5-7: Crystal data and structure refinement for **4.9**

Identification Code	**4.9**
Empirical Formula	$C_{27}H_{39}N_5Pd$
Formula Weight	540.03
Temperature/K	200(2)
Wavelength/Å	1.54184
Crystal System	Orthorhombic
Space Group	P 21 21 21
a/Å	13.0075(3)
b/Å	13.8577(3)
c/Å	30.5052(6)
α/°	90
β/°	90
γ/°	90
Volume/Å^3	5498.7(2)
Z	8
Density (Calculated)/Mg/cm^3	1.305
Absorption Coefficient/mm^{-1}	5.604
F(000)	2256
Crystal Size mm^3	0.330 x 0.200 x 0.060
Theta Range for Data Collection	3.503 to 72.974°
Index Ranges	-15<=h<=14, -16<=k<=11, -37<=l<=31
Reflections collected	20571
Independent reflections	10654 [R(int) = 0.0346]
Completeness of Theta = 67.684°	99.9%
Absorption Correction	Gaussian
Max. and Min. Transition	1.000 and 0.594
Refinement Method	Full-matrix least-square on F^2
Data/Restraints/Parameters	10654 / 39 / 633
Goodness-of-fit on F^2	1.016
Final R indexes [I>=2σ (I)]	R1 = 0.0346, wR2= 0.0790
R indexes [all data]	R1 = 0.0376, wR2 = 0.0813
Extension Coefficient	n/a
Largest diff. peak/hole / e Å^{-3}	0.412 and -0.574

Table 5-8: Crystal data and structure refinement for **4.10**

Identification Code	**4.10**
Empirical Formula	$C_{30.50}H_{43}Cl_{0.56}N_{2.43}O_{1.31}Pd$
Formula Weight	591.11
Temperature/K	200(2)
Wavelength/Å	1.54184
Crystal System	Monoclinic
Space Group	P 21/c
a/Å	15.5793(11)
b/Å	15.2563(6)
c/Å	15.0120(10)
α/°	90
β/°	118.591(9)
γ/°	90
Volume/Å^3	3133.0(4)
Z	4
Density (Calculated)/Mg/cm^3	1.253
Absorption Coefficient/mm^{-1}	5.402
F(000)	1236
Crystal Size mm^3	0.289 x 0.154 x 0.043
Theta Range for Data Collection	4.341 to72.827^o
Index Ranges	-15<=h<=18, -16<=k<=18, -16<=l<=18
Reflections collected	11980
Independent reflections	6064 [R(int) = 0.0315]
Completeness of Theta = 67.684^o	100.0%
Absorption Correction	Gaussian
Max. and Min. Transition	1.000 and 0.601
Refinement Method	Full-matrix least-square on F^2
Data/Restraints/Parameters	6064 / 205 / 400
Goodness-of-fit on F^2	1.030
Final R indexes [I>=2σ (I)]	R1 = 0.0548, wR2 = 0.1454
R indexes [all data]	R1 = 0.0713, wR2 = 0.1638
Extension Coefficient	n/a
Largest diff. peak/hole / e Å^{-3}	0.584 and -1.077

Table 5-9: Crystal data and structure refinement for **4.11**

Identification Code	**4.11**
Empirical Formula	$C_{55}H_{42}BF_{24}N_3Pd$
Formula Weight	1318.12
Temperature/K	200(2)
Wavelength/Å	154184
Crystal System	Triclinic
Space Group	P -1
a/Å	21.3056(5)
b/Å	25.7420(6)
c/Å	33.2741(7)
α/°	78.134(2)
β/°	81.989(2)
γ/°	78.883(2)
Volume/Å^3	17429.3(7)
Z	12
Density (Calculated)/Mg/cm^3	1.507
Absorption Coefficient/mm^{-1}	3.627
F(000)	7920
Crystal Size mm^3	0.260 x 0.250 x 0.160
Theta Range for Data Collection	3.522 to 73.040°
Index Ranges	-26<=h<=26, -31<=k<=31, -30<=l<=41
Reflections collected	132768
Independent reflections	67670 [R(int) = 0.0441]
Completeness of Theta = 67.684°	99.8%
Refinement Method	Full-matrix-block least-squares on F^2
Data/Restraints/Parameters	67670 / 864 / 4585
Goodness-of-fit on F^2	1.028
Final R indexes [I>=2σ (I)]	R1 = 0.0835, wR2 = 0.2339
R indexes [all data]	R1 = 0.1123, wR2 = 0.2774
Extension Coefficient	n/a
Largest diff. peak/hole / e Å^{-3}	2.704 and -2.079

Table 5-10: Crystal data and structure refinement for **4.12**

Identification Code	**4.12**
Empirical Formula	$C_{61}H_{54}BF_{24}N_3Pd$
Formula Weight	1402.28
Temperature/K	296(2)
Wavelength/Å	0.71073
Crystal System	Triclinic
Space Group	P -1
a/Å	10.2518(4)
b/Å	17.8760(7)
c/Å	19.2834(8)
α/°	108.892(4)
β/°	97.945(3)
γ/°	92.183(3)
Volume/Å^3	3298.5(2)
Z	2
Density (Calculated)/Mg/cm^3	1.412
Absorption Coefficient/mm^{-1}	0.388
F(000)	1416
Crystal Size mm^3	0.397 x 0.317 x 0.208
Theta Range for Data Collection	3.281 to 29.756°
Index Ranges	-13<=h<=13, -24<=k<=23, -25<=l<=26
Reflections collected	35445
Independent reflections	15769 [R(int) = 0.0311]
Completeness of Theta = 25.242°	99.7%
Absorption Correction	Gaussian
Max. and Min. Transition	1.000 and 0.612
Refinement Method	Full-matrix least-squares on F^2
Data/Restraints/Parameters	15769 / 2256 / 1087
Goodness-of-fit on F^2	1.030
Final R indexes [I>=2σ (I)]	R1 = 0.0553, wR2 = 0.1260
R indexes [all data]	R1 = 0.0925, wR2 = 0.1517
Extension Coefficient	n/a
Largest diff. peak/hole / e Å^{-3}	0.411 and -0.496

Table 5-11: Crystal data and structure refinement for **4.13**

Identification Code	**4.13**
Empirical Formula	$C_{77}H_{66}BF_{24}N_2PPd$
Formula Weight	1623.49
Temperature/K	200(2)
Wavelength/Å	0.71073
Crystal System	Triclinic
Space Group	P î
a/Å	12.9825(4)
b/Å	16.3693(6)
c/Å	18.8717(5)
α/°	110.117(3)
β/°	92.007(2)
γ/°	93.286(3)
Volume/Å^3	3753.2(2)
Z	2
Density (Calculated)/Mg/cm^3	1.437
Absorption Coefficient/mm^{-1}	0.372
F(000)	1648
Crystal Size mm^3	0.500 x 0.360 x 0.320
Theta Range for Data Collection	3.428 to 29.941°
Index Ranges	-13<=h<=18, -19<=k<=21, -25<=l<=24
Reflections collected	38273
Independent reflections	18224 [R(int) = 0.0272]
Completeness of Theta = 25.242°	99.7%
Absorption Correction	Gaussian
Max. and Min. Transition	1.000 and 0.265
Refinement Method	Full-matrix least-squares on F^2
Data/Restraints/Parameters	18224 / 1692 / 1160
Goodness-of-fit on F^2	1.029
Final R indexes [I>=2σ (I)]	R1 = 0.0468, wR2 = 0.1112
R indexes [all data]	R1 = 0.0626, wR2 = 0.1231
Extension Coefficient	n/a
Largest diff. peak/hole / e Å^{-3}	0.877 d -0.784

5.6. References:

[1] a) G. Sheldrick, *Acta Crystallographica Section A: Structural Chemistry* **2015**, *71*, 3; b) G. Sheldrick, *Acta Crystallographica Section C: Structural Chemistry* **2015**, *71*, 3.

[2] G. Pampaloni, G. Ricci, A. Sommazzi, M. Guelfi, G. Leone and F. Masi, *Bis-Imine Titanium Complex, Catalytic System Comprising Said Bis-Imine Titanium Complex and Process for the (Co) Polymerisation of Conjugated Dienes*, US Patent *11299505 B2*, **2022**.

[3] R. S. Erami, D. Díaz-García, S. Prashar, A. Rodríguez-Diéguez, M. Fajardo, M. Amirnasr and S. Gómez-Ruiz, *Catalysts* **2017**, *7*, 76.

[4] E. V. Salo and Z. Guan, *Organometallics* **2003**, *22*, 5033-5046.

[5] M. S. Brookhart, L. K. Johnson, C. M. Killian, E. F. McCord, S. J. McLain, K. A. Kreutzer, S. D. Ittel and D. J. Tempel, *Highly Branched Olefin Polymers and Their Uses.* US Patent *5880241*, **1999**.

[6] L. K. Johnson, C. M. Killian and M. Brookhart, *Journal of the American Chemical Society* **1995**, *117*, 6414-6415.